Department of Physics and Astronomy

Concentrating Solar Thermal Energy Storage Using Amide-Hydride Systems

Tam Thanh Nguyen

This thesis is presented for the Degree of
Doctor of Philosophy
of
Curtin University

November 2017

DECLARATION

To the best of my knowledge and belief this thesis contains no material previously published by any other person except where due acknowledgment has been made.

This thesis contains no material which has been accepted for the award of any other degree or diploma in any university.

Signature: _____

Tam Thanh Nguyen

Date: 15/11/17

ABSTRACT

In the imminent future, increasing energy demands will deplete fossil fuels leading to increased environmental concerns. This impending issue can be alleviated with renewable and sustainable energy sources such as solar energy, which is an abundant source of renewable energy. Furthermore, Australian deserts receive higher amounts of solar radiation than in any other country. Solar power can be utilised with focal mirrors to concentrate solar radiation onto a small area. From the conversion of solar energy to heat, Stirling engines are used to generate electricity. However, harnessing this solar power can be impractical because of the intermittent nature of the sun. Therefore, thermal storage systems can be utilised to provide thermal energy in the absence of solar energy.

The aim of this thesis is to investigate amide-imide-hydride systems for their potential as concentrated solar thermal energy storage systems. Reactions involving amides ($M_x(NH_2)_y$) and imides ($M_x(NH)_y$) with hydrides (MH_x) can be used to store heat by taking advantage of their endothermic/exothermic reactions with hydrogen. Lithium-, magnesium- and calcium-based amide-imide-hydride systems and their mixtures were investigated as potential candidates for high-temperature (> 600 °C) thermal energy storage. The hydrogen desorption during imide-hydride to nitride (M_xN_y) reactions were prioritised as they occur at high temperatures suitable for thermal energy storage. Hydrogen desorption from the amide-hydride reactions were also investigated to check the purity of as-synthesised starting reagents. Furthermore, amide-hydride reactions were investigated to reproduce the results from literature as they have been widely studied for their hydrogen storage properties at relatively low temperatures.

The following techniques were used to characterise amide-imide-nitride-hydride systems: X-ray diffraction (XRD) analysis, *in situ* synchrotron X-ray diffraction (SXRD) analysis, Fourier transform infra-red (FTIR) spectrometry, temperature programmed desorption (TPD) with the volumetric method (VM) and mass spectrometry (MS), pressure-composition-temperature (PCT) measurements and temperature programmed photographic analysis (TPPA). A novel method was also developed to obtain fast thermodynamic data by heating samples in a low volume apparatus (LVA) to maintain a near-constant hydrogen content

(NCHC) in order to satisfy the conditions to plot the van't Hoff equation. The LVA-NCHC method was developed specifically for systems with sloping plateaux (slow kinetics) that were typically observed in amide-imide-hydride systems.

The imide-hydride reaction pathway in the Li–N–H system does not proceed as expected because the imide-hydride reaction, Li_2NH + LiH (1:1), forms a solid solution of the imide and nitride hydride instead of lithium nitride (Li_3N). Inconclusive results were found in the Mg–N–H system as magnesium imide and magnesium iron hydride, MgNH + Mg_2FeH_6 (4:1), required impractical pressures (> 140 bar) at 400 °C. The thermodynamics of calcium nitride hydride, Ca_2NH + H_2 (1:1), in the Ca–N–H system were evaluated using the LVA-NCHC method. The results calculated a practical heat storage capacity of 959 ± 58 kJ kg^{-1}. Furthermore, an equilibrium hydrogen pressure of ~31 bar was predicted at an operating temperature of ~800 °C, conditions suitable for high-temperature thermal energy storage.

The hydrogenation of lithium magnesium nitride, LiMgN + H_2 (2:1), in the Li–Mg–N–H mixed system revealed a reversible hydrogen content of 1.2 wt% at 450 °C. However, the anticipated nitride product from the imide-hydride reaction did not occur at temperatures ≤ 500 °C. The anticipated formation of lithium calcium nitride (LiCaN) from the imide-hydride reactions, $Li_2Ca(NH)_2$ + LiH (1:2) and CaNH + LiH (1:1), in the Li–Ca–N–H mixed system was also not observed at temperatures ≤ 500 °C. However, the hydrogenation of LiCaN was observed at temperatures ≤ 650 °C and was estimated to have a practical heat storage capacity that ranges between 977 and 1371 kJ kg^{-1}. Therefore, the Li–Ca–N–H system has potential in high temperature applications. Magnesium amide/imide and sodium magnesium hydride in the Na–Mg–N–H system was revealed to operate at temperatures (~350 °C) not applicable for thermal energy storage.

The outcome revealed that the most potential systems for high-temperature thermal energy storage were calcium-based systems and mixed systems with calcium metal. The other systems resulted in irreversible reactions or imide-hydride reactions that occurred at non-applicable temperatures. However, the characterisation of these low-cost metal hydrides systems can be beneficial to the academic community in other applications such as hydrogen storage.

ACKNOWLEDGEMENTS

I would like to acknowledge many people for their help in the completion of this thesis. First and foremost, my humblest gratitude goes to both my supervisors, Dr. Drew Sheppard and Prof. Craig Buckley. Prof. Craig Buckley for giving me the opportunity to undertake this PhD project and Dr. Drew Sheppard for his outstanding guidance and supervision throughout this long four-year journey, you have taught me valuable lessons in research and academia. I would also like to acknowledge Dr. Mark Paskevicius for his supervision during the early years of my PhD before his transfer to Aarhus University and Dr. Brendan McGann as the chairperson of thesis committee. For financial support, I would like to thank Curtin University for providing a Curtin University Post-Graduate Scholarship (CUPS) and the Australian Commonwealth Government for providing an Australian Postgraduate Award (APA).

The completion of this thesis would not have been possible without the old and new Hydrogen Storage Research Laboratory at Curtin University. I would like to acknowledge the Powder Diffraction beamline facility at the Australian Synchrotron in Melbourne (Australia) and Dr. Kane O' Donell for his assistance. I am grateful to Dr. Catherine Kealley, Ms. Veronica Avery and Dr. Mathew Rowles for their training and assistance with XRD measurements and TOPAS analysis. An honourable mention goes to Mr. Peter Chapman from the Resources and Chemistry Precinct at Curtin University for his assistance with FTIR measurements. I would like to take this opportunity to thank the past and present members of the Hydrogen Storage Research Group for providing a friendly atmosphere and great support throughout the years. Special mentions go to Payam Javadian, Dr. Terry Humphries, Dr. Kevin Jarret, Dr. Veronica Sofianos, Dr. Petra Szilagyi, Dr. Anna-Lisa Chaudhary, Enrico Ianni, Mariana Tortoza and Arnaud Griffond.

I must also extend my gratitude to all the staff members in the Department of Physics and Astronomy for providing helpful advice and those who helped me with documentation and paperwork. A special mention to the late Melat Habtemariam who was always happy to help with all my urgent enquiries and dilemmas, such as locking myself outside buildings.

Acknowledgements

I would like to acknowledge my mum and dad for providing food, shelter and loving support, even though they do not understand what it is I do. The boys will not receive any acknowledgement for the completion of this thesis. However, thanks for all the laughter and endless banter.

Finally, the completion of this thesis would not have been possible without my best friend and better half, Kimberley Hoang. Thanks for all the loving support and sticky notes of endearment! Thank you for believing in me and helping me believe in myself. You have helped me in many ways possible and I am glad you were a part of my life in this long difficult journey.

PRESENTATIONS AND PUBLICATIONS

Nguyen, Tam T., Drew A. Sheppard, Mark Paskevicius, and Craig E. Buckley. "Lithium Amides For Thermal Storage Using Amide-Hydride Systems." *Presentation at the Australian X-Ray Association (AXAA) Conference, Perth, Australia, February 9–13, 2014*.

Nguyen, Tam T. "Concentrated Solar Thermal (CST) Energy Storage using Metal Hydrides." *Presentation on behalf of* Craig E. Buckley *at the Australia-China Symposium on Energy, Taiyuan, China, May 13–15, 2014*.

Nguyen, Tam T., Drew A. Sheppard, Mark Paskevicius, and Craig E. Buckley. "Amide/Imide-hydride systems for high temperature heat storage in concentrated solar thermal systems." *Poster session presented at the 15th International Symposium Metal-Hydrogen Systems, Interlaken, Switzerland, August 7–12, 2016.*

Nguyen, Tam T.*, Drew A. Sheppard, and Craig E. Buckley. 2017. "Lithium imide systems for high temperature heat storage in concentrated solar thermal systems." *Journal of Alloys and Compounds* 716: 291 – 298. doi: 10.1016/j.jallcom.2017.04.208.

* Full publication is available in Appendix C

TABLE OF CONTENTS

LIST OF FIGURES

LIST OF TABLES

LIST OF ABBREVIATIONS

CST	Concentration Solar Thermal
PPM	Parts Per Million
HT	High Temperature
LT	Low Temperature
$M_x(NH_2)_y$	Metal Amides
$M_x(NH)_y$	Metal Imides
M_xN_y	Metal Nitrides
RPM	Revolutions Per Minute
BTP	Ball To Powder
THF	Tetrahydrofuran
FEP	Fluorinated Ethylene Propylene
XRD	X-Ray Diffraction
SXRD	Synchrotron X-Ray Diffraction
FTIR	Fourier Transform Infra-Red
TPD	Temperature Programmed Desorption
MS	Mass Spectrometry
VM	Volumetric Method
PCT	Pressure-Composition-Temperature
TPPA	Temperature Programmed Photographic Analysis
LVA	Low Volume Apparatus
NCHC	Near-Constant Hydrogen Content
H/M	Hydrogen to Metal atomic ratio

CHAPTER 1: INTRODUCTION AND OVERVIEW

1.1 Energy in Australia

Hydrogen is touted as one of the solutions for future energy requirements. The reliance on the limited amount of fossil fuels has led to investigations of alternative forms of clean reliable energy. The use of fossil fuels also impacts the environment by increasing carbon dioxide levels (Panwar, Kaushik and Kothari 2011). Therefore, by minimising the use of fossil fuels, the consumption of fossil fuels can be prolonged until an alternative solution is discovered, improving the sustainability and preservation of life on earth. Wind, solar and tidal energy forms have been investigated to this cause. Every year, Australia receives an average of 5.8×10^{22} J of solar radiation, which is approximately 10,000 times more than its total energy consumption. However, solar energy only accounted for 0.2% of Australia's total primary energy consumption in 2011–12 (Geoscience Australia and Bureau of Resources and Energy Economics 2014). Unfortunately, solar energy is problematic due to its intermittent supply, but more importantly the production of solar energy is clean and does not harm the environment, despite having an energy density inferior to fossil fuels. The International Energy Agency (IEA) have set goals to limit the global increase in temperature by limiting the concentration of greenhouse gases (carbon dioxide). It is projected that by 2035, more than 6% of global electricity will be produced from solar photovoltaics (PV) and concentrating solar thermal (CST) to limit the concentration of greenhouse gases in the atmosphere to 450 parts per million (ppm) (International Energy Agency 2010).

1.2 Solar Thermal Energy

In order to overcome problems with solar energy, such as the intermittent supply, seasonal variance, and unpredictable weather conditions; energy storage systems are required. Thermal storage systems that utilise solar energy are the most efficient and effective means of storage as it avoids the need to convert energy from one form to another (Dinçer and Rosen 2002). There are three main

types of thermal energy storage systems: sensible, latent and chemical. The simplest 'sensible' heat storage system is typically comprised of binary liquid molten salt mixtures (60% $NaNO_3$; 40% KNO_3). However, large volumes of molten salts are required to sufficiently transfer heat (Abedin and Rosen 2011). The 'Andasol' is the first commercial solar thermal power plant, located in Spain, and requires 28,500 tons of molten salt to provide an electricity output of 50 megawatts with 7.5 hours of energy storage (Solar Millennium AG 2013). A different approach to thermal storage uses phase change materials where the 'latent' heat associated with the change of a substance from one phase to another at a fixed temperature is exploited (Abedin and Rosen 2011). However, phase change materials have a disadvantage of slow charging and discharging rates, and low thermal conductivity leading to inadequate heat transfer (Soares et al. 2013). Thermochemical energy storage is a type of 'chemical' thermal storage with the potential for high energy density and is only recently being considered intensively (Abedin and Rosen 2011). Energy is stored via an endothermic dissociation reaction whereby the heat can then be recovered by reversing the chemical reaction. However, the efficiency and design factors of these systems are not well understood (Abedin and Rosen 2011).

1.3 Concentrated Solar Thermal Coupled Hydride System

The aim of this thesis is to investigate the potential of metal hydrides as efficient thermal storage systems for concentrated solar thermal (CST) energy. A solar thermal energy storage system using metal hydrides will work much like the three main types of thermal energy storage systems with an advantage of requiring a substantially smaller volume. As shown in Figure 1.1, the schematic illustrates how concentrated solar energy is collected and used in the form of heat to power a turbine or Stirling engine to generate electricity. During the day, any excess heat is used to release hydrogen (thereby storing heat in an endothermic reaction) from the high temperature (HT) hydride bed to be absorbed by the low temperature (LT) hydride bed (Figure 1.1a). During the night, when the HT hydride bed is allowed to cool, the reverse reaction takes place, which is exothermic. The released hydrogen from the LT hydride bed is absorbed by the

HT hydride bed, releasing useful heat that can be used by the turbine or Stirling engine to generate electricity (Figure 1.1b). This design concept started in the early 1990s with the development of catalysed magnesium hydride (MgH_2) coupled with alloy 5800 (based on $TiMn_{1.5}$) as the HT hydride and LT hydride, respectively (Groll, Isselhorst and Wierse 1994; Wierse, Werner and Groll 1991). Recently, a thermal energy storage prototype has already been investigated using TiH_x ($1.53 \leq x \leq 1.75$) that operated at temperatures > 600 °C and hydrogen pressures < 5 bar with a 95% efficiency rating after 60 cycles (Rönnebro et al. 2015).

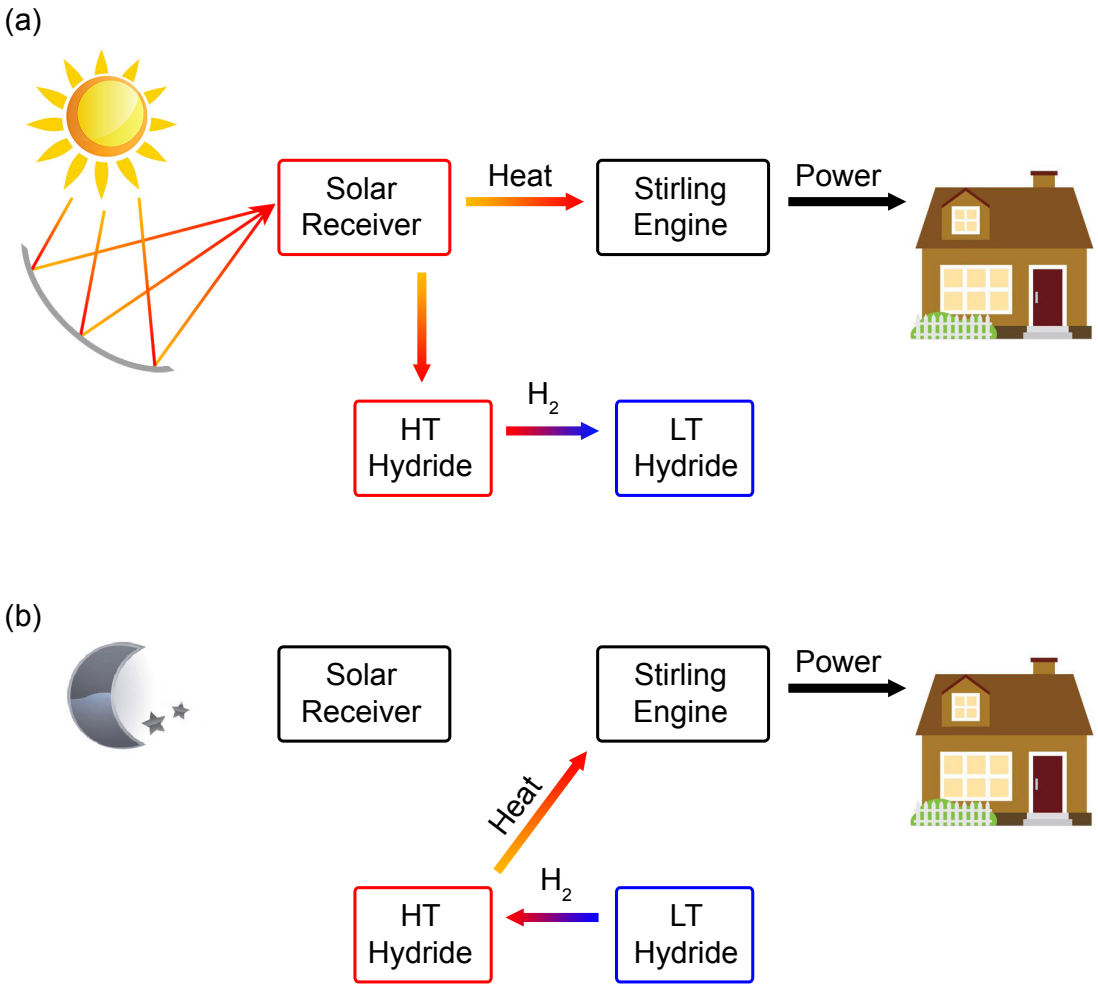

Figure 1.1: Concentrating solar thermal coupled hydride system using metal hydrides as a thermal storage medium during the (a) day and (b) night.

1.4 Metal Hydrides

Many metals and metal alloys can combine with hydrogen to form metal hydrides. One of the major benefits of utilising metal hydrides for thermal storage is that a large degree of research has already been undertaken on the use of hydrogen storage materials for mobile applications. Metal hydrides have a unique property in that they can absorb and desorb hydrogen at constant pressure. The reaction direction can be easily controlled by simply changing the applied hydrogen pressure or temperature. These reversible reactions are exothermic and endothermic, where the heat required for hydrogen desorption is approximately the same as that generated during absorption, which is why metal hydrides have been proposed as potential thermochemical energy stores (Sandrock and Snape 1986).

The hydrogen capacity is the amount of available hydrogen content or transferable hydrogen within a system. Generally, the higher the hydrogen capacity, the better, which is desirable for mobile applications such as hydrogen storage for vehicles, but is not necessarily a major factor in stationary applications such as a CST energy storage system (Sandrock, Suda and Schlapbach 1992). However, the hydrogen capacity is certainly important with regards to the cost of a thermal energy storage system. The hydrogen capacity can be determined from pressure-composition-temperature (PCT) plots, where the van't Hoff plots can be used to determine the heat storage capacity. In the case of a coupled system, the operating conditions and properties of the high temperature hydride bed, determines the amount of hydrogen that is required in the closed system.

Thermal energy storage using metal hydrides has been investigated since the mid-1970s by Libowitz (1974), but was generally applied at temperatures < 200 °C due to the limited number of hydrides known at the time. In the 1990s, the study of catalysed MgH_2 and its rapid hydrogen sorption kinetics, led to the application of metal hydrides for solar thermal energy storage at temperatures between 300 °C and 500 °C (Bogdanović, Ritter and Spliethoff 1990; Bogdanovic, Ritter and Spliethoff 1989; Groll, Isselhorst and Wierse 1994). Metal hydrides have demonstrated their engineering feasibility in a large number of

energy-related applications (Sandrock, Suda and Schlapbach 1992; Suda 1987). Therefore, with the commercialisation of CST power using parabolic troughs and power towers, metal hydrides have the potential to be the next generation of thermal energy storage media (Fellet et al. 2013; Harries et al. 2012; Lai et al. 2015; Sheppard et al. 2016).

Research for this thesis will be focused on high-temperature hydrides based on amides, imides and their mixtures with ionic hydrides, but the low-temperature hydride may be of the common intermetallic compounds (i.e. AB, AB_2, AB_5 and A_2B). The A elements (e.g. Ti, Zr, Ca, La or other rare earth elements, and Mg) tend to be expensive because of the energy required to isolate them from their ores (Sandrock, Suda and Schlapbach 1992). The cost of producing such metal hydrides can be high, especially for those that require special techniques or are sensitive to stoichiometry or impurities. Furthermore, the bulk production of metal hydrides will also differ from the small-scale methods, resulting in higher production costs (Harries et al. 2012).

With the vast amount of metal hydrides studied for different types of applications, only a small number have been considered for thermochemical heat storage. Amides ($M_x(NH_2)_y$), imides ($M_x(NH)_y$) and their mixtures with ionic hydrides (MH_x) (where M is a cation, usually an alkali or alkaline earth metal) are the focus of this thesis as potential high-temperature hydrides. The hydrogen release from the amide- and imide-hydride reactions have relatively high hydrogen content and potentially low cost. Lithium nitride (Li_3N) has been reported by Chen et al. (2002) to decompose in a two-step reaction, forming an imide-hydride (Equation 1.1) and amide-hydride product (Equation 1.2).

$$Li_3N + H_2 \leftrightarrow Li_2NH + LiH \tag{1.1}$$

$$Li_2NH + H_2 \leftrightarrow LiNH_2 + LiH \tag{1.2}$$

In the reverse reaction, lithium amide ($LiNH_2$) and lithium hydride (LiH) react to form lithium imide (Li_2NH) with a release of hydrogen at temperatures below 200 °C, this interaction is regarded as the amide-hydride reaction (Chen et al. 2003; Ichikawa et al. 2004; Equation 1.2). Li_2NH further reacts with LiH to form

Li_3N with a secondary release of hydrogen at temperatures above 320 °C, which is referred to as the imide-hydride reaction (Pinkerton 2005; Equation 1.1). The majority of the research on amides, imides and its mixtures with ionic hydrides have been attempts at lowering the operation temperature for vehicular applications; hence, no studies to date explore the high temperature reactions in the imide-nitride-hydride system (Xiong et al. 2004). In stationary applications, especially in CST energy storage systems, the high-temperature imide-hydride reactions make it a promising material for thermal energy storage.

1.5 The Potential of Metal Amides, Imides and Nitrides for High Temperature Thermal Energy Storage

Metal (M) hydrides that contain nitrogen (N) are known as amides ($M_x(NH_2)_y$) or imides ($M_x(NH)_y$), where M is usually an alkali or alkaline earth metal. The decomposition of pure metal amides involves the release of ammonia, where the addition of an ionic hydride (MH_x) quickly reacts with ammonia (NH_3) such that hydrogen can be released (Bergstrom and Fernelius 1933). These amide-hydride to imide reactions have been the focus of hydrogen storage research due to their reversibility at low operating temperatures (< 200 °C) and modest hydrogen capacity (2.0 – 7.4 wt%), but they suffer from poor kinetics that limits their practical use (Chen et al. 2002; Jain, Jain and Jain 2010). The challenge with metal amide-hydride reactions is to maximise the amount of hydrogen release with the minimal amount of ammonia release to optimise the reversibility of the system.

The imide-hydride ($M_x(NH)_y$–MH_x) to nitride (M_xN_y) reaction occurs at much higher temperatures (> 200 °C) due to the stability of imides that make it a potential candidate for high temperature thermal storage (Xiong et al. 2004; Zhang and Hu 2012). However, because of the limited number of known hydrides at the time, early studies of metal hydrides for thermal energy storage were generally focused on systems operating at temperatures < 200 °C (Bogdanović, Ritter and Spliethoff 1990; Bogdanović et al. 1999; Groll, Isselhorst and Wierse 1994). Metal hydrides used exclusively for thermal energy storage have only been studied since the mid–1970s (Libowitz 1974). With the success of CST power plants, the

next generation of thermal storage material could possibly be metal hydrides (Fellet et al. 2013; Harries et al. 2012; Lai et al. 2015; Sheppard, Humphries and Buckley 2016). In comparison to existing molten salt energy storage, metal hydrides are up to 20 times more energy dense than molten salt mixtures (Abedin and Rosen 2011). The U.S. Department of Energy has set the target operating temperature range of thermal energy storage for the next generation CST systems as 650 – 800 °C; hence, candidate metal hydrides should operate in or close to this range (International Energy Agency 2010). An added benefit of working at high temperatures is improving the Carnot efficiency of Stirling engines that convert thermal energy to electrical energy.

Many potential metal hydride-based thermal energy storage systems predominately use low cost metals such as magnesium (Bogdanović et al. 1999; Felderhoff and Bogdanović 2009; Wierse, Werner and Groll 1991). The low-cost systems make them economically attractive based on raw material price, but cost calculations require proper characterisation of the hydrogen properties including: thermodynamics, kinetics, shape of plateau/PCT curve and cyclic stability (Felderhoff and Bogdanović 2009; Paskevicius et al. 2015; Ward et al. 2016).

1.6 Metal Amides, Imides and Nitride Systems

This thesis looks at three pure systems: lithium- (Li–N–H), magnesium- (Mg–N–H) and calcium-based (Ca–N–H) systems. The reason these materials have been selected is due to the similar hydrogen storage properties across different alkali and alkaline earth metals: Li, Mg and Ca (Gregory 2008). Therefore, by analogy of the widely known Li–N–H system, the system properties of the Mg–N–H and Ca–N–H system can be investigated.

1.6.1 Lithium-based System

Based on the decomposition of Li_3N by Chen et al. (2002), the hydrogen release from the amide-hydride reaction between $LiNH_2$ and LiH in the Li–N–H system occurs in a two-step reaction, forming first an imide (Equation 1.3) and then a nitride product (Equation 1.4).

$$LiNH_2 + LiH \rightarrow Li_2NH + H_2, \qquad 6.5\ wt\%\ H_2 \tag{1.3}$$

$$Li_2NH + LiH \rightarrow Li_3N + H_2, \qquad 5.5\ wt\%\ H_2 \tag{1.4}$$

$LiNH_2$ reacts with LiH to form Li_2NH, releasing hydrogen at temperatures below 200 °C (Chen et al. 2003; Equation 1.3). Li_2NH further reacts with LiH to form Li_3N, releasing hydrogen at predicted temperatures above 320 °C (Equation 1.4). The majority of the work done in amide-imide-hydride systems have been on lowering the operation temperature of the first-reaction step within a suitable thermodynamic range for mobile applications (Xiong et al. 2004). The second reaction has been little studied because the working temperature is deemed too high for mobile applications. Therefore, no further studies have taken advantage of the high-temperature imide-hydride reactions for thermal energy storage.

Recent work on the Li–N–H system has shown that the reaction pathway may be more complex than originally indicated by Chen et al. (2002). The mechanism of both hydrogenation and dehydrogenation of the Li–N–H system involves the formation of non-stoichiometric intermediates (Makepeace et al. 2014). There have been reports that a phase transition (non-stoichiometric) occurs between the tetragonal amide phase ($LiNH_2$) to a cubic imide phase (Li_2NH) (Bull et al. 2010; Tapia-Ruiz et al. 2013). Given the formation of Li_3N from the imide-hydride reaction, lithium nitride hydride (Li_4NH) is formed from the reaction between Li_3N and LiH at temperatures > 490 °C (Marx 1997). However, Li_4NH undergoes no dehydrogenation or decomposition below 400 °C, limiting the reversible reaction in the Li–N–H system.

Bull et al. (2010) proposed two models that show the possibility of non-stoichiometric phases during the $LiNH_2$ to Li_2NH transition, $Li_{2-y}NH_{1+y}$ ($0 \leq y \leq 1$), and the Li_2NH to Li_4NH transition, $Li_{2+y}NH$ ($0 \leq y \leq 2$). Both intermediates explain the non-stoichiometric phases across the entire Li–N–H system. Furthermore, Tapia-Ruiz et al. (2013) also proposed a possible reaction pathway between Li_2NH and Li_4NH. These phases were proposed to react and form a non-stoichiometric solid-solution known as lithium imide-nitride hydride, $Li_{4-2x}N_{1-x}H_{1-x}(NH)_x$ ($0 \leq x \leq 1$):

$$x\mathrm{Li_2NH} + (1-x)\mathrm{Li_4NH} \rightarrow \mathrm{Li_{4-2x}N_{1-x}H_{1-x}(NH)_x} \quad (1.5)$$

Given the complexity of characterising non-stoichiometric phases in the Li–N–H system, further investigation is required on the reversibility of the Li_2NH and Li_4NH reaction in Equation 1.5 at high operating temperatures suitable for thermal energy storage.

1.6.2 Magnesium-based System

Nakamori, Kitahara, and Orimo (2004) were among the first to investigated the Mg–N–H system. Magnesium amide ($Mg(NH_2)_2$) was synthesised by heating magnesium hydride (MgH_2) at various temperatures under an ammonia (NH_3) pressure of 5 bar. X-ray diffraction (XRD) measurements revealed that after a week at 340 °C, the product was single phase $Mg(NH_2)_2$ (Nakamori, Kitahara and Orimo 2004; Equation 1.6). The reaction that occurs in Equation 1.7 was due to the decomposition of MgH_2 below 300 °C at 1 bar (Bogdanović, Ritter and Spliethoff 1990).

$$\mathrm{MgH_2} + 2\mathrm{NH_3} \rightarrow \mathrm{Mg(NH_2)_2} + 2\mathrm{H_2} \quad (1.6)$$

$$\mathrm{Mg} + 2\mathrm{NH_3} \rightarrow \mathrm{Mg(NH_2)_2} + \mathrm{H_2} \quad (1.7)$$

The decomposition of $Mg(NH_2)_2$ was investigated by thermal gravimetric analysis (TGA) with a heating rate of 10 °C min^{-1} and showed ammonia release at 357 °C and 447 °C, corresponding to a weight loss of 25% and 32% mass, respectively (Nakamori, Kitahara and Orimo 2004). The two-step decomposition process of $Mg(NH_2)_2$ can be expressed in Equation 1.8 and 1.9. When the sample was heated in the temperature range of 27 – 600 °C, only magnesium nitride (Mg_3N_2) phases could be identified by XRD analysis.

$$\mathrm{Mg(NH_2)_2} \rightarrow \mathrm{MgNH} + \mathrm{NH_3} \quad (1.8)$$

$$\mathrm{MgNH} \rightarrow \frac{1}{3}\mathrm{Mg_3N_2} + \frac{1}{3}\mathrm{NH_3} \quad (1.9)$$

The amide-hydride reaction between $Mg(NH_2)_2$ and MgH_2 in a 1:1 and 1:2 molar ratio was investigated by Nakamori, Kitahara, and Orimo (2004). The TGA

showed ammonia release similar to the decomposition of solely $Mg(NH_2)_2$, suggesting limited kinetics between MgH_2 and NH_3 to form $Mg(NH_2)_2$ (Nakamori, Kitahara and Orimo 2004). However, when Hu et al. (2006a) prepared a mixture of $Mg(NH_2)_2$ and MgH_2 at a molar ratio of 1:1, a considerable amount of hydrogen was released with no detectable ammonia during 9 hours of ball milling at ambient temperature via the reaction in Equation 1.10.

$$Mg(NH_2)_2 + MgH_2 \rightarrow 2MgNH + 2H_2 \quad (1.10)$$

The reaction in Equation 1.10 only accounts for a hydrogen capacity of 4.9 wt% but by mixing $Mg(NH_2)_2$ and MgH_2 at a molar ratio of 1:2 and ball milling for 72 hours, a two-step reaction occurs (Hu et al. 2006a). In the first step, $Mg(NH_2)_2$ reacts with MgH_2 to form MgNH with hydrogen release (Equation 1.11). In the second step, MgNH then reacts with excess MgH_2 to yield Mg_3N_2 with hydrogen release (Hu et al. 2006a; Equation 1.12).

$$Mg(NH_2)_2 + 2MgH_2 \rightarrow 2MgNH + MgH_2 + 2H_2 \quad (1.11)$$

$$2MgNH + MgH_2 \rightarrow Mg_3N_2 + 2H_2 \quad (1.12)$$

The overall reaction of $Mg(NH_2)_2$ and MgH_2 in a 1:2 molar ratio can be written as follows (Equation 1.13):

$$Mg(NH_2)_2 + 2MgH_2 \rightarrow Mg_3N_2 + 4H_2 \quad (1.13)$$

The reaction in Equation 1.13 accounts for a hydrogen capacity of 7.4 wt%, which is high in hydrogen capacity, but the thermodynamic calculations done by Hu et al. (2006a) showed that the hydrogen release is only mildly endothermic. Differential scanning calorimetry (DSC) analysis on the decomposition of $Mg(NH_2)_2$ was used to calculate the thermodynamics in Equation 1.13. The enthalpy of desorption in Equation 1.13 was calculated as ΔH_{des} = 3.5 kJ $(mol\ H_2)^{-1}$, a low reaction enthalpy that requires impractical pressures at high operating temperatures to be thermodynamically reversible (Hu et al. 2006a).

1.6.3 Calcium-based System

The amide- and imide-hydride reactions in the Ca–N–H system were reported by Hino et al. (2005), involving calcium amide ($Ca(NH_2)_2$) and calcium hydride (CaH_2) in the first-reaction step (Equation 1.14), and calcium imide (CaNH) and CaH_2 in the second-reaction step (Equation 1.15).

$$Ca(NH_2)_2 + CaH_2 \rightarrow 2CaNH + 2H_2 \quad (1.14)$$

$$CaNH + CaH_2 \leftrightarrow Ca_2NH + H_2 \quad (1.15)$$

Their XRD profile confirms that the product after heating up to 300 °C is a cubic CaNH phase (Equation 1.14), and the product after heating up to 500 °C is calcium nitride hydride (Ca_2NH) (Equation 1.15). Chen et al. (2002) also observed that Ca_2NH could reversibly store hydrogen in the temperature range of 350 – 600 °C. PCT isotherms performed by Chen et al. (2002) observed a reversible hydrogen content of ~1.9 wt%, with the theoretical hydrogen content being 2.1 wt%.

Xiong et al. (2003) investigated the decomposition of calcium nitride (Ca_3N_2) and its interaction with hydrogen. PCT measurements at 600 °C showed the reverse (hydrogenation) reaction in the Ca–N–H system had an overall reaction as follows (Xiong et al. 2003):

$$Ca_3N_2 + 2H_2 \rightarrow Ca_3(NH_2)_2 \rightarrow 2CaNH + CaH_2 \quad (1.16)$$

The reaction in Equation 1.16 was similar to what Dafert and Miklauz (1909) found when heating Ca_3N_2 to 700 °C in a hydrogen atmosphere that had a final product as '$Ca_3(NH_2)_2$' and decomposed to CaNH and CaH_2 under ultraviolet radiation. However, Xiong et al. (2003) observed that the imide-hydride to nitride reaction was not reversible at a temperature of 550 °C as Ca_3N_2 was not regenerated in the dehydrogenation products after XRD analysis. The products after dehydrogenation were different imide phases for different hydrogen stoichiometry. This observation can be described with the following equation (Equation 1.17):

$$Ca_3N_2 + \frac{X}{2}H_2 \rightarrow Ca_mN_2H_n + (3-m)CaH_2 \quad (1.17)$$

where $X = 6 + n - 2m$, and m and n are dependent on the degree of hydrogenation (Xiong et al. 2003).

Xiong et al. (2003) prepared samples that investigated the nitride-hydride reaction by mixing Ca_3N_2 with CaH_2 in a 1:1 molar ratio. PCT measurements revealed that above 300 °C there is formation of a CaNH-like structure along with CaH_2 that remained after heating to 600 °C. However, XRD phase analysis revealed that CaH_2 was being consumed during the desorption process. Therefore, the effect of adding extra CaH_2 to the Ca_3N_2–CaH_2 mixture also improved the hydrogen desorption capacity (Xiong et al. 2003).

The existence of a solid solution of CaNH and $Ca(NH_2)_2$, also explains the appearance of a CaNH-like structure found by Xiong et al. (2003) that Chu et al. (2010) found by investigating the Li–Ca–N–H system. This reaction can be expressed as follows:

$$Li_2Ca(NH)_2 + \frac{4}{3}H_2 \rightarrow \frac{2}{3}LiNH_2 + \frac{4}{3}LiH + \frac{1}{3}[2CaNH–Ca(NH_2)_2] \quad (1.18)$$

where lithium calcium imide ($Li_2Ca(NH)_2$) reacted with hydrogen to produce $LiNH_2$, LiH and the solid-solution, $2CaNH–Ca(NH_2)_2$. Given the complexity of the reaction pathway along with the presence of unknown phases, an *in situ* XRD study will be beneficial in identifying solid solutions of amides and imides at high temperatures. The literature on the reversibility of Ca_3N_2 at high temperatures is also lacking because of studies made only at low temperatures for mobile applications. Therefore, the Ca–N–H system will be investigated at a temperature range above 650 °C, suitable for thermal energy storage.

1.7 Mixed Cation Amides, Imides and Nitride Systems

1.7.1 Li–Mg–N–H System

The amide-hydride reactions in the Li–Mg–N–H system were investigated as an alternative to the Li–N–H system for high temperature applications (Luo 2004;

Okamoto et al. 2007; Xiong et al. 2006). The amide-hydride reaction between $LiNH_2$ and MgH_2 was first studied in 2004 (Nakamori and Orimo 2004; Xiong et al. 2004; Xiong et al. 2005b). These groups investigated amide-hydride reactions with different ratios of $LiNH_2$ and MgH_2 and variations with $Mg(NH_2)_2$ and LiH.

Xiong et al. (2004) investigated the amide-hydride reaction between $LiNH_2$ and MgH_2 in a 2:1 molar ratio in the temperature range of 50 – 350 °C. They reported that hydrogen desorption occurred at a lower temperature (166 °C) than in the Li–N–H system (272 °C). XRD analysis identified the dehydrogenated product as lithium magnesium imide ($Li_2Mg(NH)_2$) that formed by the following reaction:

$$2LiNH_2 + MgH_2 \rightarrow Li_2Mg(NH)_2 + 2H_2 \quad (1.19)$$

The sample was cycled at 180 °C under a hydrogen pressure of 90 bar to investigate the stability of the system. The system was reversible with little change to the absorption/desorption temperature after each cycle. However, XRD analysis showed that the rehydrogenated products were $Mg(NH_2)_2$ and LiH rather than the original starting reagents ($LiNH_2$ and MgH_2) (Xiong et al. 2004). Therefore, the reversible hydrogenation and dehydrogenation reaction is expected to proceed by the following reaction (Xiong et al. 2005b; 5.5 wt% of H_2):

$$Mg(NH_2)_2 + 2LiH \leftrightarrow Li_2Mg(NH)_2 + 2H_2 \quad (1.20)$$

where the reaction in Equation 1.20 releases hydrogen at approximately 200 °C (Zak-Fang, Lu and Sohn 2008). However, temperature programmed desorption (TPD) analysis by Xiong et al. (2006) revealed multiple desorption events, suggesting a complex reaction pathway different to the single-step reaction in Equation 1.20.

Hu et al. (2007) proposed that the hydrogenation process could reversibly store 5.6 wt% of H_2 at 180 °C through the following two-step reaction:

$$2Li_2Mg(NH)_2 + H_2 \leftrightarrow LiH + LiNH_2 + Li_2Mg_2(NH)_3 \quad (1.21)$$

$$LiNH_2 + Li_2Mg_2(NH)_3 + 3H_2 \leftrightarrow 3LiH + 2Mg(NH_2)_2 \quad (1.22)$$

PCT analysis revealed a flat plateau corresponding to the release of hydrogen through Equation 1.21, and a sloping plateau corresponding to the release of hydrogen through Equation 1.22 (Cao et al. 2014). Because of the slow kinetics in this system, it took an exceptionally long period of time (approximately 6 hours) for a complete absorption or desorption PCT measurement (Liang et al. 2013). Efforts have been made to improve the kinetics of this system by the addition of heavier species such as $LiBH_4$ (Cao et al. 2014).

1.7.2 Li–Ca–N–H System

The amide-hydride reactions in the Li–Ca–N–H system were initially investigated by Xiong et al. (2004) in their study of ternary imides for hydrogen storage. In their comparison to the Li–Mg–N–H system, lower pressures and higher temperatures were required to desorb the theoretical maximum capacity (4.3 wt% of H_2) in the Li–Ca–N–H system (Xiong et al. 2004). In analogy to the Li–Mg–N–H system, lithium calcium imide ($Li_2Ca(NH)_2$) is the anticipated final product of the amide-hydride reaction between $LiNH_2$ and CaH_2 (Equation 1.23).

$$2LiNH_2 + CaH_2 \rightarrow Li_2Ca(NH)_2 + 2H_2 \quad (1.23)$$

$$Ca(NH_2)_2 + 2LiH \rightarrow Li_2Ca(NH)_2 + 2H_2 \quad (1.24)$$

Tokoyoda et al. (2007) prepared an amide-hydride mixture of $Ca(NH_2)_2$ and LiH in a 1:2 ratio and compared it to a mixture of $LiNH_2$ and CaH_2 in a 2:1 ratio to investigate the formation of the ternary imide, $Li_2Ca(NH)_2$ (Equation 1.24 and 1.23). TPD results revealed that hydrogen was released at ~200 °C and ~220 °C for the amide-hydride reaction in Equation 1.23 and 1.24, respectively. In both amide-hydride reactions, the dehydrogenated state at 200 – 220 °C was a mixture of calcium and lithium imide-like (CaNH and Li_2NH) phases. Furthermore, XRD analysis of both amide-hydride reactions at 400 °C revealed that the system does not form known phases but a mixture of an unknown imide phase containing Li and Ca. The reaction pathway of both amide-hydride reactions were summarised in Equation 1.25 and 1.26 (Tokoyoda et al. 2007).

$$\begin{aligned} &2LiNH_2 + CaH_2 \rightarrow CaNH + Li_2NH + 2H_2 \\ &\rightarrow \textit{"unknown imide phase"} + 2H_2 \end{aligned} \quad (1.25)$$

$$\begin{aligned} &Ca(NH_2)_2 + 2LiH \rightleftarrows CaNH + Li_2NH + 2H_2 \\ &\rightleftarrows \textit{"unknown imide phase"} + 2H_2 \end{aligned} \quad (1.26)$$

In the reverse (hydrogenation) reaction, the *unknown imide phases* in Equation 1.25 and 1.26 transformed into a mixture of $Ca(NH_2)_2$ and LiH; hence, the reversible reaction in the Li–Ca–N–H system is shown in Equation 1.26 (Tokoyoda et al. 2007).

Wu et al. (2007) prepared a mixture of $LiNH_2$ and CaH_2 in a 2:1 molar ratio and performed a TPD measurement to 300 °C, they revealed that the hydrogen-release peaked at a temperature of 140 °C and 206 °C. XRD and Rietveld refinement of the dehydrogenated product (after TPD measurement) revealed a new ternary imide phase ($Li_2Ca(NH)_2$) that adopted a trigonal anti-La_2O_3 structure, confirming the reaction in Equation 1.23. By comparing XRD data, this new phase identified by Wu et al. (2007) is the same unknown imide phase reported by Tokoyoda et al. (2007). Hence, the CaNH- and Li_2NH-like phases Tokoyoda et al. (2007) identified, were likely intermediates between $Ca(NH_2)_2$–LiH and $Li_2Ca(NH)_2$, and the unknown imide phase was likely $Li_2Ca(NH)_2$.

1.7.3 Na–Mg–N–H System

The amide-hydride reactions in the Na–Mg–N–H system were investigated by Dolotko et al. (2010), Sheppard et al. (2011a) and Xiong et al. (2005a). *Ex situ* XRD analysis revealed a complex reaction pathway that involved the formation and decomposition of $Mg(NH_2)_2$ and sodium magnesium hydride ($NaMgH_3$) as intermediary phases with the following overall reaction:

$$2NaNH_2 + 3MgH_2 \rightarrow Mg_3N_2 + 2NaH + 4H_2 \quad (1.27)$$

TPD performed on this system revealed that a significant amount of hydrogen is released between 100 °C and 200 °C, peaking at a temperature of ~160 °C with the evolution of nitrogen and ammonia above 170 °C (Xiong et al. 2005a). The results of XRD done by Dolotko, Paulson, and Pecharsky (2010) revealed that the overall amide-hydride reaction between sodium amide ($NaNH_2$) and MgH_2 in a 2:3 molar ratio occurs through a series of reactions as follows:

$$2NaNH_2 + MgH_2 \rightarrow Mg(NH_2)_2 + 2NaH \quad (1.28)$$

$$NaH + MgH_2 \rightarrow NaMgH_3 \quad (1.29)$$

$$\frac{1}{2}Mg(NH_2)_2 + MgH_2 \rightarrow \frac{1}{2}Mg_3N_2 + 2H_2 \quad (1.30)$$

$$\frac{1}{2}Mg(NH_2)_2 + NaMgH_3 \rightarrow \frac{1}{2}Mg_3N_2 + NaH + 2H_2 \quad (1.31)$$

The amide-hydride reaction in Equation 1.28, will undergo a metathesis reaction during ball milling, involving the exchange of NH_2 and H_2 between Mg and Na (Sheppard, Paskevicius and Buckley 2011a). The hydride-hydride reaction in Equation 1.29 occurs at low temperatures with no release of hydrogen. The first hydrogen release is observed from 130 °C that corresponds to the amide-hydride reaction in Equation 1.30 and releases hydrogen between 210 °C and 260 °C (Dolotko, Paulson and Pecharsky 2010). The second hydrogen release is observed at temperatures > 330 °C and corresponds to the amide-hydride reaction in Equation 1.31 (Dolotko, Paulson and Pecharsky 2010).

In their attempt to rehydrogenate the sample, Dolotko, Paulson, and Pecharsky (2010) reported that MgNH was formed after a 48 hour heat treatment at 395 °C under a hydrogen pressure of 190 bar. They also observed partial rehydrogenation of the sample with 2.1 wt% of H_2 absorbed, occurring through a reaction that forms an imide-hydride product (Equation 1.32) with a theoretical hydrogen capacity of 3.13 wt%:

$$Mg_3N_2 + NaH + 2H_2 \rightarrow 2MgNH + NaMgH_3 \quad (1.32)$$

XRD analysis of the rehydrogenated sample revealed a mixture of MgNH, Mg_3N_2 and NaH that confirms the incomplete rehydrogenation of the sample. The hydrogenation of Mg_3N_2 also required the presence of NaH at hydrogen pressures below 200 bar (Dolotko, Paulson and Pecharsky 2010).

Fourier transform infra-red (FTIR) analysis by Kersting (2011), identified an unknown imide-like structure that formed after the hydrogen release from the amide-hydride reaction between $NaNH_2$ and MgH_2. This structure did not match

those of a known MgNH phase. However, Sheppard, Paskevicius, and Buckley (2011a) identified this structure as two new magnesium-containing phases that formed during the desorption process of the amide-hydride reaction, $NaNH_2$ + MgH_2 (1:1). Their results indicated that the unknown phases are comprised of a magnesium-containing imide and nitride phase.

1.7.4 Mg–Ca–N–H System

The amide-hydride reactions in the Mg–Ca–N–H system were investigated by Hu et al. (2006b) and found that at 201 °C, hydrogen is released corresponding to the formation of a solid solution of CaNH and Ca_2NH. Therefore, a TPD measurement was halted at 260 °C (heating rate of 2 °C min^{-1}) to test the reversibility of this hydrogen release for its use in mobile applications. Only a partially reversible reaction (~1 wt% of H_2) was observed at approximately 200 °C. However, when the temperature was raised to 510 °C, 4.9 wt% of H_2 was released, but no hydrogen could be re-absorbed by the system. XRD analysis revealed that at temperatures > 510 °C, the formation of a ternary alkaline earth metal nitride ($CaMg_2N_2$) was observed. Therefore, Hu et al. (2006b) considered the possible overall amide-hydride reaction for hydrogen release at 510 °C as follows:

$$2Mg(NH_2)_2 + 4CaH_2 \rightarrow CaMg_2N_2 + Ca_2NH + CaNH + 7H_2 \quad (1.33)$$

where the final product at high temperature (≤ 700 °C) resulted in a mixture of calcium magnesium nitride ($CaMg_2N_2$), calcium nitride hydride (Ca_2NH) and calcium imide (CaNH) that showed no interaction with hydrogen in TPD analyses (Hu et al. 2006b).

The amide-hydride reaction in the Mg–Ca–N–H system was also investigated by Liu et al. (2007) who looked at the following reaction:

$$Mg(NH_2)_2 + CaH_2 \rightarrow MgCa(NH)_2 + 2H_2 \quad (1.34)$$

Most of the hydrogen was released during the milling between $Mg(NH_2)_2$ and CaH_2 according to Equation 1.34 (theoretical hydrogen content of 4.08 wt%), releasing ~3.88 wt% of H_2 after 72 hours (Liu et al. 2007). Reducing the milling

time to 12 hours showed that only ~0.6 wt% of H_2 was released during milling, with ~3.0 wt% of H_2 released during TPD measurements halted at 380 °C starting initially at vacuum. The hydrogen release that peaked at a temperature of 200 °C, showed promise for the Mg–Ca–N–H system as a potential low temperature hydrogen storage system, but when Liu et al. (2007) repeated the TPD measurement to 380 °C by starting initially at a pressure of 80 bar, more than 3.0 wt% of H_2 was released. However, the hydrogen release did not begin until it reached a temperature of 220 °C, whereas the sample initially at vacuum began to release hydrogen at a temperature as low as 100 °C. Therefore, in order for this system to be thermodynamically reversible, it requires high pressures of approximately 80 bar and a temperature > 200 °C. However, the only problem is that only 0.4 wt% of H_2 was reversibly stored, which could be due to a high kinetic barrier (Liu et al. 2007).

By analogy with the other mixed imide-nitride-hydride systems at high temperature, the imide-hydride to nitride reactions have not been completely investigated by Hu et al. (2006b) and Liu et al. (2007). Given no further hydrogen desorption was observed at temperatures ≤ 700 °C, the imide-hydride reaction in the Mg–Ca–N–H system is possible at temperatures > 700 °C, applicable for high-temperature thermal energy storage.

1.8 Summary and Objectives

It can be seen from the literature available on mixed alkali and alkaline earth metal amide-imide-nitride-hydride systems that many of them have little or no information concerning the characterisation of their reaction pathways and thermodynamics (Table 1.1); specifically, at higher temperatures where no information can be found on imide-nitride-hydride systems. Numerous results from literature in fact have contradictive observations for the desorption reaction pathways and products, such as the identification of a new lithium calcium ternary imide that was thought to be imide intermediates (CaNH and Li_2NH) due to overlapping XRD patterns (Tokoyoda et al. 2007; Wu et al. 2007).

Imide-nitride-hydride systems based on Na, Mg and Ca have shown some promise of reversibility (Chen et al. 2002; Dolotko, Paulson and Pecharsky 2010;

Hu et al. 2006b). However, little studies have been made to verify the reversibility of these reactions as they are deemed to operate at a temperature range too high for mobile storage applications. Most of the work done on these systems have been attempts at stabilising the reactions to perform in a lower temperature range (near ambient) (Xiong et al. 2004).

The overall objective of this thesis is to study the mixed alkali and alkaline earth metal amide-imide-nitride-hydride system for its application in CST energy storage systems. Amide-imide-nitride-hydride systems were characterised using X-ray diffraction (XRD) analysis, *in situ* synchrotron X-ray diffraction (SXRD) analysis, temperature programmed desorption (TPD) with the volumetric method (VM) and mass spectrometry (MS), pressure-composition-temperature (PCT) measurements and temperature programmed photographic analysis (TPPA). Furthermore, a novel method of obtaining thermodynamic data was developed to provide faster collection times than traditional PCT measurements that are used to plot the van't Hoff equation. The specific objectives of this thesis are to (1) evaluate the Li–N–H system to reproduce literature results and to become familiar with the various characterisation techniques; (2) examine the effect of thermodynamically stable hydrides in imide-nitride-hydride systems; and (3) investigate the reaction pathways and thermodynamics of mixed metal imide-nitride-hydride systems that have little characterisation in the literature, focussing on the imide-hydride to nitride reaction at temperatures suitable for thermal energy storage. The low costs of the alkali earth metals used in the amide-imide-nitride-hydride systems also make it an interesting target for CST applications. Therefore, the information obtained from these systems will be of benefit to the academic community since these systems are also applicable in the field of hydrogen storage.

Table 1.1: Summary of the aforementioned amide-imide-nitride-hydride systems.

System	Reaction	Properties	Reference
Li–N–H	Amide-Hydride	6.5 wt% of H_2 releases below 300 °C	(Chen et al. 2002)
	Imide-Hydride	Non-stoichiometric phases between Li_4NH and Li_2NH above 400 °C, solid-solution forms, non-reversible.	(Bull et al. 2010; Tapia-Ruiz et al. 2013)
Mg–N–H	Amide-Hydride	4.9 wt% of H_2 releases during ball milling.	(Hu et al. 2006a)
	Imide-Hydride	7.4 wt% of H_2 release also occurs during milling. However, $Mg(NH_2)_2$ decomposes to Mg_3N_2 at 600 °C, releasing NH_3.	(Nakamori, Kitahara and Orimo 2004)
Ca–N–H	Amide-Hydride	H_2 release at 200 – 300 °C.	(Hino et al. 2005)
	Imide-Hydride	1.9 wt% of H_2 is reversible at 350 – 600 °C. However, a CaNH-like phase appears at $T > 500$ °C.	(Chen et al. 2002; Hino et al. 2005)
Li–Mg–N–H	Amide-Hydride	Multiple desorption events, complex reaction pathway. Desorb 5.6 wt% of H_2 at 180 °C in a two-step reaction. Because of slow kinetics, takes a long time for complete absorption.	(Cao et al. 2014)
	Imide-Hydride	No information.	
Li–Ca–N–H	Amide-Hydride	H_2 release at ~200 °C, new phase of $Li_2Ca(NH)_2$ found after heating to 400 °C.	(Tokoyoda et al. 2007; Wu et al. 2007)
	Imide-Hydride	No information.	
Na–Mg–N–H	Amide-Hydride	Complex reaction pathway, H_2 release at 100 – 200 °C	[1]
	Imide-Hydride	No Information.	
Mg–Ca–N–H	Amide-Hydride	1 wt% of H_2 is reversible at ~200 °C, 4.9 wt% of H_2 can be released above 510 °C but has reversibility issues.	(Hu et al. 2006b)
	Imide-Hydride	No information.	

[1] Dolotko, Paulson, and Pecharsky (2010); Sheppard, Paskevicius, and Buckley (2011a).

CHAPTER 2: EXPERIMENTAL

2.1 Synthesis

All handling of sample materials in this thesis was undertaken in an inert argon-atmosphere glovebox (MBraun Unilab, Germany) to minimise oxygen (O_2 < 5 ppm) and water (H_2O < 5 ppm) contamination in air-sensitive compounds (Figure 2.1). The glove box is equipped with a large and small antechamber that can be used to safely transfer items inside or outside the glovebox. Most of the starting materials were powdered reagents, that were either obtained commercially or laboratory synthesised.

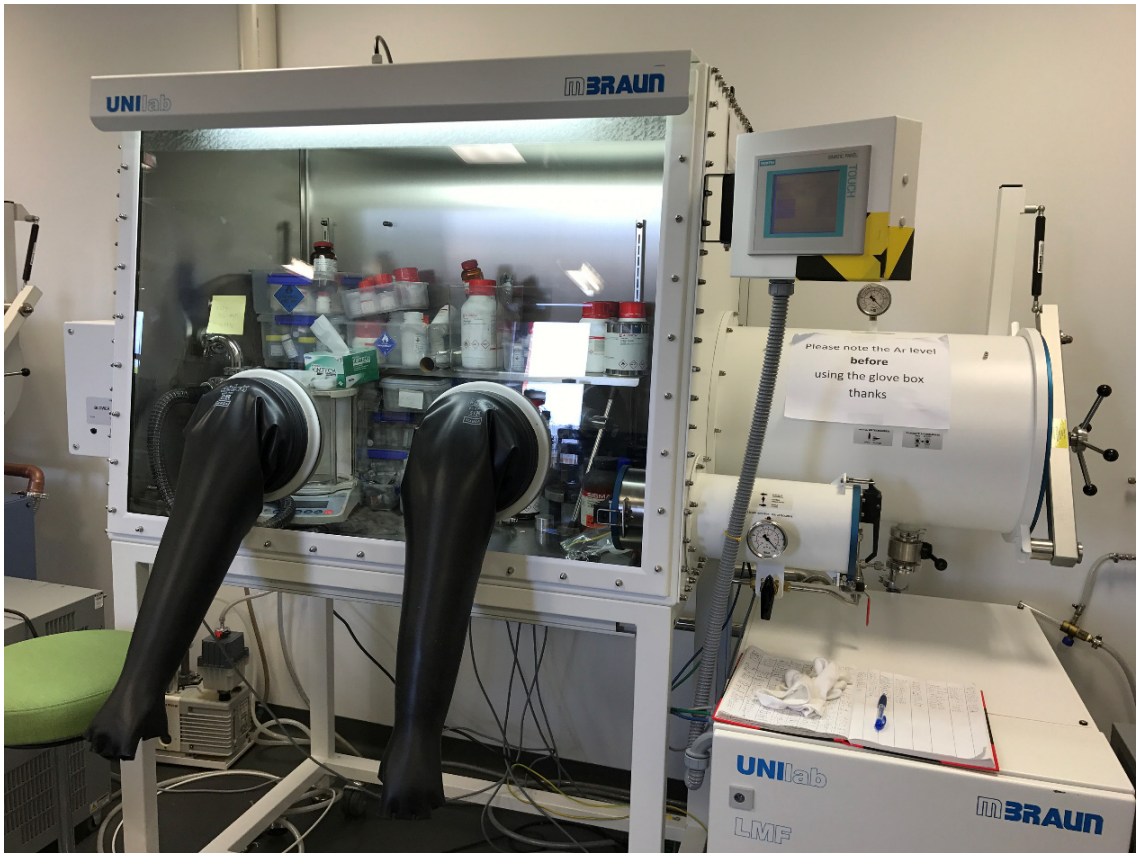

Figure 2.1: MBraun Unilab argon-atmosphere glovebox (Germany).

2.1.1 Planetary Ball Milling

The mechanochemical synthesis of materials was done by thoroughly mixing reagents in a PQ-N04 planetary ball-mill (Across International, New Jersey, USA; Figure 2.2). Ball milling times were 4 or 6 hours in a 50 mL 316 stainless-steel

ball-milling canister sealed in an argon-atmosphere with 316 stainless-steel balls sized at 10 mm and 6 mm (Figure 2.3). The ball-milling rotation was bi-directional in five-minute intervals (zero delay between directions) and was typically operated at 400 or 600 revolutions per minute (RPM) with a ball to powder (BTP) ratio of 30:1 or 60:1. Between 1 and 1.5 grams of material were typically ball milled in each 50 mL canister, for a total mass of 2 to 3 grams per mill.

Figure 2.2: The Across International PQ-N04 planetary ball-mill (New Jersey, USA).

Figure 2.3: A 50 mL 316 stainless steel ball-milling canister with and balls sized at 10 mm and 6 mm.

2.1.2 Shaker-Mixer

For the preparation of larger sample batches (> 3 grams), reagents were thoroughly mixed using a custom-built 316 stainless steel ball-milling canister with a 650 mL internal volume capable of sealing an argon atmosphere (Figure 2.4a). The canister is attached to a Turbula T2C (Glen Mills, New Jersey, USA) shaker-mixer (Figure 2.4b) with a typical mill time > 20 hours (overnight). The shaker-mixer was operated at 160 RPM with a BTP ratio of 30:1 using 316 stainless-steel balls sized at 12.7 mm and 7.9 mm. Approximately 5 g of material was typically ball milled with a maximum sample capacity of ~10 g.

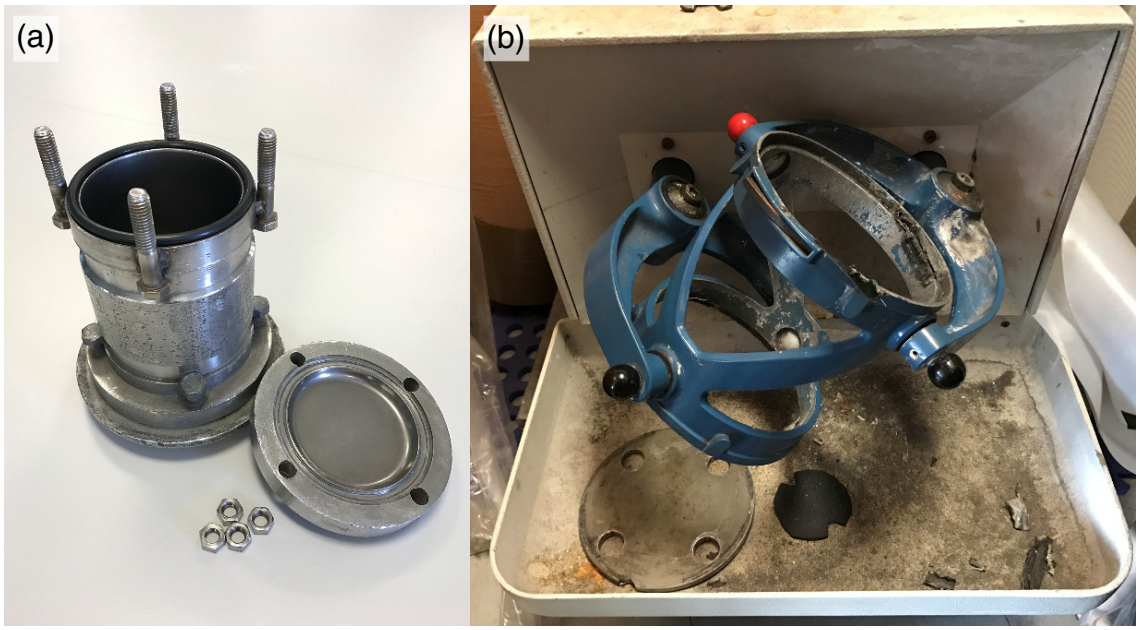

Figure 2.4: (a) A custom made 650 mL 316 stainless steel ball-milling canister and a (b) Glenn Mills Turbula T2C shaker-mixer (New Jersey, USA).

2.1.3 Cryogenic Impact Milling

Cryogenic impact milling is an alternative milling technique due to unwanted reactions occurring in the energy intensive mechanochemical synthesis of mixtures (in the planetary ball-mill or shaker-mixer). Cryogenic impact milling was performed on a 6850 Freezer/Mill (SPEX SamplePrep, New Jersey, USA; Figure 2.5a). The stainless steel grinding vials were machined to have dimensions identical to a polycarbonate grinding vial (6571 vial) with an internal volume of approximately 25 mL (including the stainless-steel impactor rod; Figure 2.5b). In

an inert argon atmosphere, a typical sample mass of 1 g was sealed using two steel end caps threaded with Teflon tape. The grinding vials were attached to the cryogenic mill and cooled by liquid nitrogen. The milling parameters were set up with 15 two-minute cycles (milling time of 30 minutes) utilising 10 impacts per second. A pause interval of one minute was set between each cycle to avoid the sample temperature rising from constant milling.

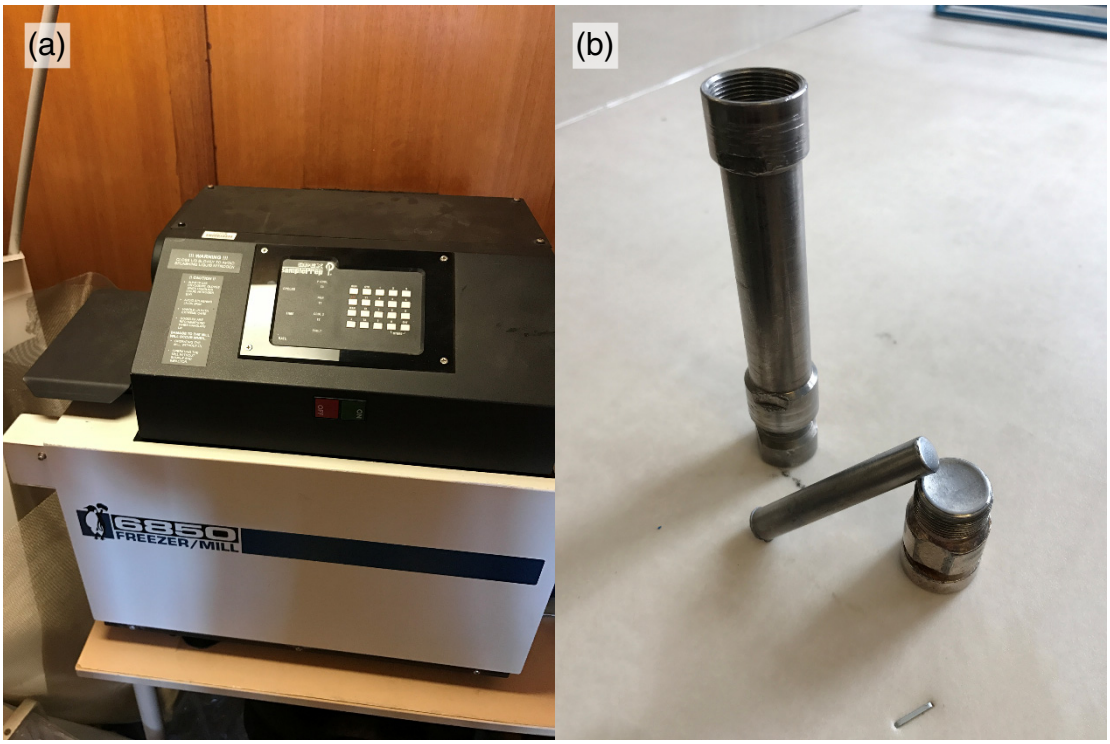

Figure 2.5: (a) The SPEX SamplePrep 6850 cryogenic impact mill (New Jersey, USA) and (b) the stainless steel grinding vial and steel impactor.

2.1.4 Tetrahydrofuran (THF) Washing

Alkaline earth metal amides can be synthesised with a metathesis reaction between lithium amide ($LiNH_2$) and alkaline salts by mechanochemical synthesis in Equation 2.1, where M = Ca or Mg.

$$2LiNH_2 + MCl_2 \rightarrow M(NH_2)_2 + 2LiCl \qquad (2.1)$$

The washing method uses tetrahydrofuran (THF) as a solvent to dissolve lithium chloride (LiCl), a by-product from the metathesis reaction in Equation 2.1. The maximum solubility of LiCl in THF is 54 g L^{-1} (Schultze, Bauer and Arington

1986). Therefore, assuming an 80% solubility, approximately 1.74 g of LiCl can be dissolved in 40 mL of THF (the approximate volume of the centrifuge tube).

Ball-milled samples (with a stir bar) were dissolved in THF in a fluorinated ethylene propylene (FEP) centrifuge tube (40 mL). The FEP tube threaded with Teflon was sealed in an argon atmosphere. The sample solution was stirred on a CH2090-001 magnetic stirrer (Industrial Equipment & Control, Australia; Figure 2.6a) for 38 minutes to ensure the dissolution of LiCl and then placed in a Universal 320 (Hettich, Germany) centrifuge running at 9000 RPM for 2 minutes, to separate the metal amide from the THF-LiCL solution (Figure 2.6b).

In an inert argon atmosphere, the THF-LiCl solution was decanted with a pipette so that only solid amide remained, where an example of the first centrifuge is shown in Figure 2.7. The FEP tube and its contents were evacuated in the small antechamber to evaporate residual THF. The first wash was evacuated for an hour and the THF-washing steps were repeated (twice) to completely remove residual LiCl. The final THF wash was evacuated overnight, to completely remove and evaporate residual THF.

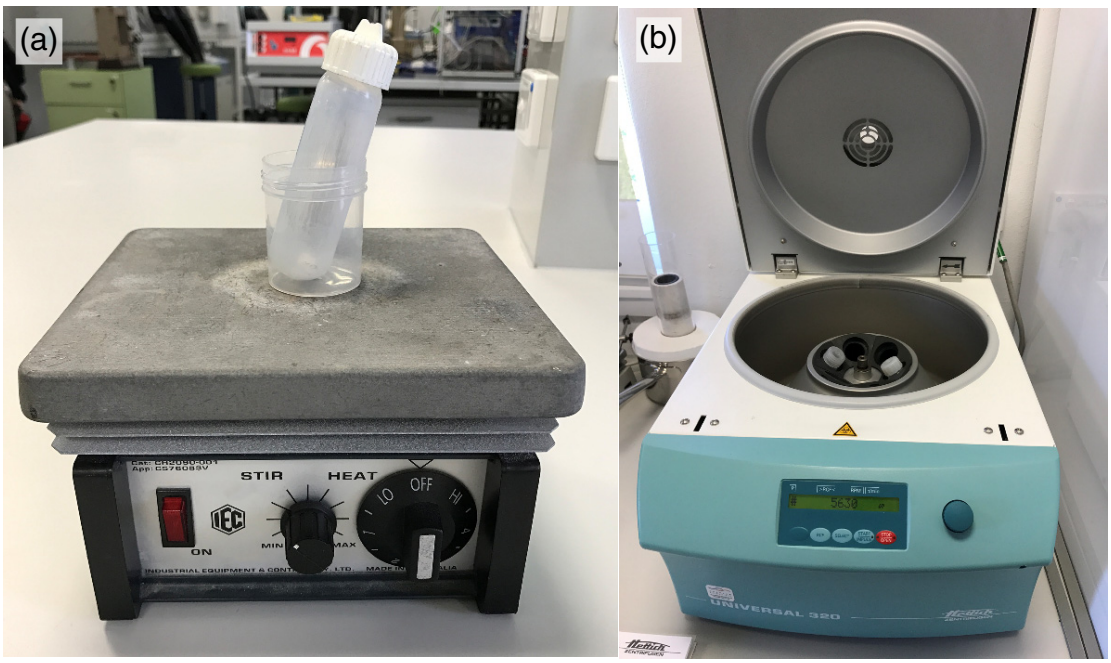

Figure 2.6: (a) The Industrial Equipment & Control magnetic stirrer (Australia) and (b) the Hittech Universal 320 centrifuge with a 1620A rotor (Germany).

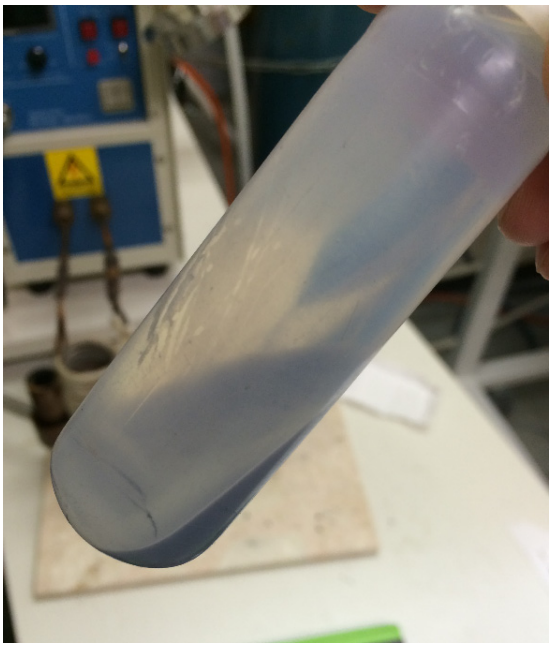

Figure 2.7: Centrifuge result of washed $Mg(NH_2)_2$ and THF-LiCl solution in a 50 mL fluroinated ethylene propylene (FEP) centrifuge tube.

2.1.5 Sample Preparation

The starting materials used for sample preparation were either obtained commercially or laboratory synthesised at Curtin University. Table 2.1 summarises the synthesis conditions used to synthesise pure metal amides and imides, and mixed cation amides, imides and nitrides. Further details about each synthesis method can be found in their relevant system chapters. The investigation of potential amide-imide-nitride-hydride systems are also summarised in Table 2.2, listing the starting reagents used, molar ratios and impurities identified in each sample. The use of impure starting reagents for the preparation of some samples were due to time constraints on the beamline visit at the Australian Synchrotron. Hence, the purity of the starting reagents could not be checked before the synchrotron-beam deadline, and was identified using the synchrotron X-ray diffraction data or analysed by laboratory X-ray diffraction after the beamline visit.

Table 2.1: Summary of synthesis conditions used for non-commercial starting reagents.

System	Starting Reagent	Synthesis Conditions
Li–N–H (Chapter 4)	Li_2NH	Ball milling (BM) of $LiNH_2$ + Li_3N (1:1) and heated at 220 °C under dynamic vacuum for ~12 hours.
Mg–N–H (Chapter 5)	$Mg(NH_2)_2$	BM of $LiNH_2$ + $MgCl_2$ (2:1) and THF-washed.
	MgNH	BM of $Mg(NH_2)_2$ + MgH_2 (1:1) and annealed at 200 °C under dynamic vacuum for 35 hours.
	Mg_2FeH_6	BM of MgH_2 + Fe (2:1) and hydrogenated at 508 °C under a H_2 pressure of 110 bar for 24 hours.
Ca–N–H (Chapter 6)	$Ca(NH_2)_2$	BM of $LiNH_2$ + $CaCl_2$ (2:1) and THF-washed.
	CaNH	Heat treated $Ca(NH_2)_2$ at 366 °C under dynamic vacuum for 13 hours.
	Ca_2FeH_6	BM of CaH_2 + Fe (2:1) and hydrogenated at 500 °C under a H_2 pressure of 120 bar for 4 days.
	Ca_2NH	BM of Ca_3N_2 + CaH_2 (1:1) and annealed at 530 °C under dynamic vacuum for ~24 hours.
Li–Mg–N–H (Chapter 7)	$Li_2Mg(NH)_2$	BM of $LiNH_2$ + MgH_2 (2:1) and annealed at 300 °C under dynamic vacuum for 18 hours.
	LiMgN	BM of Li_3N + Mg_3N_2 (1:1) and annealed at 500 °C under a N_2 pressure of 3.4 bar for 5 days.
	$Li_6Mg_{0.5}(NH)_3Cl$	BM of Li_2NH + $MgCl_2$ (6:1) and annealed at 400 °C under dynamic vacuum for 13 hours.
Li–Ca–N–H (Chapter 8)	$Li_2Ca(NH)_2$	BM of $LiNH_2$ + CaH_2 (2:1) and annealed at 320 °C in a closed system for 17 hours.
	LiCaN	BM of Ca_3N + Li_3N (1:1) and annealed at 580 °C under a N_2 pressure of 2.3 bar for ~11 hours.
Na–Mg–N–H (Chapter 9)	$NaMgH_3$	BM of MgH_2 + NaH (1:1) and annealed at 300 °C in a closed system for ~25 hours.

Table 2.2: Summary of potential amide-imide-nitride-hydride systems investigated and their impurities.

System	Reagents	Impurities†
Li–N–H (Chapter 4)	$LiNH_2$ + LiH (1:2)	None
	Li_2NH + LiH (1:1)	None
	Li_2NH + LiH (1:2)	None
	$LiNH_2$ + LiH (1:2) – 1 mol% $TiCl_3$	None
	$LiNH_2$ + LiH (1:2) – 1 mol% TiN	None
Mg–N–H (Chapter 5)	MgNH* + Mg_2FeH_6 (4:1)	$Mg(NH_2)_2$, MgH_2
	Mg_3N_2 + Fe + H_2 (2:1:5)	None
Ca–N–H (Chapter 6)	Ca_2NH + H_2 (1:1)	None
	CaNH* + Ca_2FeH_6* (2:1)	LiCl, CaH_2, Fe
Li–Mg–N–H (Chapter 7)	$Li_2Mg(NH)_2$* + LiH (1:2)	$Li_2Mg(NH)_2$, $Li_xMg_yN_z$ and $Li_{2-y}NH_{1+y}$
	$LiNH_2$ + MgH_2 + LiH (2:1:2)	None
	MgNH* + LiH (1:1)	$Mg(NH_2)_2$, MgH_2
	$Mg(NH_2)_2$ + MgH_2 + LiH (1:1:2)	None
	LiMgN + H_2 (1:1)	None
	$Li_6Mg_{0.5}(NH)_3Cl$* + H_2 (1:3)	Li_2NH, $MgCl_2$
Li–Ca–N–H (Chapter 8)	$Li_2Ca(NH)_2$* + LiH (1:2)	2CaNH–$Ca(NH_2)_2$, $LiNH_2$, LiH
	CaNH* + LiH (1:1)	LiCl
	LiCaN + H_2 (1:1)	None
Na–Mg–N–H (Chapter 9)	$Mg(NH_2)_2$ + MgH_2 + NaH (1:2:1)	None
	MgNH* + $NaMgH_3$ (2:1)	$Mg(NH_2)_2$, MgH_2

* Incomplete synthesis or impure starting reagent.

† All samples contained a low amount of oxides (< 10 wt%).

2.2 X-Ray Diffraction

X-ray diffraction (XRD) is a non-destructive method utilising X-rays to analyse the crystallographic structure and phase composition of unknown samples. Identification of phases can be achieved by comparing the XRD pattern with patterns from a known reference database. A typical XRD pattern contains several peaks (reflections) that are characterised by their position and intensity. The position of the peaks depends on the arrangement of atoms and the wavelength used, providing qualitative phase analysis and information on the lattice parameters. The intensity of the peaks depends on the sample preparation and crystal structure, providing quantitative phase analysis and information on the crystal structure (Ermrich and Opper 2013).

The scattering of X-rays results in constructive interference at specific angles depending on the arrangement of atoms in the sample. Bragg's Law (Equation 2.2) describes the reflections of the atomic planes of the crystal lattice from the diffraction and interference of X-rays:

$$2d \sin\theta = n\lambda \tag{2.2}$$

where d = interplanar spacing d_{hkl} (hkl = miller indices), 2θ = angle between the incident and reflected beam, n = an integer (normally n = 1) and λ = wavelength of the incident X-ray beam. Figure 2.8 shows a graphical representation of Bragg's Law. The XRD pattern for each crystalline material is unique, and therefore the position and the intensity of the reflections can be used to identify unknown crystalline samples.

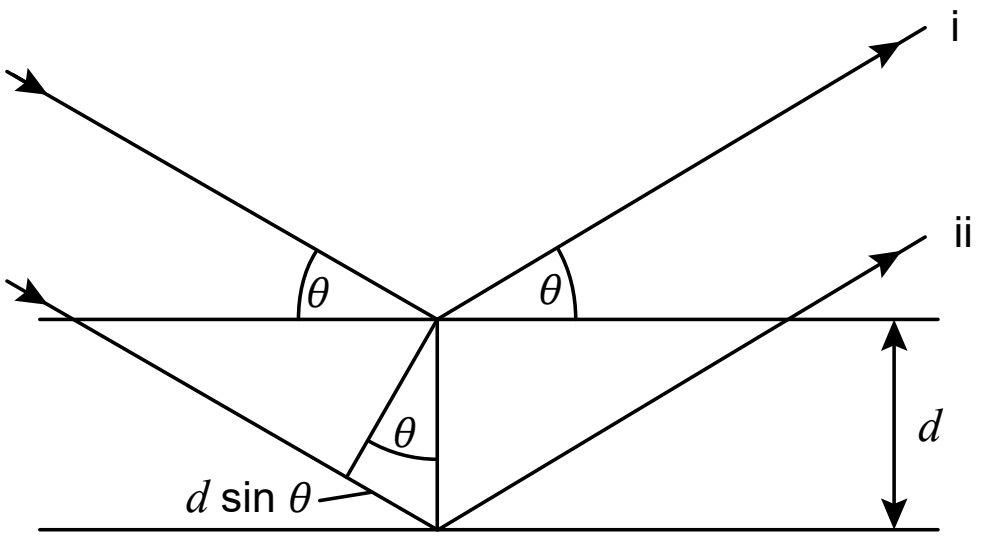

Figure 2.8: X-ray diffraction as described by Bragg's Law (Ermrich and Opper 2013).

2.2.1 Laboratory X-ray Diffraction (XRD)

Laboratory XRD measurements were performed using a Bruker D8 Advance diffractometer (Curtin University, Australia) using Cu $K\alpha$ radiation (λ = 1.54059 Å) with a LynxEye detector. The diffractometer was configured in a Bragg-Brentano geometry with a primary and secondary goniometer circle radius at 250 mm (Figure 2.9a). The 2θ angular range of the LynxEye detector window size was 3° with a fixed divergence slit of 0.3°. The tube focal length was 12 mm that scans a 25 mm diameter of irradiated sample. The receiving slit length was 17 mm with primary and secondary Soller slit angles both at 2.5°. The scans were taken at a 2θ range between 10° and 80° with a 0.03° angle step size and a total collection time of ~60 minutes. The samples were sealed within an argon filled glovebox using a bubble dome holder made of poly(methyl methacrylate) (PMMA) to avoid any oxygen/moisture contamination during data collection (Figure 2.9b). Because of the low quantity of samples used for sorption measurements, the preparation of XRD measurements using the bubble dome holder may be insufficiently packed. Therefore, a low background holder was used with a PMMA dome to seal the sample in low amounts (Figure 2.9c).

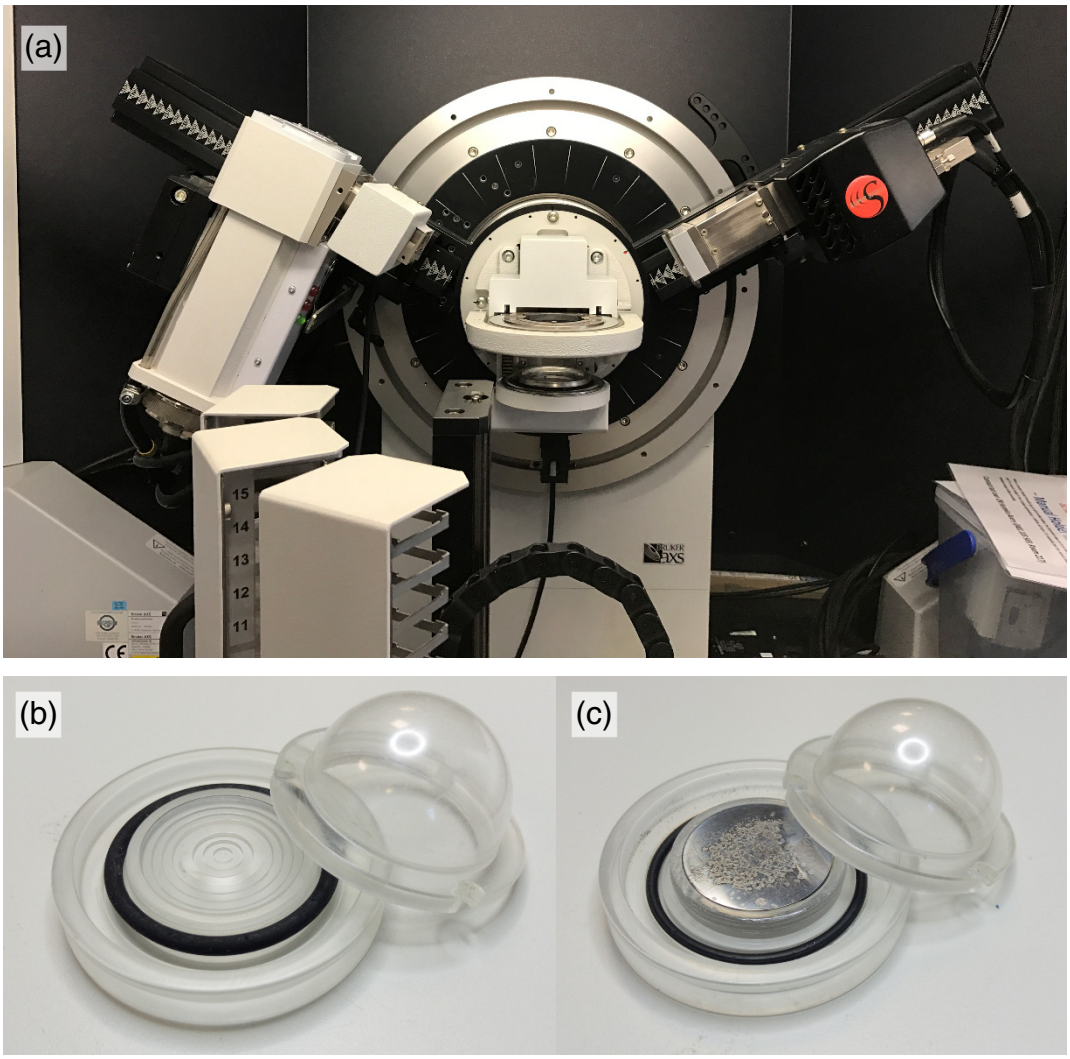

Figure 2.9: (a) The Bruker D8 Advance diffractometer (Curtin University). (b) PMMA bubble dome holder along with a (c) low background holder.

2.2.1.1 XRD phase identification

The DIFFRAC.EVA software (Version 3.2, Bruker) was used to identify phases in XRD data by matching with the international centre of diffraction data (ICDD) database (PDF-4+ 2015) (Berg, Nielsen and Sørensen 2006). The search/match module can evaluate XRD data to interpret peaks with automatic background subtraction (including the PMMA bubble dome). Chemical filters were applied to narrow down the number of search results for an accurate phase identification.

Once the majority of phases were matched via EVA software, the XRD dataset was imported into the Total Pattern Analysis Solutions (TOPAS Version 5, Bruker) analysis program. TOPAS is a program that uses the Rietveld method for crystal structure refinement using the Fundamental Parameters (FP) approach

(Cheary, Coelho and Cline 2004). Profile shapes were characterised in terms of physical parameters, where optical elements and aberrations were convoluted to directly contribute to refined values that represent reality (final profile shape). From the Rietveld refinement, an experimental quantitative analysis (wt%) of unknown samples can be made.

The PMMA dome used to protect the samples from oxygen and moisture during XRD measurements produces broad humps in the pattern centred at 2θ values of ~20°. Therefore, this feature was included in the Rietveld refinement model.

2.2.2 Synchrotron X-ray Diffraction (SXRD)

The Australian Synchrotron (Melbourne, Australia) was important in this thesis to undertake *in situ* synchrotron X-ray diffraction (SXRD) analysis of kinetically fast reaction processes at high temperature, which could not be measured on a laboratory X-ray source. Some of the samples could also melt before the hydrogen desorption reaction, resulting in valuable phase information that can only be obtained with *in situ* SXRD data. Furthermore, these molten events can cause difficulties with *ex situ* XRD due to phase segregation and inconsistent reaction products.

In preparation for SXRD, samples were densely packed in 0.5 mm borosilicate capillaries (Charles Supper Company, Massachusetts, USA) with polyimide/ graphite ferrules (Chromalytic Technology, Victoria, Australia). The sample capillaries had to be pre-mounted using Swagelok (Australia) fittings (Figure 2.10) at Curtin University (Australia) in an inert argon-atmosphere glovebox. However, the hardness of the ferrules (polyimide/graphite) used to seal the sample capillary to the mount, proved challenging because applying too much torque (to tighten the nut) would cause the capillary to fracture, whereas too little would result in a poor seal of the capillary, allowing contamination during transit and measurements. Furthermore, given the synchrotron-beam deadline, leak tests were not achievable based on the time utilised for sample synthesis, packing capillaries and pre-mounting. To maximise the beam time productivity, quick-connect fittings were used to readily attach pre-mounted samples to a custom-built gas handling system (Swagelok, Australia; Figure 2.11) to perform

measurements under different conditions, which has been previously operated at the Australian Synchrotron. Once the sample capillaries were mounted to the goniometer head of the Powder Diffraction beamline at the Australian Synchrotron, automatic capillary alignments were performed to ensure the sample remained in the irradiated section during measurements. The capillary oscillated 120° around goniometer face to avoid entanglement of the vacuum tubing and interference with the sample capillary during measurements.

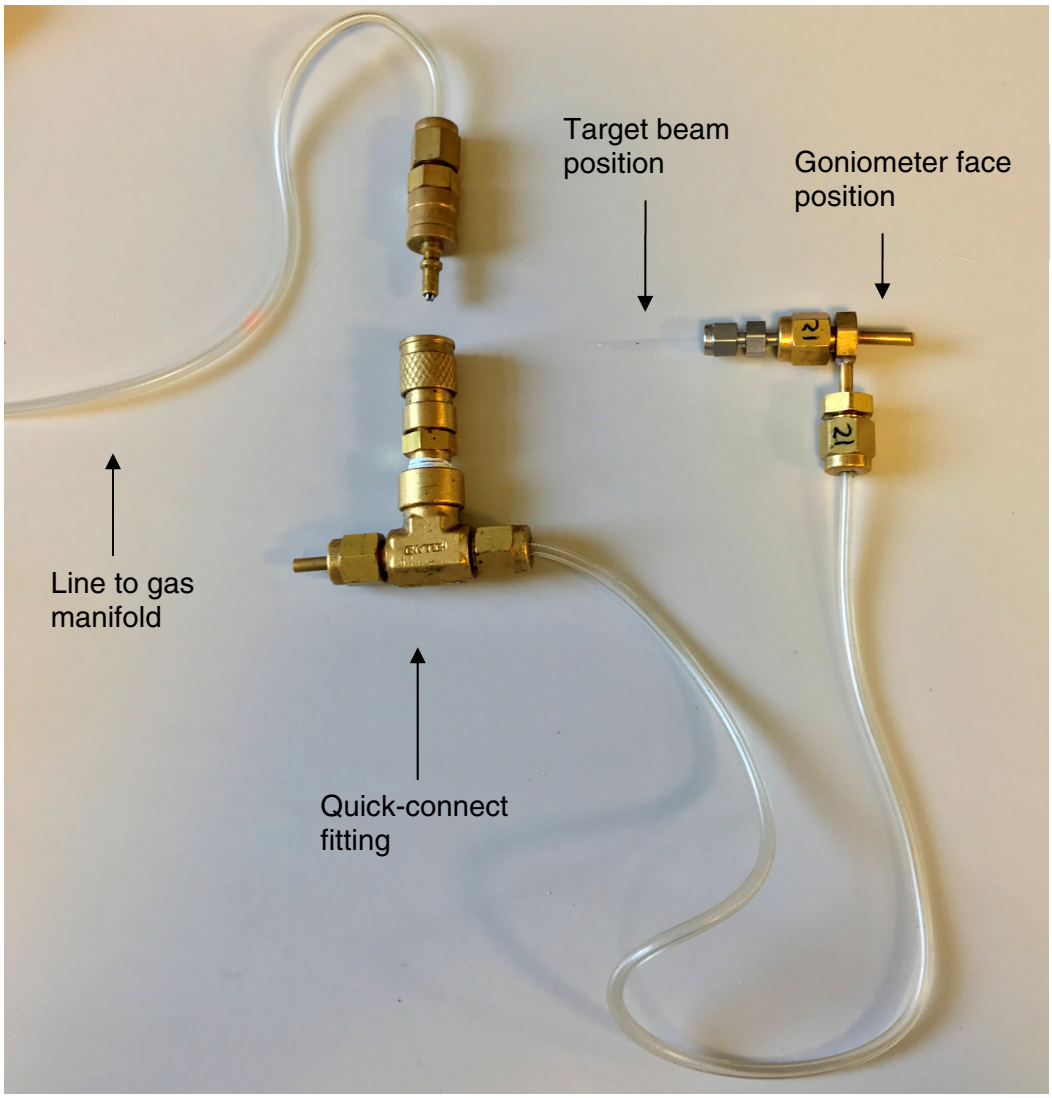

Figure 2.10: Swagelok 1/8” tube fitting that is connected via 1/8” tubing to a miniature quick-connect fitting (Australia).

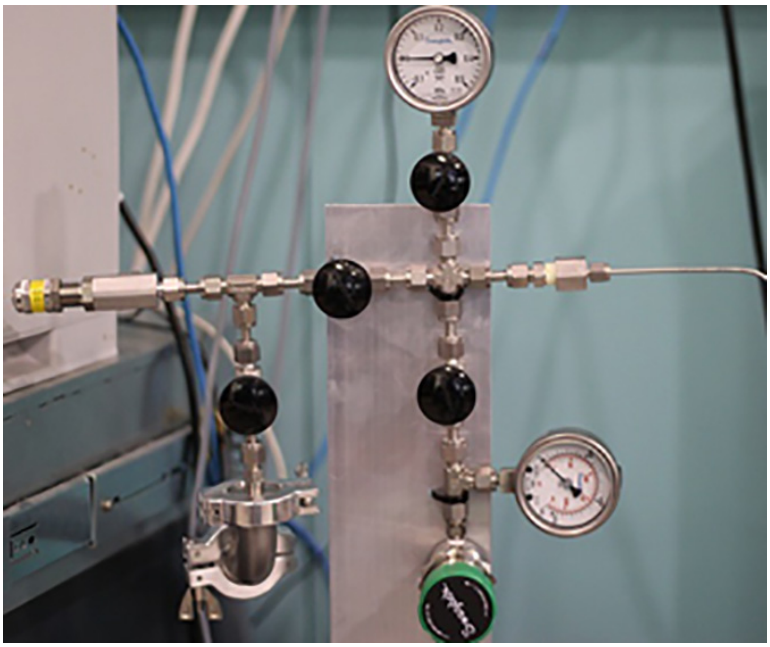

Figure 2.11: Swagelok gas handling system manifold setup for synchrotron X-ray diffraction (Australia).

Synchrotron X-ray diffraction measurements were performed under two experimental conditions, dynamic vacuum and a hydrogen back pressure. The samples were typically heated at a rate of 5 °C min^{-1} using a hot-air blower (Cyberstar, France). Because of the involvement of hydrogen in amide-imide-hydride systems, a maximum temperature of 500 °C was measured to adhere to the Australian Synchrotron safety limits. The Mar165 (marXperts GmbH, Germany) charge-coupled device (CCD) area detector was used with a beam stop to avoid the X-ray source directly hitting the detector (Figure 2.12). Data collection times for each SXRD scan were 26 seconds with 4 seconds of readout time. An initial heat ramp was performed on a temperature standard (sodium chloride). To determine the actual temperature at each frame, the change in lattice parameter was measured in correlation to the temperature recorded from SXRD data. The temperature was recorded in 5 second intervals using a script command that was manually matched with each SXRD scan frame (using the recorded time stamps).

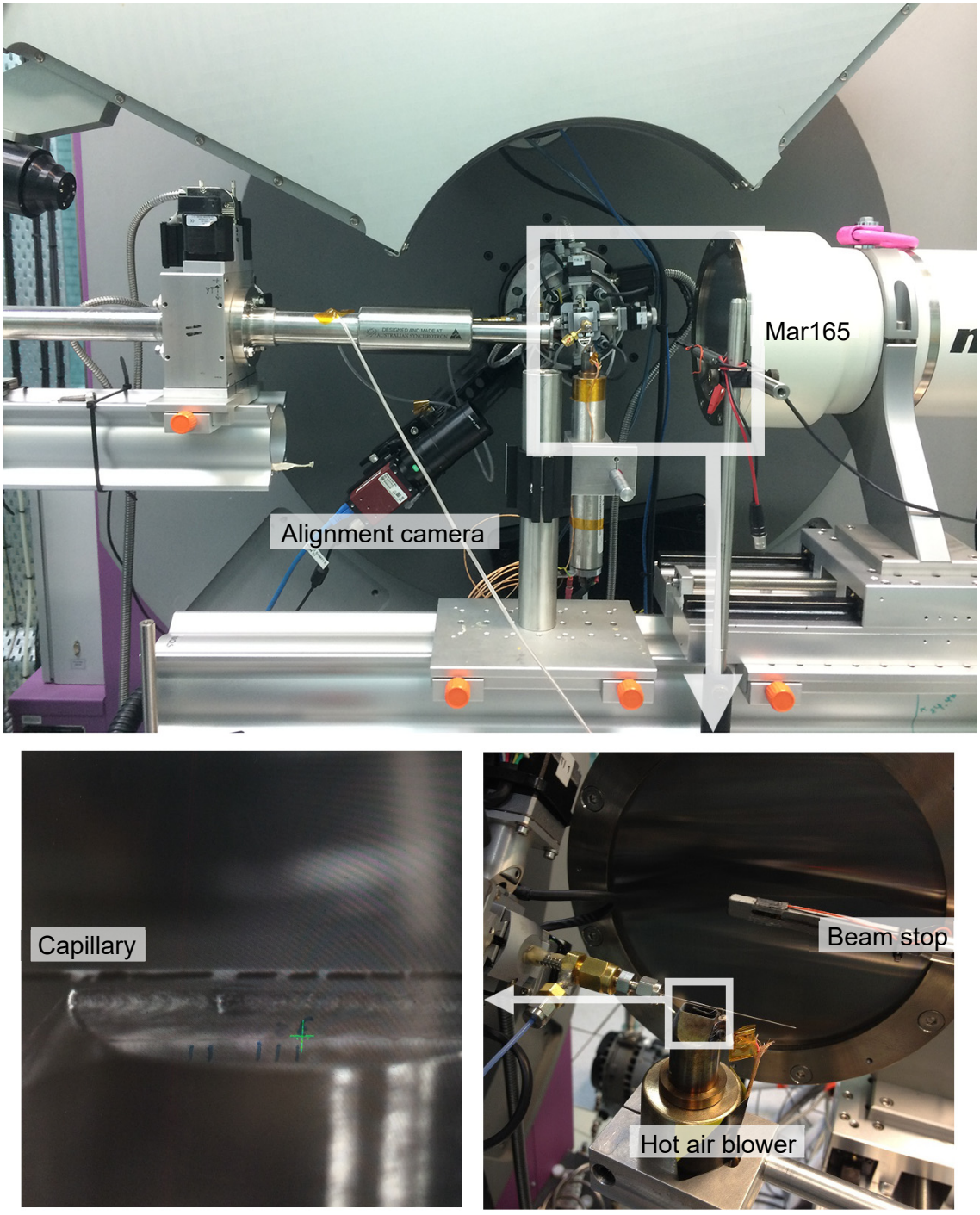

Figure 2.12: Experimental hutch setup using the Powder Diffraction Beamline at the Australian Synchrotron (Melbourne, Australia).

2.2.2.1 *In situ* SXRD phase identification

Fit2D (Version 12.077, Hammersley 1997) is a software program used for data processing SXRD scan data. Each scan from the SXRD measurement is saved as a ring pattern (.TIF file) (Figure 2.13a). An inverted polygon mask is applied to exclude data affected by the beam stop and the ring pattern is integrated using the Fit2D software to output the measurement data (.XY file) (Figure 2.13b).

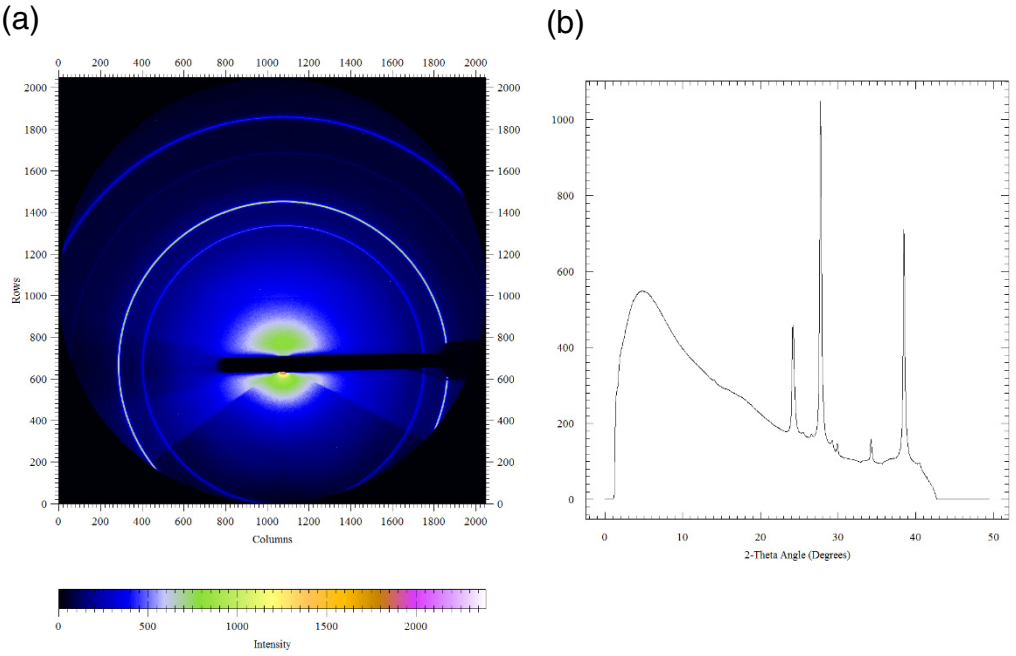

Figure 2.13: (a) Ring pattern from SXRD and the (b) integrated two-dimensional pattern for SXRD analysis.

In situ SXRD analysis using the Powder Diffraction beamline at the Australian Synchrotron, used X-rays with a radiation wavelength of 1.00036 Å. To allow these data sets to be readily analysed by EVA software, the 2θ values had to be converted to a wavelength of 1.54059 Å, the same Cu $K\alpha$ radiation used in laboratory XRD (Equation 2.3):

$$2\theta_{new} = \frac{2\times 180}{\pi}\sin^{-1}\left(\frac{\lambda_{new}}{\lambda_{old}}\sin\left(\frac{\pi}{2\times 180}2\theta_{old}\right)\right) \qquad (2.3)$$

where $2\theta_{new}$ is the converted 2θ value for the X-ray Cu $K\alpha$ wavelength of λ_{new} = 1.54059 Å and $2\theta_{old}$ is the old 2θ value for the synchrotron X-ray wavelength of λ_{old} = 1.00036 Å. This conversion was convenient for the comparison of laboratory XRD and SXRD data using the EVA software package and TOPAS.

The two-dimensional scans were imported into the Igor Pro 6.31 (WaveMetrics, Oregon, USA) software package, capable of producing three-dimensional surface plots, example in Figure 2.14.

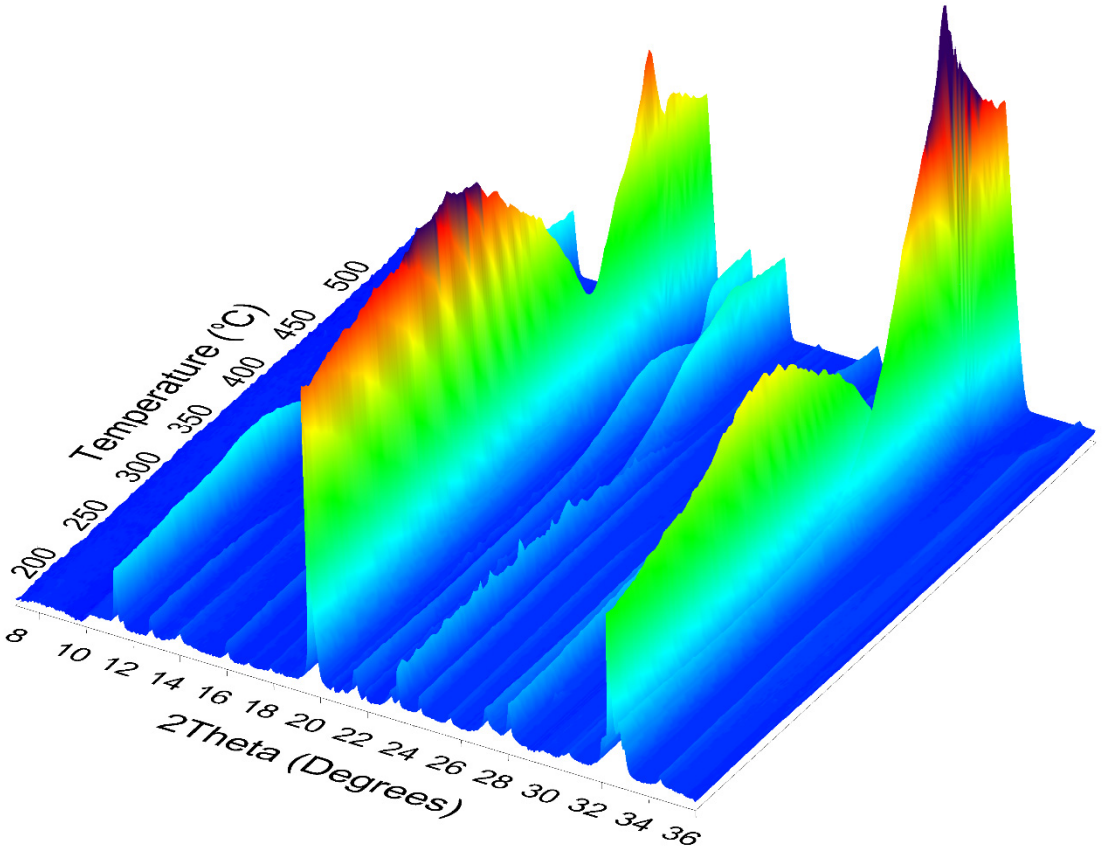

Figure 2.14: Three-dimensional surface plot from *in situ* SXRD data, where z-axis = peak intensity (a.u.).

2.3 Fourier Transform Infra-Red

The crystal structure of some alkali and alkaline earth metal amides and imides are similar in that overlapping patterns are often identified by XRD analysis. Therefore, Fourier transform infra-red (FTIR) analysis is a useful technique that can identify the N–H bonds of each phase often observed between amides, imides and nitrides (Kojima and Kawai 2005). Hence, a better understanding of the reaction pathway can be determined for amide-imide-hydride systems at high temperature. FTIR spectrometry was performed using a Bruker IFS 66 FT-IR (Resources and Chemistry Precinct, Curtin University). The instrument is highly sensitive to atmospheric oxygen/water; therefore, samples were sealed within

potassium bromide (KBr) pellets. KBr (Sigma-Aldrich, ≥ 99%) was outgassed (near vacuum) at 600 °C over a period of three days to remove any residual moisture resulting from the commercial synthesis process. The FTIR sample pellets were prepared using a dry pressing die set made of stainless steel (Across International, New Jersey, USA) within the argon-atmosphere glovebox. A ~40 mg homogeneous layer of sample and KBr were mixed in a 1:7 concentration ratio (~5 mg sample in ~35 mg KBr). The homogenous layer is sandwiched between 80 mg layers of loose KBr powder for a total pellet weight of 200 mg. An Atlas 25T (Specac, England) manual hydraulic press was used to crystallise the mixed KBr samples into 13 mm pellets under a weight of 8 tonnes.

The spectrometer was purged with dry nitrogen and 5 blank/background scans were performed with a blank KBr pellet followed by 4 sample pellet scans. Multiple sample pellets (pressed in KBr) were stored in silica gel bags for batch FTIR measurements due to the limited usage of the FTIR spectrometer. However, FTIR analysis revealed that over long periods of time (weeks), the sample pellets degraded from the absorption of oxygen and moisture from the air, resulting in the appearance of water/hydroxide features in FTIR spectra. Therefore, future FTIR scans should be performed as soon as the sample pellets are pressed for optimum results.

2.4 Temperature Programmed Desorption

Temperature programmed desorption (TPD) measurements were useful in identifying the hydrogen desorption reaction pathway(s) in amide-imide-hydride systems. The TPD measurement involves heating the sample with a constant heat rate (1, 2 or 5 °C min^{-1}). Two TPD methods were performed: the first measured the partial pressure under dynamic vacuum on a PCT-Pro E&E (Hy-Energy, California, USA) attached to a residual gas analyser (RGA) Series 300 coupled with a quadrupole mass spectrometer (MS) (Stanford Research Systems, California, USA), and the second measured the absolute pressure in a closed system on the PCT-Pro E&E using the volumetric method (VM). In both methods, the temperature was measured using a K-type thermocouple (Hinco Instruments, Australia).

2.4.1 Mass Spectrometry

Temperature programmed desorption coupled with a mass spectrometer (TPD-MS) was used to identify the phase change of materials corresponding to the release of gases (identified by mass spectrometry) at various temperatures. Approximately 10 mg of sample was outgassed to an approximate vacuum (1×10^{-3} bar) at room temperature overnight. Under dynamic vacuum, the samples were heated to the desired temperature with a constant heat rate. As the temperature increases, the gases evolved are detected by MS and identified by their atomic mass units (amu). The RGA Windows analysis software provided by Stanford Research Systems (SRS) was the software interface used to detect gases during TPD measurements. By measuring the partial pressure, the amount of gases released were also calculated from the intensity of each gas detected as a function of time (or temperature). Figure 2.15 shows the PCT-Pro E&E attached to the RGA-300 MS.

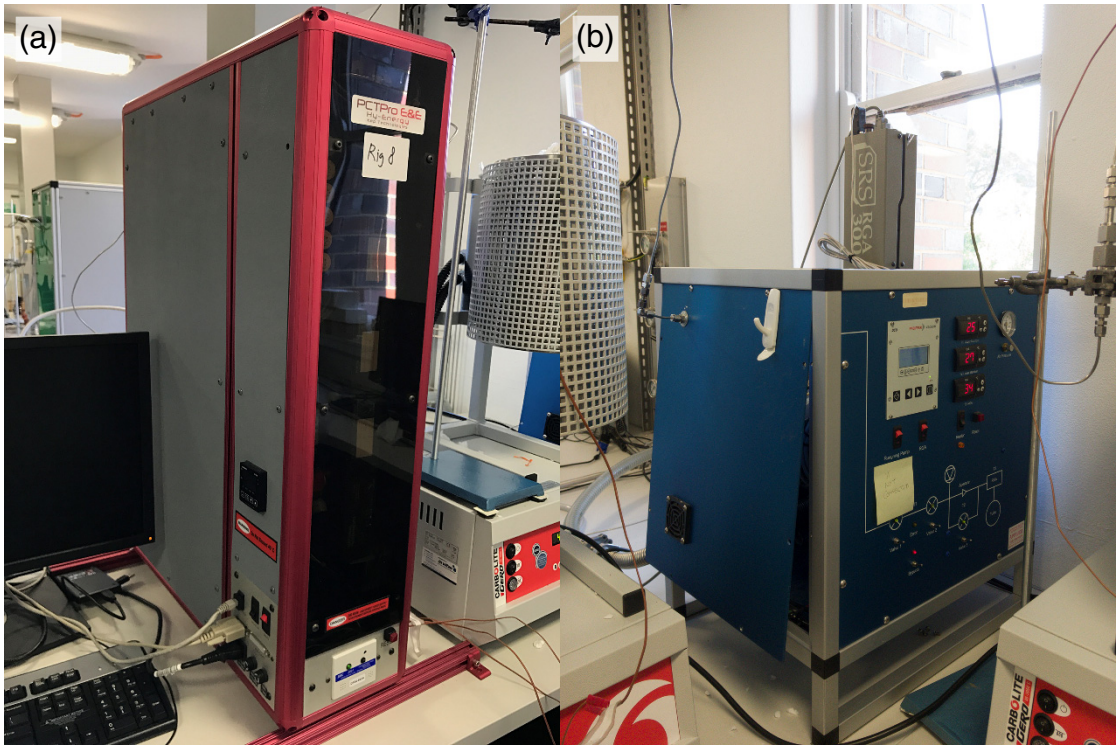

Figure 2.15: (a) The Hy-Energy PCT-Pro E&E (California, USA) and (b) Stanford Research Systems RGA 300 with a mass spectrometer (California, USA).

2.4.2 Volumetric Method

Temperature programmed desorption with the volumetric method (TPD-VM) uses a Sieverts type apparatus to measure the evolved gas pressure against time to identify the phase change in materials at various temperatures. Therefore, larger sample masses (~500 mg) were required to minimise any background noise from the MKS 628D pressure transducer (MKS Instruments, Massachusetts, USA) with an uncertainty reading of 1%. After the sample is outgassed overnight to a pressure near vacuum, the TPD-VM measurement commences by heating the sample to a target temperature with a constant heat rate to allow the evolution of gases into a closed system with a known volume (~191.7 cm^3 for the PCT-Pro E&E). As the temperature increases, the absolute gas pressure is measured, where the desorption intensity (a.u.) is derived from the rate of change in pressure associated with time (or temperature) that corresponds to the gas content in the gaseous phase (i.e. the amount of gas desorbed). Unlike TPD-MS, TPD-VM cannot differentiate what gas or combination of gases are responsible from the generated gas pressure. Furthermore, it should be noted that the gas back pressure created during measurements may influence the results. The hydrogen capacity can also be calculated (assuming the evolution of H_2 gas) from the equilibrium pressure at the final temperature given the known system volume.

2.5 Pressure-Composition-Temperature

Pressure-composition-temperature (PCT) data were collected on an automated custom-built hydrogen sorption apparatus at Curtin University (Australia) utilising 316 stainless-steel components (Swagelok, Australia). The absolute pressure was measured using a Rosemount 3051S pressure transmitter (Emerson Process Management, Australia) with 0.01% precision and 0.02% accuracy. For gauges that were not set up for absolute pressure, a Baromec Type M1975 (Mechanism Ltd., England) atmospheric barometer was used to measure the atmospheric pressure then converted to an absolute pressure value. The temperature was recorded and measured by a K-type thermocouple (Hinco Instruments, Australia).

The typical sample mass for PCT measurements ranged from 0.5 g to 1.0 g of sample. The apparatus uses the volumetric (also called manometric or Sieverts') method to determine hydrogen sorption of a sample. There are two distinct volumes used for sorption measurements: the sample cell volume (Part A of Figure 2.16) and the reference volume (Part B of Figure 2.16).

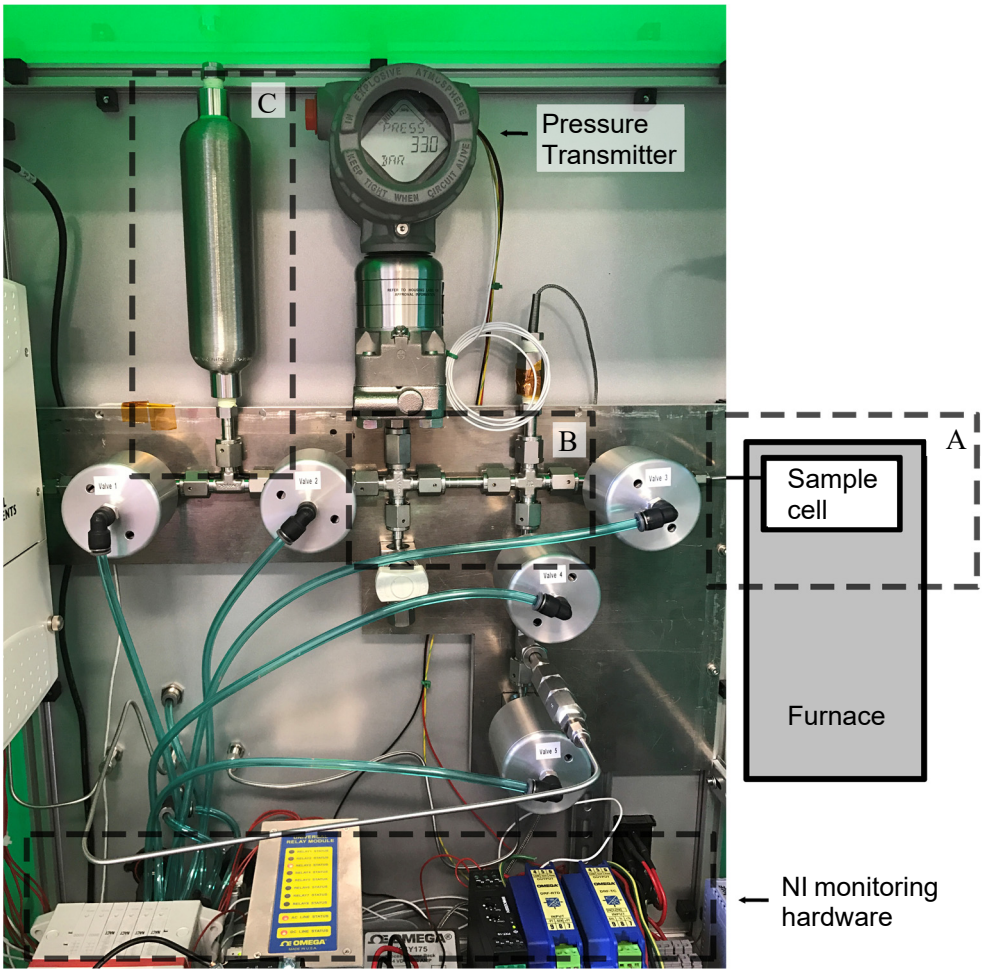

Figure 2.16: Hydrogen sorption apparatus with National Instruments (NI) automation, where A = sample cell volume, B = reference volume and C = hydrogen store.

For hydrogen absorption measurements, the method consists of putting hydrogen gas into a known reference volume (V_r) at a measured temperature (T_r) and pressure (P_r). Hence, the number of hydrogen moles present in the reference volume can be determined. This hydrogen pressure is then allowed to enter the known sample cell volume (V_s) that contains the sample of interest. The equilibrium pressure (P_{eq}) and temperature (T_{eq}) are recorded and the negative change in pressure determines the amount of hydrogen absorbed by the sample.

For hydrogen desorption measurements, the sample side pressure (P_s) and temperature (T_s) are recorded and closed off from the reference volume. When the reference volume is sufficiently evacuated ($V_r \approx 0$ bar), the sample side volume (V_s) is allowed to enter the reference volume (V_r) and the equilibrium pressure (P_{eq}) and temperature (T_{eq}) are recorded. From the positive change in pressure, the amount of hydrogen desorbed by the sample can be determined.

A graphical user interface programmed in LabVIEW (Version 14.0.1, National Instruments, Texas, USA) automates the sorption procedures in a step-wise manner to produce a hydrogen sorption curve using monitoring hardware, Model USB-6281 (National Instruments, Texas, USA). The interface provides manual control of the valves with live pressure and temperature information of the apparatus and allows input of experimental configurations for PCT measurements. The hydrogen sorption calculations for samples at non-ambient temperatures can be found in Appendix B.

2.5.1 Leak Corrections for Non-Ambient Measurements

The stainless-steel sample cells should only be used at temperatures < 400 °C, any higher and the permeation of hydrogen through the walls of the stainless steel becomes an issue, and the measured hydrogen content after PCT measurements need to be corrected for the hydrogen loss. The hydrogen loss through the stainless-steel sample cell can be calculated by the diffusional flux of hydrogen (San Marchi, Somerday and Robinson 2005; Equation 2.4).

$$J_\infty = \frac{\Phi}{t_s}\sqrt{P} \tag{2.4}$$

where J_∞ = the steady state diffusional flux of hydrogen (in units of mol m^{-2} s^{-1}), Φ = the permeability of hydrogen at a given temperature (in units of mol m^{-1} s^{-1} $MPa^{-1/2}$), t_s = the thickness of stainless steel (in units of m) and P = the pressure of hydrogen at a given temperature (in units of MPa). A surface area to thickness (SA/t_s) factor is determined by performing a high-pressure leak test over several days at a temperature above the permeation of hydrogen (> 400 °C) through 316 stainless steel. Given $J_\infty = \Delta n\, SA^{-1}\, \Delta t_e^{-1}$, the SA/t_s factor can be calculated by rearranging Equation 2.4 as follows:

$$\frac{SA}{t_s} = \frac{\Delta n}{\Delta t_e \, \Phi \sqrt{P}} \tag{2.5}$$

where Δn = change in hydrogen moles (in units of mol) and Δt_e = change in time elapsed (in units of s).

The leak rate measurement involves adding a known pressure of hydrogen to a blank sample cell. The sample cell was heated to a target temperature close to experimental temperatures, and the system pressures were recorded for approximately 40 hours. The SA/t_s factors were calculated (from Equation 2.5) using each 4 hour time block within the 40 hour measurement, where the SA/t_s factors were averaged to determine the SA/t_s factor of the sample cell. Other time blocks (1, 2, 3 and 5 hour) were calculated but the 4 hour time block showed the least standard deviation from the calculated averages.

The absorption of hydrogen in steel is also another factor that needs consideration when performing hydrogen sorption measurements at high temperature. The solubility of hydrogen in 316 stainless steel is determined by the following equation:

$$K = K_0 \exp\left(-\Delta H_s / R\,T\right) \tag{2.6}$$

where K is the solubility of hydrogen in stainless steel (in units of mol m^{-3} $MPa^{-1/2}$), R is the universal gas constant, 8.31447 J K^{-1} mol^{-1} and T is the non-ambient temperature. For 316 stainless steel the values of K_0 and ΔH_s are 135 mol H_2 m^{-3} $MPa^{-1/2}$ and 5900 J mol^{-1}, respectively (San Marchi, Somerday and Robinson 2005). The moles absorbed within stainless steel at a particular temperature and pressure is given by the following equation:

$$n\left(\mathrm{H}_2\right) = K\,V\sqrt{P} \tag{2.7}$$

where V is the non-ambient volume of stainless steel in the sample cell (in units of m^3) and P is the final pressure (in units of MPa). Between each step, the moles of hydrogen absorbed/desorbed can be determined using Equation 2.6 and 2.7; hence, appropriate absorption corrections can be made to the final measurement.

2.6 Temperature Programmed Photographic Analysis

Temperature programmed photographic analysis (TPPA) is a technique used to determine the macroscopic behaviour of complex hydrides during decomposition/ melting at high temperatures. Although *in situ* XRD provides the best method of determining the phase composition at high temperatures, it is not always the easiest approach. TPPA provides an alternative *in situ* method, provided the colour and behaviour of the sample may help to reveal the identity of the phase at high temperature (Ley et al. 2014; Paskevicius et al. 2012; Paskevicius et al. 2013). A typical experimental setup inside a fume hood is shown in Figure 2.17.

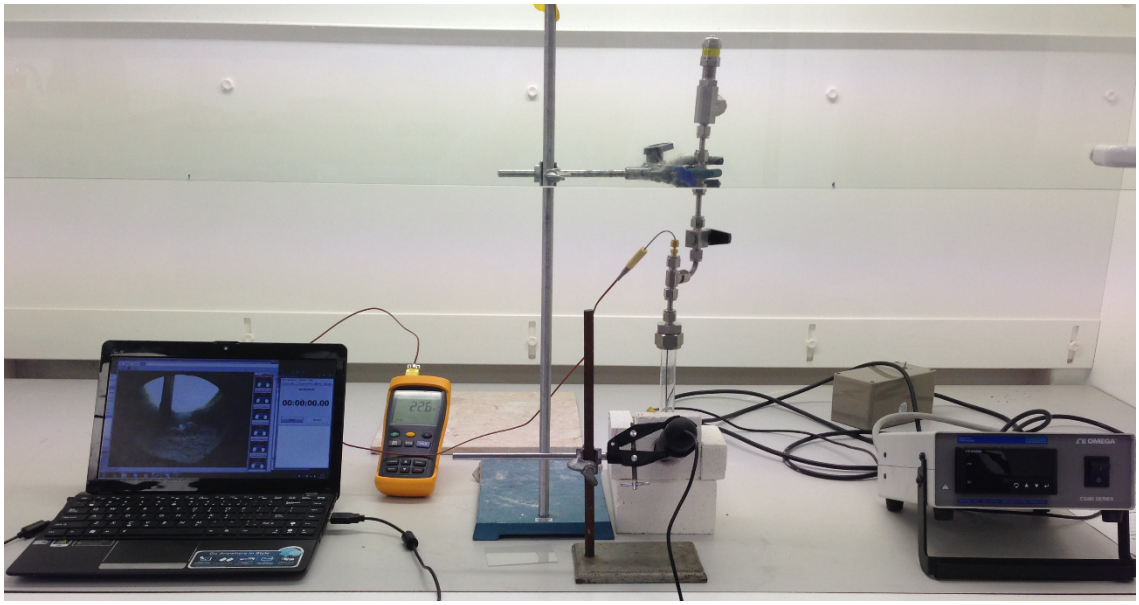

Figure 2.17: Experimental setup of the TPPA inside a fume hood.

TPPA was performed by collecting photographs using a digital Plugable microscope (Plugable Technologies, Washington, USA) and a specially designed heating-block sample holder, capable of heating samples at 10 °C min^{-1} in the temperature range of 25 – 500 °C (Ley et al. 2014; Paskevicius et al. 2012; Paskevicius et al. 2013). Transparent glass vials were used to seal samples in argon and connected to a pressure relief valve set to 1 bar to maintain atmospheric pressure (Figure 2.18c). A Thermocouple was inserted within the glass vial to monitor the sample temperature during a programmed-temperature ramp (Figure 2.18d). The aluminium heating block was engineered with open viewing windows for photographic analysis, provided by near-uniform heating

with rod heaters, interfaced to a temperature controller (Figure 2.18a and 2.18b). A light source was positioned above the setup along with the light-emitting diodes included on the pluggable microscope to evenly illuminate the sample.

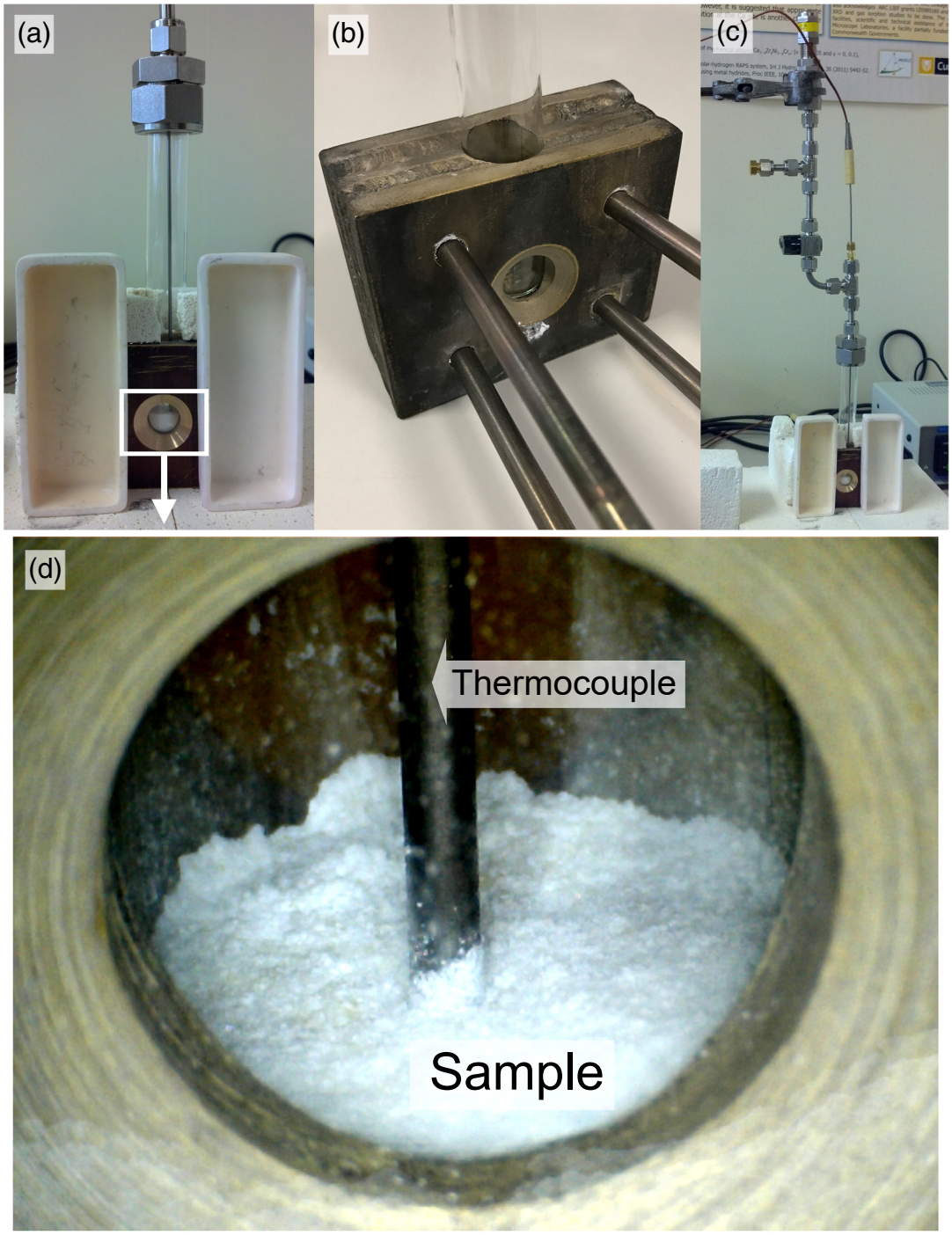

Figure 2.18: (a) Front view of the windowed heating block with test tube inserted. (b) Back view of the heating block with heating rods in place. (c) The pressure relief valve set to 1 bar. (d) View from the Plugable microscope of the sample with thermocouple inserted.

CHAPTER 3: NOVEL METHOD OF OBTAINING FAST THERMODYNAMIC DATA

3.1 Introduction

The formation enthalpy of hydrides determines the amount of heat that is released during hydrogen absorption and hence, the amount of heat required in the case of desorption. Measuring the thermodynamic data of hydride systems allows the estimation of operating temperature and pressure ranges to determine whether the system will be suitable for concentrated solar thermal (CST) energy storage. However, the traditional method of obtaining thermodynamic data involves performing multiple pressure-composition-temperature (PCT) measurements (Figure 3.1) to evaluate the equilibrium plateau pressure (P_{eq}) at various temperatures (T_1, T_2, T_3 etc.). By taking the logarithm of the plateau pressure against 1/T, the van't Hoff plot is obtained (straight line in Figure 3.1) to calculate the enthalpy (ΔH) and entropy values (ΔS) (Dornheim 2011).

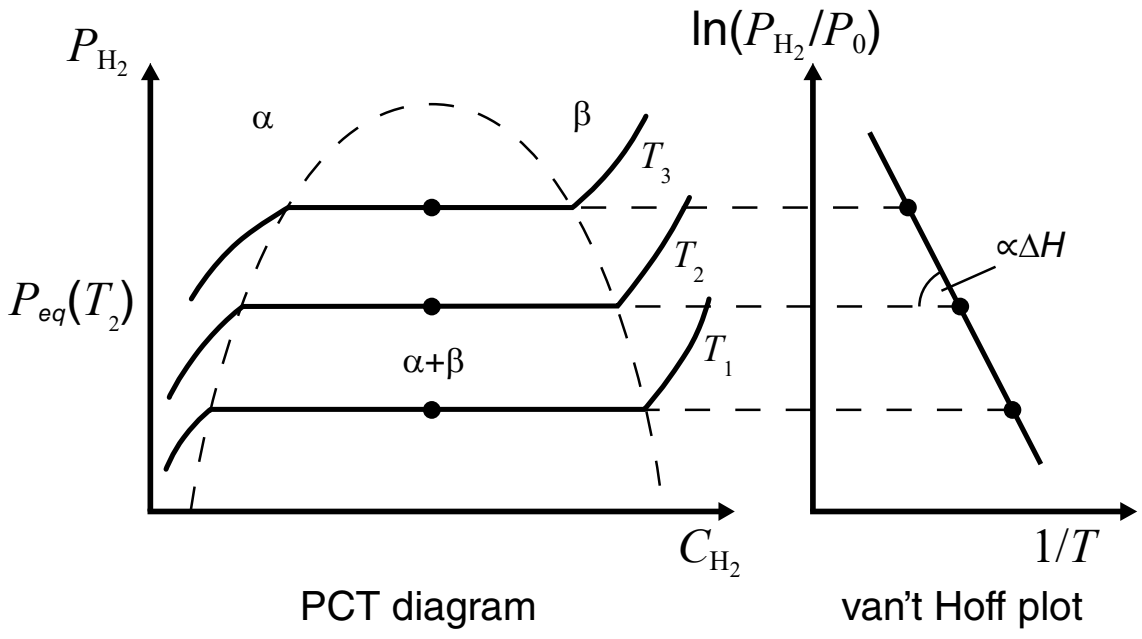

Figure 3.1: Schematic of a PCT diagram (left-hand side) and the corresponding van't Hoff plot on the right-hand side (Dornheim 2011).

The Gibbs free energy change (ΔG) can be expressed in Equation 3.1:

$$\Delta G = \Delta H - T\,\Delta S \tag{3.1}$$

where T = temperature in kelvin (K) and the equilibrium pressure (P_{eq}) is related to the Gibbs free energy change in Equation 3.2:

$$\Delta G = -R\,T\,\ln\left(P_{eq}/P_0\right) \tag{3.2}$$

where R is the universal gas constant, 8.31447 J K^{-1} mol^{-1} and P_0 = 1 atm. Therefore, this expression can be rewritten so that the natural log of P_{eq} is a function of the temperature (T) as follows:

$$\ln\left(\frac{P_{eq}}{P_0}\right) \propto \frac{-\Delta H}{R}\left(\frac{1}{T}\right) + \frac{\Delta S}{R} \tag{3.3}$$

where Equation 3.3 defines the straight line of the van't Hoff plot. The slope of the straight line is proportional to the change in enthalpy (ΔH) and the intercept (when $1/T$ = 0) will give the change in entropy (ΔS). However, the values for hydrogen absorption are negative ($-\Delta H_{abs}$ and $-\Delta S_{abs}$) and the values for hydrogen desorption are positive ($+\Delta H_{des}$ and $+\Delta S_{des}$). Therefore, two equations are used to evaluate the absorption and desorption of hydrogen as shown in Equation 3.4 and 3.5, respectively.

$$\ln\left(\frac{P_{eq}}{P_0}\right) = \frac{\Delta H_{abs}}{R}\left(\frac{1}{T}\right) - \frac{\Delta S_{abs}}{R} \tag{3.4}$$

$$\ln\left(\frac{P_{eq}}{P_0}\right) = \frac{-\Delta H_{des}}{R}\left(\frac{1}{T}\right) + \frac{\Delta S_{des}}{R} \tag{3.5}$$

Figure 3.2 shows the PCT measurement of MgH_2 – 2 mol% TiB_2 cycled at 350 °C (hydrogen desorption followed by an absorption measurement). The equilibrium pressure was measured with a 5 hour wait time, completing the total absorption/desorption cycle in a duration of 10 days. Data points that were measured in the solid-solution phase (α-phase) and the hydride phase (β-phase), shown in Figure 3.1, typically required less time to reach equilibrium than the data

points measured within the two-phase region ($\alpha + \beta$). This observation was due to a kinetic barrier and is dependent on each system (Dornheim 2011). Hence, if 30 total equilibrium data points were required to construct the absorption and desorption PCT curves with a wait time of 5 hours each, it will take a minimum of ~6 days to complete one absorption/desorption PCT cycle.

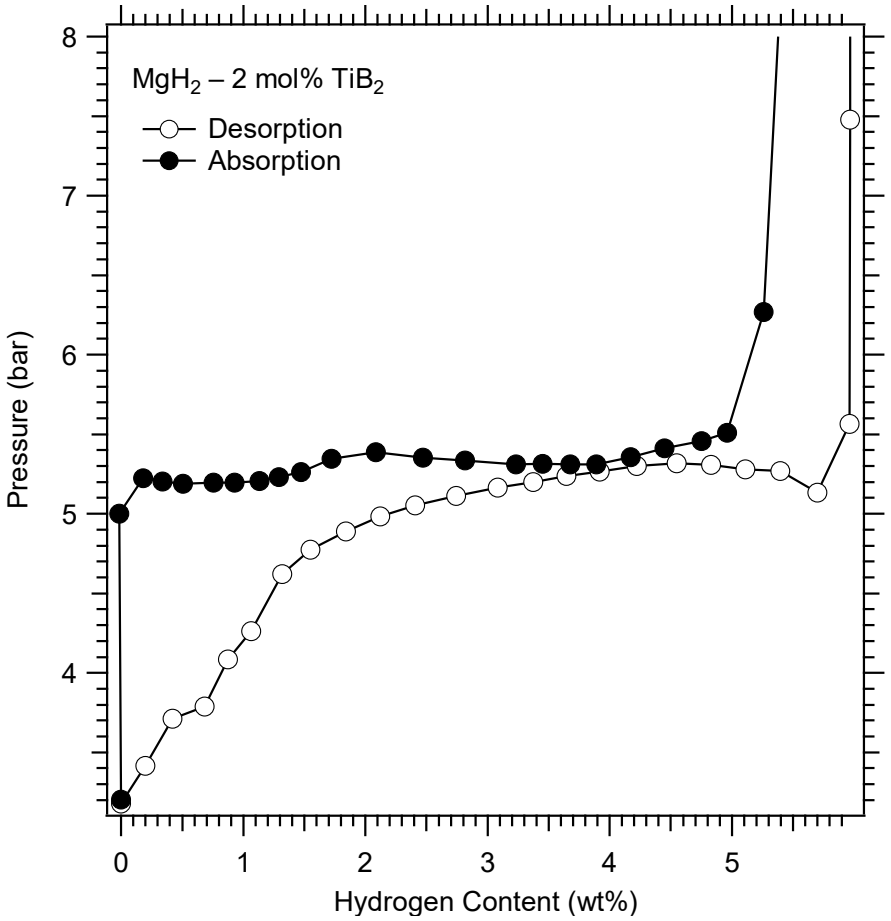

Figure 3.2: PCT cycle of MgH_2 – 2 mol% TiB_2 at 350 °C over a duration of 10 days (5 days for each absorption/desorption curve).

Pressure-composition-temperature measurements should be performed at as many temperatures as practically possible, with at least 3 cycle measurements typically used for van't Hoff plots. In the hydrogen storage field, 4 or 5 different temperature measurements are preferable for van't Hoff plots to reduce the uncertainties on the calculated change in enthalpy and entropy (Sheppard, Paskevicius and Buckley 2011b). Therefore, based on the assumption of 15 data points per absorption and desorption PCT curve (30 total data points) at 5 different temperatures, a van't Hoff plot could take up to ~31 days to obtain (~31 days for 5 temperatures and ~19 days for 3 temperatures).

The novel method of obtaining fast thermodynamics involves building a low volume apparatus (LVA) and doing step-wise temperature increments (Figure 3.3) at near-constant hydrogen content (NCHC). The general method involves minimising the change in hydrogen content during step-wise temperature increments based on the system mass and volume to satisfy the conditions for a constant (or near constant) hydrogen to metal atomic ratio (H/M). The step-wise temperature measurement has similarities to that used by Bogdanović et al. (1999) in measuring the magnesium hydride-magnesium system that modified PCT measurements in such a way that the temperature was increased (and decreased) until the next equilibrium pressure was achieved.

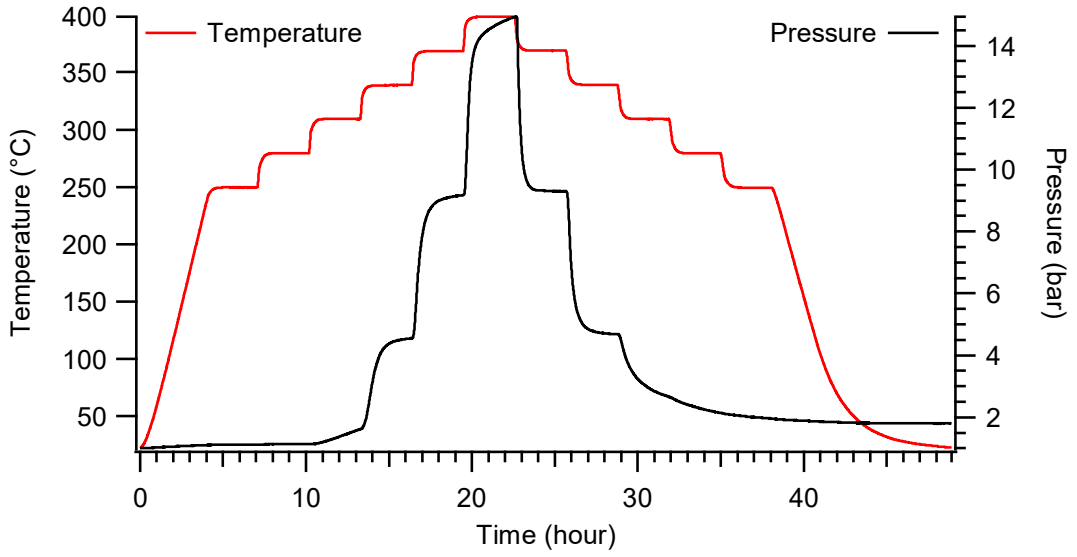

Figure 3.3: Step-wise temperature increments of MgH_2 – 2 mol% TiB_2 between 250 °C and 400 °C.

The LVA consists of three distinct volumes connected by valves: the sample cell (Part A in Figure 3.4), a small reference volume (Part B in Figure 3.4) and a large reference volume (Part C in Figure 3.4). The purpose of the LVA is to minimise the volume and hence, the change in $\Delta(H/M)$ of the system by minimising the quantity of hydrogen that the sample can release or absorb between each experimental temperature and equilibrium pressure. Using the large reference volume (Part C), an appropriate sample mass is chosen so that its hydrogen content can be quickly adjusted to the midpoint of the plateau using few steps. By then closing the valve to the large volume (Part C), the reference volume (Part B) is dramatically reduced. In doing so, the change in $\Delta(H/M)$ is minimised

between each experimental temperature such that the amount of hydrogen evolved to establish equilibrium at the new temperature, is only a small fraction of the hydrogen contained in the sample. Therefore, minimising the quantity of hydrogen required (NCHC) to establish the new equilibrium at each temperature increment.

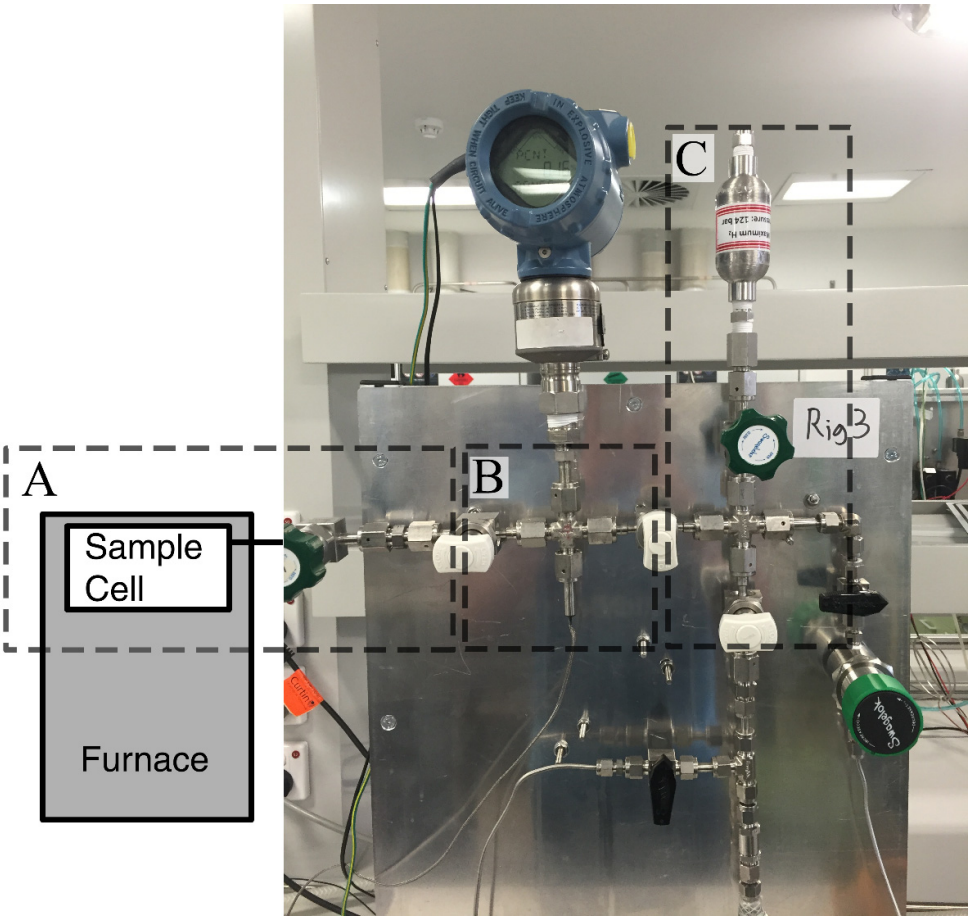

Figure 3.4: Schematic of the Low Volume Apparatus (LVA), where A = sample cell volume, B = small reference volume, C = large reference volume.

For systems with relatively flat equilibrium plateau pressures (Figure 3.5a), although the change in $\Delta(H/M)$ differs between each PCT measurement at different temperatures, the P_{eq} does not change. However, as many amide-imide-hydride systems feature sloping plateau pressures (Figure 3.5b), they are sensitive to changes in the ΔP_{eq} and $\Delta(H/M)$ at different temperatures. Therefore, to account for the plateau slope, the LVA-NCHC method involves corrections to the experimental pressure and hydrogen content to the ideal point at each PCT measurement to satisfy the conditions to plot the van't Hoff equation.

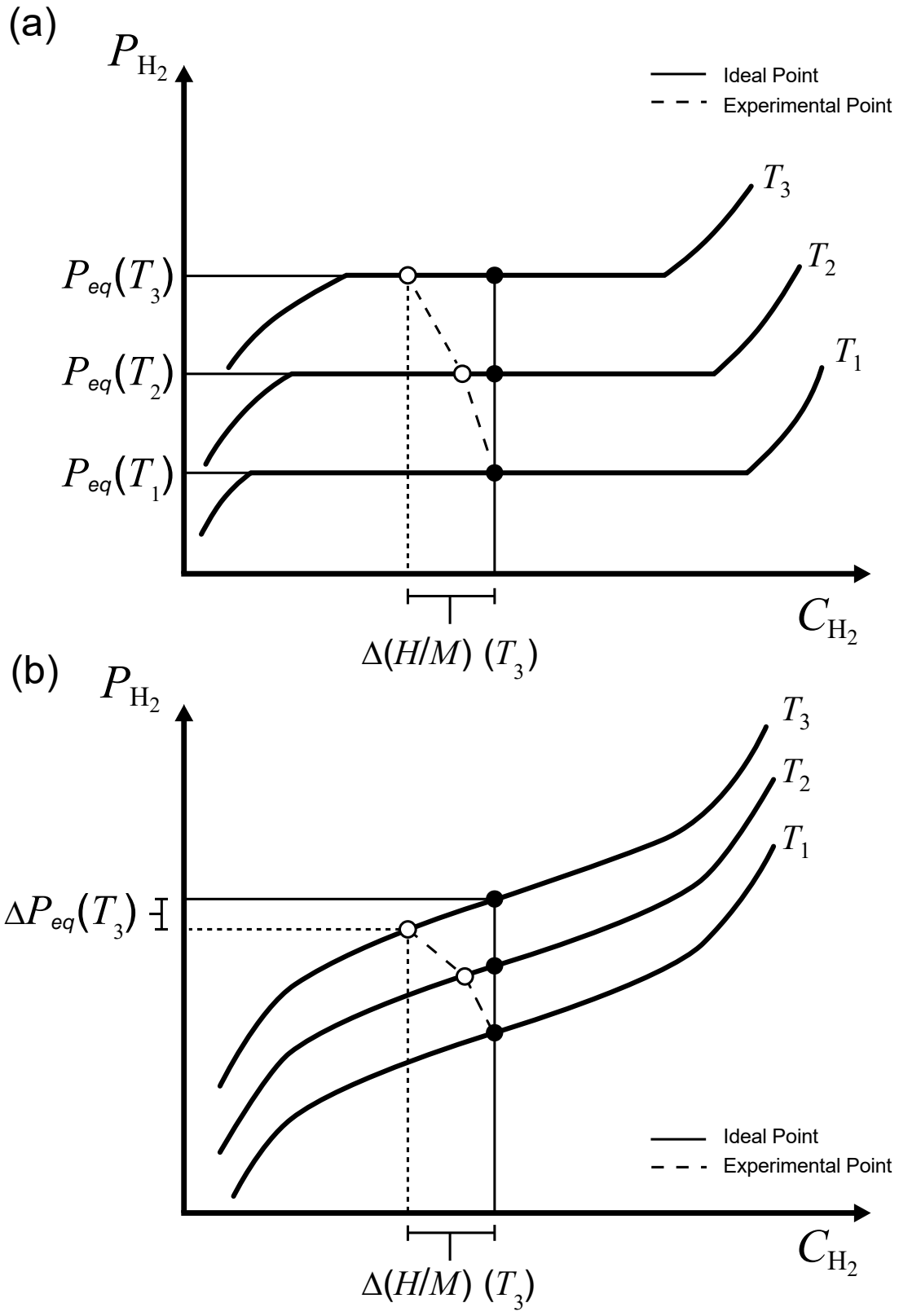

Figure 3.5: (a) The $\Delta(H/M)$ observed in PCT measurements with flat plateaux. (b) The $\Delta(H/M)$ and ΔP_{eq} observed in PCT measurements with sloping plateaux. (●) represents the midpoint of each PCT curve.

For completely new samples that have not been characterised before, a fast absorption/desorption PCT measurement is performed using an automated custom-built hydrogen sorption apparatus. This measurement provides information about the approximate absorption and desorption equilibrium pressures at the target temperature as well as information about the plateau slope, hysteresis, hydrogen capacity and kinetics. The equilibrium pressure of hydrogen can be estimated at a target range of temperatures by assuming $|\Delta S| \approx$ 130 J (mol H_2)$^{-1}$ K^{-1}, as most hydrogen reactions have a $|\Delta S|$ value of 120 – 140 J (mol H_2)$^{-1}$ K^{-1}. These lower and upper bounds on the entropy value can also estimate the equilibrium pressure range of hydrogen at high operating temperatures. Based on this information, a new sample is used on the LVA with the large reference volume open (Part C in Figure 3.4) to quickly adjust the hydrogen content to the H/M value that corresponds to the midpoint of the plateau before step-wise temperature increments are made.

3.2 Results

3.2.1 Near-constant Hydrogen Content (NCHC) Method on MgH_2 – 2 mol% TiB_2 with Flat Plateaux

The magnesium hydride-magnesium system has the following reaction:

$$MgH_2 \rightarrow Mg + H_2 \tag{3.6}$$

Thermodynamic properties of this system have been widely investigated as it has the highest hydrogen capacity of all the reversible metal hydrides and features flat plateaux in PCT measurements (Bogdanović et al. 1999; Chaise et al. 2010; Dornheim 2011). MgH_2 was doped with 2 mol% of titanium diboride (TiB_2), synthesised by Terry Humphries (2015) at Curtin University (Australia), the XRD analysis can be found in Appendix A (Figure A.1). This system was initially used to test the accuracy and application of the LVA-NCHC method (of obtaining fast thermodynamic data) by comparing the results with reliable literature values.

3.2.1.1 Step-wise temperature increments (not at NCHC)

Step-wise temperature increments were initially tested on the magnesium hydride-magnesium system using the hydrogen sorption apparatus that was mainly used for PCT measurements i.e. the automated custom-built H_2 sorption apparatus. Starting at a pressure near vacuum, step-wise temperature increments between 250 °C and 400 °C (Figure 3.3) were performed for a total of 7 usable equilibrium points (4 desorption and 3 absorption). By taking the usable equilibrium pressures and temperatures, a van't Hoff plot can be obtained (Figure 3.6). The experimental hydrogen capacity of MgH_2 was calculated to release 80% of the theoretical content by the fourth desorption point at 400 °C.

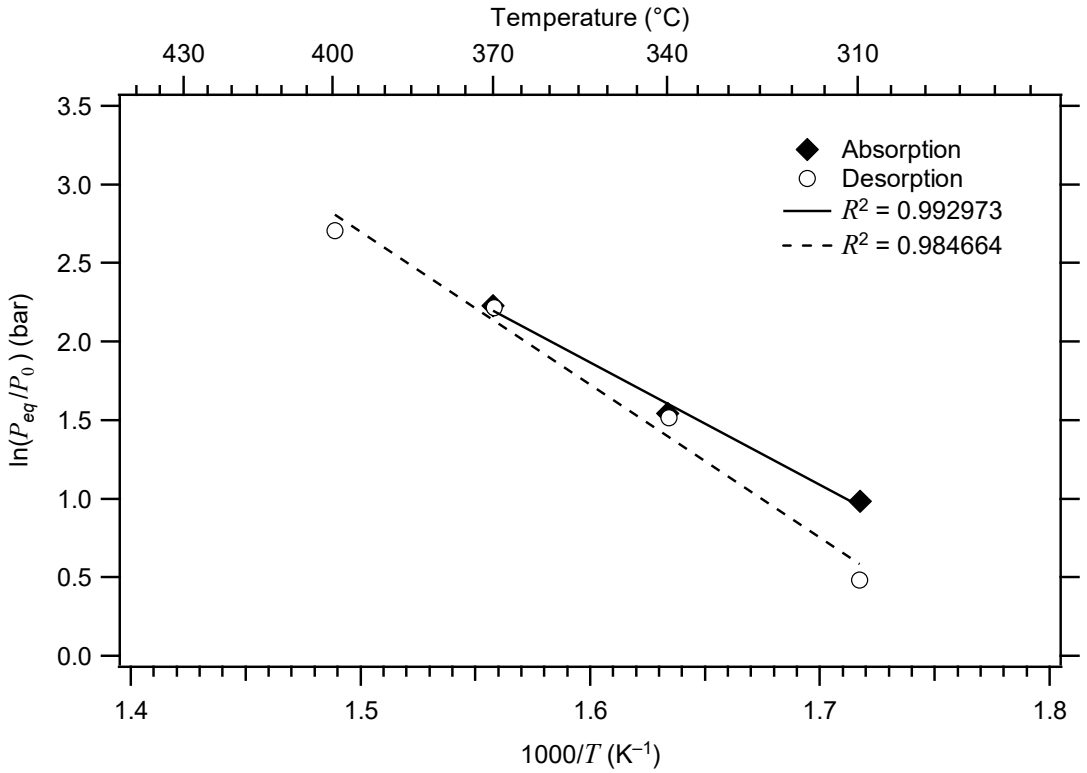

Figure 3.6: Van't Hoff plot for MgH_2 – 2 mol% TiB_2 from points obtained in Figure 3.3.

The enthalpy of absorption (ΔH_{abs}) and desorption (ΔH_{des}) from the measurements between 310 °C and 400 °C are –64.87 ± 0.49 and 80.86 ± 0.65 kJ (mol H_2)$^{-1}$, respectively. The average magnitude of these values is, $|\Delta H_{avg}|$ = 72.86 ± 8.57 kJ (mol H_2)$^{-1}$ (ΔH_{abs} = –72.86 kJ (mol H_2)$^{-1}$ and ΔH_{des} = 72.86 kJ (mol H_2)$^{-1}$). In comparison, Bogdanović et al. (1999) found the enthalpy of formation between 380 °C and 480 °C to be –74.0 kJ (mol H_2)$^{-1}$. The high

uncertainty in $|\Delta H_{avg}|$ could be related to the sample having slow kinetics at the lowest temperature (at 310 °C) to reach true equilibrium. Therefore, the lowest points at ~310 °C (in Figure 3.6) were excluded to obtain the new ΔH_{abs} and ΔH_{des} to be -74.95 ± 0.47 and 68.20 ± 0.39 kJ (mol H_2)$^{-1}$, respectively, resulting with $|\Delta H_{avg}| = 71.58 \pm 3.81$ kJ (mol H_2)$^{-1}$ ($\Delta H_{abs} = -71.58$ kJ (mol H_2)$^{-1}$ and $\Delta H_{des} = 71.58$ kJ (mol H_2)$^{-1}$). These enthalpy values are closer to the literature standard enthalpy of formation of –74.0 kJ (mol H_2)$^{-1}$ (Bogdanović et al. 1999). However, this result can be further improved by excluding the temperature data point at ~400 °C (in Figure 3.6) based on the assumption that insufficient hydrogen was in the system to reach its equilibrium pressure at high experimental temperatures. Therefore, the highest point at ~400 °C (in Figure 3.6) was excluded to obtain the new ΔH_{abs} and ΔH_{des} to be -74.95 ± 0.47 and 76.70 ± 0.49 kJ (mol H_2)$^{-1}$, respectively, resulting with $|\Delta H_{avg}| = 75.83 \pm 1.36$ kJ (mol H_2)$^{-1}$ ($\Delta H_{abs} = -75.83$ kJ (mol H_2)$^{-1}$ and $\Delta H_{des} = 75.83$ kJ (mol H_2)$^{-1}$). However, with only two points used to plot the van't Hoff equation, this result cannot be considered accurate enough to determine the true hydriding enthalpy of the Mg–MgH_2 system.

3.2.1.2 Thermodynamics at NCHC – van't Hoff equation

Step-wise temperature increments at NCHC were performed on MgH_2 – 2 mol% TiB_2 to improve the thermodynamic results using the LVA. To approximate the midpoint of the plateau that corresponds to ~50% of its hydrogen capacity, the known volumes of the LVA (including the large reference volume) were used to calculate the mass of MgH_2 required. At a temperature of 320 °C and an initial pressure near vacuum, ~1 g of MgH_2 would release ~28% of its maximum hydrogen content when the sample cell volume (Part A in Figure 3.4) is open to the large reference volume (~60 cm^3) (Part B and C). Therefore, two desorption steps into the large reference volume were required in order for the hydrogen content of the sample to reach the midpoint of the plateau (~50% hydrogen content).

The equilibrium pressures at each stepped temperature in Figure 3.7 were used to obtain the van't Hoff plot in Figure 3.8. From the measurements between ~320 °C and ~400 °C, $\Delta H_{abs} = -76.03 \pm 0.41$ kJ (mol H_2)$^{-1}$ and $\Delta H_{des} = 76.35 \pm$

0.47 kJ (mol H_2)$^{-1}$. The average magnitude of the absorption and desorption is, $|\Delta H_{avg}|$ = 76.19 ± 0.60 kJ (mol H_2)$^{-1}$, whereas the literature enthalpy of formation between 280 °C and 370 °C is –74.3 kJ (mol H_2)$^{-1}$ (Bogdanović et al. 1999). Furthermore, the change in entropy of absorption (ΔS_{abs}) and desorption (ΔS_{des}) determined from these measurements between ~320 °C and ~400 °C is similar at –136.82 ± 0.47 and 136.31 ± 0.53 J (mol H_2)$^{-1}$ K^{-1}, respectively, compared to a value of –136.0 J (mol H_2)$^{-1}$ K^{-1} (ΔS_{abs}) reported by Bogdanović et al. (1999) for measurements between 280 °C and 370 °C. Therefore, with the additional equilibrium points used to plot the van't Hoff equation in Figure 3.8, the LVA-NCHC method has vastly improved the previous van't Hoff plot obtained in Figure 3.6, where only two equilibrium points were used.

For completely new systems with no thermodynamic data, the uncertainty on the enthalpy (ΔH_{des}) value can be estimated by assuming an entropy (ΔS_{des}) value that ranges between 120 and 140 J (mol H_2)$^{-1}$ K^{-1}. Based on the equilibrium pressure from a single PCT measurement at a given temperature, the equilibrium pressure of hydrogen at a higher temperature can then be estimated. For example, the measured equilibrium pressure of MgH_2 – 2 mol% TiB_2 was 16.68 bar at ~400 °C. Therefore, the predicted equilibrium pressure at 500 °C ranges between ~75 bar and ~102 bar as shown in Table 3.1. This approximation helps calculate the required mass and volume of the system to accordingly adjust the hydrogen content to the midpoint of the plateau for step-wise temperature increments at NCHC measurements.

Table 3.1: Estimated uncertainty on the enthalpy of desorption and equilibrium pressure of H_2 assuming an entropy value of 120 – 140 J (mol H_2)$^{-1}$ K^{-1}, based on the equilibrium H_2 pressure of 16.68 bar at 400 °C.

Assumed ΔS_{des} (J (mol H_2)$^{-1}$ K^{-1})	120	130	140
Estimated ΔH_{des} (kJ (mol H_2)$^{-1}$)	65.0	71.8	78.5

Temperature (°C)	Estimated desorption P_{eq} (bar)		
400	16.68	16.68	16.68
425	25.3	26.4	27.6
450	37.2	40.5	44.0
475	53.5	60.3	68.0
500	75.1	87.6	102.3

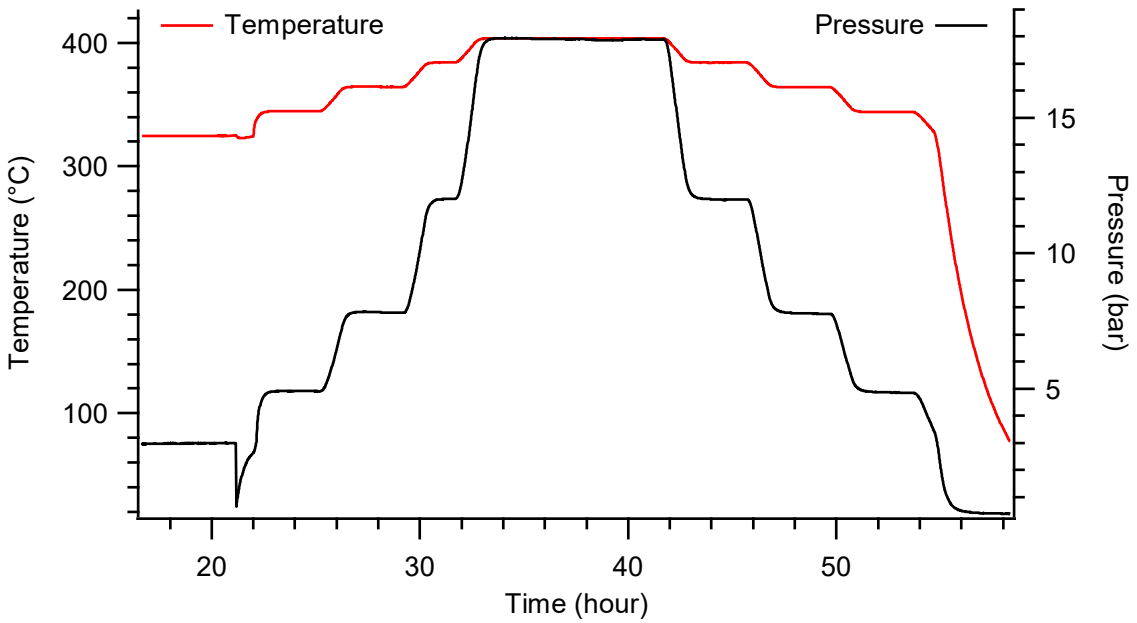

Figure 3.7: Step-wise temperature increments of MgH_2 – 2 mol% TiB_2 at near-constant hydrogen content between ~320 °C and ~400 °C.

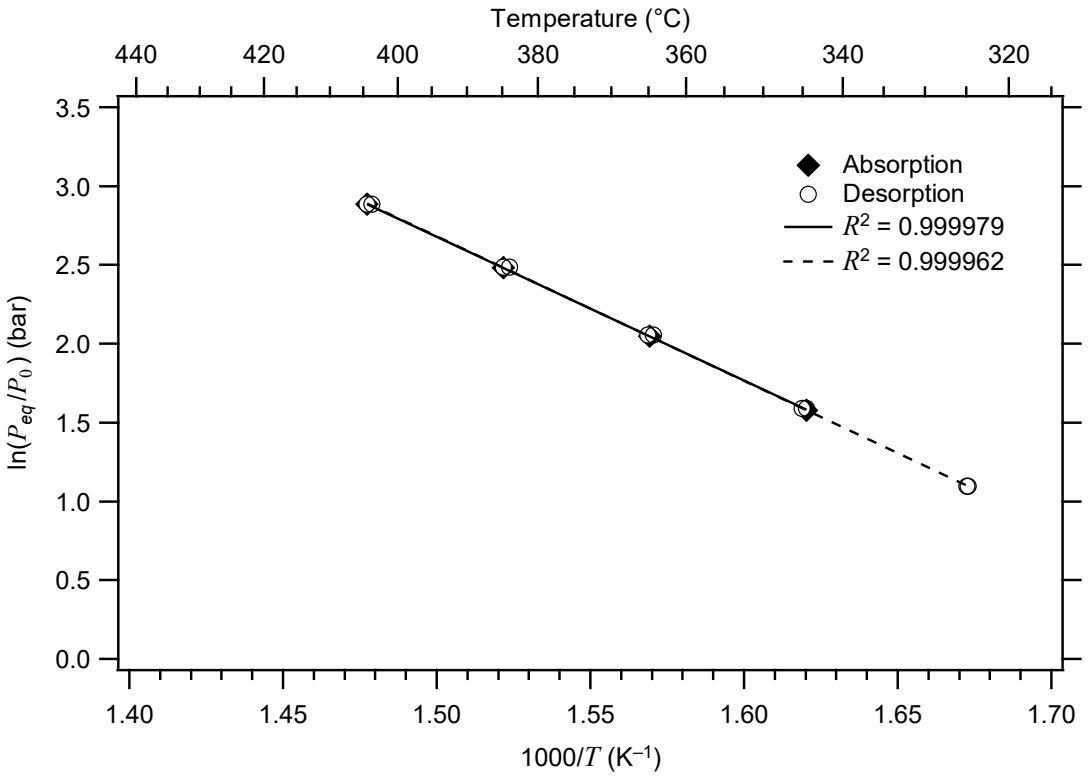

Figure 3.8: Van't Hoff plot for MgH_2 – 2 mol% TiB_2 obtained using LVA-NCHC method.

3.2.2 Near-constant Hydrogen Content (NCHC) Method on Amide-Imide-Hydride Systems with Sloping Plateaux

The fast thermodynamic data obtained from systems that feature flat plateaux (MgH_2 – 2 mol% TiB_2) using the LVA-NCHC method showed promising results with the applied conditions. However, the amide-imide-hydride systems investigated in this thesis typically feature sloping plateaux. Therefore, an adjustment to the LVA-NCHC method for sloping plateaux was derived to quickly obtain thermodynamic data to identify potential thermal energy storage materials.

3.2.2.1 Corrections for Sloping Plateaux

To determine the thermodynamic data of amide-imide-hydride systems, a quick PCT measurement of a sorption cycle is performed using an automated custom-built H_2 sorption apparatus. This measurement is required to quickly identify the equilibrium pressure at a targeted temperature (T_{mid}), preferably at the midpoint of the temperature range that will be used for step-wise temperature increments at NCHC measurements. Corrections were made for both the diffusion and absorption of hydrogen through 316 stainless steel as described in Chapter 2: Section 2.5.1. From the PCT measurements (Figure 3.9), a determination is made on the practical fraction of the theoretical hydrogen content (~90% in the case of the Ca–N–H system). The midpoint of the sloping plateau corresponds to the equilibrium pressure, $\ln(P_{eq})$, at a hydrogen content, $(H/M)_{T_{mid}}$.

From the definition of the slopes for the absorption and desorption curves in Figure 3.9, the relationship can be expressed as follows:

$$m_{slope} = \frac{\Delta \ln(P_{eq})}{\Delta(H/M)} \tag{3.7}$$

where:

$$\Delta \ln(P_{eq}) = \ln(P_{ideal}) - \ln(P_{exp}) \tag{3.8}$$

$$\Delta(H/M) = \left[(H/M)_{T_{mid}} - (H/M)_{exp} \right] \tag{3.9}$$

$\ln(P_{exp})$ is the experimental pressure and $\ln(P_{ideal})$ is the ideal pressure that would be measured at the experimental temperature if we were at the equivalent $(H/M)_{T_{mid}}$ value rather than at $(H/M)_{exp}$. By substituting Equation 3.8 and 3.9 into Equation 3.7 with some rearranging, the following equations can be obtained for $\ln(P_{ideal})$:

$$\ln(P_{ideal}) = m_{slope}(\text{abs})\left[(H/M)_{T_{mid}} - (H/M)_{exp}\right] + \ln(P_{exp}) \tag{3.10}$$

$$\ln(P_{ideal}) = m_{slope}(\text{des})\left[(H/M)_{T_{mid}} - (H/M)_{exp}\right] + \ln(P_{exp}) \tag{3.11}$$

These values are used to correct the experimental pressures (absorption and desorption) from step-wise temperature increments at NCHC (constant H/M) to obtain the van't Hoff plot.

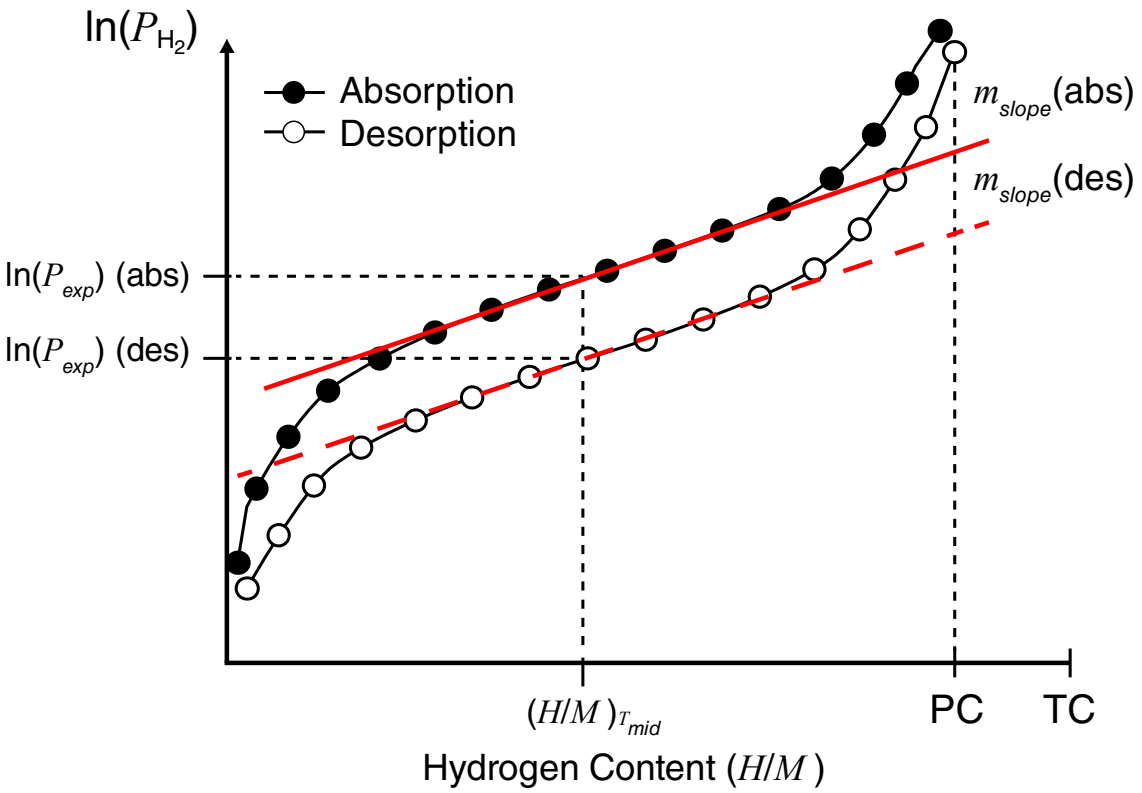

Figure 3.9: PCT curves with sloping plateaux for absorption and desorption, where $(H/M)_{T_{mid}}$ is the midpoint of the sloping plateau, PC is the practical content and TC is the theoretical content.

3.2.2.2 Discussion

Using the LVA, step-wise temperature increments at NCHC were performed to identify the experimental pressures (P_{exp}) in a temperature range around the midpoint of the single PCT measurement (T_{mid}). Figure 3.10 shows an example of step-wise increments with increasing (and decreasing) temperature at each equilibrium pressure, where the step times may vary depending on the kinetics of the system (2 – 4 hour steps). By applying the pressure corrections as described in Section 3.2.2.1, the ideal pressure at constant H/M are met so that the van't Hoff equations can be plotted and thermodynamic properties calculated. This thermodynamic data can then be used to estimate the heat storage capacity and equilibrium pressures at high temperatures suitable for thermal energy storage. Additionally, given the equilibrium pressure obtained from the quick PCT measurement, we can make an assumption for $|\Delta S|$ and substitute P_{eq} and T_{mid} into the van't Hoff equation (Equation 3.3) to calculate an approximate value for $|\Delta H|$. Using this approximation, the heat storage capacity can also be estimated depending on the range of $|\Delta S|$ values in cases where step-wise temperature increments (Figure 3.10) were not performed.

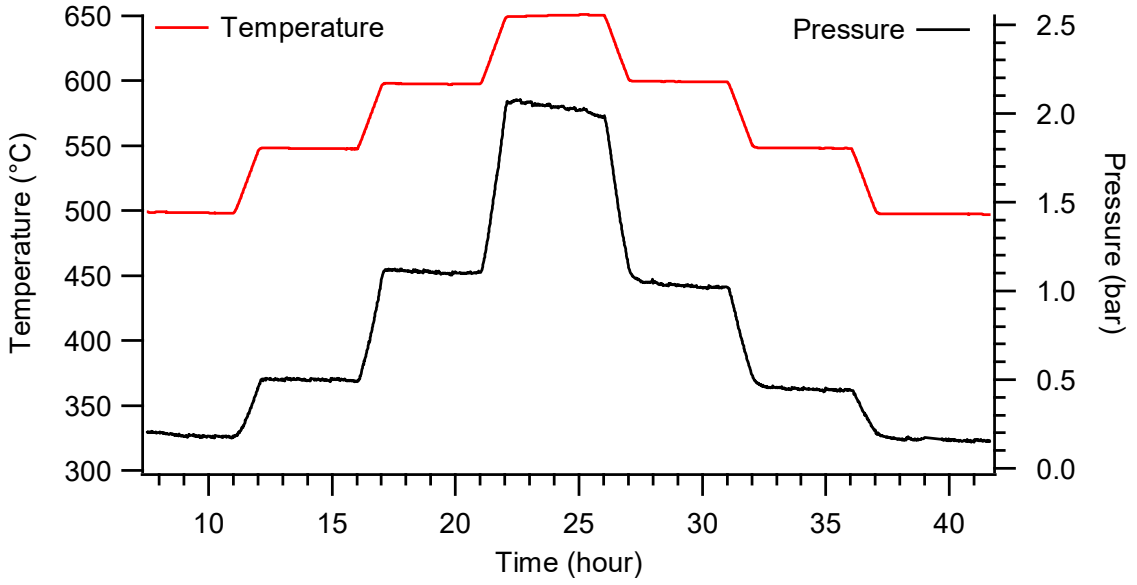

Figure 3.10: Step-wise temperature increments of amide-imide-hydride systems at near-constant hydrogen content between 500 °C and 650 °C.

The LVA-NCHC method assumes that the plateaux do not change with temperature and so uncertainties in the thermodynamic values calculated with this method involve the fact that, experimentally, the plateau slope for absorption and desorption may vary with temperature. This uncertainty can be minimised by determining the plateau slope (or performing a PCT curve) at a temperature near the middle of the range to be used for step-wise temperature increments at NCHC measurements. An additional contribution to the uncertainty in thermodynamics calculated with the LVA-NCHC method arises from uncertainty in determining the plateau slope from the experimental PCT curve. This uncertainty is because experimental PCT data is not a smooth curve but is comprised of step-wise data. Hence, it is often difficult to determine exactly when the plateaux start and finish, where the choices may affect the slopes obtained.

3.3 Conclusion

The thermodynamics of metal hydrides can be characterised using multiple PCT curves to plot the van't Hoff equation. However, it takes up to ~31 days (minimum of 5 curves) to perform enough PCT curves to satisfy the conditions to plot the van't Hoff equation. Step-wise temperature increments using the low volume apparatus (LVA) was tested on the Mg–MgH_2 system at near-constant hydrogen content (NCHC) for its well-known thermodynamic data. From the obtained van't Hoff plot, the average of the magnitude of absorption and desorption was, $|\Delta H_{avg}| = 76.19 \pm 0.60$ kJ (mol H_2)$^{-1}$ ($\Delta H_{abs} = -76.03 \pm 0.41$ kJ (mol H_2)$^{-1}$ and $\Delta H_{des} = 76.35 \pm 0.47$ kJ (mol H_2)$^{-1}$). This value has a difference of ~2 kJ (mol H_2)$^{-1}$ compared to the values obtained by Bogdanović et al. (1999). Drawing from the results obtained from a system that has its thermodynamic data widely published, we can be confident that this novel method of obtaining fast thermodynamic data, was an acceptable approximation for the Mg–MgH_2 system and possible systems with flat plateaux.

The LVA-NCHC method was designed for amide-imide-hydride systems with sloping plateaux. PCT curves with sloping plateaux (known for slow kinetics) generally take longer to reach equilibrium, multiplying the time required to perform enough PCT curves to satisfy the van't Hoff equation. A minimum of five PCT

measurements (that take approximately 31 days to perform) are typically required to plot the van't Hoff equation for obtaining enthalpy and entropy values. In comparison, the LVA-NCHC method can be performed in a little over three days (or 1 week, including a fast PCT measurement) to complete.

The novel method, with the advantage of faster collection times than traditional PCT measurements, also has a few disadvantages and uncertainties, specifically for systems with sloping plateaux. Compared to traditional PCT measurements, a large sample mass is required to minimise the change in $\Delta(H/M)$ during step-wise temperature increments. Furthermore, PCT measurements typically require between 0.5 and 1 grams of sample, whereas the LVA system typically requires between 3 and 4 grams of sample and is dependent on the properties of the sample and the volume of the LVA system. This requirement can be disadvantageous when the synthesis quantities are low. Because the LVA was constructed using readily available components in the laboratory. The apparatus can be further improved using custom components to reduce the system volume such that the amount of sample would in turn be reduced for NCHC measurements. The LVA-NCHC method also assumes that the plateau slope does not change within the temperature range of the step-wise measurement. Therefore, additional uncertainties can arise if this slope varies greatly with temperature.

In conclusion, compared to the ~31 days traditionally required to plot a van't Hoff equation using several PCT measurements, this novel method of obtaining fast thermodynamic data utilising an LVA with step-wise temperature increments at NCHC, has promising applications that have the potential to quickly advance the search for thermal energy storage materials at high temperature.

CHAPTER 4: LITHIUM-BASED SYSTEMS

4.1 Introduction

Imide-hydrides have been studied as possible high temperature metal hydrides as they are notorious for operating at high temperatures > 500 °C (Xiong et al. 2004; Zhang and Hu 2012). Lithium-based amide-hydride systems are among the most widely studied material owing to their high hydrogen contents (Chen et al. 2002). The amide- and imide-hydrides were characterised, focusing on their: decomposition mechanics, material characteristics, thermodynamic properties, sorption kinetics and the cyclic stability. Furthermore, X-ray diffraction (XRD) was used in characterising the decomposition structures of nitrides and imides.

Based on the decomposition of Li_3N by Chen et al. (2002), the lithium-based amide-hydride system has a two-step reaction as follows:

$$LiNH_2 + LiH \rightarrow Li_2NH + H_2 \tag{4.1}$$

$$Li_2NH + LiH \rightarrow Li_3N + H_2 \tag{4.2}$$

However, there has been little evidence of the imide-hydride reaction pathway in Equation 4.2. This observation is due to the formation of lithium nitride hydride (Li_4NH) that reacts with lithium imide (Li_2NH) at high temperatures to form lithium imide-nitride hydride ($Li_{4-2x}N_{1-x}H_{1-x}(NH)_x$), a non-stoichiometric solid-solution (Bull et al. 2010; Tapia-Ruiz et al. 2013). The proposed reaction can be expressed as follows:

$$x\,Li_2NH + (1-x)\,Li_4NH \rightarrow Li_{4-2x}N_{1-x}H_{1-x}(NH)_x \tag{4.3}$$

Three reactions were investigated in this chapter: the amide-hydride reaction, $LiNH_2$ + LiH (1:2), the imide-hydride reaction, Li_2NH + LiH (1:1) and the imide-hydride (with excess LiH) reaction, Li_2NH + LiH (1:2). In addition, known catalysts were also investigated on $LiNH_2$ + LiH (1:2) to improve the hydriding kinetics.

4.2 Results

4.2.1 $LiNH_2$ + LiH (1:2)

4.2.1.1 Preparation

Lithium amide ($LiNH_2$) and lithium hydride (LiH) in a 1:2 molar ratio was prepared by ball-milling using the starting reagents $LiNH_2$ (Sigma-Aldrich, 95%) and LiH (Sigma-Aldrich, 95%). The reagents were thoroughly mixed in a planetary ball-mill, where three different batches were made with their synthesis details summarised in Table 4.1.

Table 4.1: Summary of the synthesis batch details of $LiNH_2$ + LiH (1:2).

Batch no.	Mill Time	RPM	BTP ratio
1 (Powder)	4 hours	400	30:1
2 (Powder)	6 hours	600	60:1
3 (Pellet)	6 hours	600	60:1

Batch 3 was pressed into three individual 8 mm diameter pellets in a 1:2 molar ratio ($LiNH_2$:LiH). This pellet batch was prepared because of a problem with the powder batches melting and blocking sample cell filters. More details about this batch can be found in temperature-programmed photographic analysis (TPPA) in Section 4.2.1.4.

4.2.1.2 Fourier transform infra-red (FTIR) analysis

Fourier transform infra-red measurements were performed to distinguish the identity of lithium imide and amide phases due to its overlapping XRD patterns. Figure 4.1 shows the result of the FTIR analysis for the mixture of $LiNH_2$ and LiH in a 1:2 molar ratio. The broad band that occurs at ~3676 cm^{-1} is due to the O–H stretching vibrations that are due to atmospheric water absorbed by the KBr pellet. The N–H symmetric and asymmetric stretching vibrations of $LiNH_2$ occur at 3314 cm^{-1} and 3260 cm^{-1}, respectively. These absorption bands are in agreement with those reported by Kojima and Kawai (2005). Furthermore, Yu et al. (2011) reported the same N–H bands corresponding to $LiNH_2$ at 1564 cm^{-1} and 1537 cm^{-1} that also appear in the FTIR spectra (Figure 4.1).

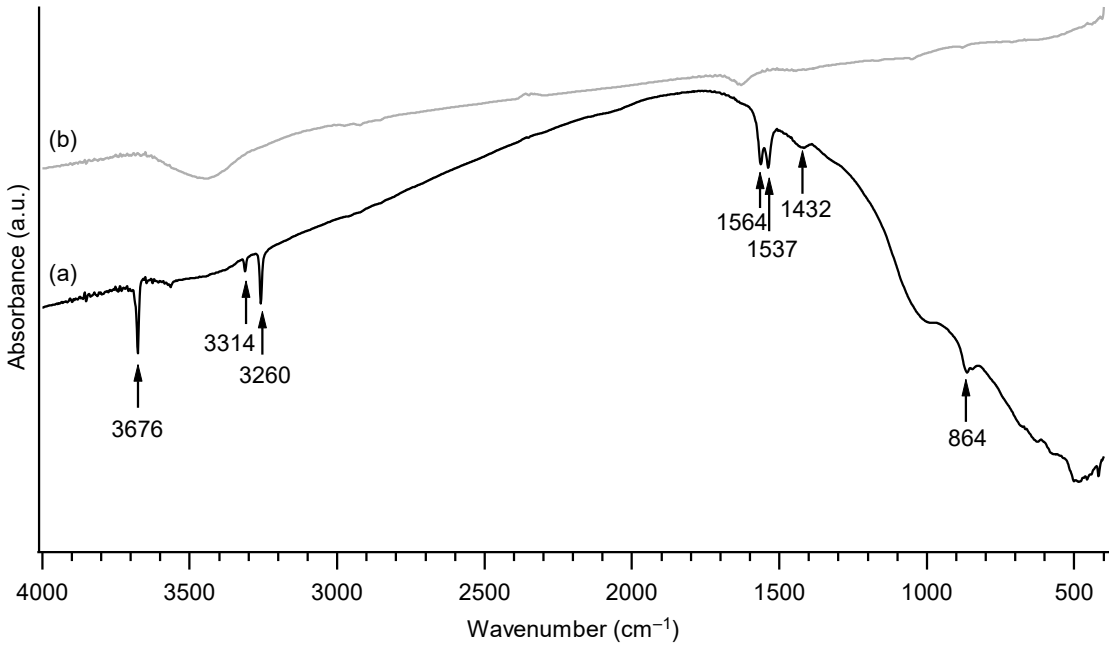

Figure 4.1: FTIR spectra of (a) $LiNH_2$ + LiH (1:2) and (b) blank KBr pellet.

4.2.1.3 Pressure-composition-temperature (PCT) measurements

To further understand the thermodynamic properties of the Li–N–H system, Figure 4.2 shows the PCT measurements of $LiNH_2$ and LiH in a 1:2 molar ratio that was performed over a period of five days with absorption and desorption steps varying from one hour (before and after the plateau) to approximately five hours (on the plateau slope). Figure 4.2a shows that the equilibrium pressure at 415 °C was approximately 14 bar at the midpoint of the sloping plateau. The conclusion from these observations in Figure 4.2 is that only one single-reaction step was observed corresponding to the sloping plateau that extends between a hydrogen capacity of 1 – 5 wt%. In the logarithmic pressure scale (Figure 4.2b), the initial shape of the PCT curve below ~1 wt% of H_2 suggests a solid-solution behaviour between $LiNH_2$ and Li_2NH. Furthermore, the absence of a second plateau below ~1 wt% of H_2 suggests that the anticipated second reaction step in Equation 4.2 did not occur under the applied experimental conditions. After performing the second desorption step, the system was able to re-absorb a hydrogen capacity of ~5.5 wt% (6.5 wt% of H_2 in Equation 4.1)

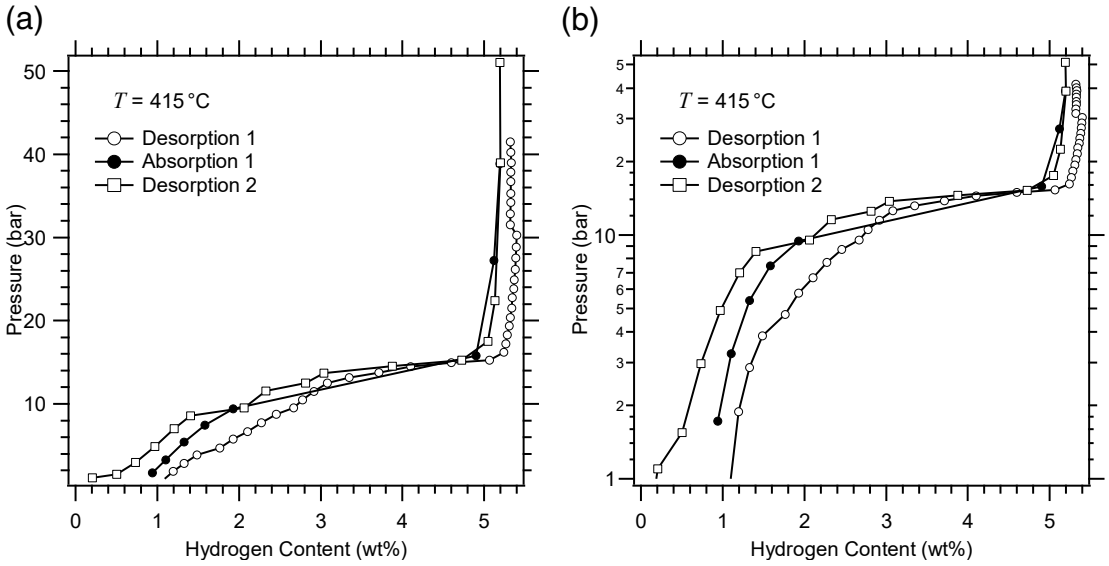

Figure 4.2: PCT measurement of Batch 1 – $LiNH_2$ + LiH (1:2) at 415 °C with a (a) linear pressure scale and (b) logarithmic pressure scale.

4.2.1.4 Temperature programmed photographic analysis (TPPA)

Measurements involving the Li–N–H system had a common problem at high temperatures where the powdered samples appeared molten. Figure 4.3, shows the $LiNH_2$ + LiH (1:2) system after hydrogen cycling at 475 °C. The inner walls of the stainless-steel sample cell appeared sintered with yellow sample. Given the state of the sample cell after working at such temperatures, it is quite possible that the solid-solution sample is melting, preventing the desirable second-reaction step in Equation 4.2.

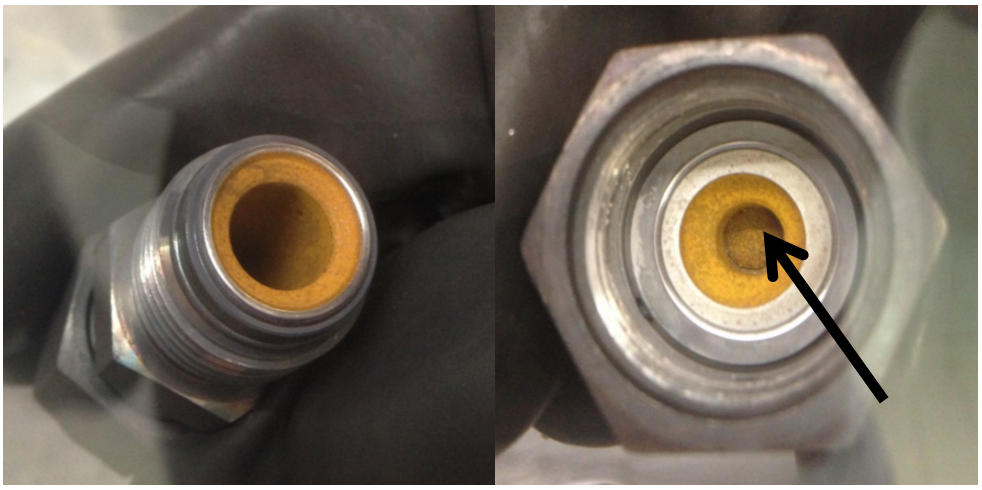

Figure 4.3: Images of a sample cell containing $LiNH_2$ + LiH (1:2) after hydrogen cycling at 475 °C, where the arrow indicates the blocked sample filter.

Indicated by the arrow in Figure 4.3, the metal filter gasket was blocked by a sintered coating of sample, having a detrimental effect on PCT data. By repeating the volume calibration on the same sample cell, a reduction in the calibrated volume confirmed that the filter was blocked during PCT measurements. In an attempt to circumvent this problem, the mixtures of $LiNH_2$ and LiH in a 1:2 molar ratio were pressed into three individual 8 mm diameter pellets. The three sample pellets were stacked inside the sample cell, where the remaining void was packed with stainless-steel wool to prevent any movement of the pellets as the system underwent evacuation. At a temperature of ~475 °C, the diffusion rate of hydrogen through the sample-cell walls (316 stainless steel) was problematic, especially during measurements over long periods of time. Several leak corrections were performed using the permeability of hydrogen through 316 stainless steel using the methods detailed in Chapter 2: Section 2.5.1. Figure 4.4 shows the state of the sample cell after hydrogen cycling $LiNH_2$ + LiH (1:2) pellets, although the problem of blocked filter gaskets was eliminated, it did not deter the sample from melting and forming a solid mass.

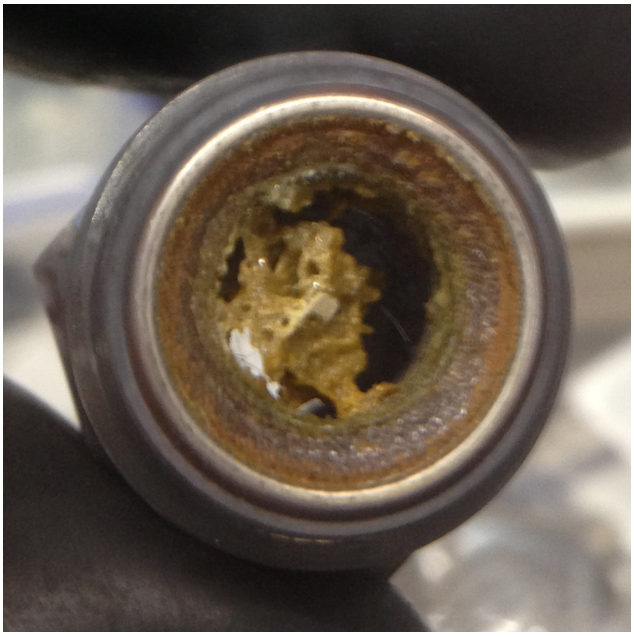

Figure 4.4: Image of $LiNH_2$ + LiH (1:2) sample pellet that melted over steel wool after cycling measurements above 475 °C (bottom view of open sample cell).

Given the difficulties with obtaining PCT data of $LiNH_2$ + LiH (1:2) as a result of the sample melting at high temperatures (> 475 °C), temperature-programmed

photographic analysis (TPPA) was performed on pure $LiNH_2$ (as received) and $LiNH_2$ + LiH (1:2) to explore the behaviour of the starting powders at temperatures relevant to practical applications. Furthermore, *ex situ* XRD analysis can only reveal information about the phases that exist upon cooling to room temperature. Therefore, temperature-programmed photographic measurements allowed additional insight about the *in situ* behaviour of samples by TPPA.

Figure 4.5 shows the TPPA of as-received $LiNH_2$ from Sigma-Aldrich. By observation, $LiNH_2$ started as a white powder and the glass vial accumulated a foggy appearance between 124 °C and 268 °C, likely due to the release of impurities that may be present as a result of the synthesis process from Sigma-Aldrich. This foggy appearance was most pronounced at 203 °C (Frame 1 of Figure 4.5). Juza and Opp (1951) reported that the melting point of $LiNH_2$ is ~375 °C, but the melting point appears to commence at approximately 366 °C in the TPPA (Frame 2 of Figure 4.5) and is associated with the deposition of yellow molten sample on the inner walls of the glass starting at 406 °C (Frame 3 of Figure 4.5). Because of a faster heat rate used in comparison to Chen et al. (2002) and Juza and Opp (1951) (10 and 1 °C min^{-1}, respectively), the expected melting point should occur at a higher temperature (> 375 °C). Therefore, the difference in melting points could be explained by the presence of impurities. After heating up to approximately 453 °C, the sample appeared to bubble continuously from the evolution of ammonia, according to Equation 4.4:

$$LiNH_{2}(s) \rightarrow Li_{2}NH(s) + NH_{3}(g) \tag{4.4}$$

At a temperature of 484 °C, a second layer of molten sample begins to deposit over the first layer on the glass vial with an opaque yellow colour (Frame 4 of Figure 4.5). As the sample cooled, the sudden temperature drop caused the glass vial to crack, revealing the molten product in Frame 5 of Figure 4.5. TPD analysis by Yao et al. (2007) revealed that a rapid release of ammonia occurs at 480 °C due to the formation of liquid $LiNH_2$. This report is in agreement with the TPPA in Figure 4.5 as the sample underwent vigorous bubbling as it transitioned from a solid to liquid state at 484 °C (Frame 4 of Figure 4.5).

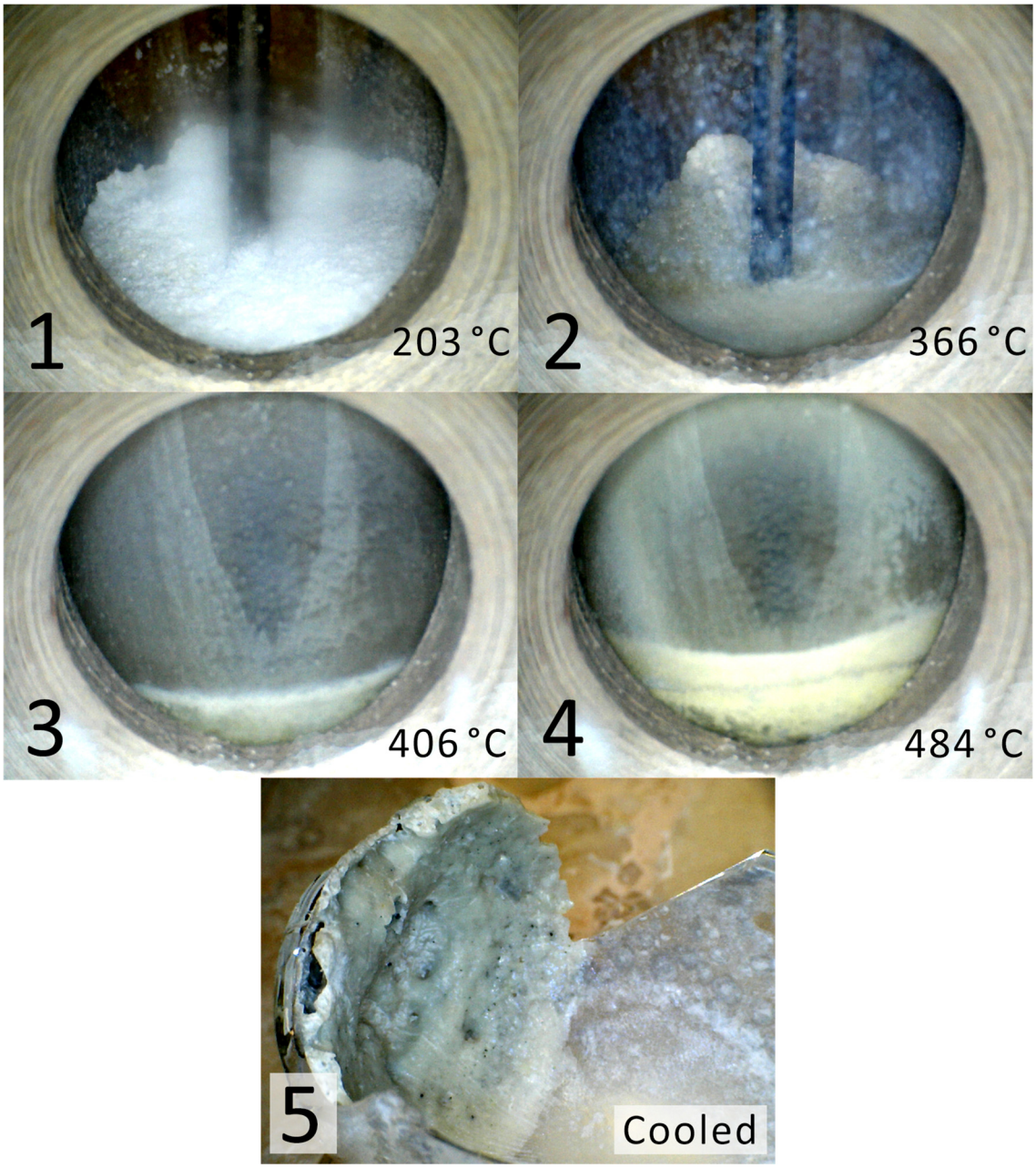

Figure 4.5 TPPA of as-received $LiNH_2$ recorded at various temperatures with a heating rate of 10 °C min^{-1}.

Figure 4.6 shows the TPPA of $LiNH_2$ + LiH (1:2) with a heating rate of 10 °C min^{-1}. The sample started as a white powder and began to shrink in size at 250 °C (Frame 1 of Figure 4.6). According to Chen et al. (2002), this observation can be attributed to the release of hydrogen according to Equation 4.1a:

$$LiNH_2 + LiH \rightarrow Li_2NH + H_2 \qquad (4.1a)$$

where this reaction was confirmed by TPD-VM analysis (Figure 4.7).

Between 400 °C and 500 °C (Frame 2 of Figure 4.6), the system underwent an abrupt colour change from white to yellow. Tapia-Ruiz et al. (2013) synthesised lithium nitride hydride (Li_4NH) pellets with an appearance of a yellow/beige colour; therefore, this colour change is a good indication of the formation of Li_4NH. At approximately 535 °C (Frame 3 of Figure 4.6), the system appeared black and began to melt with vigorous bubbling due to the evolution of unknown gases (confirmed by TPD-VM analysis in Figure 4.7). This black molten state can explain the complications seen in PCT measurements at this temperature range (including sintering and filter blocking). However, it is likely that the formation of this molten state occurs at an even lower temperature given the heating rate used (10 °C min^{-1}) and from the molten observations after PCT measurements at 475 °C (Figure 4.3).

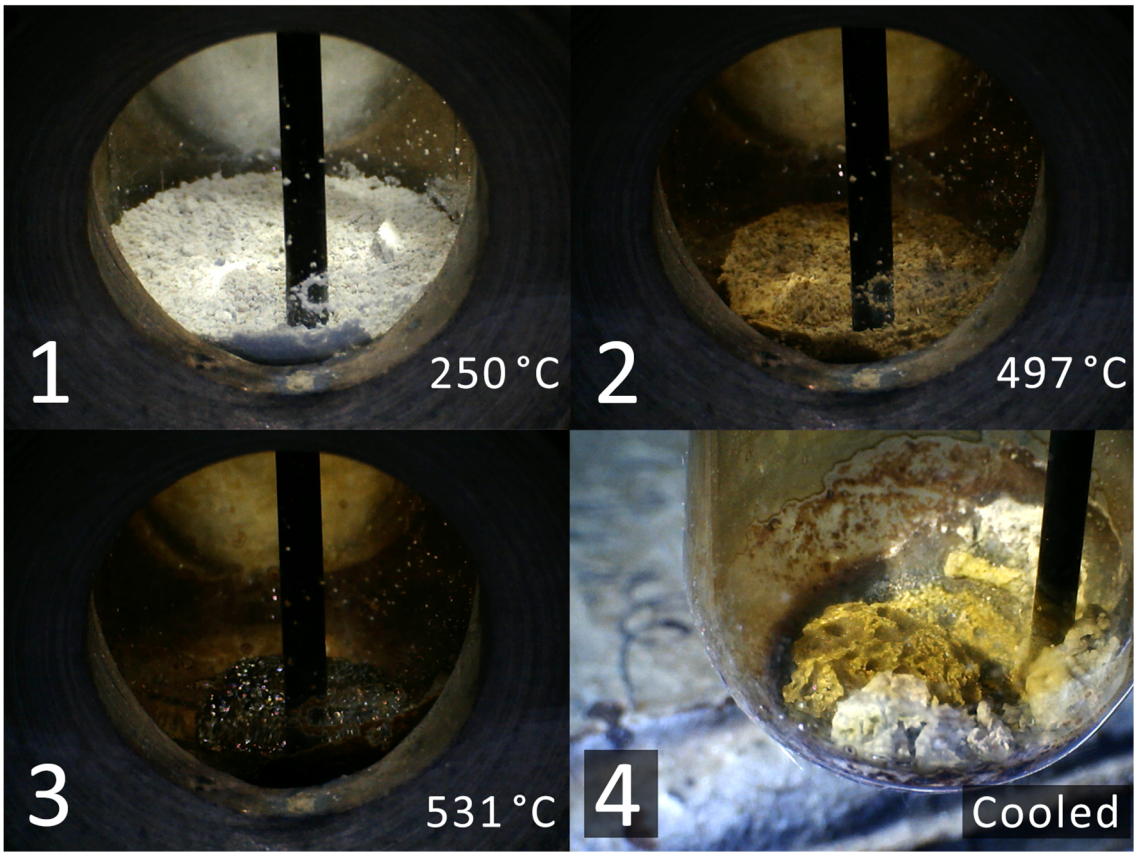

Figure 4.6: TPPA of $LiNH_2$ + LiH (1:2) at various temperatures where physical changes were observed during heating at a rate of 10 °C min^{-1}.

In temperature-programmed photographic measurements (during heating), the evolution of excess gases is vented with a pressure relief valve set to 1

atmosphere. As a result and as the sample cools, the gases could be re-absorbed to reverse the appearance of the black colour to a yellow colour (Frame 4 of Figure 4.6), suggesting a solid solution of Li_2NH and Li_4NH. However, the colour change (from yellow to black at 531 °C) may also be a consequence of the temperature.

4.2.1.5 Temperature programmed desorption with the volumetric method (TPD-VM)

Temperature programmed desorption measurements with the volumetric method were used to identify the phase change corresponding to the release of gases at various temperatures. Figure 4.7 shows the TPD-VM analysis in the temperature range of 25 – 580 °C with a heating rate of 2 °C min^{-1}, where the evolved gases from the TPD-VM analysis can be identified as NH_3, N_2, H_2 or a combination due to the absence of a gas analyser. It has been widely reported that the amide-hydride to imide reaction (Equation 4.1) releases hydrogen at approximately 230 °C (Chen et al. 2002; Ichikawa et al. 2004; Leng et al. 2005). However, the imide-hydride to nitride reaction (Equation 4.2) that should occur above 230 °C seems to be absent in TPD-VM analysis based on the amount of hydrogen that would be released by Equation 4.1 and 4.2 (6.5 and 5.5 wt% of H_2, respectively). A peak with smaller intensity to the amide-hydride reaction occurs at 534 °C, this desorption event coincides with the melting behaviour and evolution of gases (bubbling) observed in the TPPA of $LiNH_2$ + LiH (1:2) (Frame 3 of Figure 4.6).

The TPD-VM analysis of Batch 2 – $LiNH_2$ + LiH (1:2) was repeated at a slower heating rate of 1 °C min^{-1} and a larger sample size (~1 g) (Figure 4.8). Decreasing the heating rate and increasing the sample size, allowed better separation of the hydrogen release events in the system. As a result, a feature that was not previously seen in Figure 4.7 appears in Figure 4.8 as a secondary hydrogen desorption peak at ~305 °C. This secondary peak suggests that another reaction took place soon after the reaction in Equation 4.1 (230 °C). Therefore, further analysis is required to determine whether this feature contributes to the absence of the nitride product in the imide-hydride reaction at higher temperatures (> 230 °C).

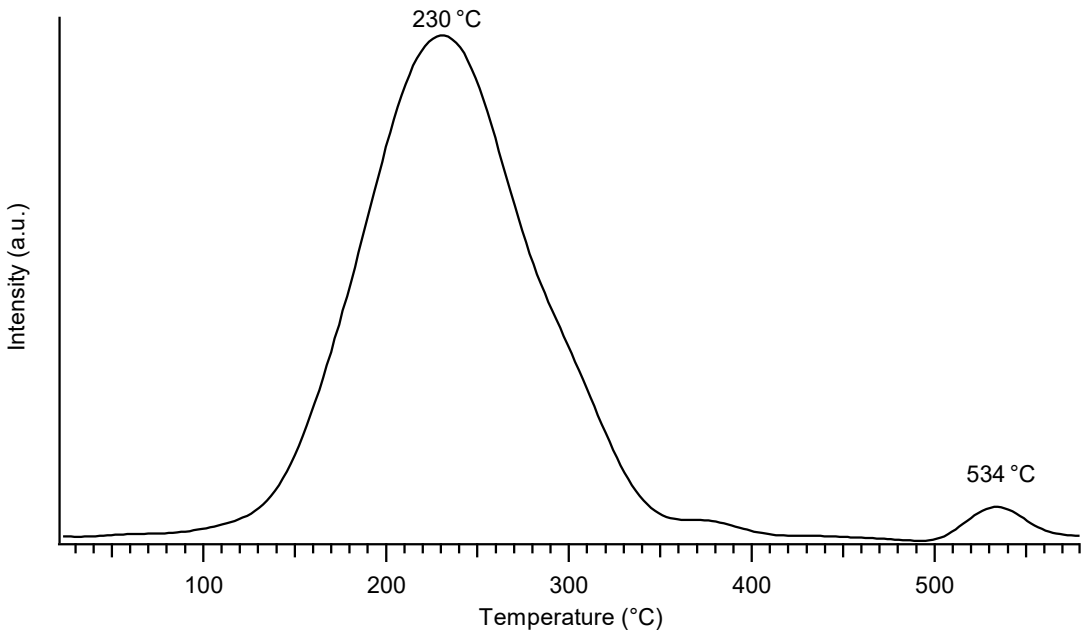

Figure 4.7: TPD-VM analysis of ~100 mg of Batch 2 – $LiNH_2$ + LiH (1:2) in the temperature range of 25 – 580 °C, where the heating rate was 2 °C min^{-1} starting at vacuum.

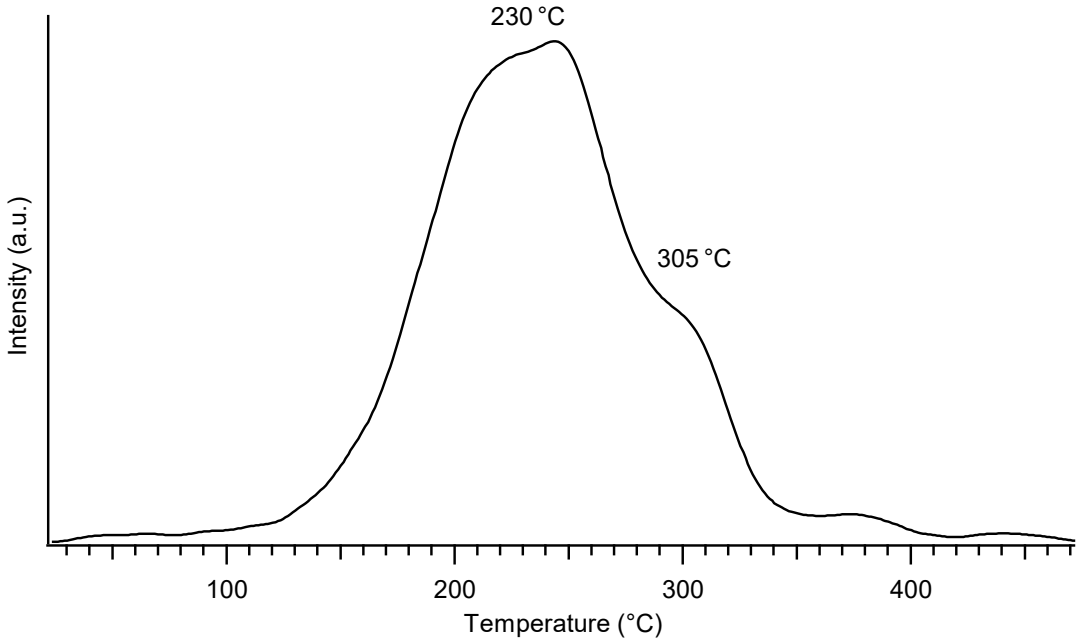

Figure 4.8: TPD-VM analysis of ~1 g of Batch 2 – $LiNH_2$ + LiH (1:2) in the temperature range of 25 – 470 °C, where the heating rate was 1 °C min^{-1} starting at vacuum.

4.2.1.6 X-ray diffraction (XRD) analysis

X-ray diffraction analysis can identify the phases at stages of the reaction pathway in the TPPA and TPD analysis after they have cooled to room temperature. Figure 4.9 shows the *ex situ* XRD analysis of $LiNH_2$ + LiH (1:2) collected after TPD measurements halted at different temperatures. By 300 °C (Figure 4.9b), it is evident that the non-stoichiometric intermediate between $LiNH_2$ and Li_2NH ($Li_{2-y}NH_{1+y}$) has already been formed with no Li_3N present. With increasing temperature ≥ 430 °C (Figure 4.9c and 4.9d), there is a decrease in lattice parameter of the lithium imide-nitride hydride ($Li_{4-2x}N_{1-x}H_{1-x}(NH)_x$) structure as the stoichiometry changes, resulting in a peak shift to higher angles.

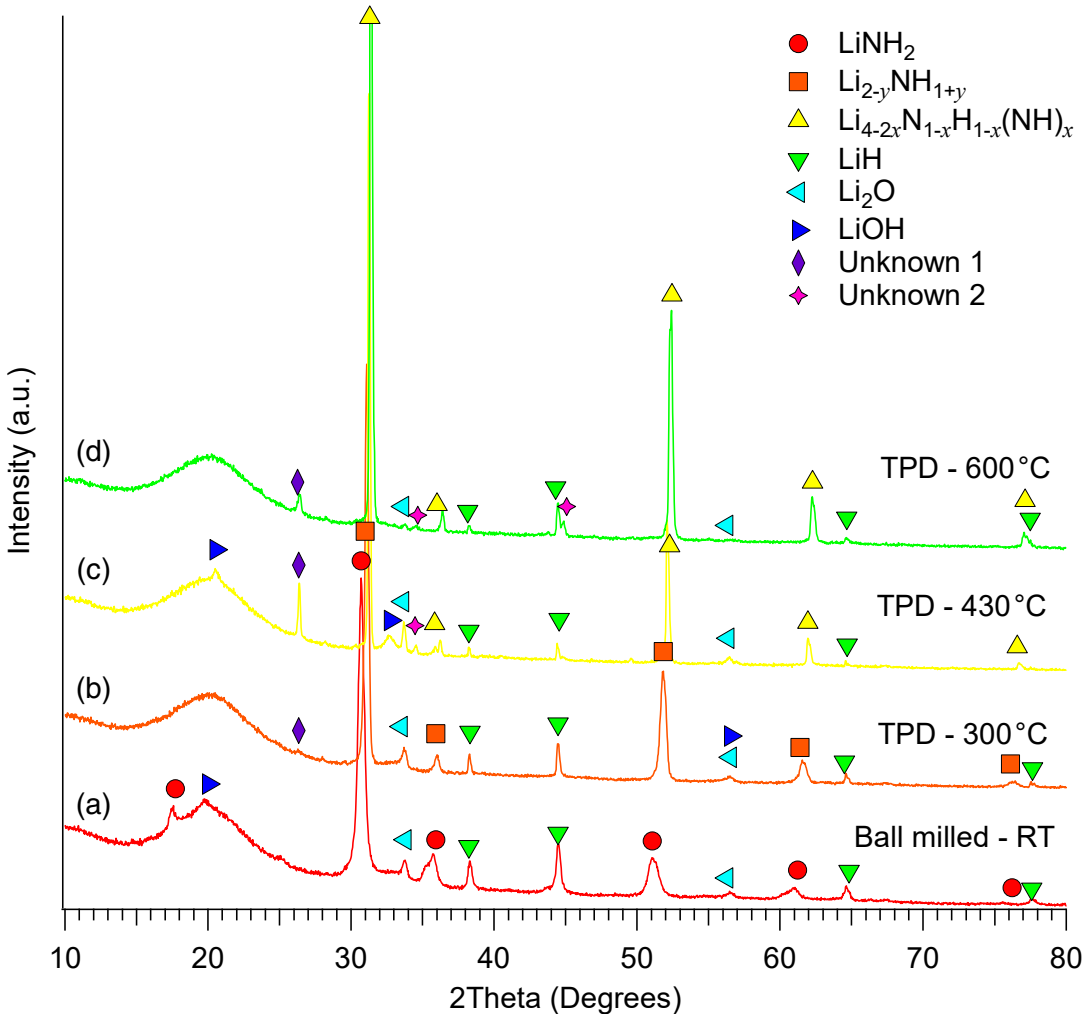

Figure 4.9: *Ex situ* XRD analysis of $LiNH_2$ + LiH (1:2) after (a) ball milling and TPD at (c) 300 °C, (c) 430 °C and (d) 600 °C, where $Li_{2-y}NH_{1+y}$ ($0 \leq y \leq 1$) and $Li_{4-2x}N_{1-x}H_{1-x}(NH)_x$ ($0 \leq x \leq 1$) are non-stoichiometric phases.

A small amount of lithium oxide can be found likely due to contaminants in the starting products (Figure 4.9a). The unknown peak identified at a 2θ angle of ~27° (Unknown 1; ♦) could be trace amounts of SiO_2 (quartz) from XRD sample preparation using glass slides. Excessive packing of the sample may have caused fragments of glass to contaminate the sample from the abrasive action of flattening the sample for XRD analysis. The absence of this peak in Figure 4.9a, and different intensities in Figure 4.9c and 4.9d, further suggest that the quartz is not a part of the sample but an unknown contaminant.

4.2.1.7 Discussion of $LiNH_2$ + LiH (1:2)

The amide-hydride reaction, $LiNH_2$ + LiH (1:2), was initially measured to reproduce the results of Chen et al. (2003). In the initial attempts, there were difficulties in a dehydrogenation pathway that resulted to a Li_3N product based on the hydrogenation pathway of Li_3N by Chen et al. (2002), despite using similar experimental conditions. The non-stoichiometric phases ($Li_{2-y}NH_{1+y}$ and $Li_{4-2x}N_{1-x}H_{1-x}(NH)_x$) identified by XRD analysis, showed crystallographic structures similar to lithium imide. Hence, overlapping peak positions made it difficult to determine the exact phases present for TPD measurements halted at various temperatures.

Pressure-composition-temperature measurements revealed the lithium amide-hydride system exhibited poor kinetics due to the molten state that occurs at high temperatures, hindering the reversibility of this system as identified in TPPA. The formation of a solid solution of amide and imides, also contributed to the complexity of problems in the Li–N–H system. In addition to the molten problem, the diffusion and absorption of hydrogen through 316 stainless-steel was a factor that required consideration when operating above the sample-cell temperature limit (~537 °C). This engineering factor also included durability issues caused by the repeated use of the same sample cell.

4.2.2 Li_2NH + LiH (1:1) and Li_2NH + LiH (1:2)

The main objective of the Li–N–H system was to investigate the reversibility of the imide-hydride reaction, Li_2NH + LiH (1:1), to operate at a temperature range suitable for thermal energy storage. In the amide-hydride reaction, we were

consistent in achieving a non-stoichiometric product proposed by Tapia-Ruiz et al. (2013) as lithium imide-nitride hydride ($Li_{4-2x}N_{1-x}H_{1-x}(NH)_x$) that involved a reaction pathway that forms a solid-solution between Li_2NH and Li_4NH (Equation 4.3). From mixtures of amide/imide and LiH, the proposed reaction for the formation of Li_2NH and Li_4NH is expressed as follows:

$$Li_{2-x}NH_{1+x} + (2-x)LiH \rightarrow Li_{4-2x}NH + H_2 \quad (4.5)$$

where Li_2NH and Li_4NH are formed when x = 1 and x = 0, respectively. Equation 4.5 suggests that a molar ratio of 1:2 (Li_2NH:LiH) is required for the formation of Li_4NH. Therefore, the reversibility of this reaction can be improved if the formation of Li_4NH was more abundant, i.e. LiH was no longer the limiting reagent.

The lithium imide-hydride reaction was investigated with different compositions, Li_2NH + LiH in a 1:1 and 1:2 ratio. The investigation of the imide-hydride decomposition reaction, Li_2NH + LiH (1:1), was based on the hydrogenation of Li_3N by Chen et al. (2002) to form an imide-hydride product. The imide-hydride reaction (with excess LiH), Li_2NH + LiH (1:2), was investigated to verify the reaction in Equation 4.5 to form Li_4NH. Furthermore, by starting with the imide-hydride reaction (Li_2NH–LiH) instead of the amide-hydride reaction ($LiNH_2$–LiH), measurements at higher temperatures can theoretically be performed without the complications associated with the melting of $LiNH_2$ that occurs at 366 °C as seen in TPPA (Figure 4.5).

4.2.2.1 Synthesis of Li_2NH

Li_2NH was laboratory synthesised by annealing $LiNH_2$ and Li_3N at 220 °C in a closed system at vacuum for 1 hour using an ultra-fast reaction based on the experimental method by Hu and Ruckenstein (2006) that can be expressed as follows:

$$LiNH_2 + Li_3N \rightarrow 2Li_2NH \quad (4.6)$$

The reagents were thoroughly mixed in a planetary ball-mill for 1.5 hours in a 1:1 molar ratio (Li_3N:$LiNH_2$). The planetary ball-mill was operated at 400 RPM with a BTP ratio of 30:1 using 316 stainless-steel balls sized at 10 mm and 6 mm.

Figure 4.10 shows the XRD analysis after ball-milling to compare with the XRD analysis after heating to 220 °C. A homogenous mixture of the starting reagents were present; however, Li_3N existed in two phases (α- and β-phase) after ball milling. At this stage (after ball milling), XRD analysis revealed oxygen contamination of the sample as indicated by the appearance of a Li_2O phase, which shows a small sharp peak at ~34° (2θ). This low level contamination was likely already present in the starting reagents used.

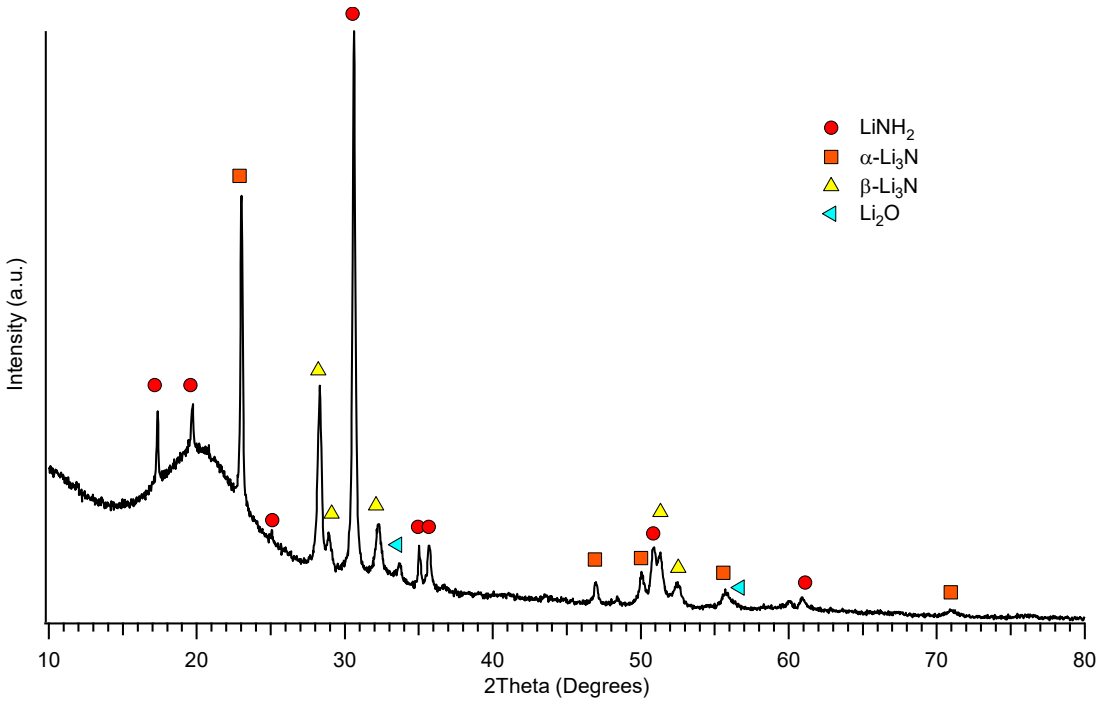

Figure 4.10: XRD analysis of the mixture: Li_3N and $LiNH_2$, after a milling time of 1.5 hours.

Li_3N and $LiNH_2$ was annealed at a furnace set point of 220 °C for 30 minutes under the assumption that the furnace temperature setting was equivalent to the real-time sample temperature. XRD analysis of the annealed sample (Appendix A: Figure A.2) identified the sample contained a mixture of its starting reagents, suggesting that the synthesis of Li_2NH did not occur. In previous $LiNH_2$–LiH measurements that resulted in the formation of Li_2NH, the sample appeared as a grey powder. However, Li_3N (as a starting reagent) was red and visual observation of the annealed sample remained unchanged (red colour) to qualitatively confirm that the reaction between $LiNH_2$ and Li_3N was incomplete, which can be found in Appendix A (Figure A.2). Furthermore, subsequent measurements showed that the actual sample temperature was, depending on

the furnace, between 170 °C and 185 °C as compared to the furnace set point temperature of 220 °C.

After annealing the same mixture of Li_3N and $LiNH_2$ (in Figure A.2) at the correct temperature for one hour, Li_2NH was successfully synthesised as confirmed by XRD analysis in Appendix A (Figure A.3); hence, confirming the Li_2NH synthesis method by Hu and Ruckenstein (2006). In this case, a K-type thermocouple attached to the sample cell, accurately measured the sample temperature. In another synthesis attempt of Li_2NH at an actual temperature of 220 °C under dynamic vacuum (overnight), XRD analysis in Figure 4.11 revealed a lower number of unknown peaks compared to the XRD analysis in Figure A.3, this difference can be due to the minimal handling steps involved.

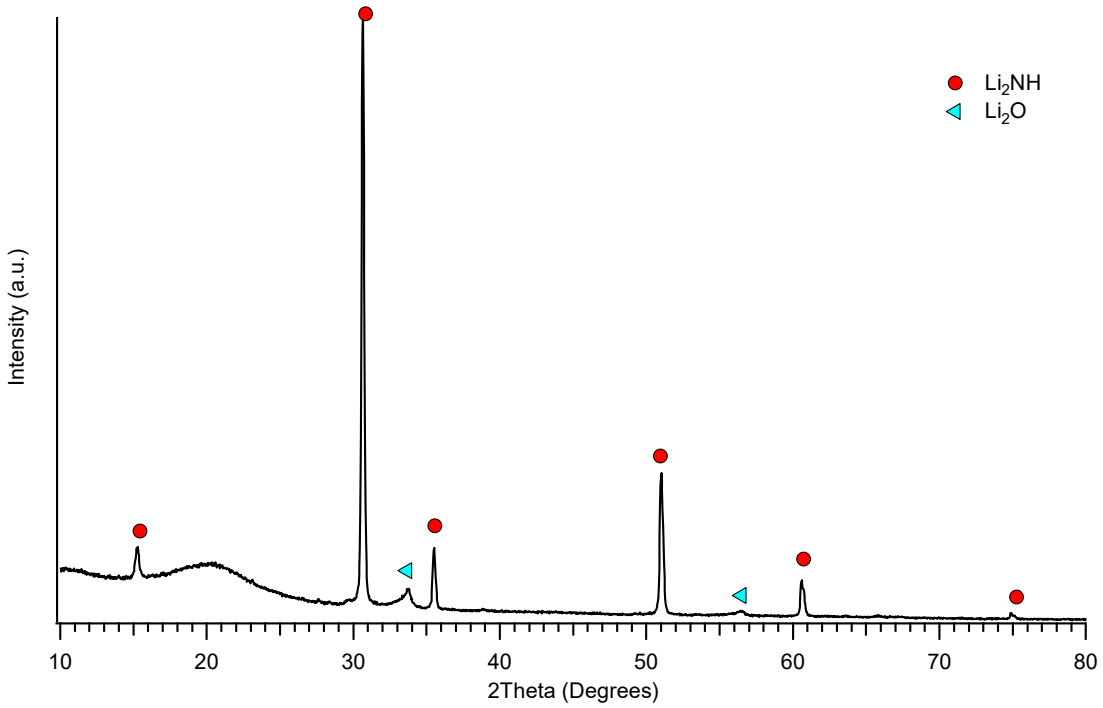

Figure 4.11: XRD analysis of the synthesis of Li_2NH by heating the mixture: Li_3N + $LiNH_2$ (1:1) at 220 °C under dynamic vacuum overnight.

Given the synthesis method by Hu and Ruckenstein (2006) was successful, a new batch was synthesised using the previous molar ratio and milling conditions. Figure 4.12 shows the XRD analysis of a mixture (Li_3N and $LiNH_2$) heated at 250 °C under dynamic vacuum for 21.5 hours. The XRD measurement had to be repeated, as the low background holder was not providing enough peak intensity in Figure 4.12a. Because of the difficulty in retrieving samples after high temperature measurements, a lubricant helped lower the torque on threaded Swagelok parts. Silver Goop (Swagelok, Australia) is an oil-based thread lubricant for high-temperature stainless-steel components that contains 40 – 50% castor oil and 25 – 30% Silver (Ag). The disadvantage of using Silver Goop is the possible contamination that occurs in the sample as the sample cell is dismantled and as a result, XRD analysis was able to reveal silver (Ag) peaks (Figure 4.12). The complication with Ag contamination is observed in XRD analysis as Ag has overlapping peak positions with LiCl, a common product in Li–N–H systems.

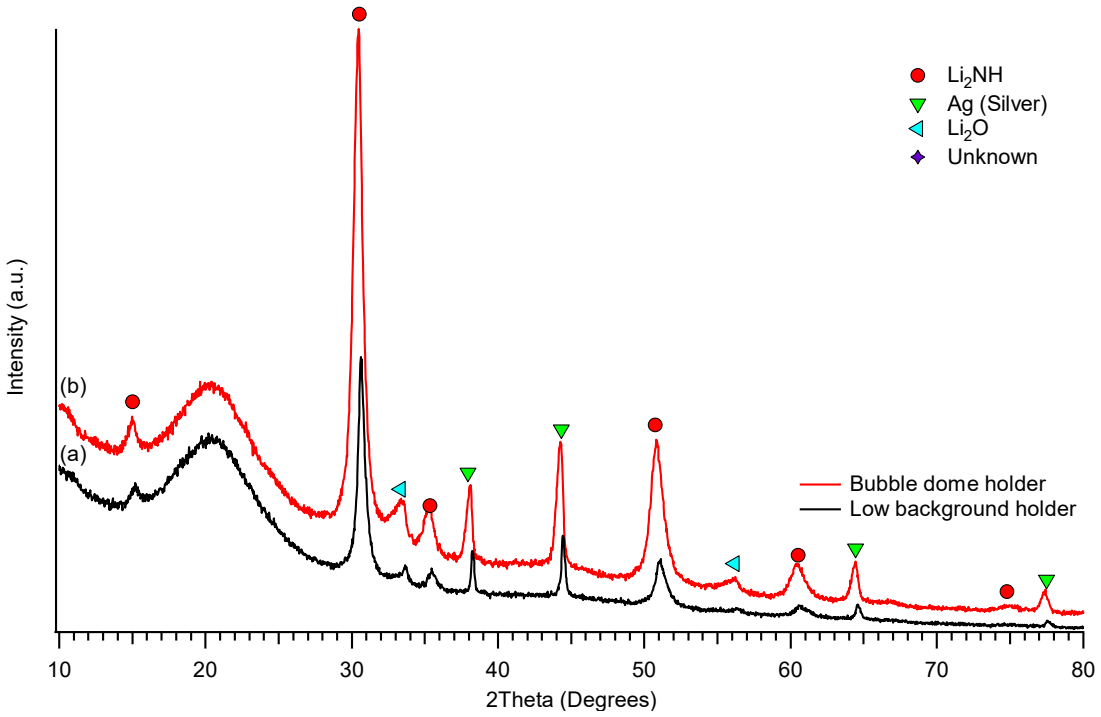

Figure 4.12: XRD analysis of the mixture Li_3N and $LiNH_2$, after heating at 250 °C under dynamic vacuum for 21.5 hours. (a) Low backgrund holder and (b) bubble dome holder.

4.2.2.2 Preparation

Li_2NH + LiH (1:1) and Li_2NH + LiH (1:2) was prepared by thoroughly mixing Li_2NH (laboratory synthesised; Section 4.2.2.1) with LiH (Sigma-Aldrich, 95%) in a planetary ball-mill for 4 hours. The planetary ball-mill was operated at 400 RPM with a BTP ratio of 30:1 using 316 stainless-steel balls sized at 10 mm and 6 mm. XRD analysis of Li_2NH + LiH (1:2) was performed in a XRD sample holder fitted with a plastic base because of the limited amount of sample prepared. However, XRD analysis in Figure 4.13 revealed that the plastic base was not X-ray amorphous and diffracted its own pattern along with the sample. Therefore, an XRD analysis of the blank plastic base was performed shown in blue of Figure 4.13 to differentiate the sample pattern.

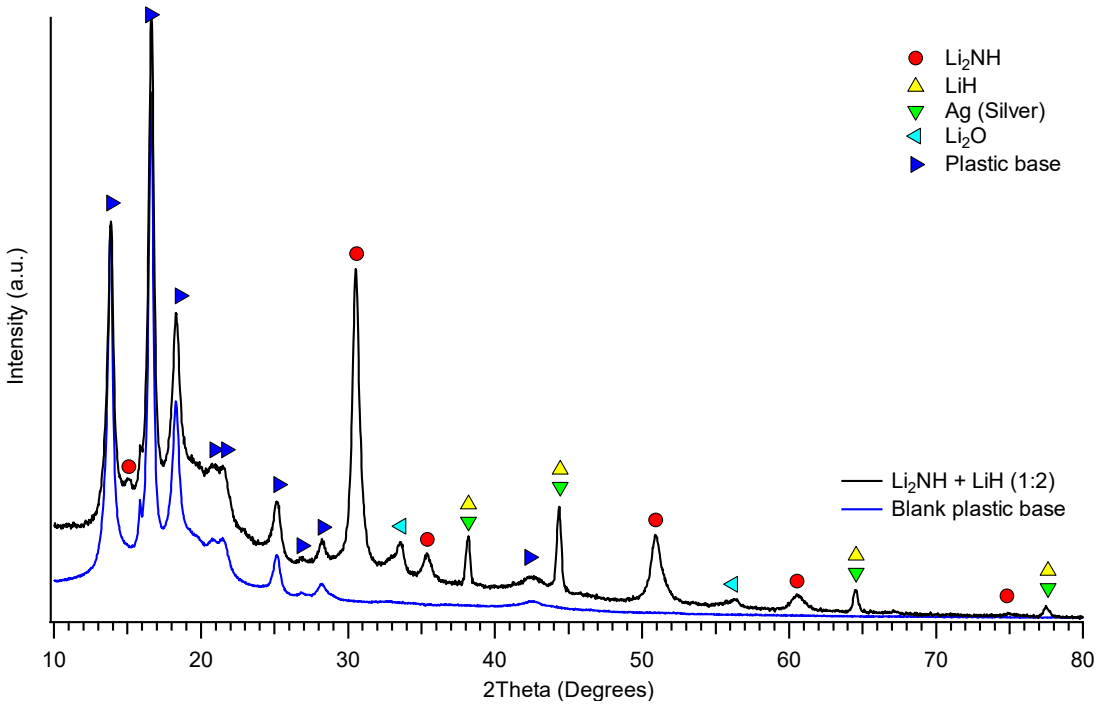

Figure 4.13: XRD analysis of Li_2NH + LiH (1:2) after ball milling for 4 hours using a plastic base in the XRD sample holder.

Ball milling of powders can result in significant heating and, in the case of hydrides, can be sufficient to cause chemical reactions to take place (Suryanarayana 2001). To ensure this observation was not the case during the planetary ball milling of Li_2NH and LiH, a mixture was cryogenically impact milled for 30 minutes. XRD analysis in Figure 4.14 revealed the appearance of an oxide phase (Li_2O), probably resulting from an imperfect seal on the impact cylinder vial. With little difference between the planetary ball-milled and cryogenically-milled samples, subsequent Li_2NH and LiH mixtures were milled using the reliable planetary ball-mill method.

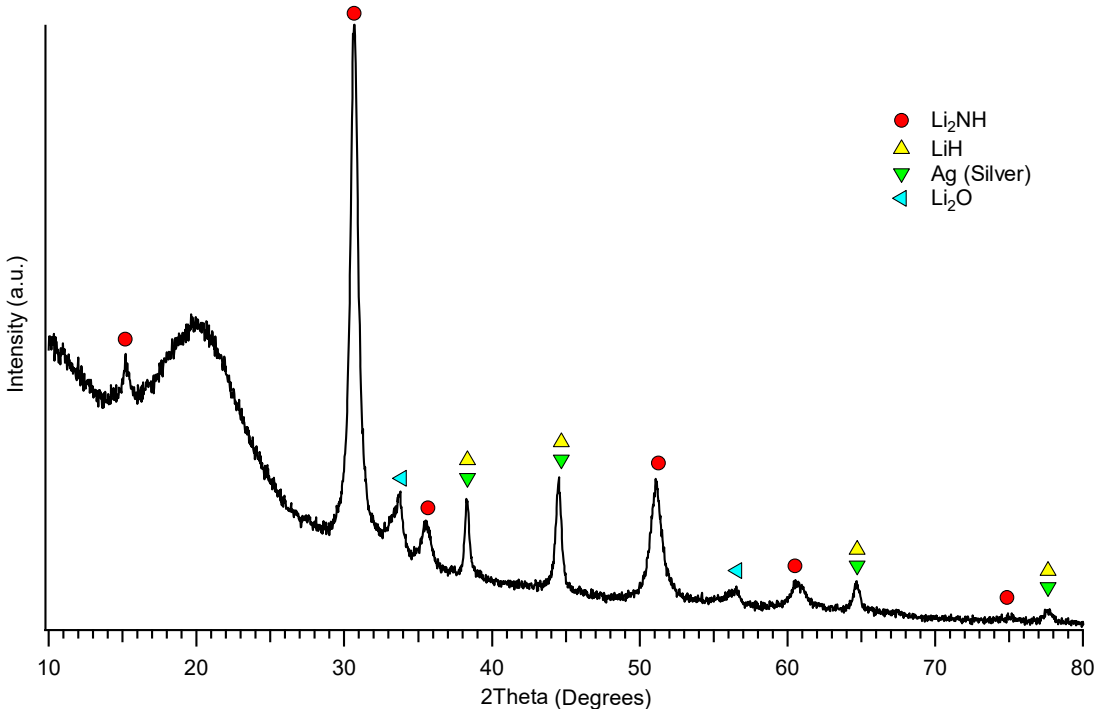

Figure 4.14: XRD analysis of Li_2NH + LiH (1:2) after cryogenic impact milling for 30 minutes.

4.2.2.3 Temperature programmed photographic analysis (TPPA)

Temperature programmed photographic analysis is a useful technique to observe the physical changes on bulk samples at high temperatures including volume changes and melting events. Figure 4.15 shows the results from the TPPA of laboratory synthesised Li_2NH with a heating rate of 10 °C min^{-1}. By observation, Li_2NH started as a grey powder (Frame 1 of Figure 4.15). As Li_2NH was heated to 500 °C, a small volume change is observed in the sample powder with a

distinct colour change from grey to white in the temperature range of 275 – 475 °C (Frame 3 of Figure 4.15).

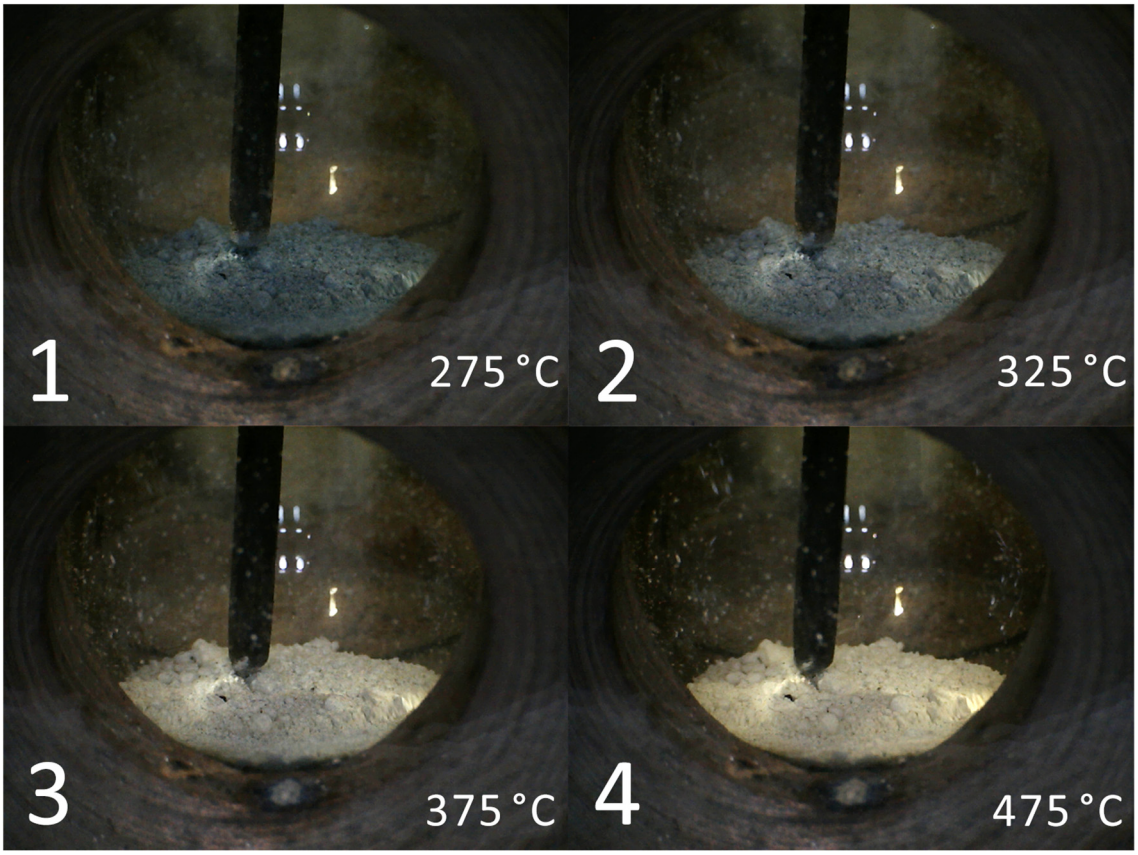

Figure 4.15: TPPA of Li_2NH at various temperatures where physical changes were observed during heating at a rate of 10 °C min^{-1}.

In a successful attempt to retrieve the sample without having the glass vial break upon cooling, XRD analysis of the white sample after temperature-programmed photographic measurements up to ~500 °C (Figure 4.16b) revealed that the final sample remained as Li_2NH. This observation suggests that the colour change from grey to white may be associated with the complete synthesis of Li_2NH from its starting reagents ($LiNH_2$ and Li_3N) upon heating. Hence, the previous annealing temperature of 220 °C may not be enough. Comparative XRD analysis in Figure 4.16 showed that most of the unknown peaks that appeared before the temperature-programmed photographic measurement (Figure 4.16a) have disappeared afterwards (Figure 4.16b). In conclusion, TPPA of pure Li_2NH did not melt at temperatures as high as 500 °C. The appearance of oxygen contamination (Li_2O) possibly originated from either the handling process or from a reaction with the glass vial.

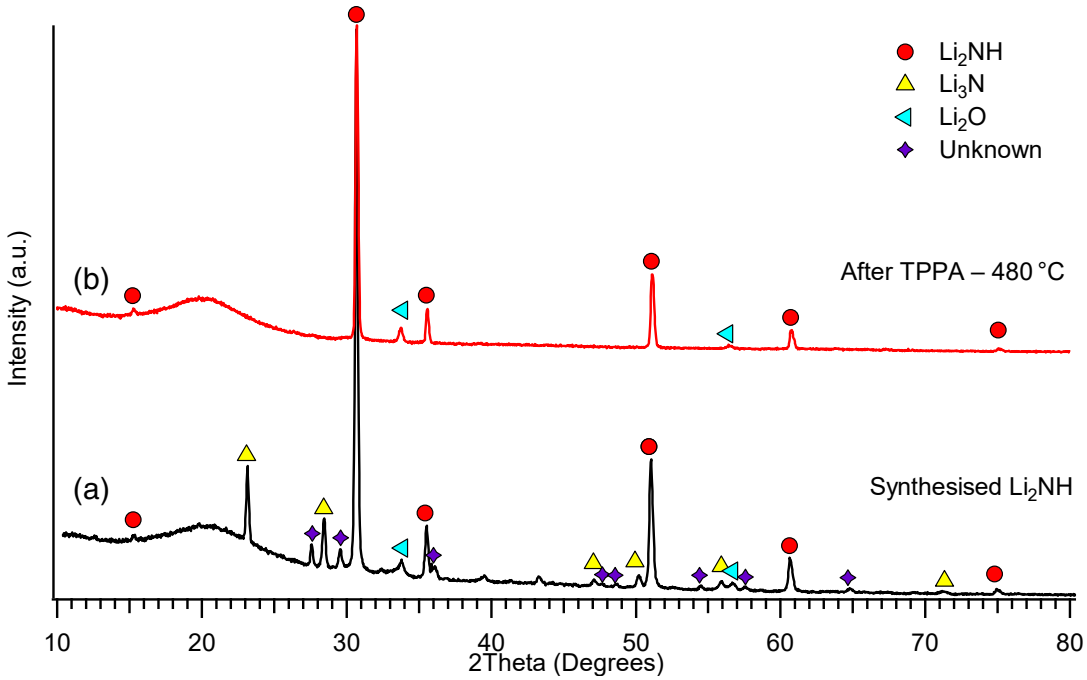

Figure 4.16: Comparitive XRD analysis of Li_2NH (a) before (as synthesised) and (b) after temperature-programmed photographic measurements up to 480 °C.

Temperature programmed photographic analysis of a mixture of Li_2NH and LiH in 1:1 molar ratio was performed to assess the behaviour of the bulk powder during heating. Figure 4.17 showed that the imide-hydride system started as a grey powder (Frame 1 of Figure 4.17). There was a notable volume change in the bulk sample that starts at 200 °C, where TPD-VM analysis associated this event to the evolution of gas. At a temperature of 300 °C, the sample began to change colour and by 400 °C it had completely changed from a grey to a white powder (Frame 3 of Figure 4.17). This colour change from grey to white was in agreement with the TPPA of pure Li_2NH shown in Figure 4.15 and from the XRD analysis in Figure 4.16b. Therefore, this colour change may be associated with the removal of unknown peaks (impurities) resulting in high purity of Li_2NH in the sample. At a temperature of ~480 °C, the sample colour began to change from a white to yellow, and by 500 °C (Frame 4 of Figure 4.17), the system ended with a yellow colour, a colour previously shown to indicate the formation of Li_4NH.

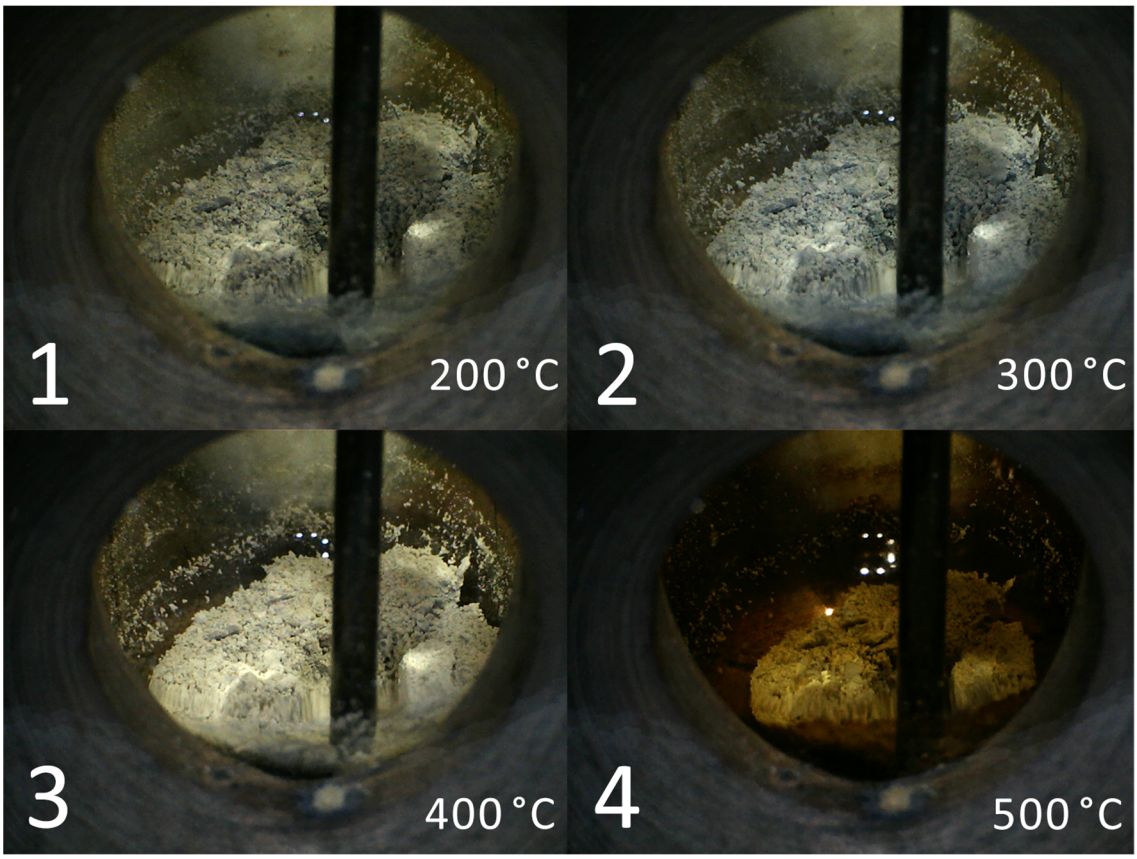

Figure 4.17: TPPA of Li_2NH + LiH (1:1) at various temperatures where physical changes were observed during heating at a rate of 10 °C min^{-1}.

4.2.2.4 Temperature programmed desorption with the volumetric method (TPD-VM) of Li_2NH + LiH (1:1)

To identify the phase changes with increasing temperature, TPD-VM measurements were performed on Li_2NH + LiH (1:1) in the temperature range of 25 – 580 °C with a heating rate of 2 °C min^{-1} (Figure 4.18). However, because of a temperature safety limit built into the software of the PCT-Pro E&E, which closes all valves, one of the measurements stopped recording at temperatures > 500 °C. The repeat TPD measurement (Figure 4.18b) showed a desorption event that peaked at ~206 °C, this peak may have corresponded to residual $LiNH_2$ reacting with LiH to form Li_2NH, suggesting the synthesis of Li_2NH was incomplete in the ball-milling mixture of Li_2NH + LiH (1:1). This desorption peak could also be related to the colour changes seen in TPPA from grey to white between 275 °C and 475 °C (Frame 3 of Figure 4.17). Therefore, the grey colour of the sample may correspond to a mixture of $LiNH_2$ and partially-synthesised Li_2NH and the white colour corresponds to a complete formation of Li_2NH.

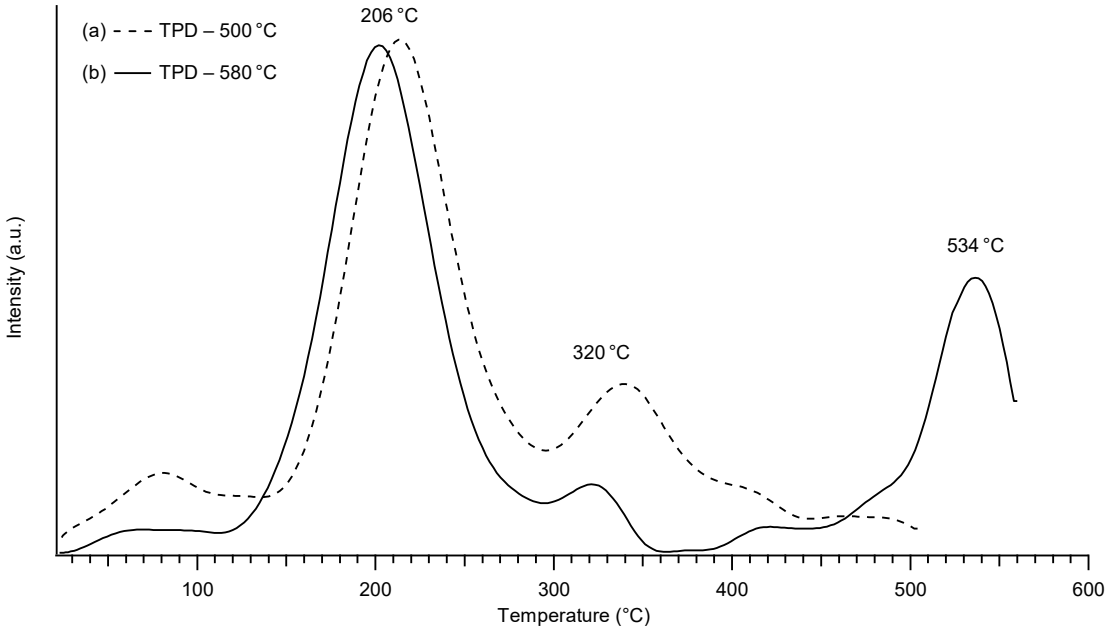

Figure 4.18: TPD-VM analysis of Li_2NH + LiH (1:1) in the temperature range of (a) 25 – 500 °C and (b) 25 – 580 °C, where the heating rates were 2 °C min^{-1} starting at vacuum.

After the TPD measurement was halted at 580 °C, two layers were found in the sample, a green outer layer and a yellow inner layer. Figure 4.19 shows the XRD analysis of both layers, where the green outer layer (Figure 4.19a) consisted of oxides, and the yellow inner layer (Figure 4.19b) consisted of the sample of interest. Based on the previous TPD-VM analysis of $LiNH_2$ + LiH (1:2) in Figure 4.7, the smaller desorption event that peaked at ~534 °C likely corresponds to a solid solution of Li_2NH and Li_4NH, depicted by the yellow colour seen in TPPA (Frame 4 of Figure 4.17) and subsequently confirmed by XRD analysis (Figure 4.19b). XRD analysis after TPD measurements also showed that the hydrogen desorption event that peaked at ~534 °C (Figure 4.18b), is likely the solid-solution (Li_2NH–Li_4NH) forming lithium imide-nitride hydride ($Li_{4-2x}N_{1-x}H_{1-x}(NH)_x$). However, because of the overlapping XRD patterns of Li_2NH and $Li_{4-2x}N_{1-x}H_{1-x}(NH)_x$, the quantitative analysis has yet to be confirmed at these temperatures.

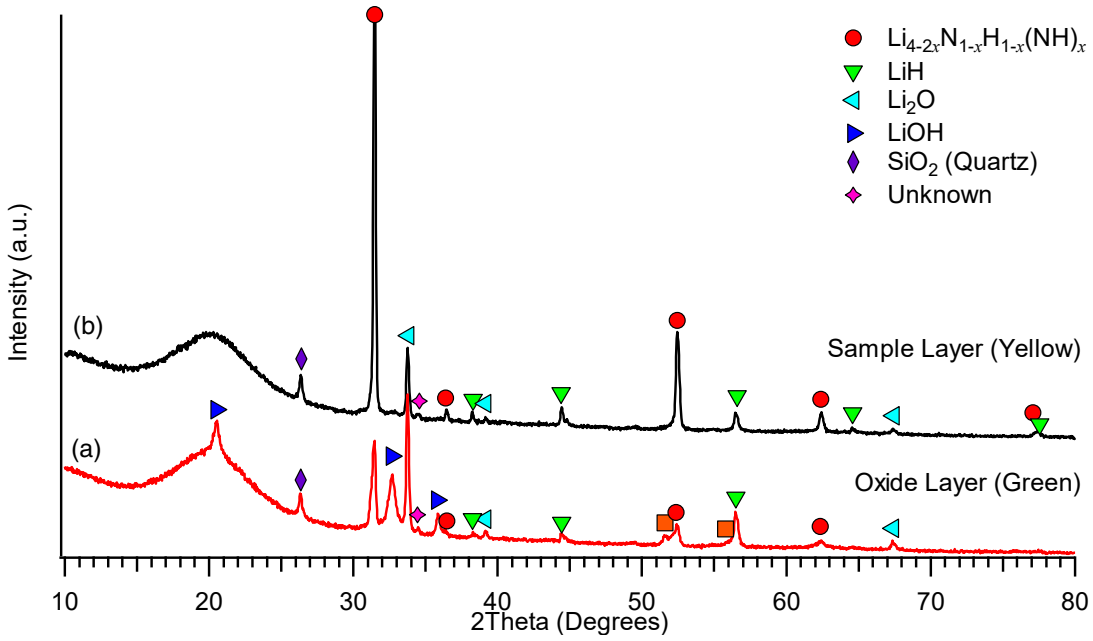

Figure 4.19: XRD analysis of Li_2NH + LiH (1:1) after TPD measurement halted at 580 °C with a (a) green oxide layer and a (b) yellow sample layer.

4.2.2.5 Pressure-composition-temperature (PCT) measurements of Li_2NH + LiH (1:2)

Initial TPD measurements showed that the imide-hydride reaction, Li_2NH + LiH (1:1), did not form Li_3N as previously suggested in the literature, but instead forms a solid-solution (Li_2NH–Li_4NH) as the end product in the Li–N–H system. Hence, PCT measurements were focused on the imide-hydride reaction (with excess LiH), Li_2NH + LiH (1:2), to understand the thermodynamic properties of the solid-solution frequently formed. Figure 4.20 shows the PCT measurements of Li_2NH + LiH (1:2) at 480 °C, but after the first absorption measurement (~5 wt% of H_2) the reversibility of the sample is severely hindered with a decrease in hydrogen capacity (reversible capacity of ~1 wt% of H_2). Upon cooling the sample to room temperature (Figure 4.21), it was observed that the molten sample had compacted into a dense mass that required a drill bit to remove. The poor reversibility could also be due to the molten sample affecting the porous filter. Furthermore, the sample appeared to sinter along the walls of the sample cell (Figure 4.21) possibly from the formation of bubbles at high temperature in accordance with the TPPA of $LiNH_2$ + LiH (1:1) in Figure 4.6, suggesting the sample contained residual $LiNH_2$. Therefore, the reversibility of Li_2NH + LiH (1:2)

cannot be investigated in this particular PCT measurement due to the sample melting at 480 °C.

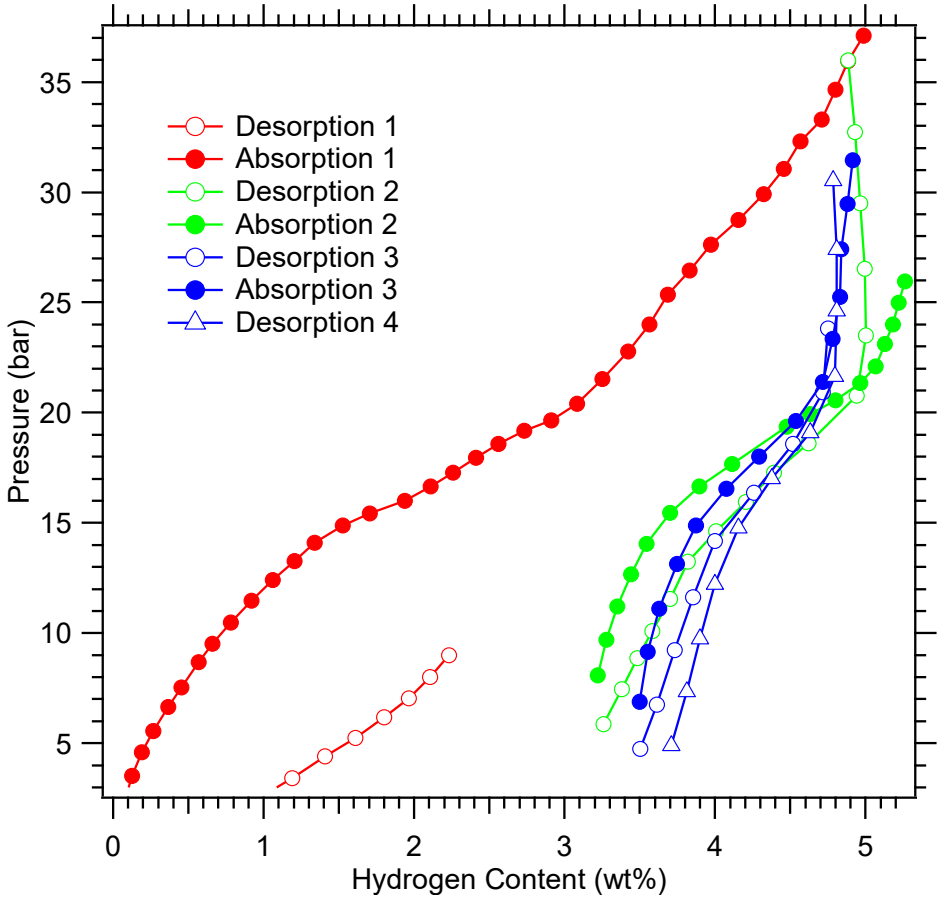

Figure 4.20: PCT measurement of Li_2NH + LiH (1:2) at 480 °C.

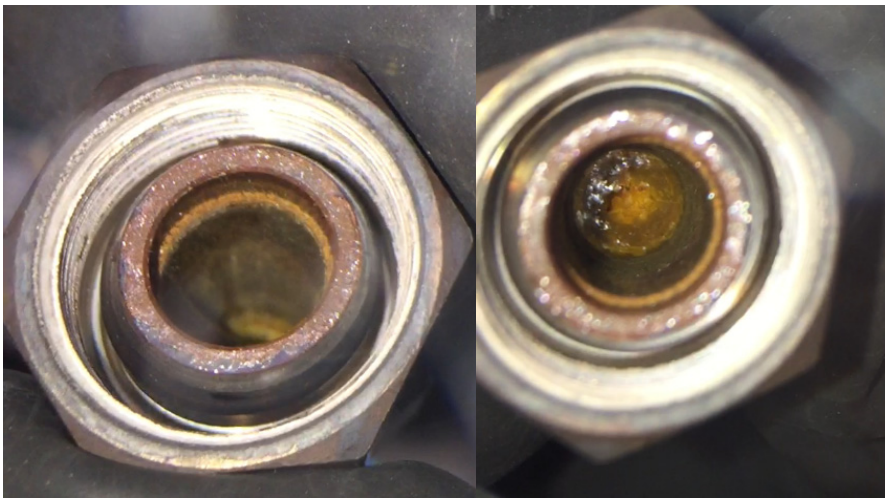

Figure 4.21: The state of the sample cell after PCT measurement of Li_2NH + LiH (1:2) at 480 °C.

4.2.2.6 Temperature programed desorption with the volumetric method (TPD-VM) of Li_2NH + LiH (1:2)

Temperature programmed desorption is a technique used to measure the quantity of gas that corresponds to a phase change at different temperatures. Figure 4.22 shows the TPD-VM analysis of Li_2NH + LiH (1:2) in the temperature range of 60 – 500 °C on three different instruments, Rig #1 (—), Rig #2 (—) and Rig #3 (—) with a heating rate of 2.1, 2.2 and 1.9 °C min^{-1}, respectively. Each TPD-VM analysis showed similar peak positions in the temperature range of 60 – 500 °C, where any difference is due to the slightly different heat rates of each experiment and/or the different internal reference volumes of each instrument used, which influences the gas pressures evolved. A hydrogen desorption event for all measurements in Figure 4.22 occurred at ~322 °C and a smaller release event at ~430 °C.

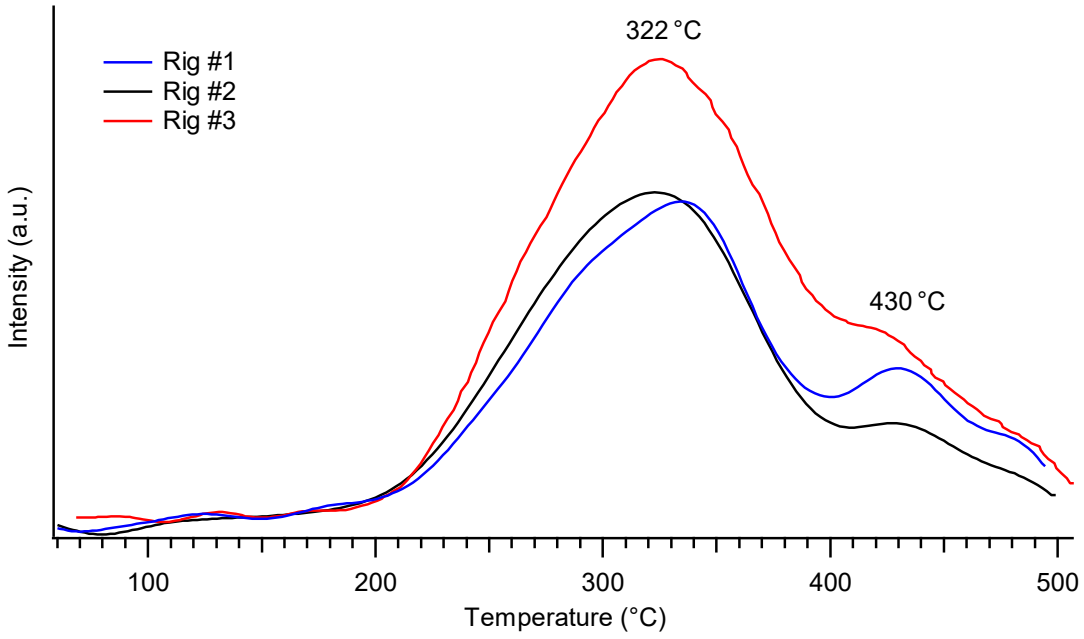

Figure 4.22: TPD-VM analysis of Li_2NH + LiH (1:2) in the temperature range of 60 – 500 °C. Rig #1, #2 and #3 had a heating rate of 2.1, 2.2 and 1.9 °C min^{-1}, respectively, all starting at vacuum.

X-ray diffraction analysis was performed after repeat TPD measurements halted at 500 °C. Rig #1 and Rig #2 are shown in Figure 4.23a and 4.23b, respectively. XRD analysis of Rig #1 (Figure 4.23a) does not show that it contains any oxide phases. However, XRD analysis of Rig #2 (Figure 4.23b) appears to show it contains a LiOH phase, whose presence does not seem to result in any difference between both TPD measurements. Therefore, the oxygen contamination originated from a leak in the bubble dome holder during XRD measurements. The XRD analysis of both samples showed that the final products contained lithium imide-nitride hydride ($Li_{4-2x}N_{1-x}H_{1-x}(NH)_x$). The presence of LiH in both samples and the absence of Li_4NH further indicate that the reaction between Li_2NH and LiH in a 1:2 molar ratio has not gone to completion.

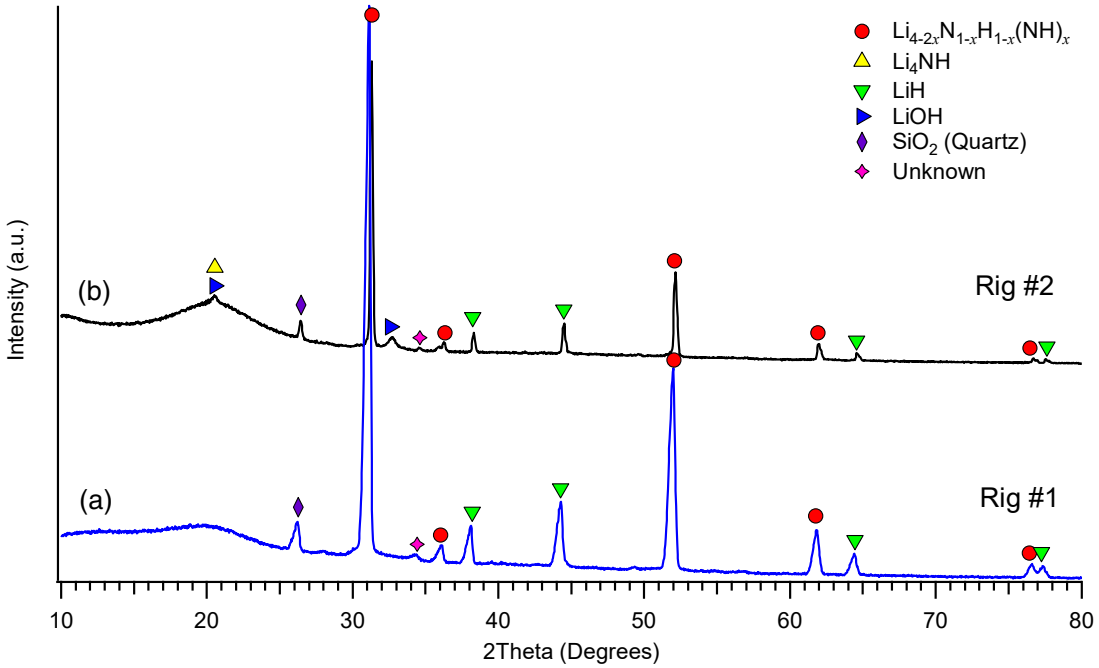

Figure 4.23: XRD analysis of Li_2NH + LiH (1:2) after TPD measurements, (a) Rig #1 and (b) Rig #2 halted at 500 °C.

To investigate the hydrogen desorption events at temperatures > 500 °C, repeat TPD-VM measurements were performed on Li_2NH + LiH (1:2) (—) in the temperature range of 25 – 600 °C. Figure 4.24c revealed two small hydrogen release events occurring at 552 °C and 558 °C. However, the expected imide-hydride reaction occurred at a lower temperature (250 °C < 322 °C) compared to the TPD-VM analysis of Li_2NH + LiH (1:2) (Figure 4.22). This temperature difference suggests that the sample contained residual $LiNH_2$ that reacted with LiH to release hydrogen at low temperatures (~250 °C). The TPD-VM analysis of $LiNH_2$ + LiH (1:2) (—) and Li_2NH + LiH (1:1) (—) are shown in Figure 4.24a and 4.24b, respectively, where both measurements revealed a small hydrogen release peak at 534 °C. The temperature corresponding to the first desorption peak occurs at 200 °C and 250 °C for Li_2NH + LiH (1:1) (—) and Li_2NH + LiH (1:2) (—), respectively. The higher desorption temperature suggests that the extra addition of LiH to the system influenced the desorption temperature. However, to better understand this temperature difference, XRD analysis of both measurements were performed.

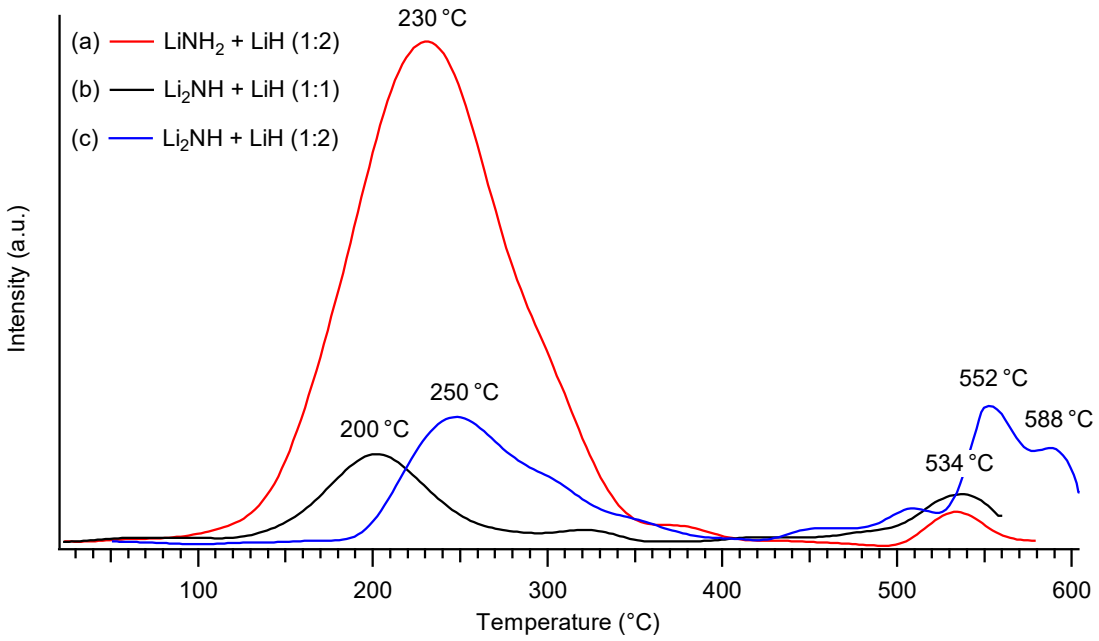

Figure 4.24: TPD-VM analysis of (a) $LiNH_2$ + LiH (1:2), (b) Li_2NH + LiH (1:1) and (c) Li_2NH + LiH (1:2) in the temperature range of 25 – 600 °C, where the heating rates were 2 °C min^{-1} starting at vacuum.

Examining the XRD analysis (Figure 4.25) after each TPD measurement in Figure 4.24, some samples were observed to have oxygen contamination, probably resulting from either contaminants already in the starting reagents or poor sample handling during measurements. Therefore, it is quite possible that the Li_2O phase in those samples had a catalytic effect on the desorption temperature for the first hydrogen release. Li_2NH + LiH (1:1) (—) had higher intensity Li_2O phase peaks than $LiNH_2$ + LiH (1:2) (—), which consequently had a lower desorption operating temperature. After the TPD measurement of Li_2NH + LiH (1:2) was halted at 600 °C, XRD analysis revealed that the Li_4NH phase appears at a 2θ angle of ~20° (Figure 4.25c). This analysis confirms that by having excess LiH, the system was able to form enough Li_4NH between 500 °C and 600 °C to appear in the XRD analysis, which did not appear in previous systems where the quantity of LiH was limited (Figure 4.25a and 4.25b).

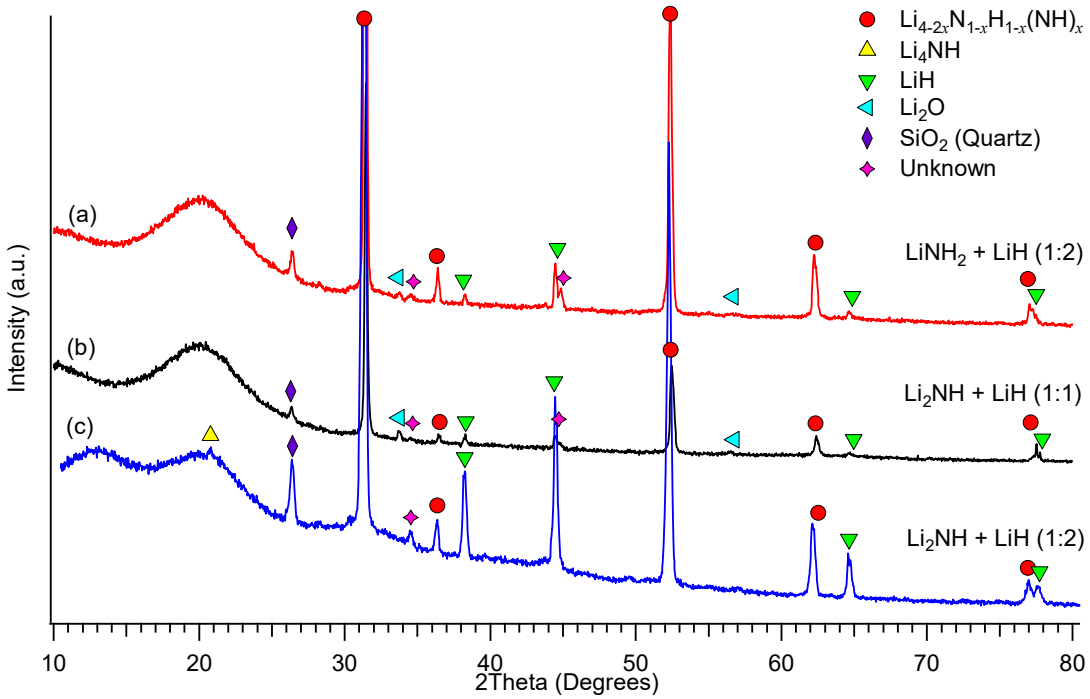

Figure 4.25: XRD analysis of (a) $LiNH_2$ + LiH (1:2), (b) Li_2NH + LiH (1:1) and (c) Li_2NH + LiH (1:2) after TPD measurements halted at 600 °C.

Figure 4.26 shows the *ex situ* XRD analysis of Li_2NH + LiH (1:2). The final product after the TPD measurement halted at 600 °C is determined to be lithium imide-nitride hydride (Figure 4.26d). After PCT measurements at 480 °C, two coloured sample layers were found; an inner yellow layer and a white outer layer. XRD

analysis of the white outer layer, which can be found in Appendix A (Figure A.4), revealed the formation of an oxide layer. Therefore, XRD analysis of the yellow inner layer had some level of contamination on the hydrogen cycled sample (Figure 4.26c), which resulted in a high peak intensity for Li_2O. Given the consistent formation of the lithium imide-nitride hydride product at temperatures > 480 °C, the *ex situ* XRD analysis showed little difference compared to the *ex situ* XRD analysis of the amide-hydride reaction, $LiNH_2$ + LiH (1:2), in Figure 4.9. Therefore, further work is required to investigate the formation of a nitride product from the imide-hydride reaction.

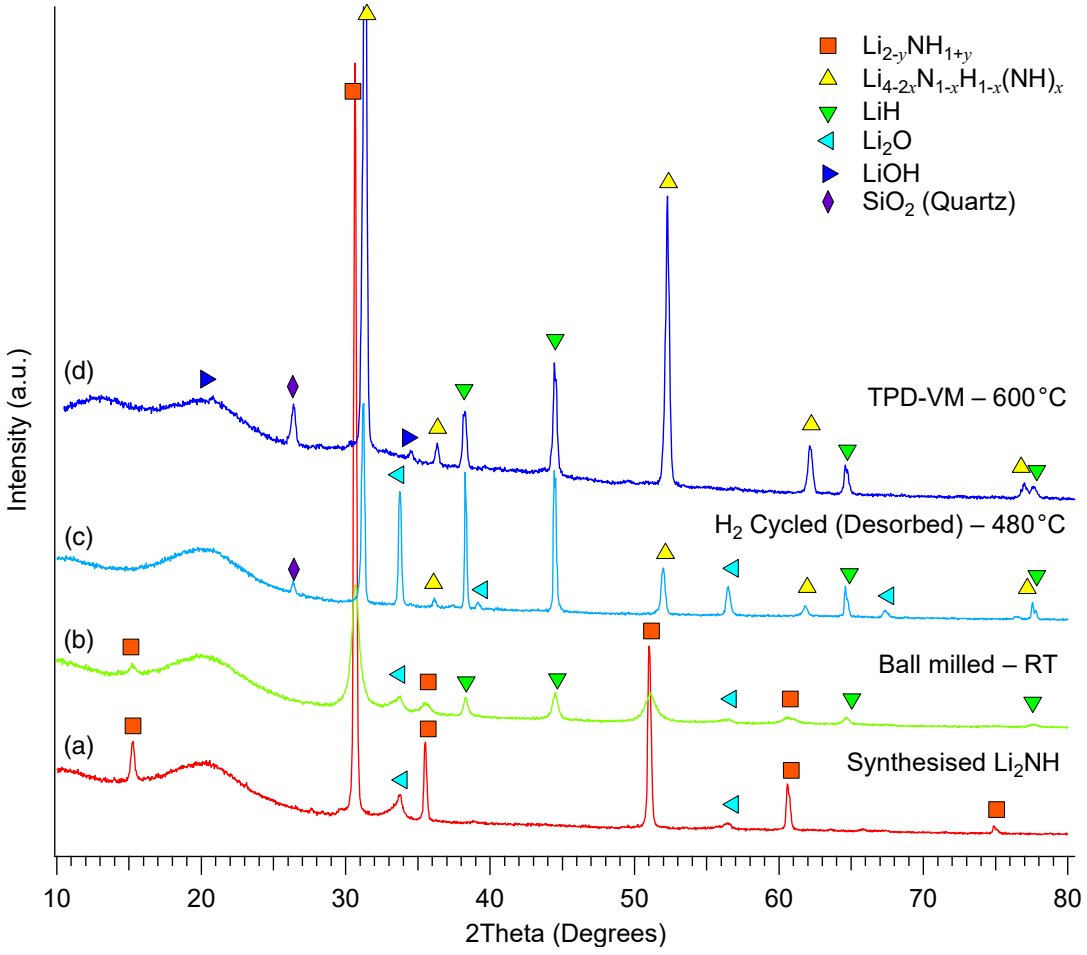

Figure 4.26: *Ex situ* XRD analysis of Li_2NH + LiH (1:2) after (b) ball milling, (c) H_2 desorbed and (d) TPD-VM – 600 °C, where $Li_{2-y}NH_{1+y}$ ($0 \leq y \leq 1$) and $Li_{4-2x}N_{1-x}H_{1-x}(NH)_x$ ($0 \leq x \leq 1$) are non-stoichiometric phases. (a) Synthesised Li_2NH for reference.

4.2.2.7 *In situ* synchrotron X-ray diffraction (SXRD) analysis of Li_2NH + LiH (1:5)

Li_2NH and LiH in a 1:2 molar ratio was prepared by ball-milling using the starting reagents in a planetary ball-mill. However, human error in the mass calculations resulted in a mixture of Li_2NH with excess LiH, for an actual molar ratio of 1:5 (Li_2NH:LiH). The *in situ* SXRD measurement was performed under dynamic vacuum with a heating rate of 7.5 °C min^{-1} in the temperature range of 100 – 500 °C. Figure 4.27 shows the *in situ* SXRD phase analysis of Li_2NH with excess LiH in a 1:5 molar ratio under dynamic vacuum. Li_3N (1) can be identified because of the incomplete synthesis of Li_2NH (using Li_3N and $LiNH_2$) at 200 °C and disappears by 350 °C such that a complete formation of Li_2NH occurred. At temperatures between 225 °C and 300 °C, the lattice parameter of Li_2NH shifts to slightly higher angles but shifts back at temperatures > 300 °C. From previous measurements, it is at approximately this temperature that the solid solution of Li_4NH and Li_2NH begins (2). As the sample cools (above the white line in Figure 4.27), the lattice parameters reduce as the peak positions shift to higher angles. Having excess LiH (3) did not help facilitate the formation of Li_4NH in this applied experiment as a single phase of Li_4NH could not be found during *in situ* SXRD.

The identification of oxide phases (Li_2O 4) in Figure 4.27 were observed to reach their peak intensity at a temperature of ~400 °C. These oxides could either be already present in the sample reagents or introduced during the measurement. This contamination is possible from the hard polyimide/graphite ferrules used, resulting in a poor seal between the capillary and capillary mount. An unknown peak (5) at a 2θ value of ~17° appears at 375 °C. This phase closely matches with SiO_2 (quartz); however, the existence of this (quartz) phase was due to contamination from glass slides. Since the preparation steps for SXRD do not involve quartz and appears after heating (> 375 °C), this unknown phase may have been a part of the sample in previous laboratory XRD measurements. Another explanation is that it may be due to the residual sand used as a cleaning agent in the ball-milling canisters.

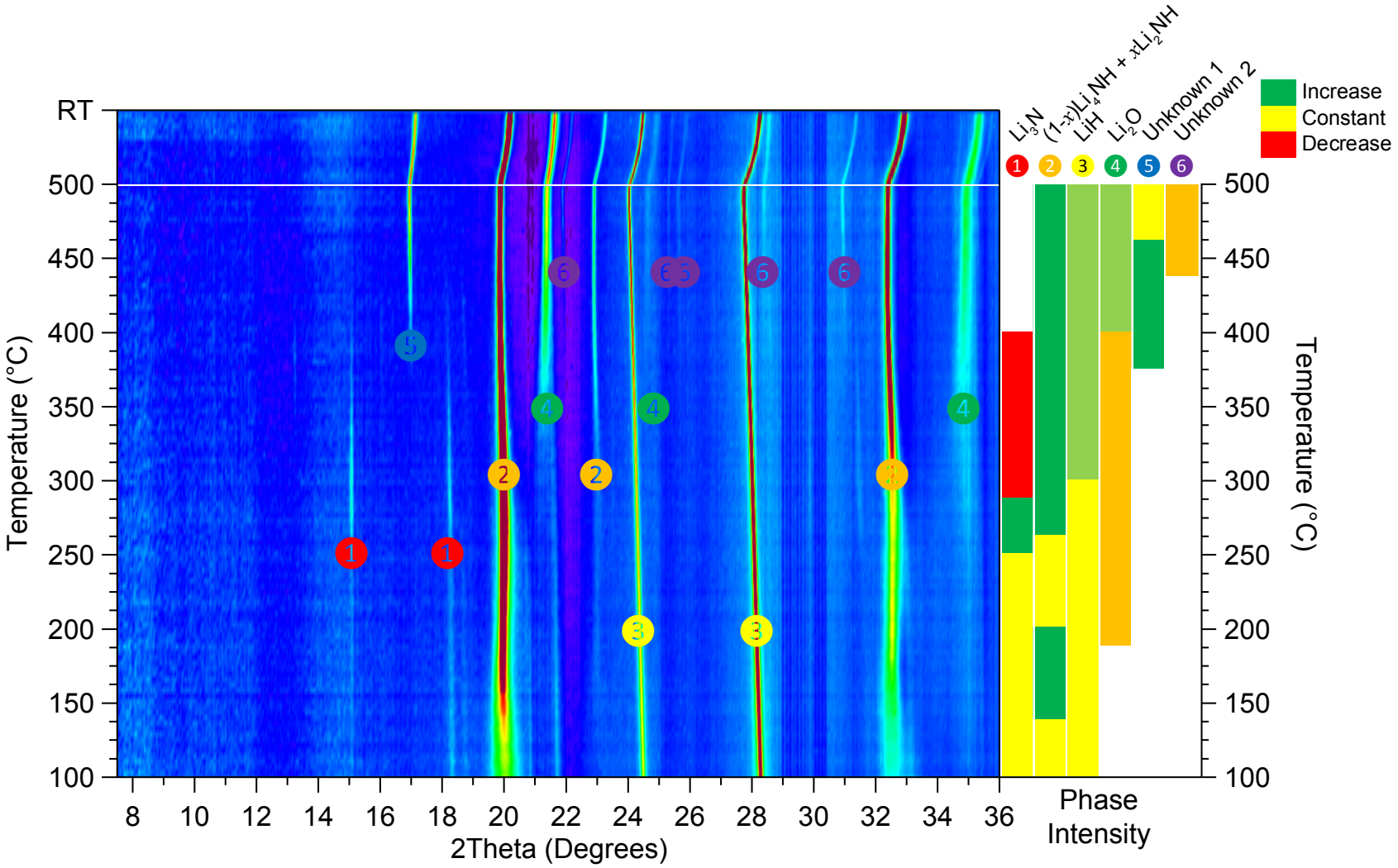

Figure 4.27: *In situ* SXRD analysis (λ = 1.00036 Å) of Li_2NH + LiH (1:5) under dynamic vacuum with phase identifcation.

The desorption reaction pathway that occurs under vacuum conditions may be different under other conditions. Therefore, Figure 4.28 shows the *in situ* SXRD measurement of Li_2NH + LiH (1:5) under a hydrogen back pressure with a heating rate of 5 °C min^{-1} in a temperature range of 100 – 500 °C. The gauge pressure decreased from 2 bar to 1.4 bar as the pressurised reference volume was opened to the evacuated sample capillary. However, this observation could also suggest a leak that explains the oxides observed *in situ* from the appearance of the oxide phase (Li_2O 4) between start to finish of the SXRD measurement. $LiNH_2$ (7) and Li_3N (1) were identified at the start of the measurement (100 °C) because of the incomplete synthesis of Li_2NH. However, the presence of hydrogen may explain the observation of $LiNH_2$ formation ($Li_2NH + H_2$). At temperatures > 250 °C, $LiNH_2$ (7) disappears as it reacts with excess LiH (3) to form Li_2NH, which forms a solid solution (2) with Li_4NH. Therefore, there is little difference observed between the dynamic vacuum and the hydrogen back-pressure measurement in Figure 4.27 and 4.28, respectively.

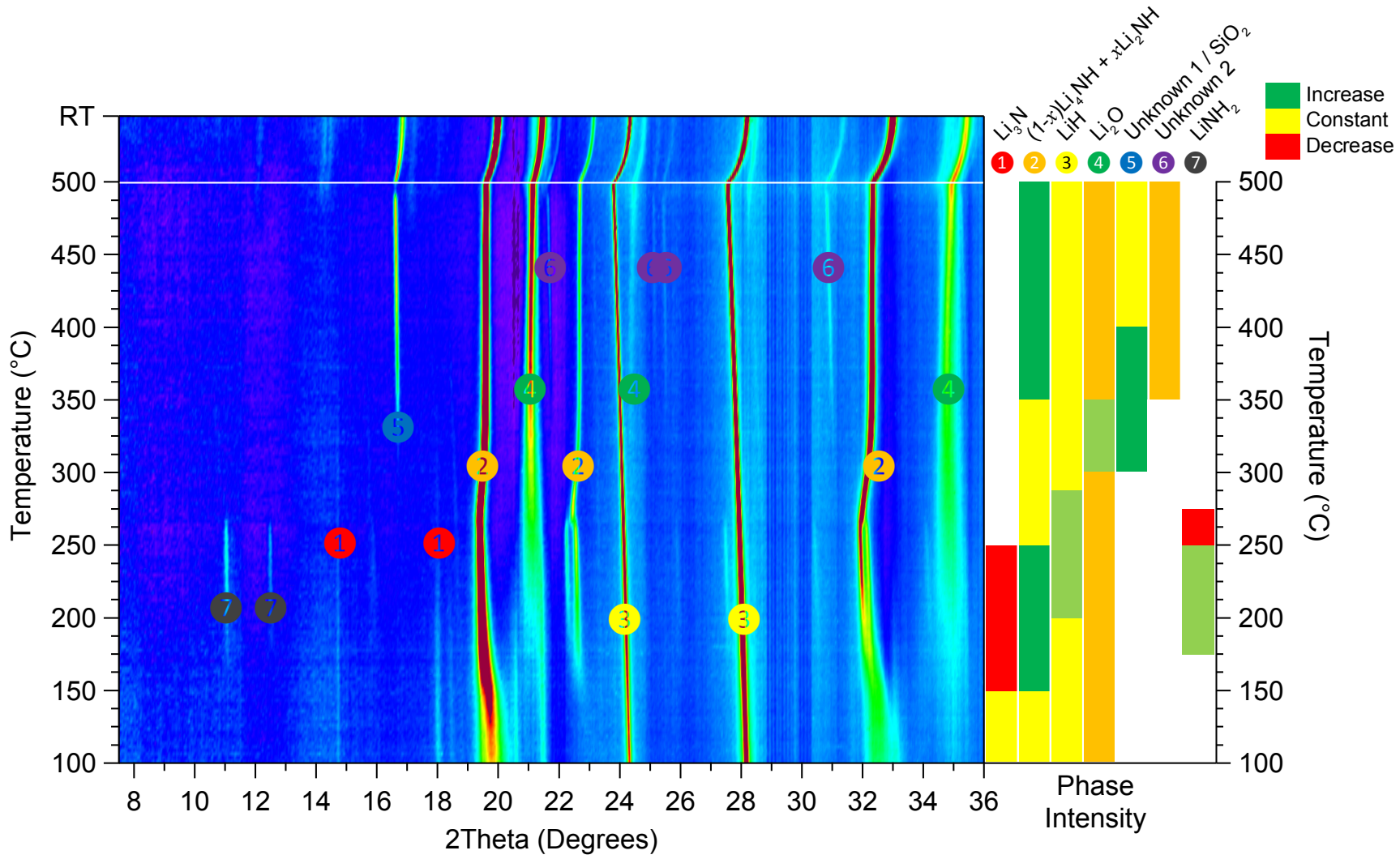

Figure 4.28: *In situ* SXRD analysis (λ = 1.00036 Å) of Li_2NH + LiH (1:5) under a hydrogen back pressure of 1.4 bar with phase identification.

4.2.2.8 Discussion of Li_2NH + LiH (1:1) and Li_2NH + LiH (1:2)

The imide-hydride to nitride reactions, Li_2NH + LiH (1:1) and Li_2NH + LiH (1:2), were investigated by means of TPPA, TPD, PCT and *in situ* SXRD. However, a Li_3N decomposition product was not observed at temperatures as high as 600 °C, and instead the lithium imide-nitride hydride phase ($Li_{4-2x}N_{1-x}H_{1-x}(NH)_x$) was present (as seen in the amide-hydride to imide reaction). As proposed in the discussion of $LiNH_2$ + LiH (1:2) in Section 4.2.1.7, the reversibility of the lithium imide-nitride hydride product from Equation 4.3 was investigated with the addition of excess LiH to facilitate the formation of Li_4NH. PCT and TPD measurements of Li_2NH + LiH (1:2) and Li_2NH + LiH (1:1) revealed that the addition of LiH had little impact on the hydrogen desorption reaction and its thermodynamics properties. Any differences observed were due to minor quantities of oxide phases resulting from the contamination of the sample from air. If any residual $LiNH_2$ remained in the sample, the reversibility of Li_2NH + LiH (1:2) was difficult to investigate due to the molten state achieved at high temperatures (as confirmed by TPPA).

The identification of a solid solution between Li_2NH and Li_4NH was observed by *in situ* SXRD. However, the reaction pathway as a result of possible products above 500 °C could not be observed. This limitation is because of the maximum temperature safety limit (≤ 500 °C) for experiments involving hydrogen gas on the Powder Diffraction beamline at the Australian Synchrotron. Therefore, solely from this observation, it is difficult to analyse due to the overlapping XRD phases that are possible in the Li–N–H system.

4.2.3 Addition of Catalyst in Li–N–H System

In this section, two catalysts were investigated in the Li–N–H system that have been known to improve the kinetics of metal hydrides for low temperature applications, the addition of titanium chloride ($TiCl_3$) and titanium nitride (TiN) nanoparticles.

4.2.3.1 Addition of Titanium Chloride

Titanium chloride ($TiCl_3$) was selected as a catalyst as it has shown success in enhancing the kinetics and reversibility of hydrogen uptake in sodium alanate ($NaAlH_4$) (Singh et al. 2007). For this reason, $TiCl_3$ has also been widely tested as a catalyst for amide-hydride systems by lowering the desorption temperature, ideal for mobile applications (Isobe et al. 2005). The addition of a catalyst to the Li–N–H system was prepared by ball-milling using the starting reagents $LiNH_2$ (Sigma-Aldrich, 95%), LiH (Sigma-Aldrich, 95%) and $TiCl_3$ (Sigma-Aldrich, 99.999%). The reagents were thoroughly mixed in a planetary ball-mill for 6 hours. The planetary ball-mill operated at 600 RPM with a BTP ratio of 60:1 using 316 stainless-steel balls sized at 10 mm and 6 mm. XRD analysis of the ball-milled sample, $LiNH_2$ + LiH (1:2) – 1 mol% $TiCl_3$, showed that it contained the starting reagents, except for the catalyst ($TiCl_3$) due to its particle size (Figure 4.29). The Li_2O phases found in the sample suggest that the sample has been contaminated by air. This observation could be due to a leak caused by the PMMA sample holder dome, exposing the sample to air during the XRD measurement.

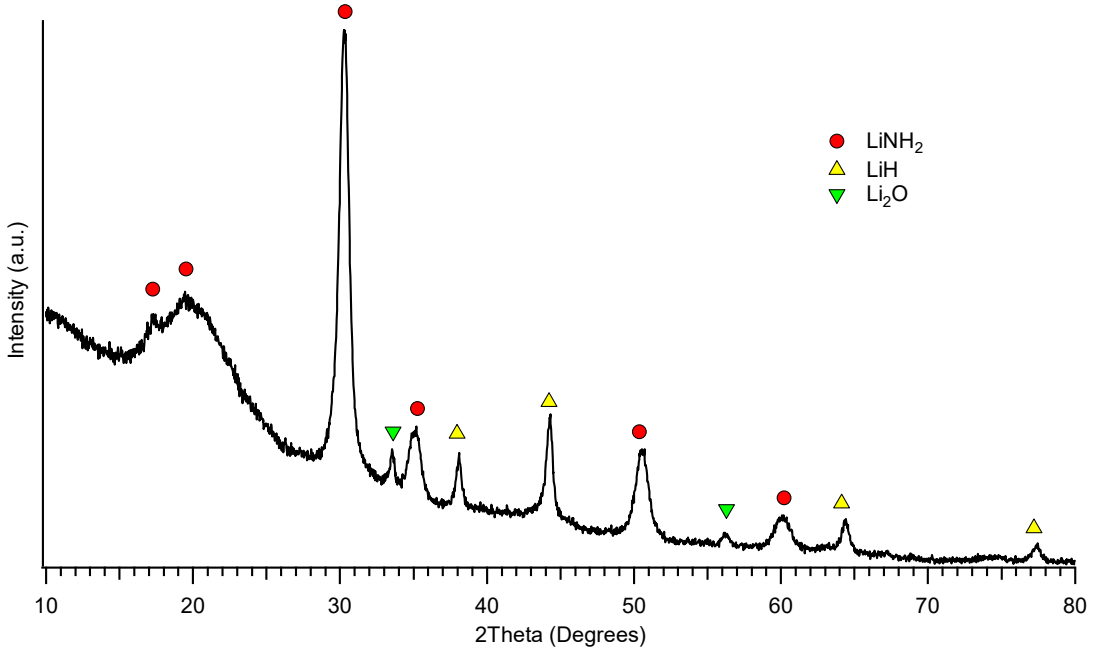

Figure 4.29: XRD analysis of $LiNH_2$ + LiH (1:2) – 1 mol% $TiCl_3$ after ball milling for 6 hours.

4.2.3.2 Temperature programmed desorption with the volumetric method (TPD-VM)

To investigate the effect of adding a catalyst to the Li–N–H system, TPD-VM measurements were performed with and without $TiCl_3$. Figure 4.30 shows the TPD-VM analysis of adding 1 mol% $TiCl_3$ to $LiNH_2$ + LiH (1:2) using a heating rate of 2 °C min^{-1}. The desorption of hydrogen before the addition of a catalyst occurred at ~239 °C with a broad peak between 150 °C and 300 °C corresponding to the rate of hydrogen release. The addition of 1 mol% $TiCl_3$ to the system improved the kinetics such that a sharper desorption peak was observed and occurred at a lower temperature (~211 °C). XRD analysis after TPD measurements halted at 300 °C (Figure 4.31) revealed the formation of a Li_2NH phase. Therefore, the hydrogen desorption event at ~211 °C is confirmation of the formation of Li_2NH. These results are in agreement with the TPD-MS analysis by Isobe et al. (2005) that revealed a peak desorption temperature at ~220 °C using a heating rate of 5 °C min^{-1}.

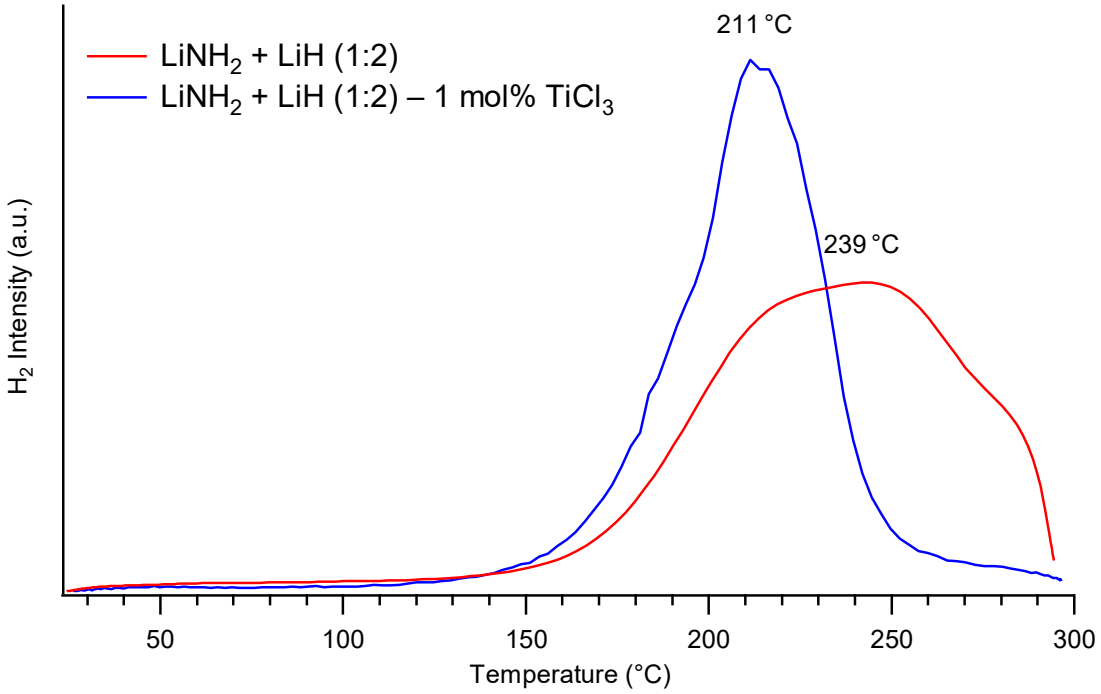

Figure 4.30: TPD-VM analysis of $LiNH_2$ + LiH (1:2) – 1 mol% $TiCl_3$ in the temperature range 25 – 300 °C, where the heating rates were 2 °C min^{-1} starting at vacuum.

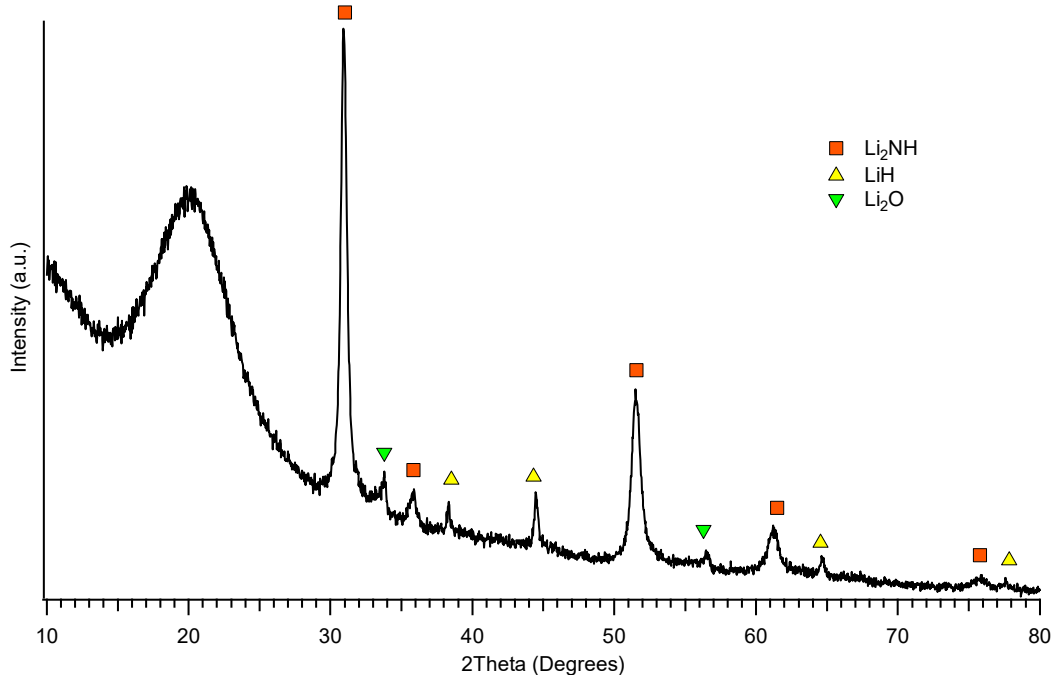

Figure 4.31: XRD analysis of LiNH + LiH (1:2) – 1 mol% TiCl after TPD measurement halted at 300 °C.

4.2.3.3 Addition of Titanium Nitride Nanoparticles

Titanium nitride (TiN) nanoparticles were chosen as they are known to be an excellent catalyst for enhancing the kinetics and reversibility of $NaAlH_4$ (Kim et al. 2009). Hence, the Li–N–H system doped with TiN nanoparticles was investigated. TiN nanoparticles were synthesised by Mark Paskevicius (2013) at Curtin University (Australia). The starting reagents obtained from Sigma-Aldrich were $TiCl_4$ (> 99.995%), Li_3N (> 99.9%), LiH (> 95%) and LiCl (> 99.9%). The TiN synthesis was carried out mechanochemically by the following reaction:

$$TiCl_{4(l)} + Li_3N + LiH \rightarrow TiN + 4LiCl + 0.5H_{2(g)} \quad (4.7)$$

To produce nanoparticles, a LiCl buffer was added to the starting reagents (Li_3N and LiH) that were first mixed in a shaker-mixer mill for 12 hours, operated at 160 RPM with a BTP ratio of 30:1 using 316 stainless-steel balls. After pre-milling to produce nanoscopic reaction sites, liquid $TiCl_4$ was added to the mixture and milled for a further 12 hours to ensure a complete reaction. The LiCl by-product is then dissolved in tetrahydrofuran (THF) solvent using the THF-washing procedure in Chapter 2: Section 2.1.4.

The addition of laboratory synthesised TiN nanoparticles to the Li–N–H system was prepared by ball-milling using the starting reagents $LiNH_2$ (Sigma-Aldrich, 95%), LiH (Sigma-Aldrich, 95%) and TiN (laboratory synthesised). The staring reagents were thoroughly mixed in a planetary ball-mill for 6 hours and operated at 600 RPM with a BTP ratio of 60:1 using 316 stainless-steel balls sized at 10 mm and 6 mm. The appearance of the ball-milled powder was dark grey, which was almost black.

X-ray diffraction analysis after ball-milling (Figure 4.32) showed the partial decomposition reaction of $LiNH_2$ to Li_2NH, resulting in the formation of a non-stoichiometric intermediate, $Li_{2-y}NH_{1+y}$ ($0 \leq y \leq 1$) between the amide and imide phase. This analysis suggests that the addition of 1 mol% TiN improved the dehydrogenation kinetics such that the heat generated during reactive ball-milling was enough for partial dehydrogenation from the amide-hydride reaction in the Li–N–H system.

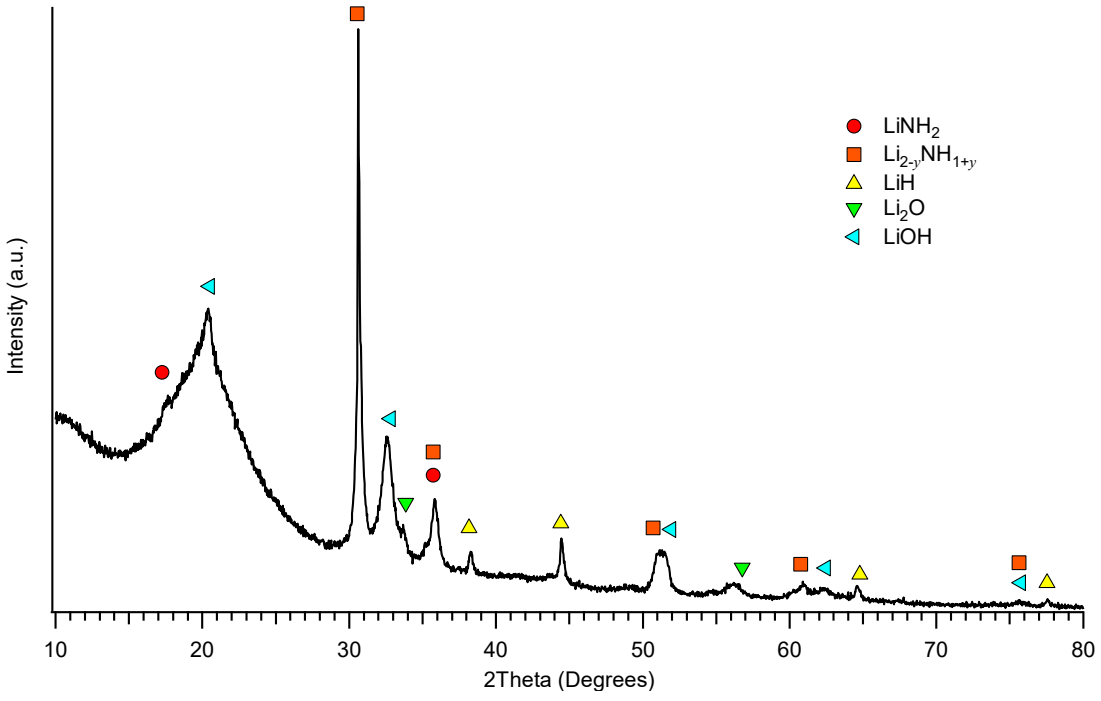

Figure 4.32: XRD analysis of $LiNH_2$ + LiH (1:2) – 1 mol% TiN nanoparticles after ball milling for 6 hours.

4.2.3.4 Discussion of catalysts

Catalysts are often used to lower the desorption temperature of materials, improving the kinetics of hydride systems. Lowering the desorption temperature may be counter intuitive in terms of a thermal storage solution but given the samples often melted after each high temperature measurement, the addition of a catalyst can be viewed to investigate the reactions that would occur at high temperatures if they did not melt and form a solid solution. However, the investigation of catalysts ($TiCl_3$ and TiN nanoparticles) in the Li–N–H system were not pursued because of its low priority in terms of high-temperature imide-hydride systems, but future work may provide a kinetically favoured reversible reaction pathway involving the formation of nitride product from the imide-hydride reaction, suitable for high-temperature thermal energy storage.

4.3 Conclusion

Three reactions were investigated in this chapter: the amide-hydride reaction, $LiNH_2$ + LiH (1:2), the imide-hydride reaction, Li_2NH + LiH (1:1) and the imide-hydride (with excess LiH) reaction, Li_2NH + LiH (1:2). TPD-VM analysis of all three reactions revealed similar events with a large hydrogen desorption event occurring at ~230 °C and a smaller hydrogen desorption event at ~530 °C. These observations suggest two things. First, the synthesis of Li_2NH was incomplete in the ball-milling mixture of Li_2NH + LiH (1:1) and Li_2NH + LiH (1:2); contributing to the release of hydrogen observed at ~230 °C. Second, the formation of Li_4NH at 530 °C results in a solid solution of Li_2NH and Li_4NH that react with each other to form a lithium imide-nitride hydride ($Li_{4-2x}N_{1-x}H_{1-x}(NH)_x$), where no Li_3N could be identified. *Ex situ* XRD and *in situ* SXRD analysis were used to characterise the reaction pathway at temperatures $\leq$ 500 °C, but was difficult because of the overlapping XRD patterns of several phases appearing in the Li–N–H system. PCT measurements were unreliable as TPPA confirmed that samples would often melt at high temperatures (> 475 °C), blocking sample cells and inhibiting the sorption properties of hydrogen.

In conclusion, lithium-based imide-hydride systems may not be suitable for high temperature thermal storage, as the reaction pathway at high temperatures is not completely understood using the characterisation methods in this chapter. The system was irreversible in PCT measurements because the samples would melt at high temperature as confirmed by TPPA. From a thermal storage application standpoint, a molten sample would only create a series of engineering problems for these systems, if lithium amide- and imide-hydrides were to be pursued in thermal storage technologies. However, the characterisation methods used to reproduce the widely studied Li–N–H system were useful for the investigation of other amide-imide-hydride systems.

CHAPTER 5: MAGNESIUM-BASED SYSTEMS

5.1 Introduction

Magnesium nitrides (Mg_3N_2) and its hydrogenation reaction at high temperature to form imides; much like the lithium system, have been little studied because of the interest in low-operation-temperature materials for mobile applications. The literature available on magnesium-based systems are focused on the amide-hydride to imide reaction, which has seen promise as a hydrogen storage material. Nakamori, Kitahara, and Orimo (2004) investigated the reaction between magnesium amide ($Mg(NH_2)_2$) and magnesium hydride (MgH_2) to form magnesium imide (MgNH) (Equation 5.1), but found that instead of the amide-hydride reaction, the decomposition of $Mg(NH_2)_2$ to MgNH occurred at low temperatures of approximately 200 °C. However, Hu et al. (2006a) reported that the two-step reaction in Equation 5.1 and 5.2 was observed at room temperature after intense mechanical ball milling.

$$Mg(NH_2)_2 + MgH_2 \rightarrow 2MgNH + 2H_2 \quad (5.1)$$

$$2MgNH + MgH_2 \rightarrow Mg_3N_2 + 2H_2 \quad (5.2)$$

This chapter aims to characterise $Mg(NH_2)_2$ and MgNH that were synthesised using a procedure that did not require the handling of gaseous ammonia, focusing on their decomposition mechanics, material characteristics and thermodynamic properties. The final decomposition product in Equation 5.2 (Mg_3N_2) is often difficult to rehydride when it is the only component in the system (Dolotko, Paulson and Pecharsky 2010; Nakamori, Kitahara and Orimo 2004). However, partial rehydrogenation has been observed in the presence of other compounds (i.e. LiH and NaH). These compounds are further discussed in Chapter 7 (Li–Mg–N–H) and Chapter 9 (Na–Mg–N–H). Based on the imide-hydride reaction in Equation 5.2, magnesium iron hydride (Mg_2FeH_6) was chosen as it has a higher thermodynamic stability than MgH_2 (Bogdanović et al. 2002; Felderhoff and Bogdanović 2009). Therefore, by substituting Mg_2FeH_6 for MgH_2 in Equation 5.2, the operation temperature should be higher and thus, suitable for thermal storage

applications. The investigation between MgNH and Mg_2FeH_6 in a 4:1 molar ratio has an overall reaction as follows:

$$4MgNH + Mg_2FeH_6 \rightarrow 2Mg_3N_2 + Fe + 5H_2 \quad (5.3)$$

where the decomposition of Mg_2FeH_6 at ~1 bar has been reported to occur at ~340 °C (Polanski et al. 2010), which is at a higher temperature (~282 °C) than MgH_2 (Paskevicius, Sheppard and Buckley 2010). Furthermore, to test the reversibility of the reaction in Equation 5.3, the hydrogenation of Mg_3N_2 and iron metal was investigated at high temperatures suitable for thermal energy storage. The addition of iron has the potential to not only reduce the cost of the system but also increase the theoretical hydrogen capacity to 3.76 wt% in Equation 5.3.

5.2 Results

5.2.1 Synthesis of $Mg(NH_2)_2$

$Mg(NH_2)_2$ was not commercially available and synthesised via a mechanochemical metathesis reaction (Equation 5.4), where a tetrahydrofuran (THF) solvent was used to remove the by-product chloride salts. The starting reagents were $LiNH_2$ (Sigma-Aldrich, 95%) and magnesium chloride ($MgCl_2$, Sigma-Aldrich, ≥ 98%).

$$2LiNH_2 + MgCl_2 \rightarrow Mg(NH_2)_2 + 2LiCl \quad (5.4)$$

The mass of starting reagents was calculated in Table 5.1 to theoretically yield a 5 g batch of $Mg(NH_2)_2$ based on the reaction in Equation 5.4. The reagents were thoroughly mixed in a shaker-mixer at 160 RPM for 20 hours with a BTP ratio of 30:1 using 316 stainless-steel balls sized at 12.7 mm and 7.9 mm. Given the solubility of LiCl in THF (1.74 g L^{-1}) and the molar mass values from Table 5.1, approximately 40 mL of THF in 2.89 g of ball-milled sample was calculated to completely dissolve LiCl (~60 wt%) in a single wash. Using the THF-washing procedure described in Chapter 2: Section 2.1.4, the first wash was evacuated for an hour, the second wash was evacuated for 15 minutes and the third and final wash was evacuated overnight to completely evaporate residual THF.

Table 5.1: Mass calculations for the starting reagents required to theoreotically yield a 5 g batch of magnesium amide, where N = no. of moles, M = molar mass, M_t = total molar mass and m = sample mass.

Molecule	N	M (g mol^{-1})	M_t (g mol^{-1})	m (g)
$LiNH_2$	2	22.967	45.934	4.0753
$MgCl_2$	1	95.205	95.205	8.4466
$Mg(NH_2)_2$	1	56.367	56.357	5.0000
LiCl	2	42.391	84.782	7.5220

X-ray diffraction analysis of THF-washed $Mg(NH_2)_2$ (Figure 5.1a; —) was compared to a batch synthesised by Mark Paskevicius (2011) (Figure 5.1b; —), who used the same synthesis method. The results were near identical and showed that in both cases, some residual LiCl is expected. Because of the existence of LiCl after the initial THF wash, a second batch with a greater number of wash steps (4× wash) was synthesised. XRD analysis of Batch 2 in Figure 5.2 revealed that the sample was contaminated by air with the appearance of MgO and Li_2O phases. The contamination was caused by either poor handling of the sample inside and/or outside the glovebox or from the THF solvent.

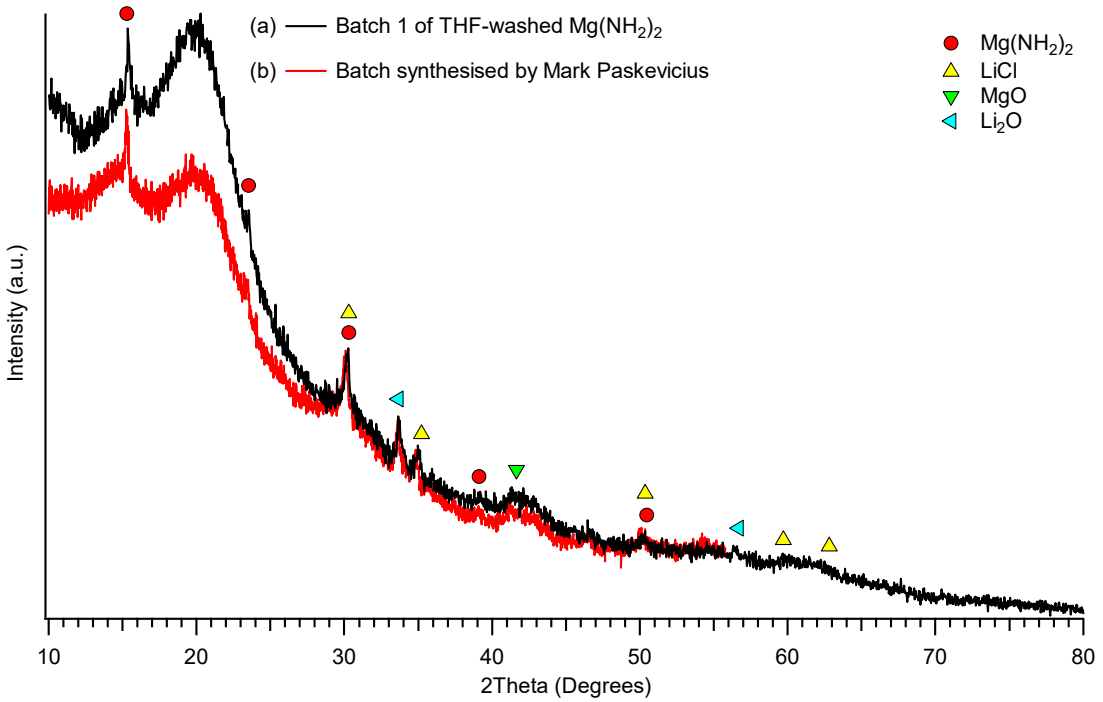

Figure 5.1 Comparitive XRD analysis of THF-washed $Mg(NH_2)_2$, (a) Batch 1 and (b) batch synthesised by Mark Paskevicius (2011).

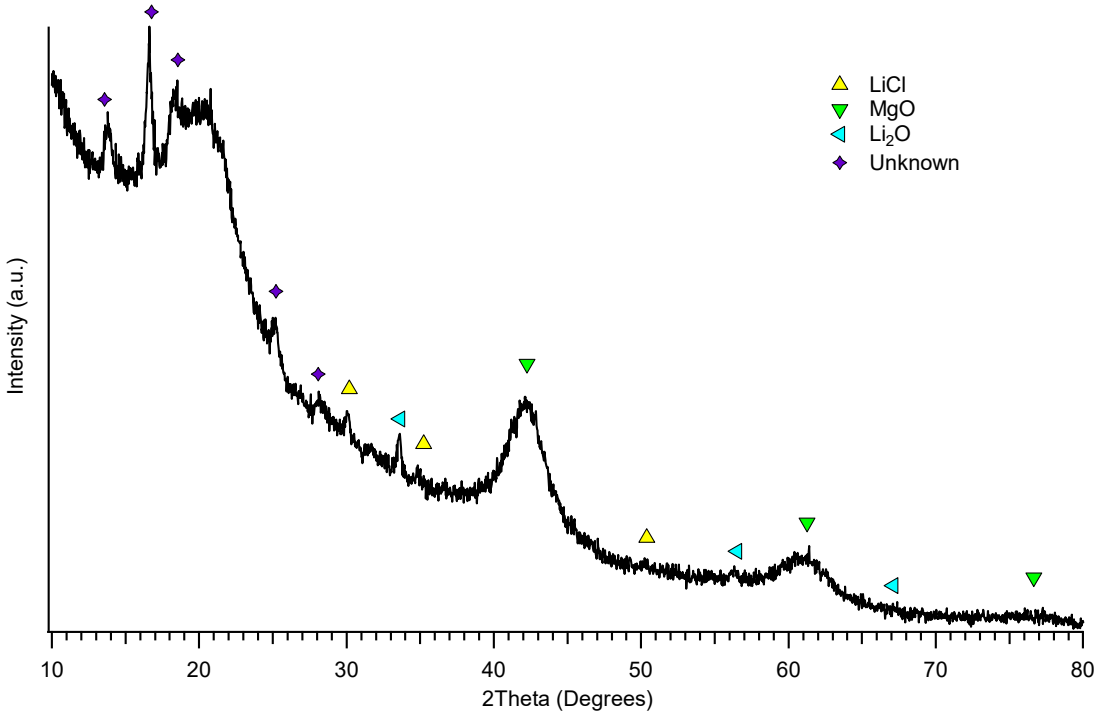

Figure 5.2: XRD analysis of Batch 2 – THF-washed $Mg(NH_2)_2$ after 4× wash.

5.2.1.1 Fourier transform infra-red (FTIR) analysis

Fourier transform infra-red analysis was performed on THF-washed $Mg(NH_2)_2$ to verify the weak diffraction peaks observed by XRD analysis (Figure 5.1). This verification was needed because of how easily $Mg(NH_2)_2$ becomes an amorphous structure after ball milling (Juza 1964; Liu et al. 2007). Figure 5.3 shows the FTIR spectra of $Mg(NH_2)_2$ that has undergone a single THF wash treatment. The absorption bands have been compared to FTIR spectra by Linde and Juza (1974), where they did an FTIR study on different amides and imides. The $Mg(NH_2)_2$ and MgNH bands are labelled in black and red arrows, respectively (Figure 5.3). The strongest bands for $Mg(NH_2)_2$ can be found at 3359, 3274, 3195, 1566 and 509 cm^{-1}, whereas the strongest bands for MgNH can be found at 1566, 1429 and 808 cm^{-1}. However, given the low intensity absorption bands for MgNH, FTIR analysis revealed that the THF-washed sample primarily consisted of $Mg(NH_2)_2$.

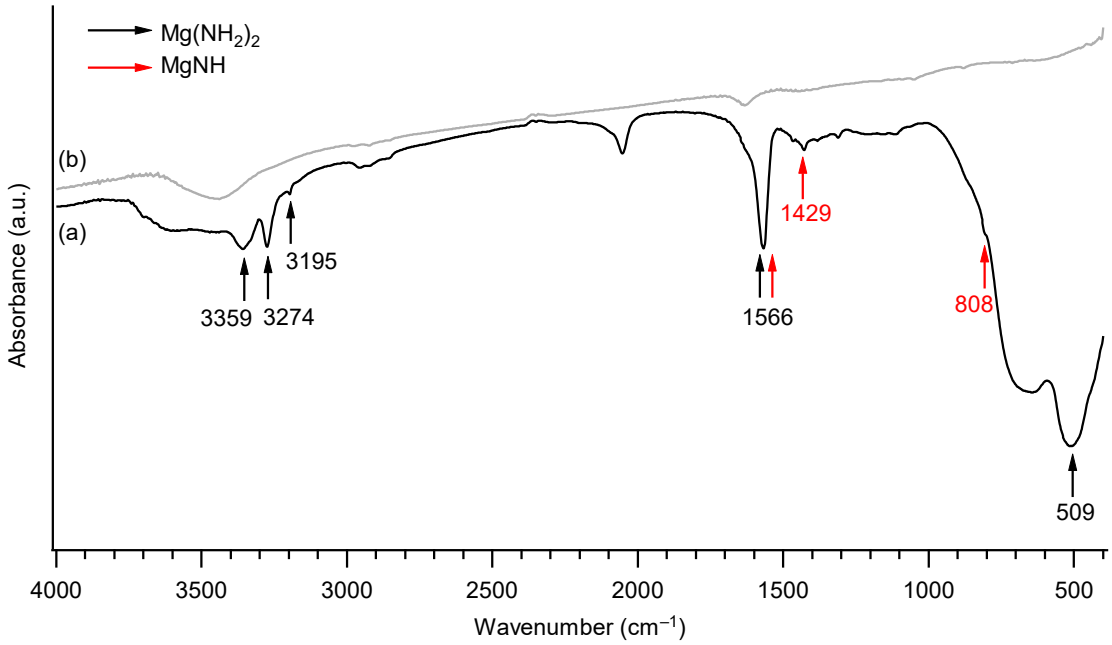

Figure 5.3: FTIR spectra of (a) THF-washed $Mg(NH_2)_2$ and (b) blank KBr pellet.

5.2.1.2 Temperature programmed photographic analysis (TPPA)

Temperature-programmed photographic measurements were performed on $Mg(NH_2)_2$ to observe the macroscopic sample behaviour in a range of temperatures (100 – 525 °C). The TPPA of THF-washed $Mg(NH_2)_2$ in Figure 5.4, showed a change in sample volume that decreased in the temperature range of 100 – 200 °C (Frame 1 and 2 of Figure 5.4). Between 200 °C and 400 °C, the sample volume increases (Frame 3 of Figure 5.4) and begins changing to a yellow colour with no other changes observed between 400 °C and 525 °C (Frame 4 of Figure 5.4). Once the temperature controller was switched off, the heating block rapidly cooled to consequently crack the sample glass vial, probably due to thermal shock, where the yellow colour of the sample faded to a green colour when in contact with air (Figure 5.5). This colour change from yellow to green was previously seen in the Li–N–H system, where a green sample layer contained oxide phases as confirmed by XRD analysis (Chapter 4: Figure 4.19).

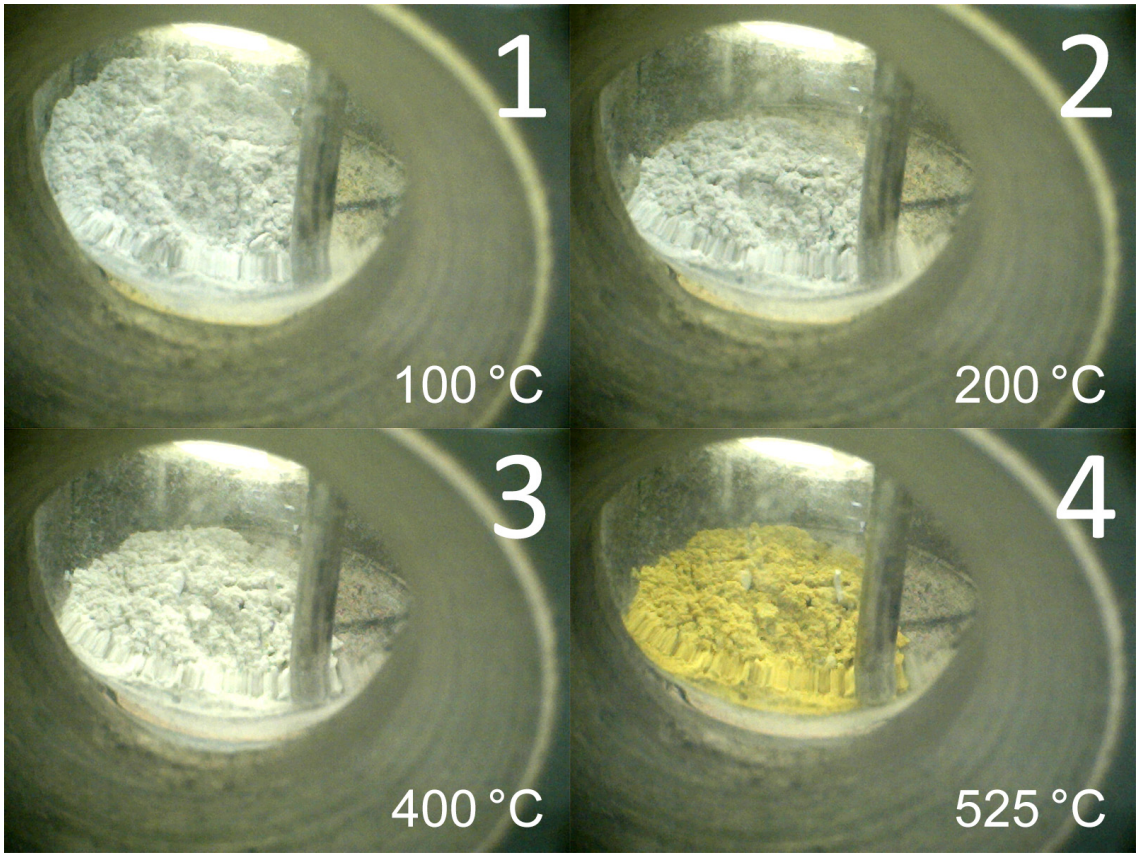

Figure 5.4: TPPA of THF-washed $Mg(NH_2)_2$ at 100, 200, 400 and 525 °C with a heating rate of 10 °C min^{-1}.

Figure 5.5: Images of THF-washed $Mg(NH_2)_2$ taken at RT after temperature-programmed photographic measurements up to 525 °C.

5.2.1.3 Temperature programmed desorption with mass spectrometry (TPD-MS)

Temperature programmed desorption measurements were performed in an effort to understand the decomposition pathway of $Mg(NH_2)_2$ via identification of the gases released during decomposition using a mass spectrometer. Additionally, TPD-MS analysis was used to confirm the synthesis of $Mg(NH_2)_2$ since MgNH can be X-ray amorphous after ball milling (Liang et al. 2010). Because of the different heating rates used (2 and 3 °C min^{-1}), slight differences were expected between the TPD-MS analysis of unwashed and THF-washed $Mg(NH_2)_2$ in Figure 5.6 and 5.7, respectively. The slightly higher heating rate may explain the difference in the decomposition temperature of unwashed and THF-washed sample at 313 °C and 335 °C, respectively. However, because the THF wash determines the amount of LiCl remaining in the sample, LiCl may have contributed to the change in decomposition temperature (for the unwashed sample). The hydrogen desorption event at 404 °C could be the decomposition of NH_3; however, because the nitrogen signal is absent at this temperature, this hydrogen desorption event is unknown.

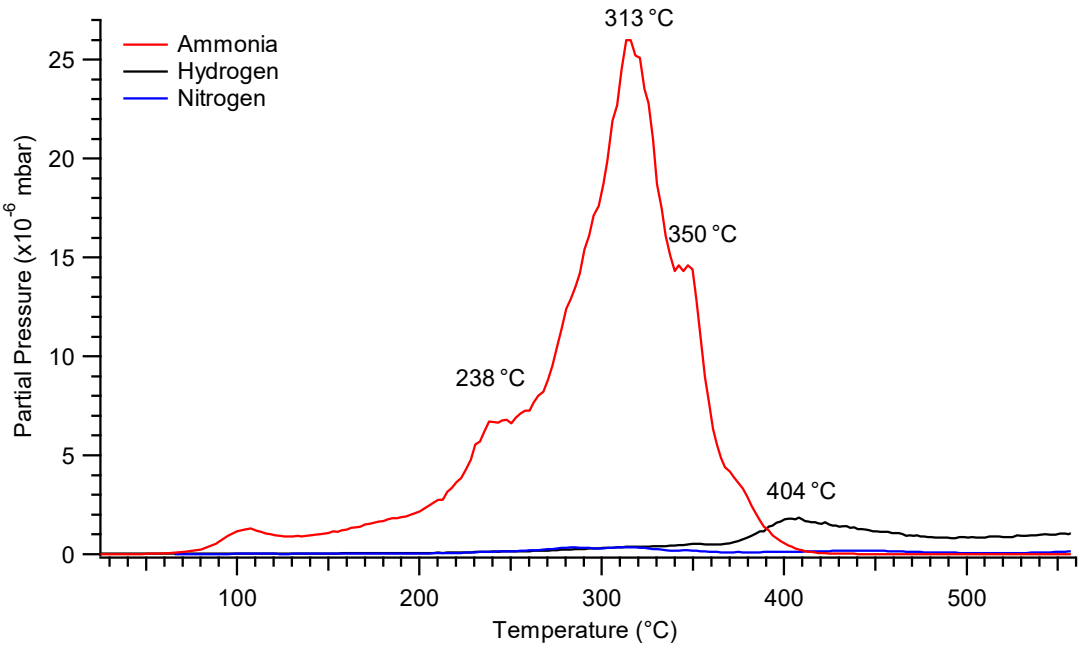

Figure 5.6: TPD-MS analysis of unwashed $Mg(NH_2)_2$ performed under dynamic vacuum in the temperature range of 25 – 560 °C, where the heating rate was 2 °C min^{-1}.

In the TPD-MS analysis of unwashed $Mg(NH_2)_2$ with a slower heat rate (Figure 5.6), there were smaller ammonia desorption events occurring at ~238 °C and ~350 °C that appeared as shoulder peaks for the desorption event at 313 °C. TPD-MS analysis of THF-washed $Mg(NH_2)_2$ (Figure 5.7) showed two possible ammonia release events peaking at 335 °C and 430 °C, whereas only one major ammonia release event (313 °C) was observed for the unwashed sample. The decrease in hydrogen intensity at ~340 °C can be explained by a background scan that was performed when the sample was insufficiently outgassed, where the background was not as low as it should have been.

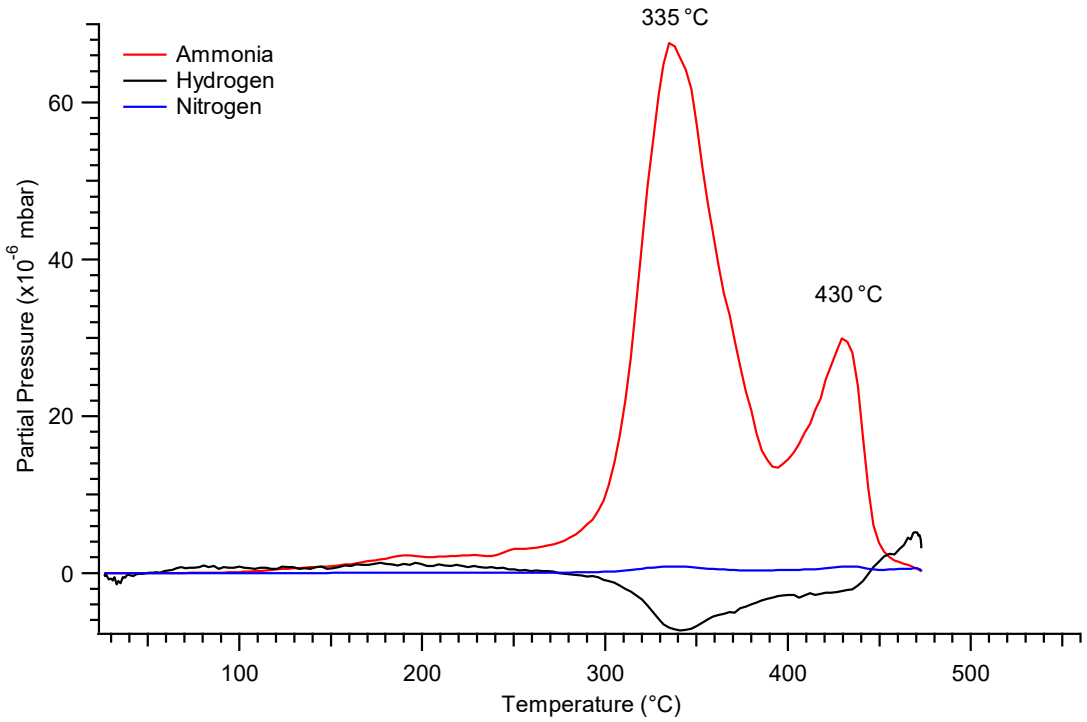

Figure 5.7: TPD-MS analysis of THF-washed $Mg(NH_2)_2$ performed under dynamic vacuum in the temperature range of 25 – 470 °C, where the heating rate was 3 °C min^{-1}.

The XRD analysis of unwashed $Mg(NH_2)_2$ after the TPD-MS measurement was halted at 560 °C is shown in Figure 5.8. Little oxygen contamination could be found with the final products identified as Mg_3N_2 with small amounts of Li_2NH. The identification of Li_2NH suggests that the desorption event that occurred at ~238 °C in the TPD-MS analysis (Figure 5.6), corresponded to the decomposition of residual $LiNH_2$. The identification of Mg_3N_2 by XRD analysis confirms the ammonia release by TPD-MS analysis corresponded to the decomposition of

$Mg(NH_2)_2$ and MgNH. However, this observation is unusual as only one ammonia desorption event was observed at ~313 °C in the TPD-MS analysis of unwashed $Mg(NH_2)_2$. Therefore, the presence of residual LiCl may have influenced the decomposition of $Mg(NH_2)_2$ and MgNH to occur at 313 °C and 350 °C, respectively. However, further work is required to investigate the effect of LiCl in the decomposition of $Mg(NH_2)_2$.

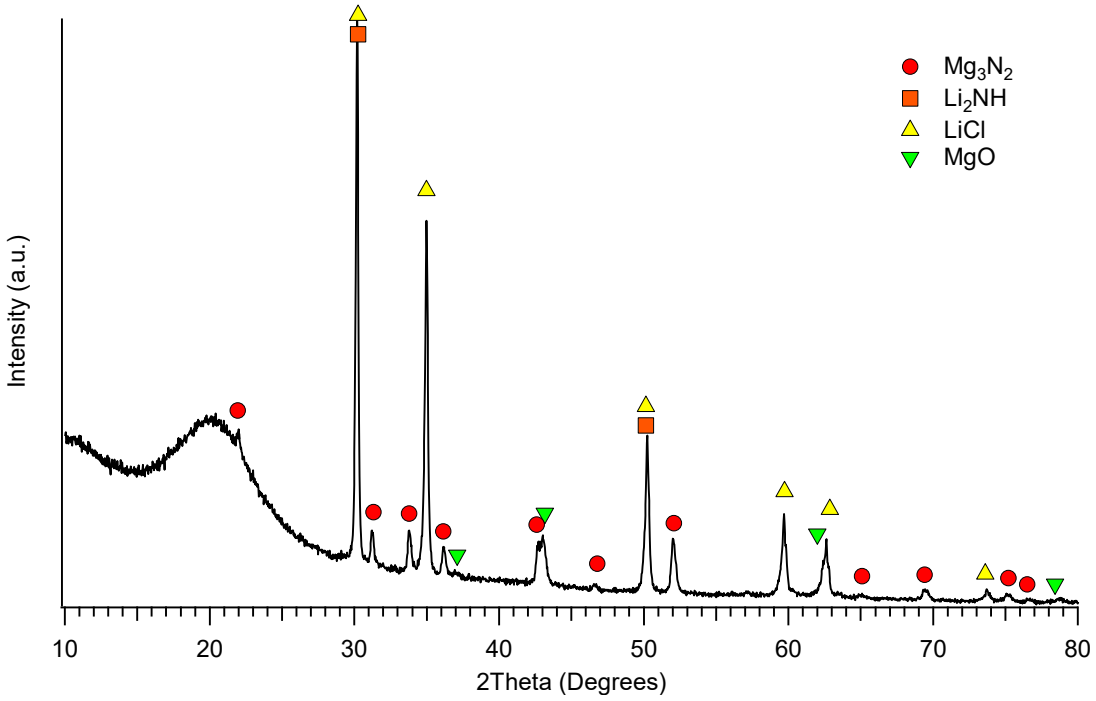

Figure 5.8: XRD analysis of unwashed $Mg(NH_2)_2$ after TPD measurement halted at 560 °C.

Temperature programmed desorption with mass spectrometry analysis of THF-washed $Mg(NH_2)_2$ revealed two ammonia release events at ~335 °C and ~430 °C (Figure 5.7). Therefore, to identify the phase change between these temperatures, XRD analysis was also performed on a sample where the TPD-MS measurement was halted at 350 °C. However, the sample was contaminated after the TPD measurement, where XRD analysis revealed the appearance of MgO phases, which can be found in Appendix A (Figure A.5).

X-ray diffraction analysis of THF-washed $Mg(NH_2)_2$ after the TPD-MS measurement was halted at 470 °C (Figure 5.9) showed the formation of Mg_3N_2 as expected in Equation 5.6. The first ammonia desorption event at 335 °C corresponds to the decomposition of $Mg(NH_2)_2$ to MgNH (Equation 5.5) and the

second desorption event at 430 °C corresponds to the decomposition of MgNH to Mg_3N_2 (Equation 5.6), where these desorption events are in agreement with literature results (Leng et al. 2004).

$$Mg(NH_2)_2 \rightarrow MgNH + NH_3 \tag{5.5}$$

$$MgNH \rightarrow \frac{1}{3}Mg_3N_2 + \frac{1}{3}NH_3 \tag{5.6}$$

The presence of an unknown phase could also be identified with the strongest peaks appearing at 2θ angles of ~32° and ~45°. This unknown phase could be a contaminant phase given the high amount of oxygen contamination (~24 wt% of MgO) observed. Rietveld refinement of unwashed and THF-washed samples also revealed that approximately 86% of LiCl was washed using the THF-washing procedure in Chapter 2 (Section 2.1.4).

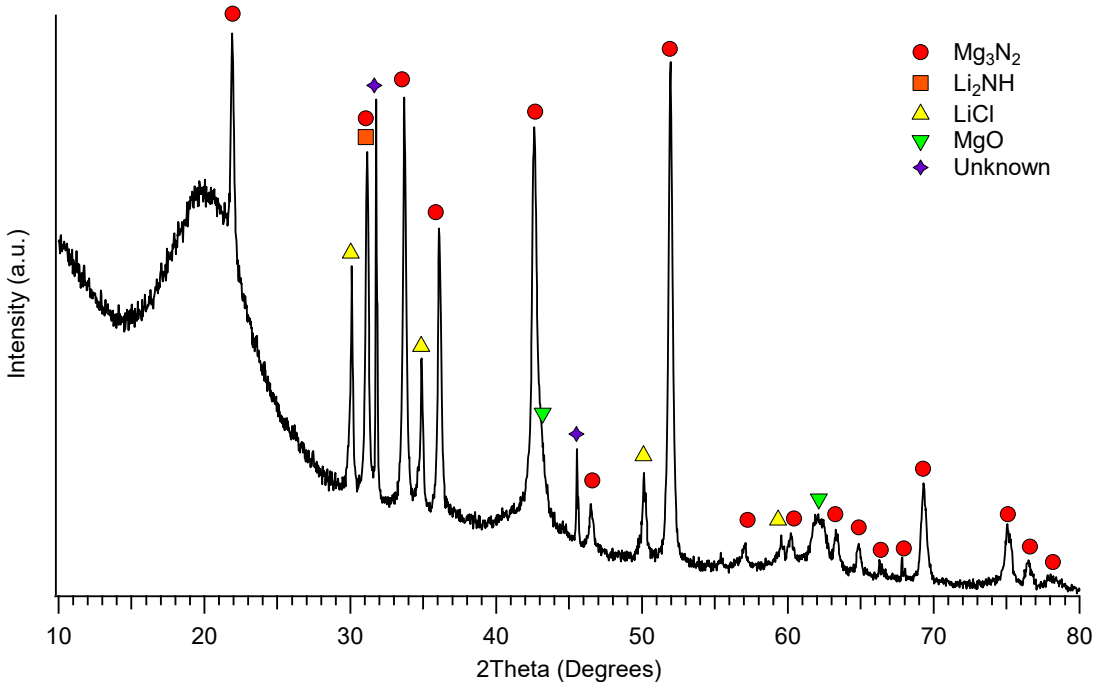

Figure 5.9: XRD analysis of THF-washed $Mg(NH_2)_2$ after TPD measurement halted at 470 °C.

Oxygen contamination was often observed in samples prepared for TPD analysis and confirmed by XRD analysis. The TPD-MS analysis of contaminated $Mg(NH_2)_2$ in the temperature range of 25 – 550 °C and the room temperature XRD analysis after the TPD measurement can be found in Appendix A: Figure A.6 and A.7,

respectively. However, given that the sample was severely contaminated with MgO, no constructive conclusions could be obtained from these results.

5.2.1.4 High temperature analysis

Unwashed samples of $Mg(NH_2)_2$ were subjected to a high temperature heat treatment (700 °C) to identify the source of oxygen contamination in previous experiments and to test a new type of sample cell. The sources of contamination could either be introduced after the ball-milling metathesis reaction between $MgCl_2$ and $LiNH_2$ or the THF washing of $Mg(NH_2)_2$. Because of the operation temperature limits of Swagelok components (< 537 °C), a high temperature sample cell made of silicon carbide (SiC) was tested using unwashed and THF-washed $Mg(NH_2)_2$. XRD analysis of unwashed $Mg(NH_2)_2$ after heat treatment at 700 °C (Figure 5.10) revealed severe oxygen contamination such that the expected final phase of Mg_3N_2 could not be identified. Furthermore, multiple unknown phases were present with the appearance of Li_2O and $Mg(OH)_2$ after heating to 700 °C.

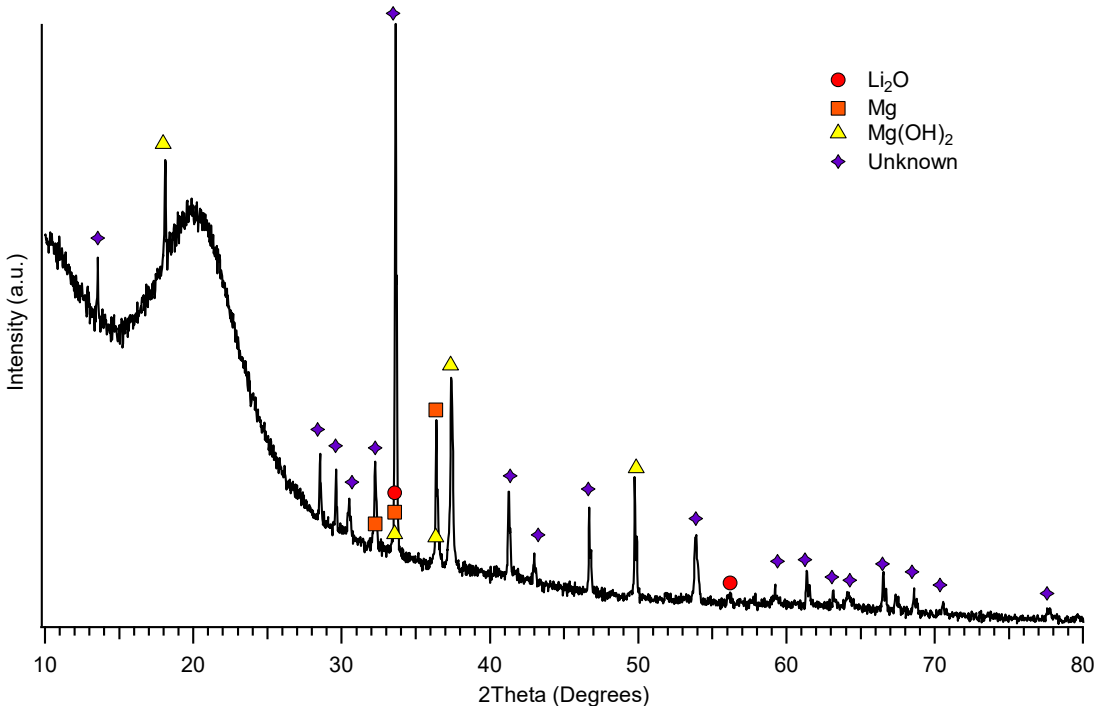

Figure 5.10: XRD analysis of unwashed $Mg(NH_2)_2$ after heat treatment at 700 °C.

High temperature measurements with the SiC sample cell were also performed on THF-washed $Mg(NH_2)_2$. When the sample was allowed to cool, a layer of clear

sample was found above a layer of yellow sample. The clear sample was hand crushed (with an agate mortar and pestle) into a powdered sample for XRD measurements. XRD analysis of the clear sample in Figure 5.11b, revealed the peak positions corresponded to LiCl but the relative peak intensities do not as the strongest peak should occur at ~30° (2θ). Because the highly crystalline sample was not crushed finely enough, the correct peak intensities were not diffracted i.e. depending on the diffraction angle, XRD analysis of the same sample would result in a pattern with the same peak positions but different relative peak intensities. Further evidence that supports the clear sample being LiCl can be confirmed by the melting point of LiCl (> 610 °C) obtained from the HSC Chemistry software (HSC version 6.12, Outotec Research Oy). Compared to the XRD analysis of unwashed $Mg(NH_2)_2$ at 700 °C (Figure 5.10), no other oxide phases could be identified other than MgO in Figure 5.11a. Therefore, the source of oxygen contamination was not due to contaminated THF, but possibly from sample cell leaks or contamination during XRD measurements from the bubble dome holder.

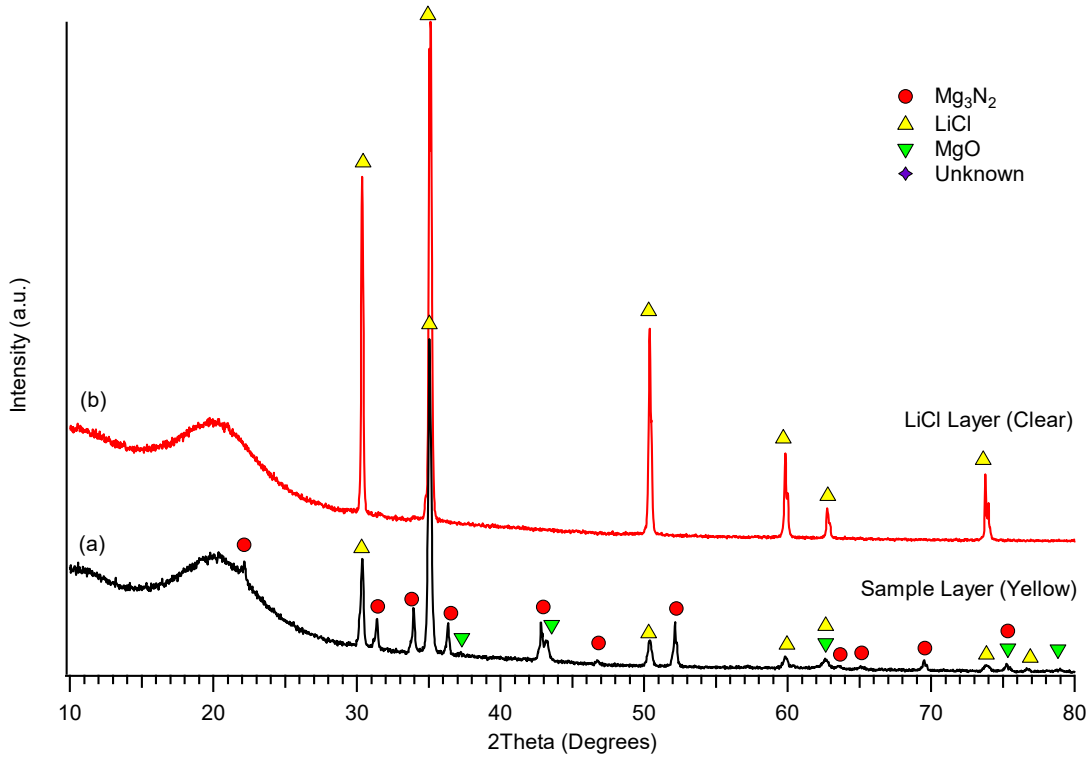

Figure 5.11: XRD analysis of THF-washed $Mg(NH_2)_2$ after heat treatment at 700 °C with a (a) yellow sample layer and a (b) clear sample layer.

5.2.2 Synthesis of MgNH

MgNH was synthesised to investigate the proposed imide-hydride decomposition reaction in Equation 5.2 to form Mg_3N_2. Furthermore, by using MgNH as a starting reagent instead of $Mg(NH_2)_2$, sample preparation for high-temperature measurements can be made without the risk of unknown phases forming from contaminated $Mg(NH_2)_2$ as previously seen in Figure 5.10. MgNH was prepared by mechanochemical synthesis (Equation 5.1a) following the method published by Hu et al. (2006a) using the starting reagents $Mg(NH_2)_2$ (laboratory synthesised; Section 5.2.1) and MgH_2 (Alfa-Aesar, 98%). The reagents were thoroughly mixed in a planetary ball-mill for 6 hours in a 1:1 molar ratio ($Mg(NH_2)_2$:MgH_2), and operated at 600 RPM with a BTP ratio of 60:1 BTP using 316 stainless-steel balls sized at 10 mm and 6 mm.

$$Mg(NH_2)_2 + MgH_2 \rightarrow 2MgNH + 2H_2 \qquad (5.1a)$$

Upon opening the ball-mill canisters inside the argon-atmosphere glovebox, the O_2 glovebox reading spiked up to 15 ppm, a reading that could be triggered erroneously by the release of hydrogen generated during milling, which is in agreement with Equation 5.1a.

X-ray diffraction analysis of as-synthesised MgNH after ball milling for 6 hours is shown in Figure 5.12. The crystal structures of $Mg(NH_2)_2$ (tetragonal) and MgNH (hexagonal) were absent after the ball-milling treatment as they transformed into an amorphous state during energetic ball milling (Hu et al. 2006a; Liang et al. 2010). However, the broad peaks located approximately at a 2θ angle of 41° and 59°, corresponded to a cubic phase of MgNH that was modelled by Rietveld refinement with the periclase MgO structure, similarly found by Dolci et al. (2010). Furthermore, the reaction was thought to be incomplete because of the presence of MgH_2 by XRD analysis. Therefore, the sample was further annealed at 200 °C using a closed volume that was evacuated at a pressure near vacuum for 17 hours (Figure 5.13b; —) and a further 18 hours (Figure 5.13c; —) under dynamic vacuum. The results in Figure 5.13 revealed that with increasing heat-treatment time, the intensity peaks for MgH_2 decrease while the MgNH peaks appear broader. Heat treatment of the sample under dynamic vacuum also had the

advantage of decomposing any residual $Mg(NH_2)_2$ to MgNH (Nakamori, Kitahara and Orimo 2004).

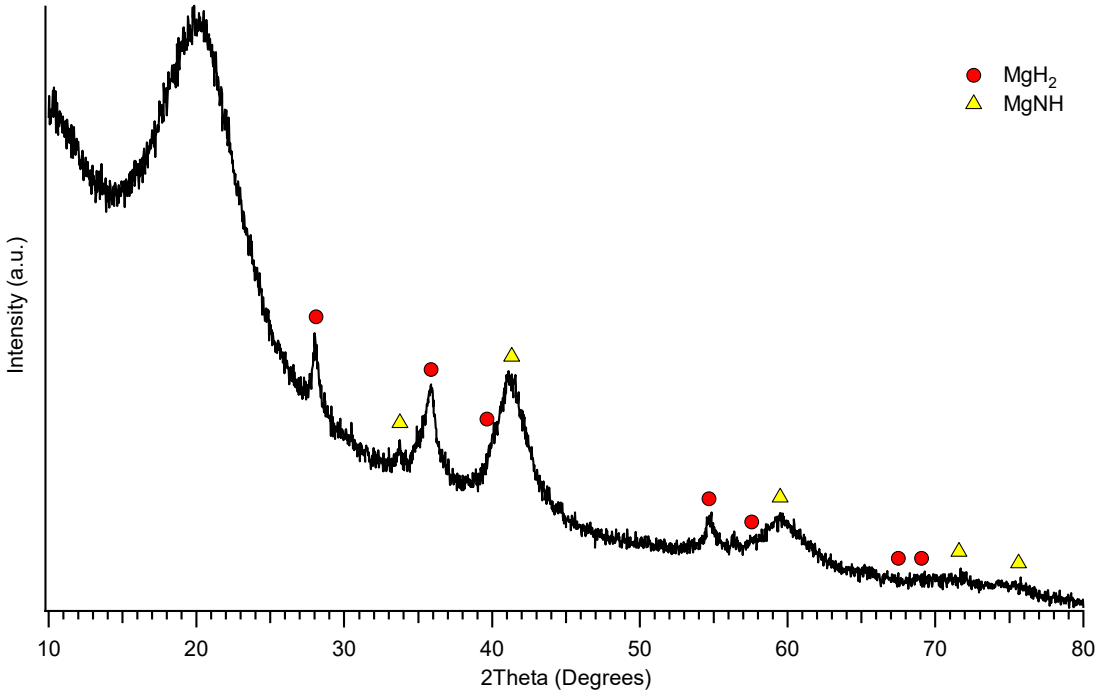

Figure 5.12: XRD analysis of $Mg(NH_2)_2$ + MgH_2 (1:1) after a milling time of 6 hours.

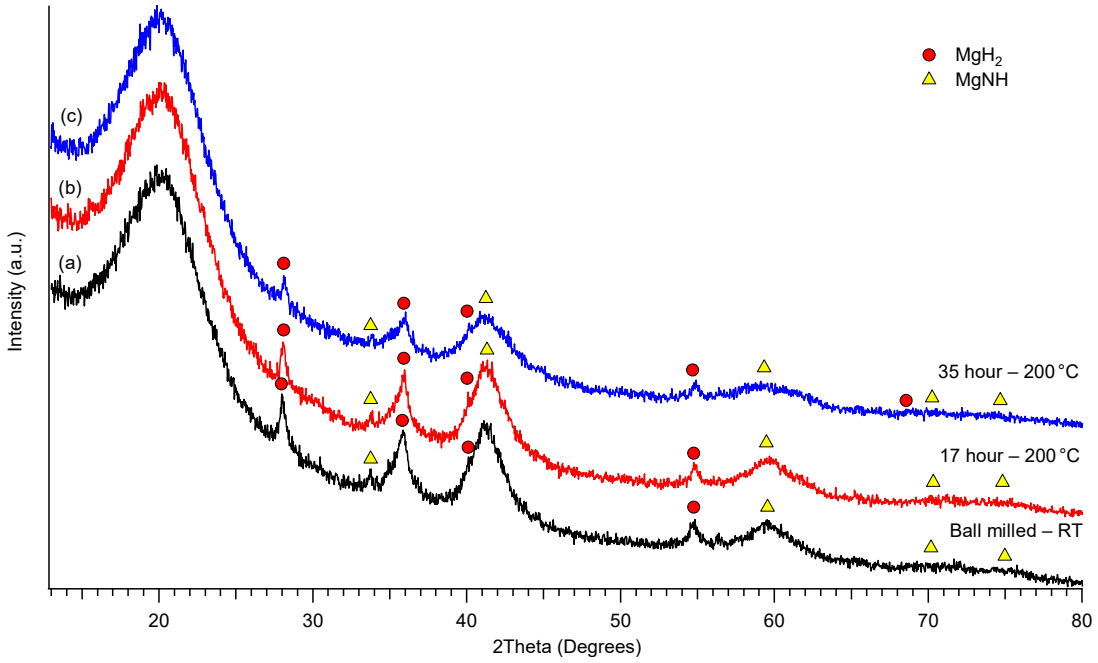

Figure 5.13: XRD analysis of $Mg(NH_2)_2$ + MgH_2 (1:1) after (b) heating at 200 °C for 17 hours and (c) a further 18 hours (35 hour total).

5.2.2.1 Temperature programmed desorption with mass spectrometry (TPD-MS)

Temperature programmed desorption analysis by Hino, Ichikawa, and Kojima (2010) revealed that pure MgNH decomposes to release ammonia at temperatures > 350 °C. The formation of Mg_3N_2 from pure MgNH can be expressed as follows:

$$MgNH \rightarrow \frac{1}{3}Mg_3N_2 + \frac{1}{3}NH_3 \qquad (5.6a)$$

TPD-MS analysis in Figure 5.14 revealed that the release of ammonia at 371 °C is consistent with the decomposition of MgNH according to Hino, Ichikawa, and Kojima (2010) and confirmed as-synthesised MgNH was pure. However, there was a considerable amount of hydrogen release at 260 °C and 343 °C. These hydrogen release peaks corresponded to the decomposition of residual MgH_2 from the synthesis of MgNH (Figure 5.13c). The release of hydrogen is also possible from a reaction between residual starting reagents $Mg(NH_2)_2$ and MgH_2 (Equation 5.1a). However, Nakamori, Kitahara, and Orimo (2004) reported that the decomposition of $Mg(NH_2)_2$ is likely to occur (at $T \approx 200$ °C) before it can react with MgH_2 to form MgNH and thus, releasing hydrogen.

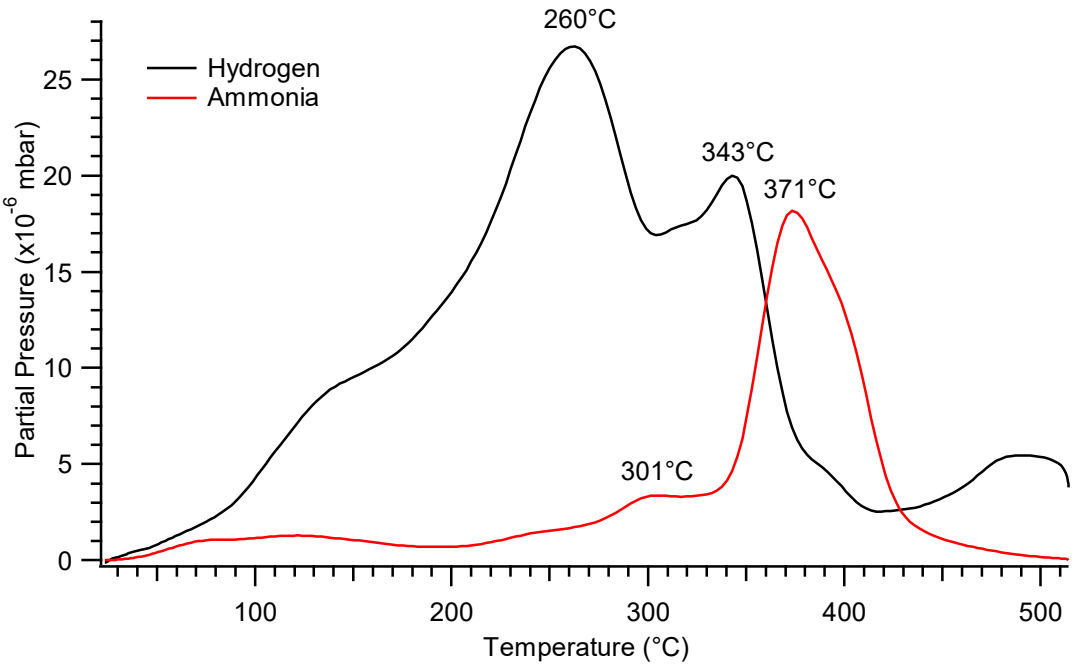

Figure 5.14: TPD-MS analysis of MgNH performed under dynamic vacuum in the temperature range of 25 – 520 °C, where the heating rate was 2 °C min^{-1}.

X-ray diffraction analysis of MgNH after the TPD-MS measurement was halted at 520 °C is shown in Figure 5.15. Rietveld refinement of the XRD pattern revealed that the final product phases were Mg_3N_2 and MgO in a 1:1 weighted ratio. Given that the decomposition events by TPD-MS analysis (Figure 5.14) were in agreement with literature and the oxidation of MgH_2 would have inhibited the release of hydrogen, oxygen contamination likely occurred after the TPD-MS measurement. Furthermore, the TC110 turbo vacuum pump (Scitek, Australia) of the mass spectrometer was not able to achieve a vacuum pressure below 1.2×10^{-3} bar. Therefore, after the TPD-MS measurement under dynamic vacuum, the sample was exposed to air from a leak in the sample cell that resulted in the oxidation of the sample observed by XRD analysis (Figure 5.15).

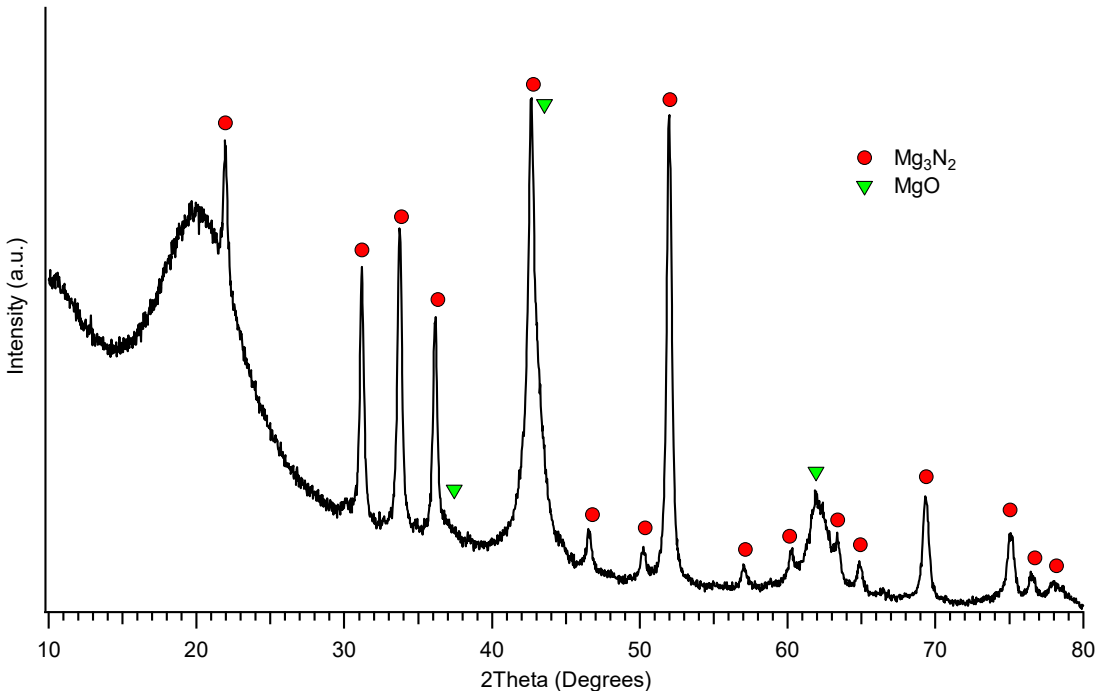

Figure 5.15: XRD analysis of MgNH after TPD measurement halted at 520 °C.

5.2.2.2 Fourier transform infra-red (FTIR) analysis

Fourier transform infra-red analysis was performed on MgNH (pressed in a KBr pellet) because of the overlapping XRD patterns of possible amides and imides with similar structure. The FTIR spectra in Figure 5.16 showed that the absorption bands at 3697 and 3488 cm^{-1} corresponded to the O–H stretching vibrations of hydroxyl groups present on the pellet surface due to moisture, where the absorption band at 1650 cm^{-1} was attributed to the bending vibration of water.

The strongest bands for Mg–O vibrations have appeared at 511, 470, 440 and 403 cm^{-1} due to atmospheric contaminants in the pellet, which is in agreement with the absorption bands found by Tamilselvi et al. (2013). The strongest absorption bands for MgNH have been reported by Linde and Juza (1974) to occur at 3360, 3251, 3199, 1560, 1430 and 808 cm^{-1}. However, the broad bands that correspond to moisture/water and MgO overlap most of the MgNH absorption bands. Therefore, no qualitative conclusions could be made from the FTIR spectra of as-synthesised MgNH.

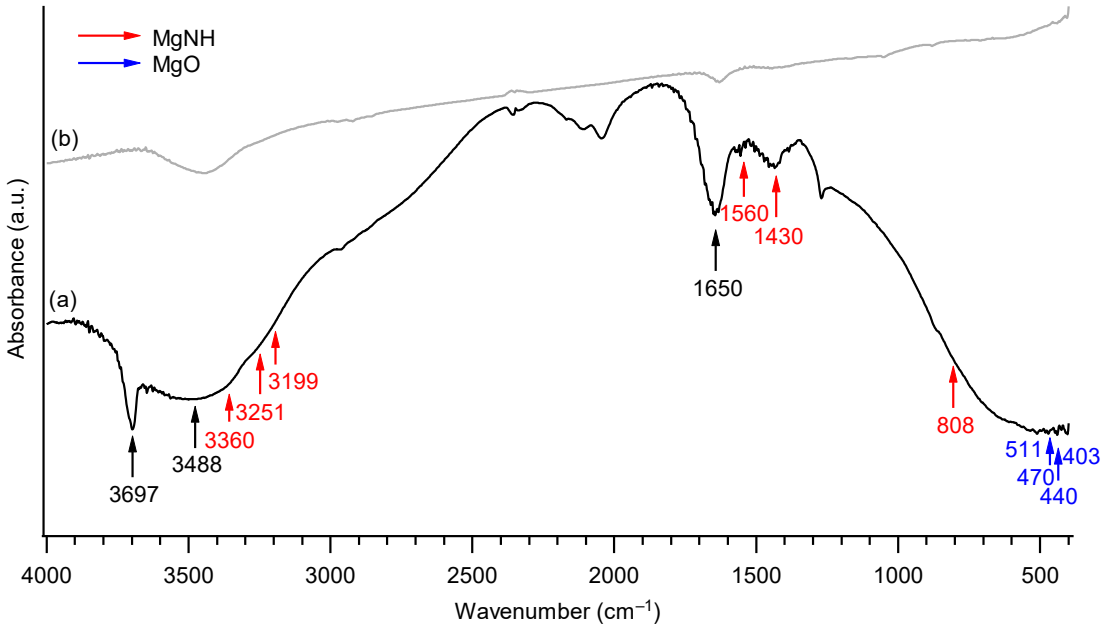

Figure 5.16: FTIR spectra of (a) MgNH and (b) blank KBr pellet.

5.2.3 MgNH + Mg_2FeH_6 (4:1)

5.2.3.1 Synthesis of Mg_2FeH_6

Mg_2FeH_6 was synthesised by Drew Sheppard (2013) at Curtin University (Australia). The starting reagents were MgH_2 (Alfa-Aesar, 98%) and Fe (Sigma-Aldrich, > 99.99%) that were thoroughly mixed in a planetary ball-mill for 3 hours in a 2:1 molar ratio (MgH_2:Fe). The planetary ball-mill was operated at 600 RPM with a BTP ratio of 30:1 using 316 stainless-steel balls sized at 10 mm. Mg_2FeH_6 has a hydrogen equilibrium pressure of ~11.3 bar at 400 °C and ~28.5 bar at 450 °C (Bogdanović et al. 2002). Based on these equilibrium pressures, the ball-milled sample (Mg_2FeH_6) was cycled between 400 °C and 450 °C (absorption and

desorption, respectively) using a 2 hour cycle time with a system hydrogen pressure of ~15 bar. This hydriding-cycle was repeated five times, where on the fifth absorption cycle; the hydrogen pressure was increased to ~98 bar and held for 17 hours.

X-ray diffraction analysis and Rietveld refinement revealed that the sample synthesis was incomplete and contained ~41 wt% of MgH_2 and ~43 wt% of Mg_2FeH_6, which can be found in Appendix A (Figure A.8). Therefore, the cycled Mg_2FeH_6 was further ball milled for 1 hour at 600 RPM, then hydrogenated with ~79 bar of H_2 at 460 °C for 42 hours. The sample was allowed to cool to room temperature before it was evacuated and hydrogenated with ~110 bar of H_2 at 508 °C for 24 hours. XRD analysis in Figure 5.17 and Rietveld refinement revealed that the sample yield was acceptable with 81.3 wt% of Mg_2FeH_6.

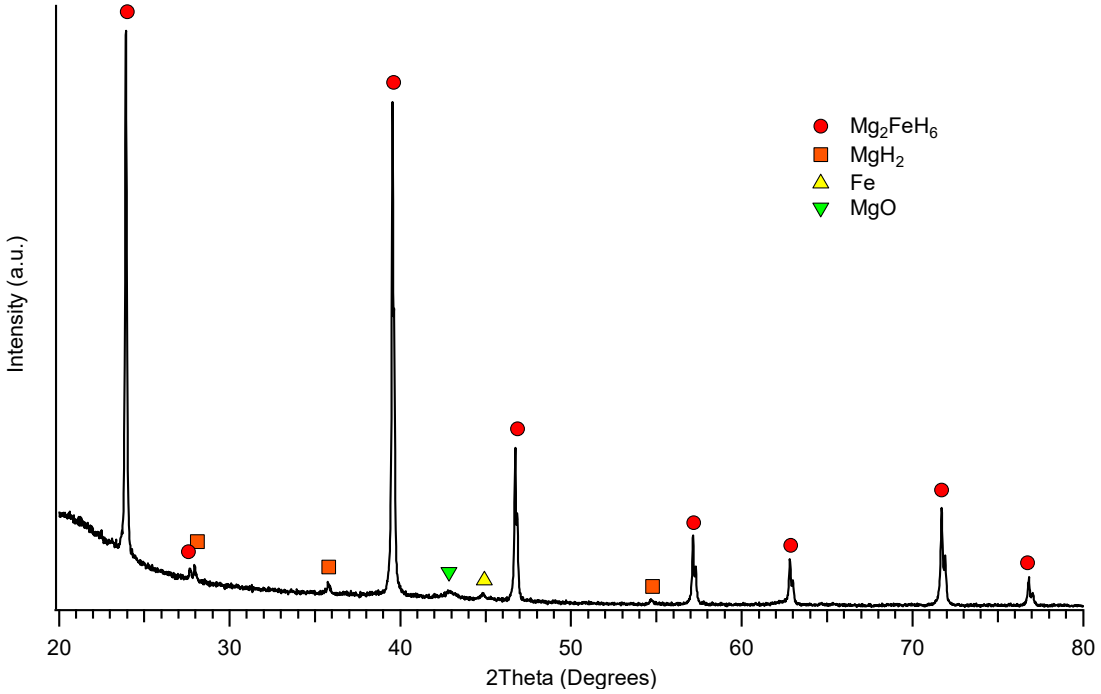

Figure 5.17: XRD analysis of Mg_2FeH_6 after further cycling at 508 °C under a hydrogen pressure of 110 bar by Drew Sheppard (2013).

5.2.3.2 Preparation of MgNH + Mg_2FeH_6 (4:1)

Based on the reaction in Equation 5.3, MgNH + Mg_2FeH_6 (4:1) was prepared by ball-milling using the starting reagents MgNH (laboratory synthesised; Section 5.2.2) and Mg_2FeH_6 (laboratory synthesised; Section 5.2.3.1). The reagents were

thoroughly mixed in a planetary ball-mill for 4 hours operating at 400 RPM with a BTP ratio of 31:1 using 316 stainless-steel balls sized at 10 mm and 6 mm. The ball-milled samples were packed in 0.5 mm borosilicate capillaries with polyimide/graphite ferrules using a custom mount in preparation for synchrotron X-ray diffraction (SXRD).

5.2.3.3 *In situ* synchrotron X-ray diffraction (SXRD) analysis

In situ SXRD provides the fastest measurement to determine whether a system has the potential for thermal energy storage. The *in situ* SXRD analysis of MgNH + Mg_2FeH_6 (4:1) shown in Figure 5.18 was performed under dynamic vacuum with a heating rate of 5 °C min^{-1} in the temperature range of 100 – 500 °C. The presence of MgH_2 (2) in the starting phase at 100 °C suggests that the starting reagent of as-synthesised MgNH was incomplete and possibly contained a residual mixture of $Mg(NH_2)_2$ and MgH_2. Furthermore, $Mg(NH_2)_2$ has been known to become X-ray amorphous after ball milling (Juza 1964; Liu et al. 2007). This amorphous phase explains the absence of $Mg(NH_2)_2$ and presence of MgH_2 (2) in the starting phase at 100 °C in Figure 5.18. A phase change was observed starting at 300 °C from the formation of Mg_3N_2 (3) with low intensity peaks, but requires temperatures ≤ 500 °C to observe a complete decomposition of the starting materials, Mg_2FeH_6 (1), MgH_2 (2) and possibly amorphous $Mg(NH_2)_2$. An unknown peak (6) identified at the start of the measurement, appeared sharper between 200 °C and 250 °C, but remained constant throughout the measurement showing little interaction with the other phases. The peak intensity of MgO (4) increases as it becomes more crystalline between 200 °C and 500 °C. The relatively low intensity suggests that it originated from the starting reagents used.

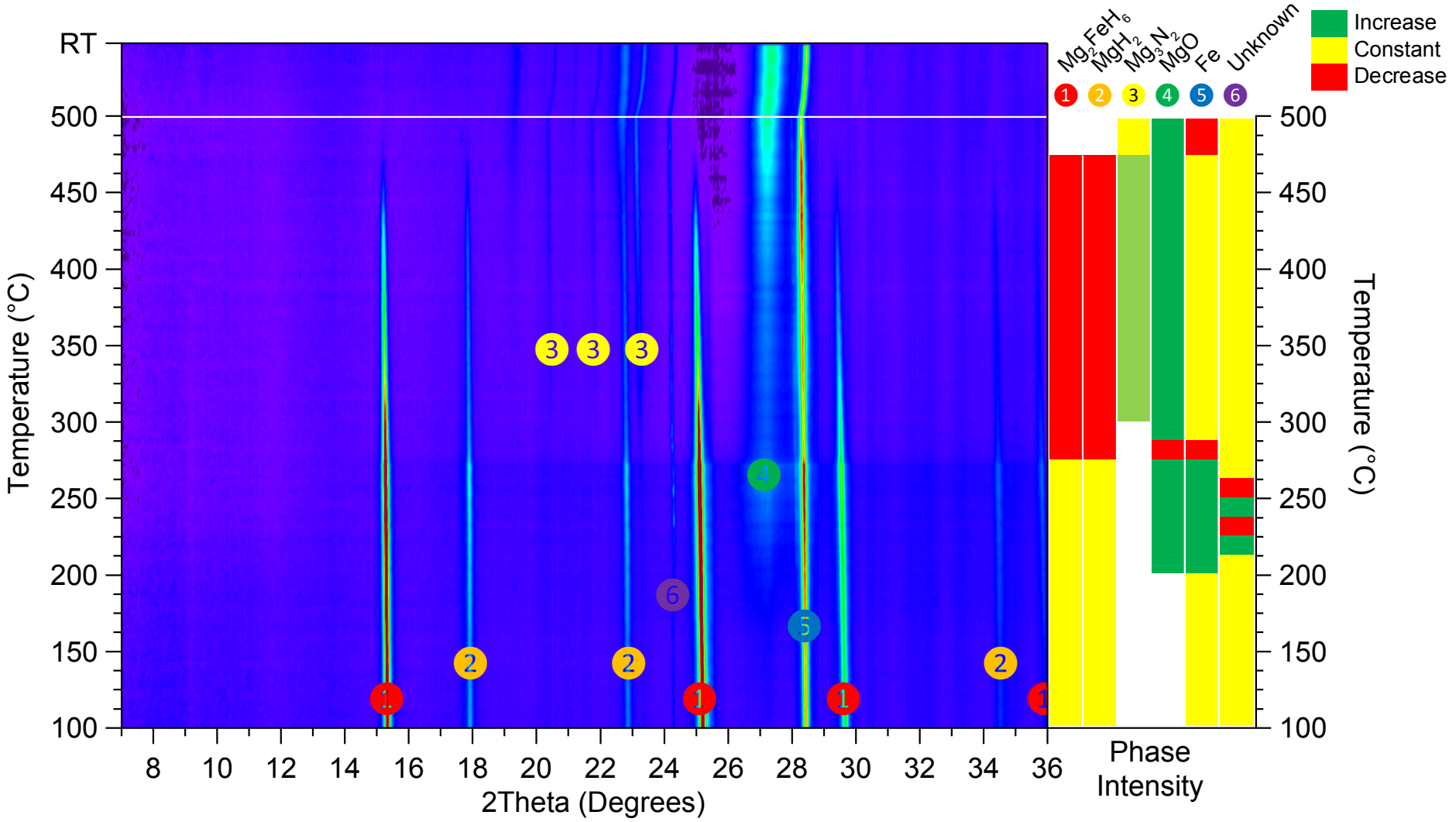

Figure 5.18: *In situ* SXRD analysis (λ = 1.00036 Å) of MgNH + Mg_2FeH_6 (4:1) under dynamic vacuum with phase identification.

To observe the desorption properties of the sample under different conditions, Figure 5.19 shows the *in situ* SXRD analysis of MgNH + Mg_2FeH_6 (4:1) under a hydrogen back pressure of 1.4 bar. The heating rate was 5 °C min^{-1} in the temperature range of 100 – 500 °C before the sample was allowed to cool to room temperature. It appears that the introduction of hydrogen in the system showed little difference to the identification of the final phases as seen in Figure 5.18, except for the appearance of MgO (4), which suggests a possible leak in the sample capillary. However, it is unusual that the MgH_2 phase (2) decomposes at a higher temperature than Mg_2FeH_6 (1), given that Mg_2FeH_6 is more stable (Felderhoff and Bogdanović 2009). Due to the identification of MgO (4), if the sample has been exposed to air, an oxide layer may have formed on the surface of MgH_2 (2), creating a kinetic barrier that inhibited the release of hydrogen and explains the higher decomposition temperature of MgH_2 (2).

5.2.3.4 Mg_3N_2 + Fe + H_2 (2:1:5)

In situ SXRD analysis revealed that the formation of Mg_3N_2 observed in the temperature range 400 – 500 °C (Figure 5.19), suggests that the reaction pathway follows Equation 5.3. Hence, the hydrogenation reaction was investigated to test the reversibility of the system for thermal energy storage. A potential absorption reaction is the reverse of Equation 5.3 and can be expressed as follows:

$$2Mg_3N_2 + Fe + 5H_2 \rightarrow 4MgNH + Mg_2FeH_6 \qquad (5.7)$$

Mg_3N_2 and Fe in a 2:1 molar ratio was prepared by ball-milling using the starting reagents Mg_3N_2 (Alfar-Aesar, 99.6%) and Fe (Sigma-Aldrich, > 99.99%). The planetary ball-mill operated for 4 hours at 400 RPM with a BTP ratio of 30:1 BTP using 316 stainless-steel balls sized at 10 mm and 6 mm. Given that Mg_3N_2 and Fe are commercially available, this mixture avoids the risk of oxygen contamination that occurs with the synthesis of MgNH (metathesis reaction followed by a THF wash).

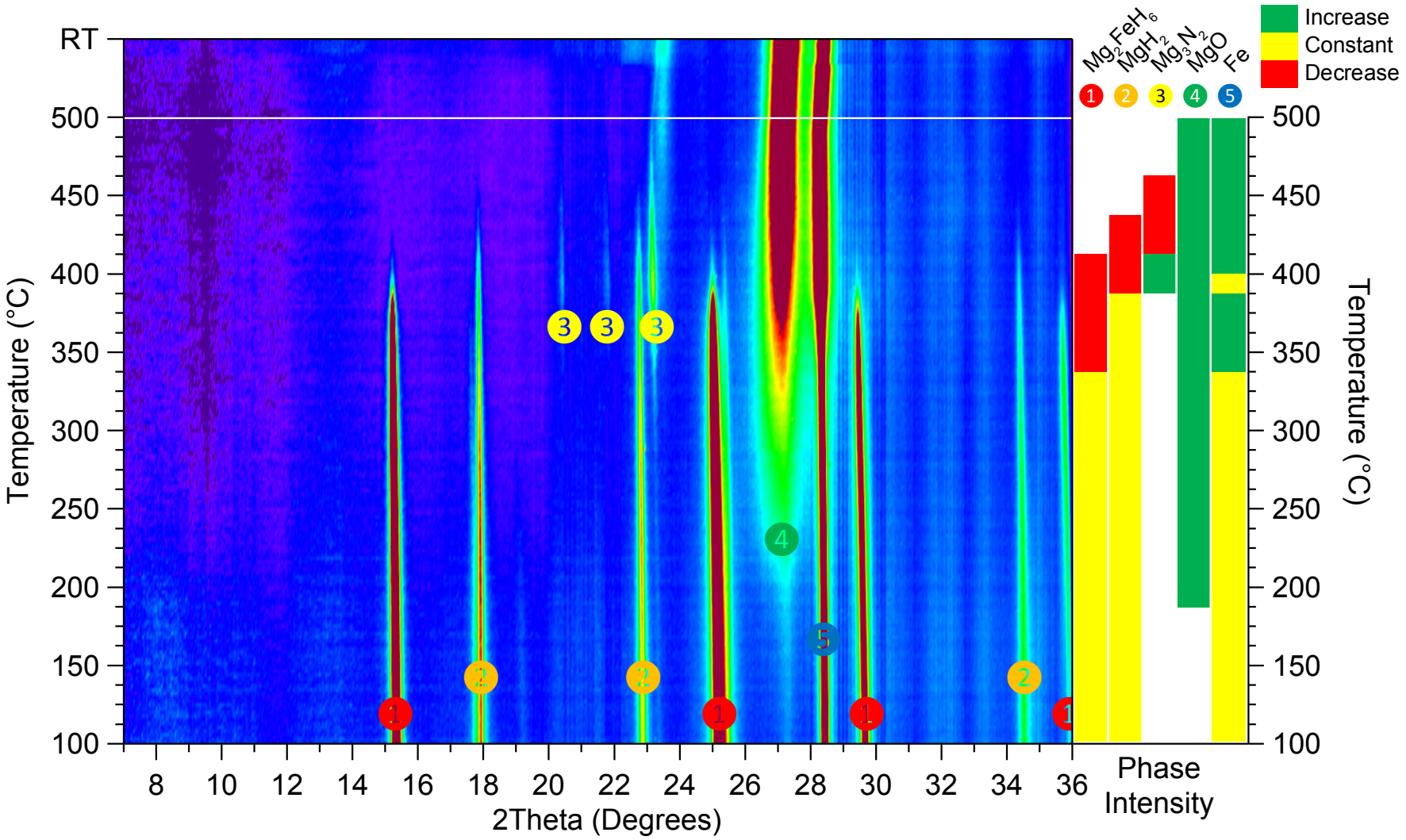

Figure 5.19: *In situ* SXRD analysis (λ = 1.00036 Å) of MgNH + Mg_2FeH_6 (4:1) under a H_2 back pressure of 1.4 bar with phase identification.

Using the maximum hydrogen pressure allowed from the storage bottle, a hydrogen pressure of ~80 bar was added to Mg_3N_2 + Fe (2:1) at 400 °C. XRD analysis after a hydrogen pressure of 80 bar in Figure 5.20a shows that the starting reagents remained unchanged. Therefore, using a high pressure apparatus utilising a low temperature hydride store ($TiMn_{1.5}$ alloy), a hydrogen pressure of 175 bar was achieved and added to Mg_3N_2 + Fe (2:1) at 400 °C. However, XRD analysis after a hydrogen pressure of 175 bar in Figure 5.20b revealed that the system does not absorb any hydrogen to form MgNH and/or Mg_2FeH_6 under these applied conditions.

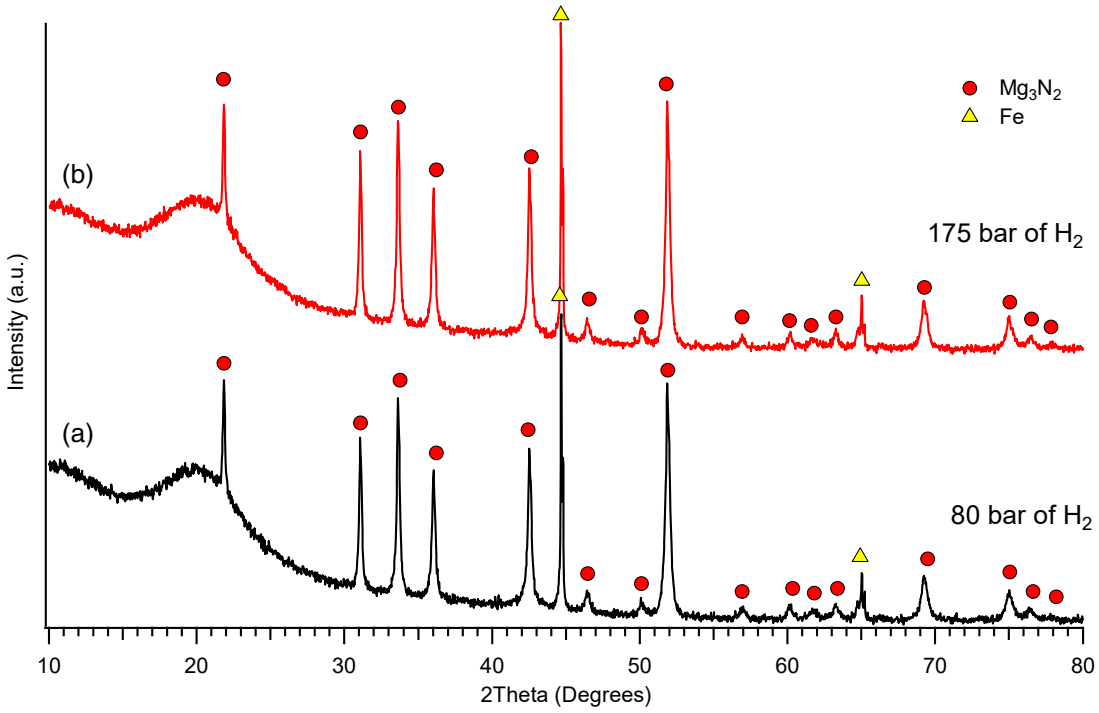

Figure 5.20: XRD analysis of the hydrogenation of Mg_3N_2 + Fe (2:1) at 400 °C under a hydrogen pressure of (a) 80 bar and (b) 175 bar.

5.2.3.5 Discussion

Although as-synthesised MgNH was incomplete, *in situ* XRD analysis (Figure 5.18 and 5.19) showed that the formation of Mg_3N_2 began at 300 °C. Therefore, a temperature of 400 °C was chosen for the hydrogenation of Mg_3N_2 + Fe (2:1). However, the nitride-iron system may be irreversible as the anticipated products, MgNH and Mg_2FeH_6, were not observed at 400 °C with hydrogen pressures of 80 – 175 bar (Figure 5.20). This result is in agreement with the thermodynamic analysis done by Hu et al. (2006a) who reported that the overall reaction in

Equation 5.8 is mildly endothermic (ΔH_{des} ≈ 3.5 kJ (mol H_2)$^{-1}$), indicating that Mg_3N_2 alone will not hydride to $Mg(NH_2)_2$ or MgNH under appropriate hydrogenation conditions.

$$Mg(NH_2)_2 + 2MgH_2 \rightarrow Mg_3N_2 + 4H_2 \quad (5.8)$$

However, Dolotko, Paulson, and Pecharsky (2010) observed that the hydrogenation of Mg_3N_2 will occur with the addition of NaH at a hydrogen pressure of 195 bar at 395 °C, where Mg_3N_2 and NaH hydrogenated to form MgNH and $NaMgH_3$ as follows:

$$Mg_3N_2 + NaH + 2H_2 \rightarrow 2MgNH + NaMgH_3 \quad (5.9)$$

where the imide-hydride reaction in Equation 5.9 is investigated in Chapter 9 (Na–Mg–N–H).

Although the addition of iron does not improve the thermodynamics of Mg_3N_2 with a hydrogen pressure of 80 – 175 bar, the addition of other compounds can improve the reversibility (e.g. NaH with 200 bar of hydrogen at 395 °C) and requires further investigation. In summary, the MgNH + Mg_2FeH_6 (4:1) system is not suitable for thermal energy storage due to the thermodynamic limitations of the reverse reaction.

5.3 Conclusion

This chapter had three main aims. First, to investigate an alternative synthesis method for $Mg(NH_2)_2$ and MgNH that did not require the handling of ammonia gas. Second, to characterise the decomposition process of $Mg(NH_2)_2$ and MgNH. Third, to investigate the MgNH + Mg_2FeH_6 (4:1) system as the higher thermodynamic stability of Mg_2FeH_6 compared to MgH_2, predicted an operation temperature that should be higher than MgNH + MgH_2 (1:1), suitable for thermal storage applications.

To avoid the use of dangerous ammonia gas, a synthesis method of $Mg(NH_2)_2$ was performed by THF-washing of the mechanochemical reaction between $LiNH_2$

and $MgCl_2$. XRD analysis revealed that the synthesis method was a success; however, some batches were severely contaminated by oxygen with the appearance of MgO phases. TPPA of THF-washed $Mg(NH_2)_2$ revealed an increasing volume change between 200 °C and 400 °C, accompanied by a yellow colour change. This change in volume and colour are associated with the release of ammonia from the decomposition of $Mg(NH_2)_2$ at 335 °C as confirmed by TPD-MS analysis. TPD-MS analysis also revealed another ammonia release event at 430 °C that was likely associated with the decomposition of MgNH as confirmed by XRD analysis, where a final product of Mg_3N_2 was observed.

Oxygen contamination was frequently observed in samples washed with THF. Therefore, unwashed samples were investigated to determine the source of oxygen contamination. TPD-MS analysis of unwashed $Mg(NH_2)_2$ revealed that the overall release of ammonia occurred at a lower temperature than THF-washed $Mg(NH_2)_2$; peaking at a temperature of 313 °C and 335 °C for unwashed and THF-washed $Mg(NH_2)_2$, respectively. XRD analysis of THF-washed $Mg(NH_2)_2$ revealed that at temperatures $\leq$ 470 °C, the sample contained a final product of Mg_3N_2 and residual LiCl as expected. Unusually, TPD-MS analysis revealed that the presence of residual LiCl influenced the decomposition temperature of MgNH such that it was decreased from 430 °C to 350 °C. It was also concluded that the THF solvent was not contaminated and any contamination seen in previous samples was due to poor handling during experiments and/or the preparation of XRD measurements.

MgNH was synthesised by mechanochemical ball milling $Mg(NH_2)_2$ and MgH_2, and heat treated at 200 °C under dynamic vacuum to decompose residual $Mg(NH_2)_2$. In two batches, the formation of a cubic MgNH structure was consistently identified by XRD analysis and modelled after cubic MgO by Rietveld refinement. However, due to the amorphous phase of $Mg(NH_2)_2$ after ball milling, the presence of MgH_2 by XRD analysis also revealed that the initial synthesis of MgNH was incomplete. TPD-MS analysis revealed that the release of ammonia at 371 °C corresponded to the decomposition of MgNH to Mg_3N_2 as confirmed by XRD analysis of the final product. The release of hydrogen observed by TPD-MS analysis was due to the decomposition of residual MgH_2 from the synthesis of

MgNH, releasing hydrogen at a temperature between 200 °C and 400 °C (Paskevicius, Sheppard and Buckley 2010). This observation suggests that the initial synthesis of MgNH was incomplete under the applied conditions.

Having characterised MgNH, the substitution of Mg_2FeH_6 for MgH_2 was investigated to improve the operating temperature of the imide-hydride to nitride reaction in the Mg–N–H system. Although as-synthesised MgNH was incomplete, *in situ* SXRD revealed that the formation of Mg_3N_2 started at 300 °C and the decomposition of the starting reagents (Mg_2FeH_6, MgH_2 and possibly amorphous $Mg(NH_2)_2$) completed by 500 °C. The hydrogenation of Mg_3N_2 with Fe metal was investigated to study the reverse reaction of MgNH + Mg_2FeH_6 (4:1). However, the reaction was not observed at temperatures $\leq$ 400 °C and at hydrogen pressures of 80 – 175 bar. Therefore, this system may not be suitable for thermal energy storage, but the characterisation of $Mg(NH_2)_2$ and MgNH will be beneficial in the investigation of mixed amide/imide systems.

CHAPTER 6: CALCIUM-BASED SYSTEMS

6.1 Introduction

Calcium belongs in the same group on the periodic table as magnesium and the decomposition of its amide ($Ca(NH_2)_2$) to imide (CaNH) starts at ~60 °C and peaks at a temperature of 300 °C (Hino et al. 2005; Equation 6.1), whereas the decomposition of magnesium amide ($Mg(NH_2)_2$) starts at 200 °C (Hu et al. 2006a). Though $Ca(NH_2)_2$ has been shown to be less stable than $Mg(NH_2)_2$, the opposite is true for the imides (Hino et al. 2005).

$$Ca(NH_2)_2 \rightarrow CaNH + NH_3 \quad (6.1)$$

A reversible imide-hydride reaction has been reported involving CaNH and CaH_2 to form calcium nitride hydride (Ca_2NH) with a theoretical hydrogen capacity of 2.07 wt% (Hino et al. 2005; Equation 6.2). Chen et al. (2002) reported that the reaction in Equation 6.2 could reversibly store ~1.9 wt% of H_2 with an absorption and desorption equilibrium plateau pressure of ~0.3 bar and ~0.1 bar, respectively, at 500 °C. Ca_2NH was also reported to have fast kinetics with a substantial amount of hydrogen absorbed under a hydrogen pressure of 30 bar within 10 minutes. Since the reaction in Equation 6.2 is reversible, occurs at high temperatures and uses low-cost components, the hydrogenation of Ca_2NH in the Ca–N–H system was investigated at temperatures suitable for thermal energy storage.

$$CaNH + CaH_2 \leftrightarrow Ca_2NH + H_2 \quad (6.2)$$

Based on the substitution of magnesium hydride (MgH_2) with the more stable magnesium iron hydride (Mg_2FeH_6) in the imide-hydride reaction of the Mg–N–H system (Chapter 5: Section 5.2.3; Equation 5.3a). The reaction between CaNH and calcium iron hydride (Ca_2FeH_6) in a 2:1 molar ratio was investigated with an overall reaction proposed in Equation 6.3. The substitution of Ca_2FeH_6 for CaH_2 in Equation 6.2 was predicted to occur at a higher temperature than CaNH–CaH_2

due to the higher stability of Ca_2FeH_6 (Hagemann et al. 2011). The substitution of Ca_2FeH_6 also increases the theoretical hydrogen capacity to 2.40 wt%. Furthermore, this system has not been investigated for its specific use in high temperature thermal energy storage.

$$4MgNH + Mg_2FeH_6 \rightarrow 2Mg_3N_2 + Fe + 5H_2 \quad (5.3a)$$

$$2CaNH + Ca_2FeH_6 \rightarrow 2Ca_2NH + Fe + 3H_2 \quad (6.3)$$

6.2 Results

6.2.1 Synthesis of $Ca(NH_2)_2$ and CaNH

6.2.1.1 Synthesis of $Ca(NH_2)_2$ by planetary ball milling

Based on the mechanochemical synthesis of $Mg(NH_2)_2$, $Ca(NH_2)_2$ was synthesised via a metathesis reaction (Equation 6.4) between lithium amide ($LiNH_2$) and calcium chloride ($CaCl_2$), followed by a tetrahydrofuran (THF) wash to dissolve the by-product salts (LiCl). The starting reagents were $LiNH_2$ (Sigma-Aldrich, 95%) and $CaCl_2$ (Sigma-Aldrich, ≥ 96.0%).

$$2LiNH_2 + CaCl_2 \rightarrow Ca(NH_2)_2 + 2LiCl \quad (6.4)$$

The mass of starting reagents was calculated in Table 6.1 to theoretically yield a 5 g batch of $Ca(NH_2)_2$ based on the reaction in Equation 6.4. The reagents were thoroughly mixed in a shaker-mixer at 160 RPM for 4 hours with a BTP ratio of 30:1 using 316 stainless-steel balls sized at 12.7 mm and 7.9 mm.

Table 6.1: Mass calculations for the starting reagents required to theoreotically yield a 5 g batch of calcium amide, where N = no. of moles, M = molar mass, M_t = total molar mass and m = sample mass.

Molecule	N	M (g mol^{-1})	M_t (g mol^{-1})	m (g)
$LiNH_2$	2	22.97	45.93	8.1850
$CaCl_2$	1	110.98	110.98	7.6950
$Ca(NH_2)_2$	1	72.11	72.11	5.0000
LiCl	2	42.39	84.78	5.8787

X-ray diffraction analysis after 4 hours of ball milling (Figure 6.1a) showed that the $CaCl_2$ phase was present in the sample, suggesting that an incomplete metathesis reaction occurred. Therefore, the sample was mixed again in the shaker-mixer for a further 8 hours (12 hour total). XRD analysis in Figure 6.1b showed that after a total milling time of 12 hours, the $CaCl_2$ phase was consumed with the formation of a LiCl phase as observed by the increase in peak intensity at a 2θ angle of ~30°. This observation confirms the metathesis reaction pathway in Equation 6.4 after a total milling time of 12 hours. However, a cubic phase of CaNH was formed instead of $Ca(NH_2)_2$ due to a combination of the low stability of $Ca(NH_2)_2$ and the heat generated during the ball-milling according to this reaction (Equation 6.5):

$$Ca(NH_2)_2 \rightarrow CaNH + NH_3 \qquad (6.5)$$

where the XRD patterns for cubic CaNH and LiCl are similar such that they overlap at the same peak positions in Figure 6.1b. Residual products ($LiNH_2$ and LiCl) were identified by XRD analysis (Figure 6.1b) that suggest further milling was required to complete the metathesis reaction pathway. However, since the sample was no longer $Ca(NH_2)_2$, no further milling was performed.

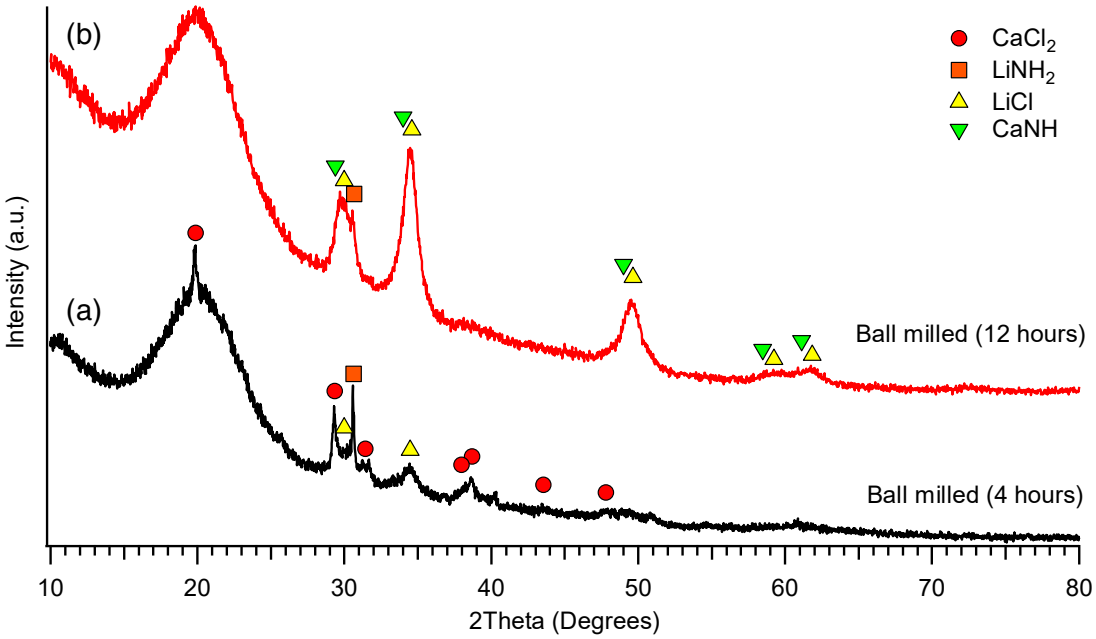

Figure 6.1: XRD analysis of the metathesis reaction between $LiNH_2$ and $CaCl_2$ in a 2:1 molar ratio after a total milling time of (a) 4 hours and (b) 12 hours.

6.2.1.2 Synthesis of $Ca(NH_2)_2$ by cryogenic impact milling

To avoid the formation of cubic CaNH from the heat generated in the shaker-mixer, $Ca(NH_2)_2$ was synthesised via cryogenic impact milling. This method greatly reduces the milling temperature by using liquid nitrogen to prevent the decomposition of $Ca(NH_2)_2$ during the milling process. $LiNH_2$ and $CaCl_2$ in a 2:1 molar ratio was loaded into grinding vials with a total sample mass of 1 g in an argon-atmosphere. The grinding vials were attached to the cryogenic mill at room temperature and cooled by liquid nitrogen. The milling parameters were 15 two-minute cycles with 10 impacts per second and a one-minute pause interval to allow the sample to cool down.

X-ray diffraction analysis after cryogenic milling $LiNH_2$ and $CaCl_2$ in a 2:1 molar ratio (for 1 hour) showed severe oxygen contamination, which can be viewed in Appendix A (Figure A.9). The grinding cylinder that was typically used for cryogenic milling had problems with the steel caps threaded with Teflon tape to form an air tight seal during the synthesis process. Hence, the formation of calcium chloride hydroxide, lithium hydroxide, lithium chlorate and calcium nitrate hydrate were observed by XRD analysis (Figure A.9). Furthermore, the overlapping XRD patterns (CaNH and LiCl) make it difficult to conclusively determine the successful synthesis of $Ca(NH_2)_2$ from the quantity (wt%) of LiCl. Therefore, this synthesis method was not pursued any further because of the contamination issues observed.

6.2.1.3 Tetrahydrofuran (THF) washing of CaNH

Using the ball-milled batch (12 hours) of $LiNH_2$ and $CaCl_2$ in a 2:1 molar ratio that resulted in the formation of cubic CaNH in Section 6.2.1.1 (Figure 6.1b), the LiCl by-product was washed multiple times using a THF solvent. Given the solubility of LiCl in THF (1.74 g L^{-1}) and the molar mass values from Table 6.1, approximately 40 mL of THF in 3.22 g of ball-milled sample was calculated to completely dissolve LiCl (~54 wt%) in a single wash. The THF-washing procedure (detailed in Chapter 2: Section 2.1.4) was used to remove the by-product chloride salts from CaNH, and after the first washing and centrifuge cycle, most of the THF was decanted with the residual evaporated in the small

antechamber for 50 minutes under vacuum. The second wash was evacuated for 38 minutes, the third wash for 15 minutes and the fourth and final wash was evacuated overnight to completely evaporate the THF.

In the synthesis of $Mg(NH_2)_2$ in Chapter 5: Section 5.2.1, the THF-washing method was often met with oxygen contamination. The source of oxygen contamination from previously contaminated samples was either due to the poor handling of the samples (during XRD measurements) or from the THF solvent itself. The contamination of THF is possible as it was frequently transferred between the inflammable storage cabinet and the argon-atmosphere glovebox. To verify the source of oxygen contamination, XRD analysis was performed on THF-washed (Figure 6.2a; —) and unwashed (Figure 6.2b; —) samples of cubic CaNH. Figure 6.2 showed that no oxygen contamination occurred in THF-washed CaNH; therefore, the source of oxygen contamination was not from the THF solvent. Although the XRD patterns for CaNH and LiCl overlap in Figure 6.2, the strongest peak of LiCl, present at a 2θ angle of ~30°, substantially reduced in peak intensity after the third THF wash cycle. Therefore, this reduction showed that the THF-washing method was sufficient and that residual LiCl is expected.

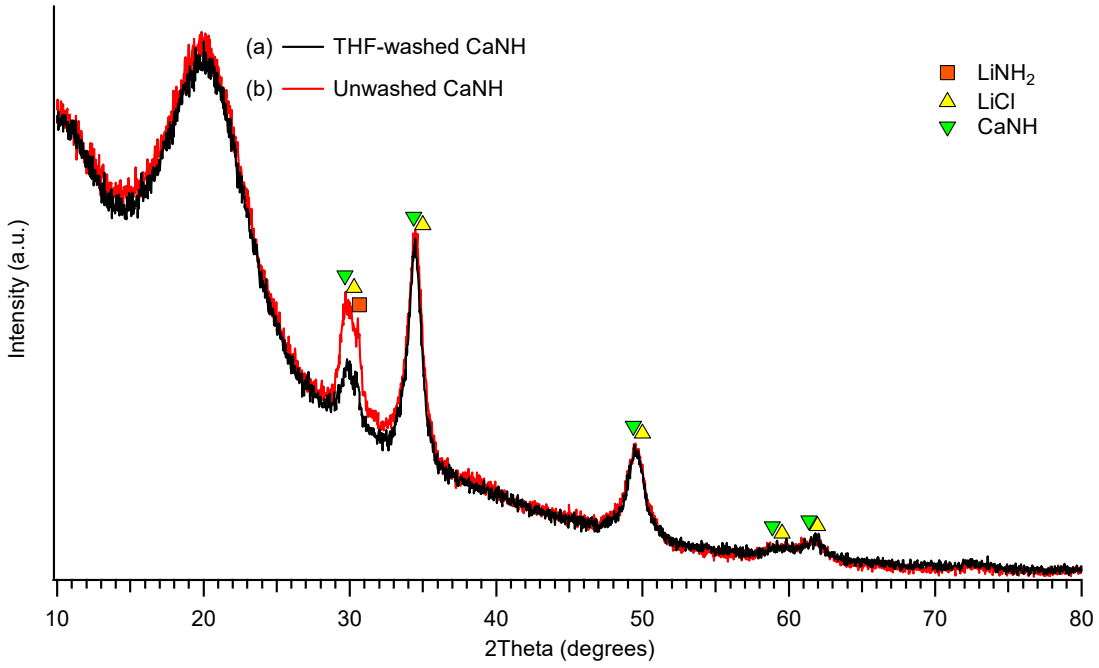

Figure 6.2: XRD analysis of (a) THF-washed CaNH and (b) unwashed CaNH.

6.2.1.4 Fourier transform infra-red (FTIR) analysis of CaNH

X-ray diffraction analysis revealed that the LiCl and CaNH phases have overlapping peak positions. Therefore, Fourier transform infra-red (FTIR) analysis of CaNH was performed to identify the imide (N–H stretching vibration) by comparing with the strongest known bands for CaNH and LiCl at 3183 cm^{-1} and 2854 cm^{-1}, respectively (Linde and Juza 1974; Hanhong Scientific 2017). However, given the high level of contamination from the absorption of moisture/air in the KBr pellet and the identification of unknown bands, FTIR analysis of THF-washed CaNH and unwashed CaNH was inconclusive and can be found in Appendix A: Figure A.10 and Figure A.11.

6.2.1.5 Synthesis of CaNH

CaNH can be prepared by thermal decomposition of calcium amide at temperatures of 300 – 400 °C as follows (Hino et al. 2005):

$$Ca(NH_2)_2 \rightarrow CaNH + NH_3 \qquad 6.1a$$

Although the formation of cubic CaNH had already occurred after 12 hours of ball milling, THF-washed CaNH (in Figure 6.2b) was heat treated at 366 °C under dynamic vacuum for 13 hours to purify and crystallise the imide phase. XRD analysis after the heat treatment and Rietveld refinement revealed that the cubic CaNH phase (~77 wt%) co-existed with crystalline LiCl (~11 wt%) such that the patterns overlap each other (Figure 6.3). However, the peaks that correspond to LiCl was positioned at a slightly higher 2θ angle compared to cubic CaNH. Because the THF solvent did not completely wash residual LiCl, it may have reacted with CaNH or $Ca(NH_2)_2$ to form an unknown lithium calcium amide/imide halide compound, represented by the unknown peaks (✦) in Figure 6.3. The appearance of CaO (~12 wt%) in relatively low amounts (Figure 6.3), suggest that some expected oxygen contamination occurred during the multiple THF-washing steps.

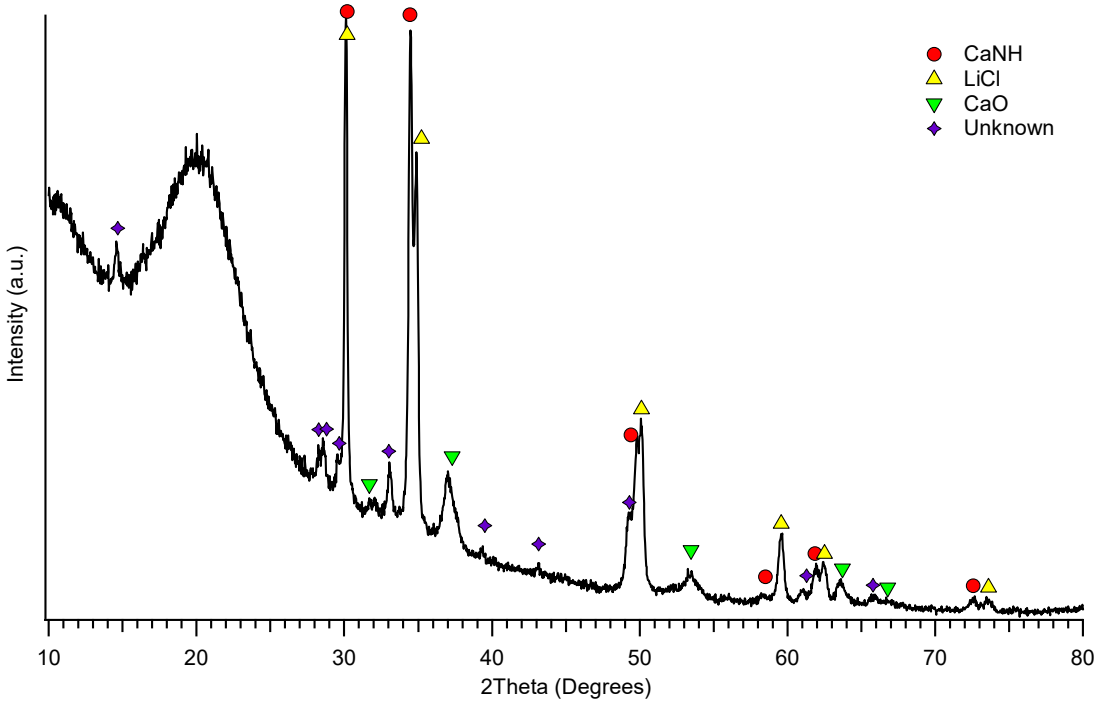

Figure 6.3: XRD analysis of THF-washed CaNH after heat treating at 366 °C for 13 hours.

6.2.2 Synthesis of CaH_2

Calcium hydride was synthesised by following the procedure from Bulanov, Troshin, and Balabanov (2004). Approximately 5 g of calcium metal granules (Sigma-Aldrich, 99%) was added to a 316 stainless-steel reactor (~15 cm^3). The evacuated reactor was heated to 360 °C in a closed system for 0.5 hours. A hydrogen pressure of 10 bar was initially added to the reactor and ramped up to 500 °C. Whenever the pressure dropped to ~0 bar, the reactor was topped up with no more than 5 bar of hydrogen, this process took multiple additions until no more absorption was observed (i.e. a zero pressure change). Because the absorption of hydrogen by calcium is highly exothermic, hydrogen was added in 5 bar increments to limit the sample from self-heating. Furthermore, this limitation assured that the 316 stainless-steel reactor remained within operational temperature limits (< 537 °C) to avoid permanent damage to the stainless-steel components.

X-ray diffraction analysis and Rietveld refinement of as-synthesised CaH_2 (Figure 6.4) revealed that this sample contained a mixture of CaH_2 (93 wt%) and CaO (7 wt%). The low level of oxygen contamination suggest that it originated from the

calcium granules obtained from Sigma-Aldrich. The hydrogenated calcium granules (as-synthesised CaH_2) become brittle with a yellow appearance, where an agate mortar and pestle was used to decrease the grain size of CaH_2 in preparation for use in other calcium-based hydride systems.

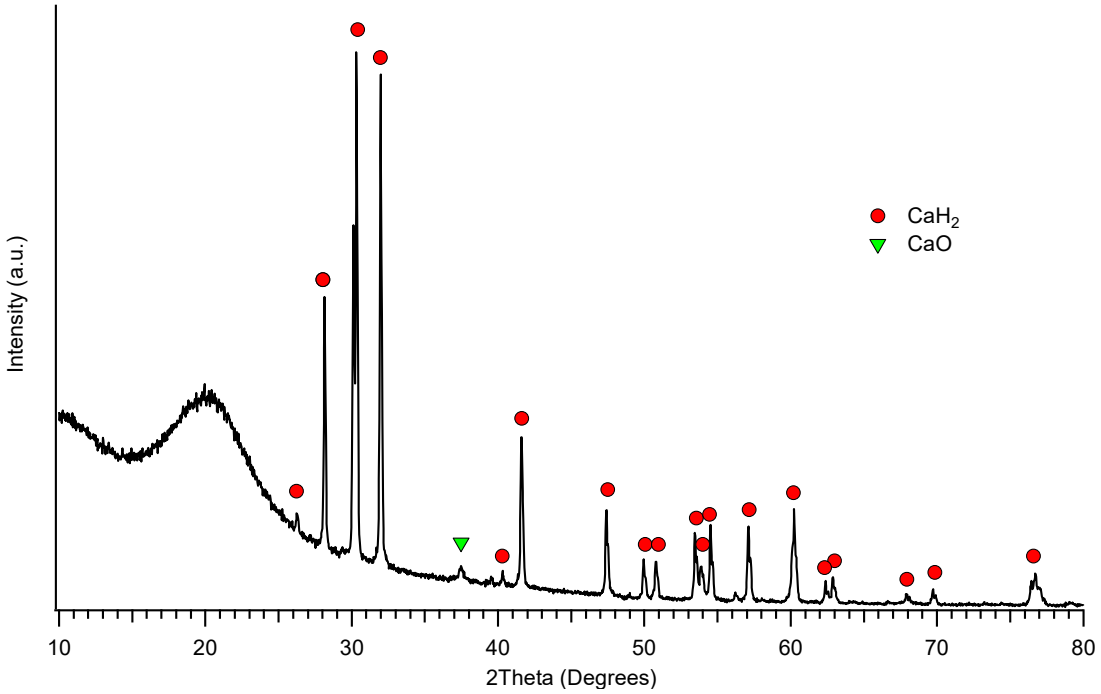

Figure 6.4: XRD analysis of laboratory synthesised CaH_2 after annealing at 500 °C.

6.2.3 $Ca_2NH + H_2$ (1:1)

6.2.3.1 Synthesis of Ca_2NH

Given the difficulties and unknown contamination observed in the synthesis of CaNH using the metathesis reaction and THF-washing method ($Ca(NH_2)_2$; Equation 6.4), an alternative approach was explored. Ca_2NH can be prepared by mixing Ca_3N_2 and CaH_2 powders and heating at 900 – 1000 °C under vacuum (Brice et al. 1976; Equation 6.6).

$$Ca_3N_2 + CaH_2 \rightarrow 2Ca_2NH \tag{6.6}$$

However, there have been reports by Chen et al. (2002) and Xiong et al. (2003) that the desorption of hydrogen from hydrogenated samples of Ca_3N_2 + CaH_2 (1:1) can occur at a lower temperature range of 500 – 550 °C. Because of the operating temperature limits (< 537 °C) of the stainless-steel reactor, a

mixture of Ca_3N_2 and CaH_2 in a 1:1 molar ratio was prepared by ball-milling using the starting reagents Ca_3N_2 (Sigma-Aldrich, 99%) and CaH_2 (laboratory synthesised; Section 6.2.2). The reagents were thoroughly mixed in a planetary ball-mill for 6 hours operating at 400 RPM with a BTP ratio of 30:1 using 316 stainless-steel balls sized at 10 mm and 6 mm. The ball-milled sample was then annealed at 530 °C using a single-use annealing tube under dynamic vacuum for approximately 24 hours. Figure 6.5 shows the XRD analysis and revealed that the synthesis of Ca_2NH was a complete success.

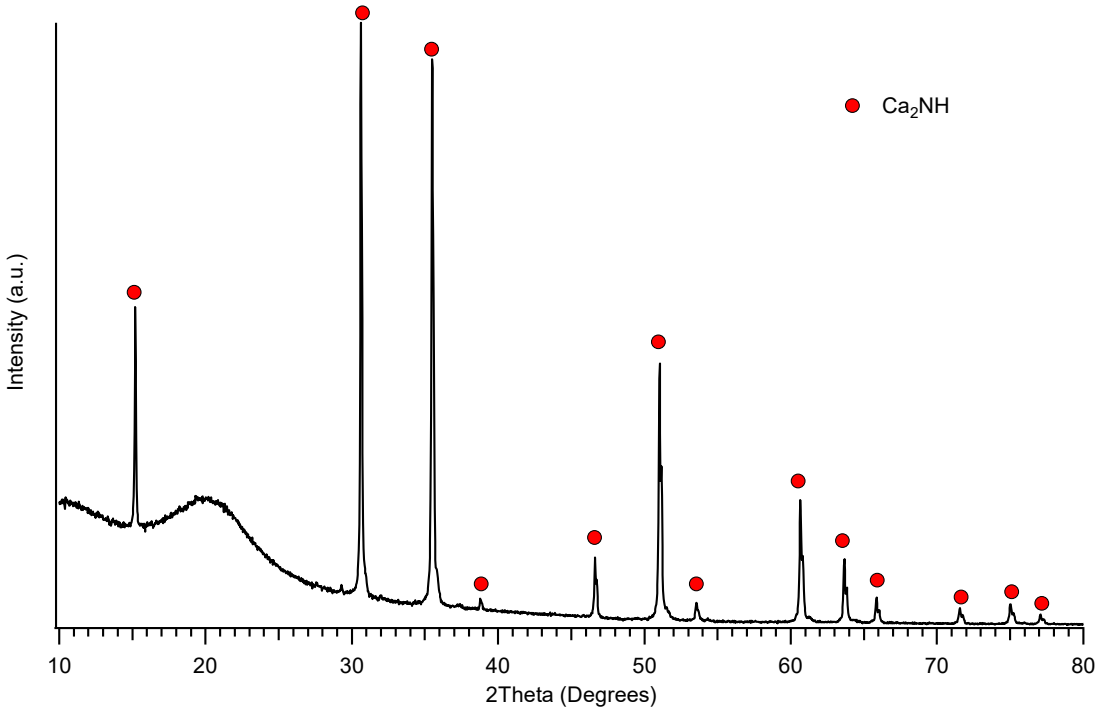

Figure 6.5: XRD analysis of Ca_3N_2 and CaH_2 after a heating at 530 °C overnight (~24h) under dynamic vacuum.

6.2.3.2 Temperature programmed absorption (TPA) with the volumetric method (VM)

Temperature programmed absorption, similarly to TPD-VM analysis, identifies the absorption of hydrogen by deriving the change in hydrogen pressure during a temperature ramp within the Sieverts system. Using the volumetric approach, the absorption intensity (a.u.) corresponds to the rate of change in hydrogen content in the sample (i.e. the amount of hydrogen absorbed). Starting from room temperature under a hydrogen back pressure of ~2.5 bar and using a heating

rate of 10 °C min^{-1}, Figure 6.6 shows that Ca_2NH started to absorb hydrogen at ~250 °C and peaked at 489 °C. However, because of the fast heating rate (10 °C min^{-1}) used, the sample was likely not given enough time to absorb hydrogen. Therefore, the absorption of hydrogen could have occurred at a lower temperature (< 489 °C) than indicated by TPA-VM analysis (Figure 6.6). However, this TPA-VM analysis provided a good approximation for a target temperature in future PCT and thermodynamic measurements.

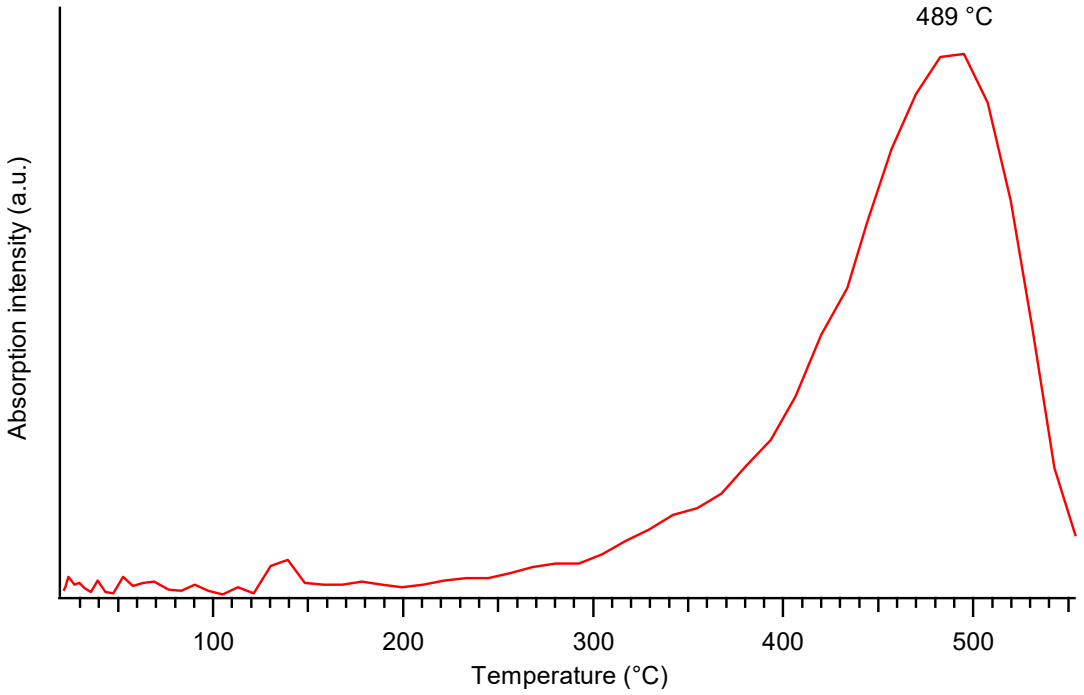

Figure 6.6: TPA-VM analysis of the hydrogenation of Ca_2NH in the temperature range of 25 – 550 °C, where the heating rate was 10 °C min^{-1} starting at a hydrogen back pressure of ~2.5 bar.

6.2.3.3 Pressure-composition-temperature (PCT) measurements

Pressure-composition-temperature measurements were performed on the hydrogenation of Ca_2NH to reproduce the results by Chen et al. (2002) of the following reversible reaction:

$$Ca_2NH + H_2 \leftrightarrow CaNH + CaH_2 \qquad (6.7)$$

During PCT measurements of Ca_2NH at 615 °C (Figure 6.7a), it was observed that a fast reaction rate occurred in the absorption of hydrogen, reaching an

equilibrium pressure of ~1 bar within 30 minutes in a two-hour step (Figure 6.7b). However, the kinetics started to slow down as the hydrogen content increased beyond ~1.0 wt% in the absorption measurement, resulting in a sloping plateau pressure after Point A of Figure 6.7b. In comparison to previous PCT measurements in the Li–N–H system, an average duration of ~4 hours was required to achieve equilibrium pressure.

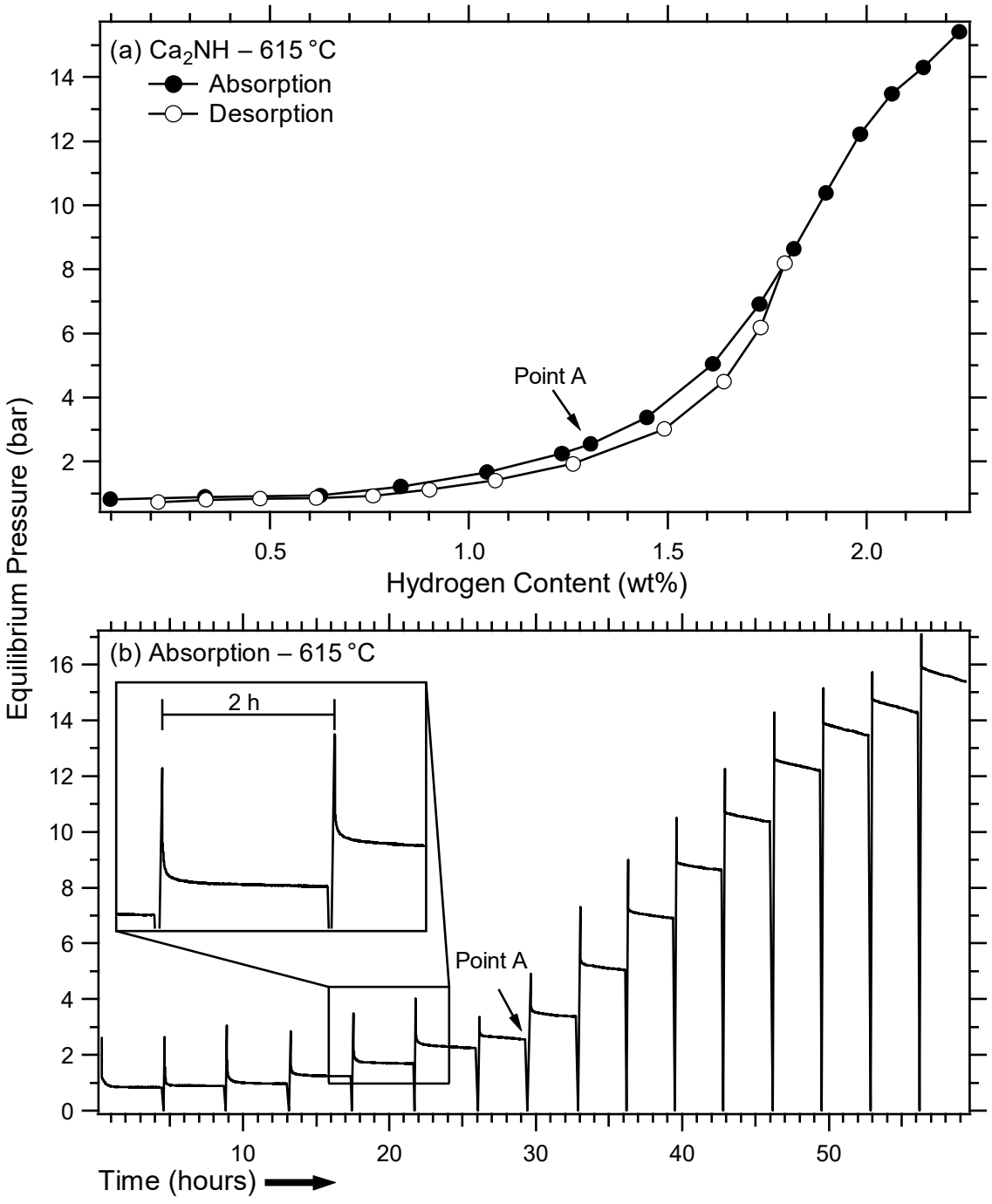

Figure 6.7: (a) PCT measurement of Ca_2NH at 615 °C. (b) Kinetic H_2 absorption data of $CaNH + CaH_2$ at 615 °C.

After the PCT measurement of Ca_2NH at 615 °C, XRD analysis revealed that the final products was comprised of CaNH (~60 wt%) and CaH_2 (~40 wt%), confirming the hydrogenation reaction in Equation 6.7. Rietveld refinement of this pattern calculated a molar ratio of 1.05:0.95 (CaNH:CaH_2), which is close to the theoretical molar ratio of 1:1 (CaNH:CaH_2). Step-wise temperature increments were performed on Ca_2NH between 600 °C and 690 °C at near-constant hydrogen content (NCHC) to satisfy the conditions to plot the van't Hoff equation used in the LVA-NCHC method (Chapter 3). However, the large volume on the low volume apparatus was erroneously open during the measurement, resulting in unreliable data for LVA-NCHC corrections. Furthermore, XRD analysis after step-wise temperature increments up to 690 °C, found identical products as those observed after the PCT measurement at 615 °C (Figure 6.8), which can be found in found in Appendix A (Figure A.12).

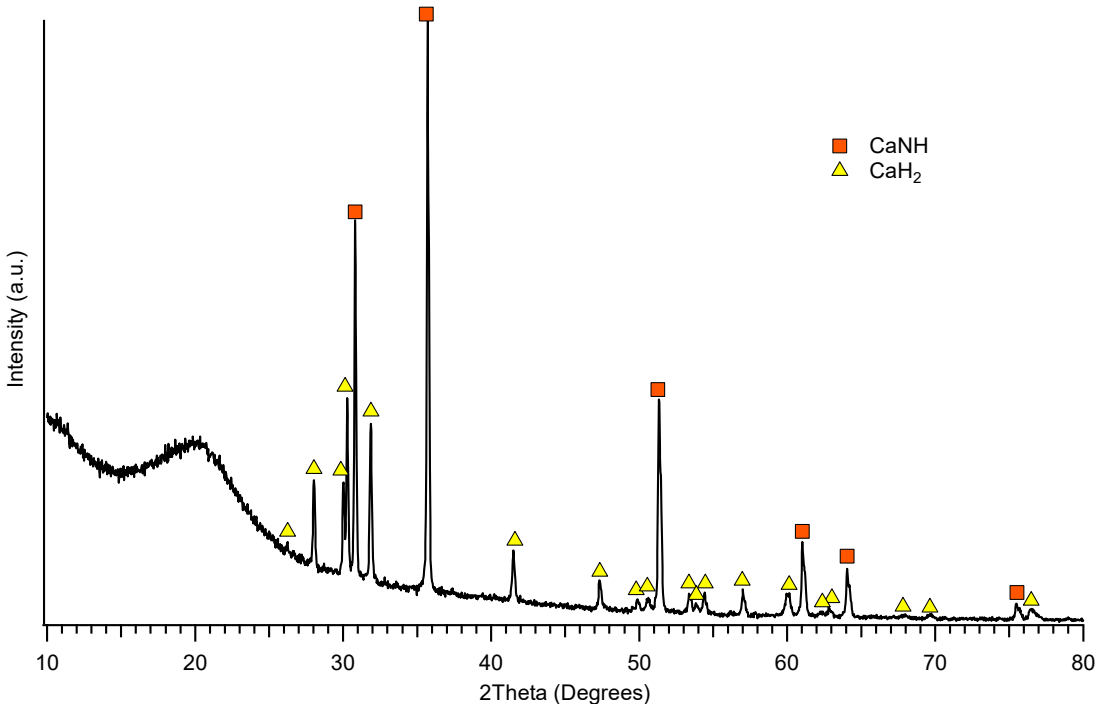

Figure 6.8: XRD analysis of the hydrogenation of Ca_2NH at 615 °C.

6.2.3.4 Thermodynamics – van't Hoff equation

The absorption and desorption PCT curves measured at 615 °C (Figure 6.7a), provided the necessary information on the approximate equilibrium pressure, hydrogen capacity, hysteresis and plateau slope. The thermodynamics properties were determined by heating a sample on a low volume apparatus to maintain a

near-constant hydrogen content (LVA-NCHC method) to satisfy the conditions to plot the van't Hoff equation, as generalised in Chapter 3. However, using the sloping plateaux (m_{slope}) in the PCT sorption cycle of Ca_2NH, the experimental pressure (P_{exp}) needs to be corrected using the change in equilibrium pressure (ΔP_{eq}) and the change in hydrogen to metal atomic ratio, $\Delta(H/M)$. From the obtained van't Hoff plots, the calculated enthalpy (ΔH) and entropy (ΔS) values can be used to characterise the calcium imide-nitride-hydride system.

The equilibrium pressure (~1 bar) obtained from the PCT sorption cycle of Ca_2NH at 615 °C was used to calculate the Ca_2NH mass required to absorb ~50% of its hydrogen capacity in the large volume that corresponds to the midpoint of the plateau. Alternatively, ΔH obtained from literature can be used to predict the equilibrium pressure to calculate the Ca_2NH mass required, where the enthalpy and entropy of absorption values are –88.4 kJ $(\text{mol } H_2)^{-1}$ and –103.3 J $(\text{mol } H_2)^{-1}$ K^{-1}, respectively (Chen et al. 2002).

To effectively measure the equilibrium plateau pressure at each temperature increment, the sample needs to be in its hydrided (absorbed) state to desorb and absorb hydrogen with increasing and decreasing temperature. Therefore, Ca_2NH was hydrogenated at 600 °C and cooled down to room temperature for ~24 hours before step-wise temperature increments were made between 500 °C and 650 °C (Figure 6.9a). However, the equilibrium pressure at 600 °C during step-wise temperature increments (~1.9 bar) was at a higher pressure than the equilibrium pressure during the initial hydrogenation of as-synthesised Ca_2NH (~1.5 bar). This pressure difference corresponded to a drastic change in hydrogen content as it was cooled to room temperature and as a result, these equilibrium pressures cannot be reliably used for the LVA-NCHC method.

A new sample of Ca_2NH was hydrogenated at 600 °C and held at 500 °C before step-wise temperature increments were made in Figure 6.9b. Step-wise temperature increments at NCHC were then measured at 500, 550, 600 and 650 °C for a total of 7 usable equilibrium points for plotting the van't Hoff equation for absorption and desorption (Figure 6.9b). It should be noted that the target PCT temperature should be near the middle of the step-wise temperature increment range (~575 °C) to decrease the uncertainties explained in corrections

for sloping plateaux in Chapter 3: Section 3.2.2.1. However, the target temperature of ~575 °C was not achieved since the PCT measurement at 615 °C was performed before the LVA-NCHC method (for sloping plateaux) was developed. Using the equilibrium pressure at the highest temperature (650 °C), the sample was calculated to release a practical hydrogen content of ~1.12 H/M, where this value is used in LVA-NCHC corrections as it corresponds to the midpoint of the plateau, $(H/M)_{T_{mid}}$ in Figure 6.7a.

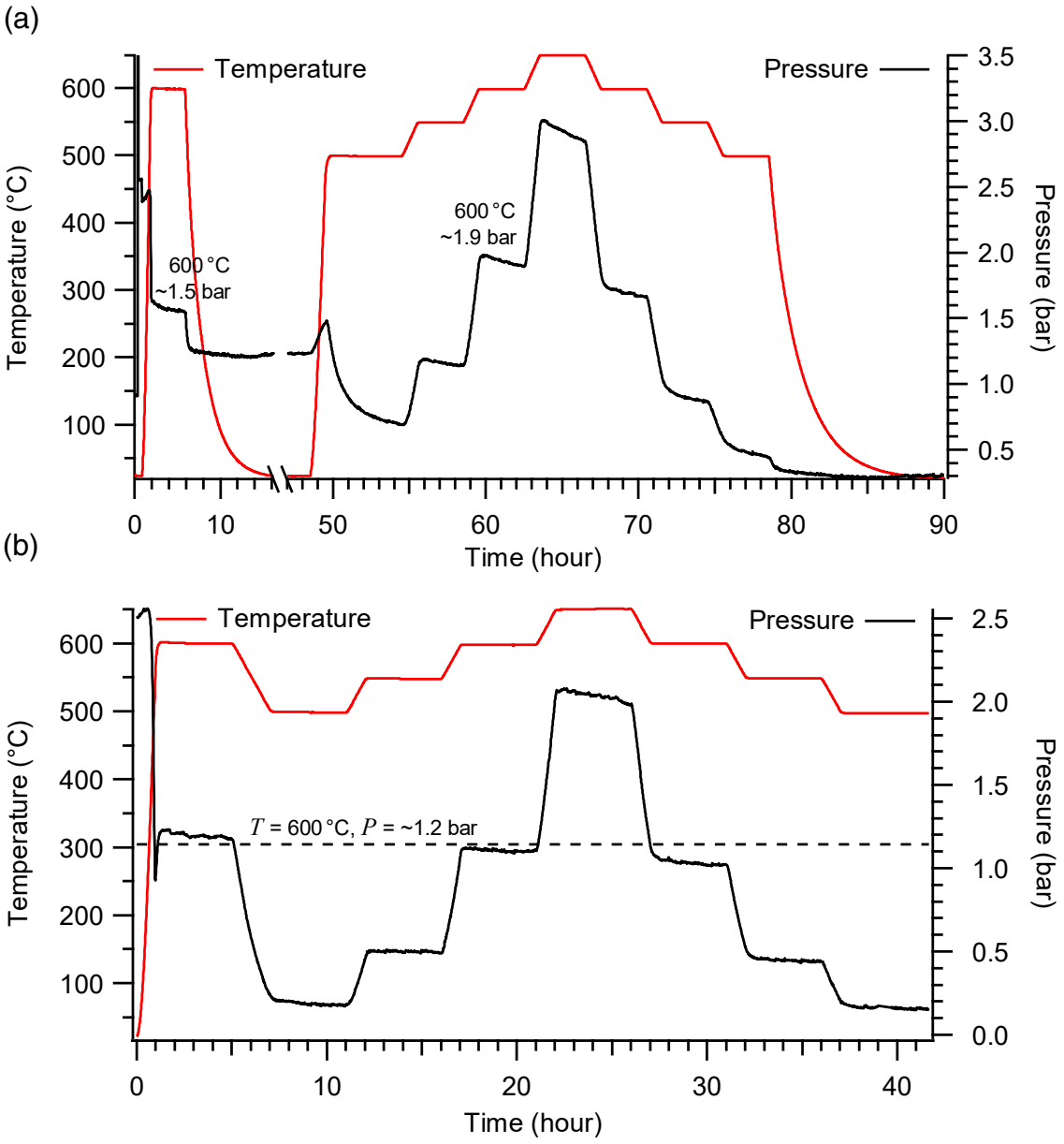

Figure 6.9: Step-wise temperature increments of Ca_2NH at near-constant hydrogen content (NCHC) between 500 °C and 650 °C, (a) before it was cooled to room temperature and (b) before it was held at 500 °C. The dashed line represents minimal change in ΔP at ~600 °C.

To plot the van't Hoff equation, corrections are applied to the experimental equilibrium pressures obtained from the step-wise temperature increments in Figure 6.9b. Using the PCT curve in Figure 6.7a and plotting H/M against ln(P), the necessary information are obtained so that the LVA-NCHC method can determine the change in experimental pressure, $\Delta\ln(P_{eq})$, and hydrogen content, $\Delta(H/M)$ (Figure 6.10). The slopes for absorption and desorption curves were 1.600(10) and 1.682(11), respectively. From these values and the definition of the slope in Equation 6.8:

$$m_{slope}(\text{abs/des}) = \frac{\Delta\ln(P_{eq})}{\Delta(H/M)} \tag{6.8}$$

The ideal pressure, $\ln(P_{ideal})$ was calculated using the following equations from corrections for sloping plateaux in Chapter 3: Section 3.2.2.1:

$$\ln(P_{ideal}) = m_{slope}(\text{abs})\left[(H/M)_{T_{mid}} - (H/M)_{exp}\right] + \ln(P_{exp}) \tag{6.9}$$

$$\ln(P_{ideal}) = m_{slope}(\text{des})\left[(H/M)_{T_{mid}} - (H/M)_{exp}\right] + \ln(P_{exp}) \tag{6.10}$$

where $(H/M)_{exp}$ is the hydrogen content and $\ln(P_{exp})$ is the experimental pressure, obtained from step-wise temperature increments at near-constant hydrogen content (Figure 6.9b).

The van't Hoff plot obtained from the ideal pressures (corrected) at each experimental temperature increment is shown in Figure 6.11. For Ca_2NH measured between a temperature of 500 °C and 650 °C, the enthalpy of absorption (ΔH_{abs}) is –107.8 ± 6.5 kJ (mol H_2)$^{-1}$ with an entropy of absorption (ΔS_{abs}) of –128.3 ± 7.3 J (mol H_2)$^{-1}$ K^{-1}. The enthalpy of desorption (ΔH_{des}) is 119.3 ± 4.6 kJ (mol H_2)$^{-1}$ with an entropy of desorption (ΔS_{des}) of 140.2 ± 5.0 J (mol H_2)$^{-1}$ K^{-1}. In comparison, Chen et al. (2002) reported an enthalpy of absorption of –88.7 kJ (mol H_2)$^{-1}$ and an entropy of –103.7 J (mol H_2)$^{-1}$ K^{-1} that was measured between a temperature of 500 °C and 550 °C. From desorption PCT measurements conducted by Chen et al. (2002), an enthalpy (ΔH_{des}) and entropy (ΔS_{des}) of desorption was extrapolated to be 94.9 ± 11.8 kJ (mol H_2)$^{-1}$ and 104.3 ± 13.6 J (mol H_2)$^{-1}$ K^{-1}, respectively. These values were closer to the experimental values than the magnitude of the reported absorption values.

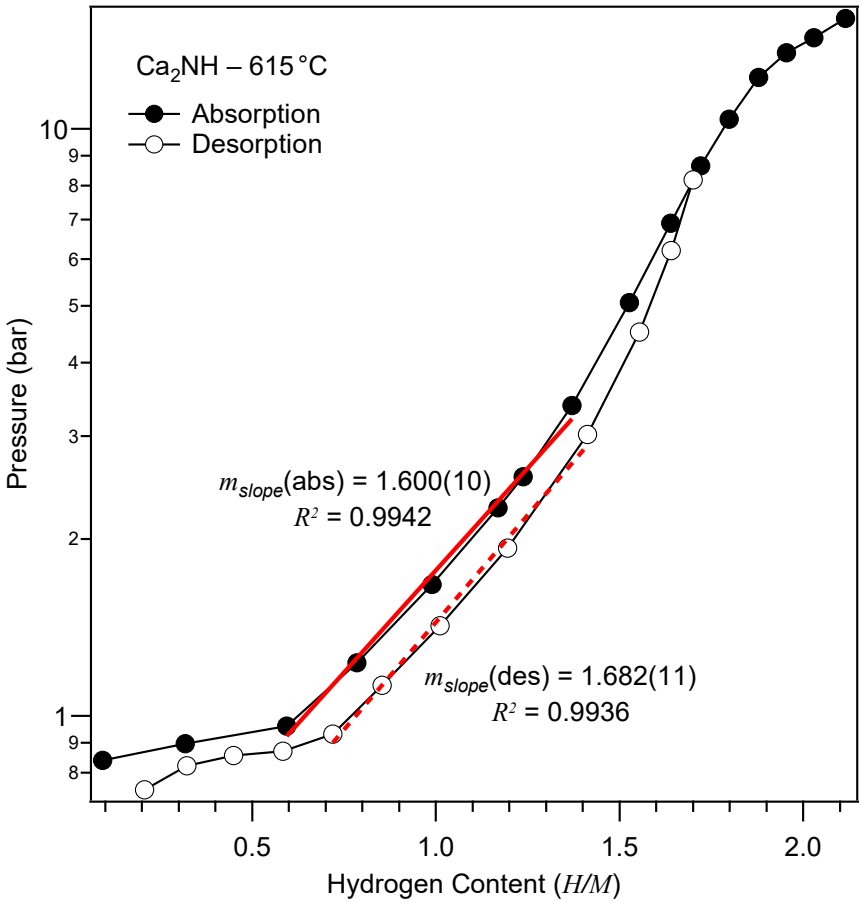

Figure 6.10: PCT measurement of Ca_2NH at 615 °C with calculated plateau slopes.

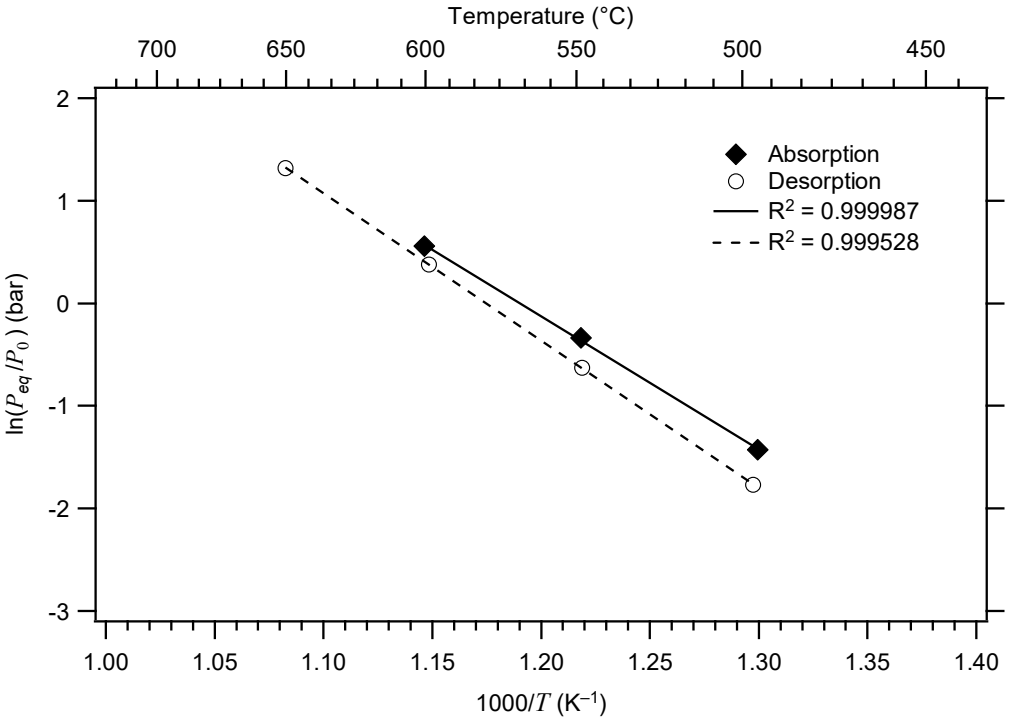

Figure 6.11: Van't Hoff plot for Ca_2NH obtained using the LVA-NCHC method.

Using the enthalpy and entropy and absorption and desorption that was measured between a temperature of 500 °C and 650 °C, the equilibrium pressure can be predicted at higher temperatures (650 – 800 °C) (Table 6.2). For high temperature thermal energy storage, the ideal temperature range is between 600 °C and 800 °C. From Table 6.2, with temperatures as high as 800 °C, the equilibrium pressures for the Ca–N–H system is not too large (~30 bar). Furthermore, a low equilibrium pressure at high temperature reduces the costs and engineering problems for storing thermochemical energy.

Table 6.2: Predicted equilibrium pressures based on $|\Delta H|$ and $|\Delta S|$ values obtained from the van't Hoff plot for Ca_2NH.

Temperature (°C)	Desorption P_{eq} (bar)	Absorption P_{eq} (bar)
600	1.52 ± 0.03	1.79 ± 0.01
650	3.71 ± 0.01	4.01 ± 0.09
700	8.25 ± 0.10	8.25 ± 0.37
750	16.97 ± 0.44	15.82 ± 1.02
800	32.62 ± 1.27	28.55 ± 2.36

6.2.3.5 Discussion

The hydrogenation of Ca_2NH in the Ca–N–H system has fast kinetics with relatively low equilibrium pressures at high temperature. It was demonstrated that Ca_2NH could reversibly store hydrogen (1.79 wt% of H_2) at 615 °C and PCT measurements revealed an equilibrium pressure of ~1 bar for both the absorption and desorption curve. A quick TPA-VM measurement revealed that the rate of absorption for Ca_2NH peaked at a temperature of ~490 °C, but the actual temperature may be a little lower because of the heat rate used (10 °C min^{-1}).

Using the novel method of obtaining thermodynamic data, the hydrogenation of Ca_2NH was measured on an LVA, doing step-wise temperature increments at NCHC. Through this method and the van't Hoff plot measured between a temperature of 500 °C and 650 °C, the enthalpy and entropy values of absorption and desorption were calculated to be ΔH_{abs} = –107.8 ± 6.5 kJ (mol H_2)$^{-1}$, ΔS_{abs} = –128.3 ± 7.3 J (mol H_2)$^{-1}$ K^{-1}, ΔH_{des} = 119.3 ± 4.6 kJ (mol H_2)$^{-1}$, ΔS_{des} = 140.2 ± 5.0 J (mol H_2)$^{-1}$ K^{-1}. However, the enthalpy of absorption reported by Chen et al.

(2002), ΔH_{abs} = –88.7 kJ (mol H_2)$^{-1}$, is quite different to the experimental value obtained from the LVA-NCHC method. This difference can be explained by the hysteresis observed in their PCT curve at 550 °C, suggesting that their measurements may have not reached true equilibrium.

Using the magnitude of $|\Delta H_{abs}|$, the practical heat storage capacity of Ca_2NH + H_2 (1:1) was calculated to be 959 ± 58 kJ kg^{-1} for a practical hydrogen content of 1.79 wt% (heat storage capacity of 1109 ± 67 kJ kg^{-1} for a theoretical hydrogen content of 2.07 wt%). In comparison, the Mg–MgH_2 system had a practical heat storage capacity of 2204 kJ kg^{-1} that operated at hydrogen pressure of 40 bar and a temperature of 450 °C (Felderhoff and Bogdanović 2009). The hydrogenation of Ca_2NH was estimated to operate at an equilibrium hydrogen pressure of ~29 bar and ~33 bar for absorption and desorption, respectively, and at a temperature of 800 °C. Given these relatively low pressures at such a high temperature, the imide-hydride to nitride hydride reaction in the Ca–N–H system has promising applications for high-temperature thermal energy storage.

6.2.4 CaNH + Ca_2FeH_6 (2:1)

6.2.4.1 Synthesis of Ca_2FeH_6

Ca_2FeH_6 was prepared by ball-milling using the starting reagents CaH_2 (laboratory synthesised; Section 6.2.2) and Fe metal powder (Sigma-Aldrich, > 99.99%). The reagents were thoroughly mixed in a planetary ball-mill for 4 hours in a 2:1 molar ratio (CaH_2:Fe) and operated at 400 RPM with a BTP ratio of 31:1 using 316 stainless-steel balls sized at 10 mm and 6 mm. The ball-milled sample was annealed at 500 °C under a hydrogen pressure of 120 bar for 4 days, where the hydrogen pressure was topped up manually to the maximum pressure of the hydrogen bottle at least once a day.

Unfortunately, the reaction did not go to completion and only partially reacted. XRD analysis in Figure 6.12 revealed that the starting reagents CaH_2 and Fe remained after annealing. Rietveld refinement of this pattern revealed that the yield under the applied conditions was ~22 wt% of Ca_2FeH_6. This result could be a consequence of differences to the original synthesis method done by Hagemann et al. (2011) who pressed their mixtures into a pellet, whereas the

samples in Figure 6.12 were in the form of powders mixed together in a planetary ball mill. However, these differences in sample preparation do not clearly explain the partial reaction observed and further investigation is required.

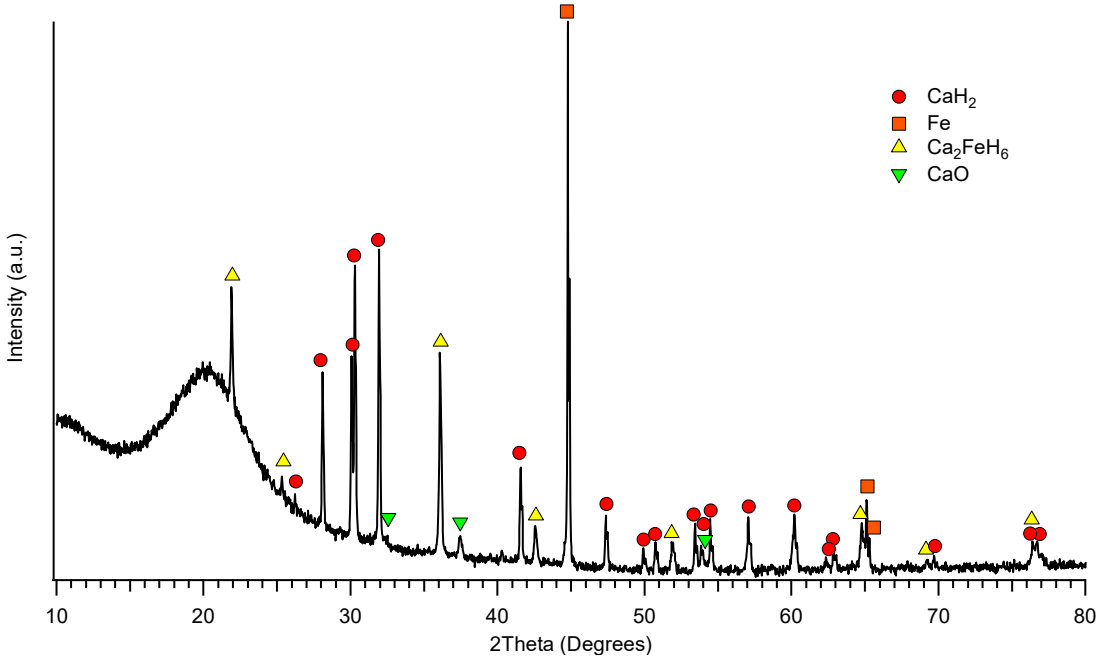

Figure 6.12: XRD analysis of Ca_2FeH_6 after annealing at 500 °C under 120 bar of H_2 for 4 days.

6.2.4.2 Preparation of CaNH + Ca_2FeH_6 (2:1)

CaNH and Ca_2FeH_6 in a 2:1 molar ratio was prepared by ball-milling using the starting reagents CaNH (laboratory synthesised; Section 6.2.1.5) and Ca_2FeH_6 (laboratory synthesised; Section 6.2.4.1). However, it should be noted that both starting reagents were impure, where CaNH contained residual LiCl from insufficient THF washing, and Ca_2FeH_6 contained residual CaH_2 and Fe. Furthermore, given the challenging synchrotron-beam deadline, the purity of the starting reagents could not be checked first at Curtin University by laboratory XRD analysis. Therefore, the impure reagents were thoroughly mixed in a planetary ball-mill for 4 hours operating at 400 RPM with a BTP ratio of 20:1 BTP using 316 stainless-steel balls sized at 10 mm and 6 mm. The ball-milled samples were packed in 0.5 mm borosilicate capillaries with polyimide/graphite ferrules using a custom mount in preparation for synchrotron X-ray diffraction (SXRD).

6.2.4.3 *In situ* synchrotron X-ray diffraction (SXRD) analysis

In situ SXRD analysis is a powerful technique to determine phase changes *in situ* to investigate reaction pathways using the Powder Diffraction beamline at the Australian Synchrotron. *In situ* SXRD was performed with a heating rate of 30 °C min^{-1} in the temperature range of 50 – 200 °C, and held for a few scans before the heating rate was decreased to 5 °C min^{-1} in the temperature range of 200 – 500 °C min^{-1} under dynamic vacuum. Given the incomplete synthesis of Ca_2FeH_6 (Figure 6.12), *in situ* SXRD analysis in Figure 6.13 showed that the initial phase at temperatures < 200 °C was Ca_2FeH_6 (1) with its starting reagents (CaH_2 3 and Fe 5), and CaNH (with overlapping LiCl 2). Some oxygen contamination (CaO 4) appeared in the initial phase with no change in peak intensity until Fe_2O_3 (6) appears briefly between 275 °C and 350 °C. Furthermore, the CaO (4) peak intensity began to increase between 350 °C and 500 °C with the appearance of Ca_2FeO_5 (7) that increased in peak intensity in the same temperature range. These contaminant phases suggest that the sample was being oxidised during the SXRD measurement. As the temperature approached ~500 °C, the Ca_2FeH_6 (1) and CaNH/LiCl (2) phases start to decompose but remain in the sample.

To observe the desorption properties of the sample under different conditions, Figure 6.14 shows the *in situ* SXRD analysis under a hydrogen back pressure of 1.4 bar. Before this measurement commenced, different sample colours were noted within the sample capillary to suggest that the sample was contaminated by air. The SXRD measurement was performed in the temperature range of 100 – 500 °C with a heating rate of 5 °C min^{-1}. The appearance of Ca_2FeO_5 (7) along with the increased crystallinity of CaO (4) in Figure 6.14, was also observed in the SXRD measurement under dynamic vacuum (Figure 6.13). Furthermore, the starting reagents Ca_2FeH_6 (1) and CaNH (2) started to decompose at the same temperature (~450 °C). However, compared to the measurement under dynamic vacuum, CaH_2 (3) disappears at temperatures > 450 °C. Additionally, an unknown phase (8) appears shortly at ~350 °C. Therefore, compared to the SXRD measurement under dynamic vacuum (Figure 6.13), the SXRD measurement under a hydrogen back pressure (Figure 6.14) showed greater levels of oxidation/leakage.

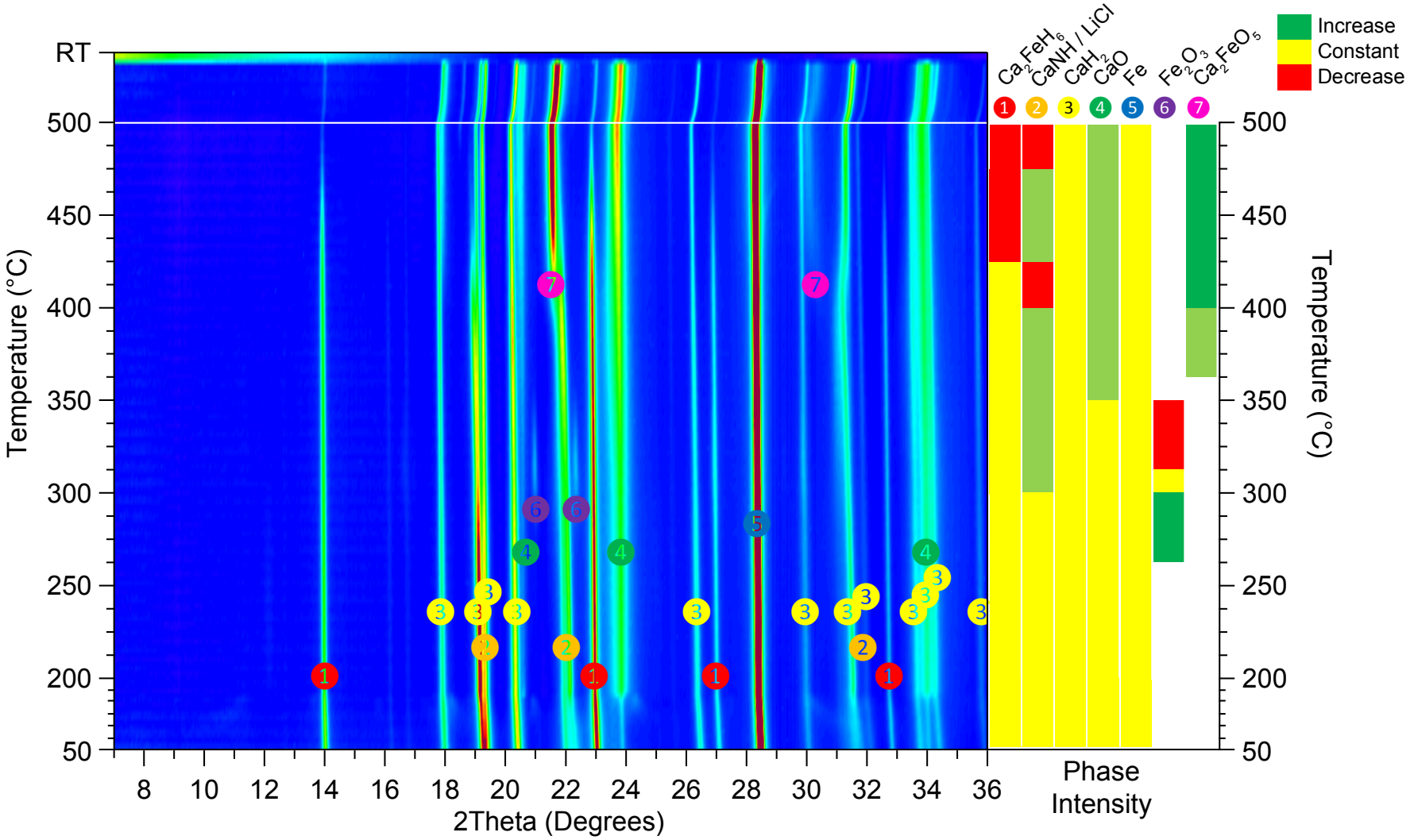

Figure 6.13: *In situ* SXRD analysis (λ = 1.00036 Å) of CaNH + Ca_2FeH_6 (2:1) under dynamic vacuum with phase identification.

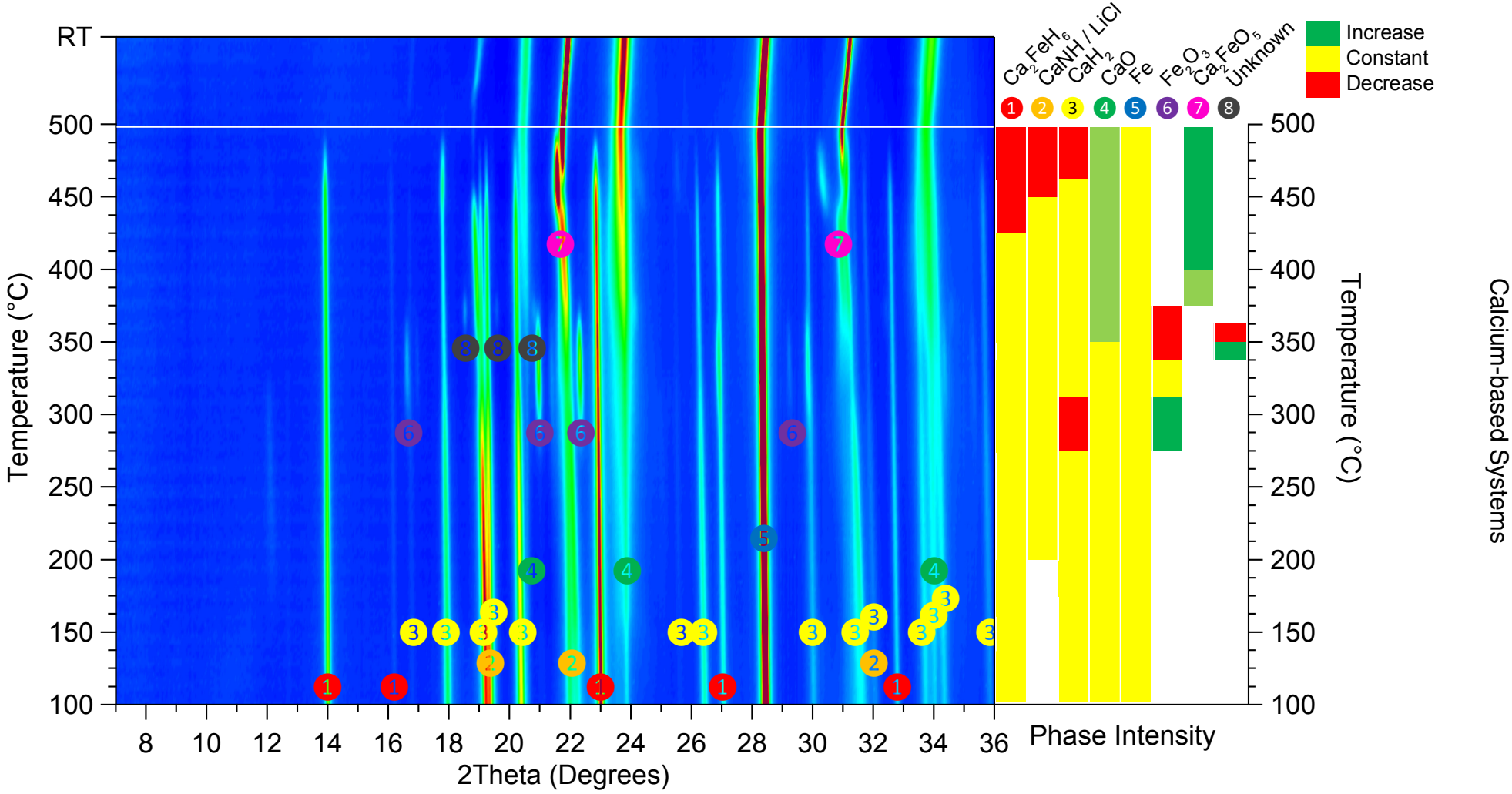

Figure 6.14: *In situ* SXRD analysis (λ = 1.00036 Å) of CaNH + Ca_2FeH_6 (2:1) under a hydrogen pressure of 1.4 bar with phase identification.

6.2.4.4 Discussion

In situ SXRD analysis of CaNH + Ca_2FeH_6 (2:1) revealed that at temperatures ≤ 500 °C, the reaction in Equation 6.3a did not proceed as the formation of Ca_2NH could not be identified. However, it appears the starting reagents started to decompose at a temperature of ~450 °C that suggest a possible reaction pathway at higher temperatures (> 500 °C). But the appearance of an unknown oxide phase between 275 °C and 350 °C, the formation of Ca_2FeO_5 and increased crystallinity of CaO at temperatures > 350 °C, suggest that the sample was being oxidised.

$$2\,CaNH + Ca_2FeH_6 \rightarrow 2\,Ca_2NH + Fe + 3H_2 \qquad (6.3a)$$

Therefore, the absence of Ca_2NH suggests two things. First, the operating temperature may not be high enough for the reaction in Equation 6.3a to proceed. Second, oxygen contamination from the appearance of oxide phases at temperatures > 350 °C, hindered any possible reaction in Equation 6.3a in the experimental temperature range of 100 – 500 °C. Therefore, further work is required towards the investigation of this imide-hydride reaction for thermal energy storage.

6.3 Conclusion

The hydrogenation of Ca_2NH was investigated at a high temperatures suitable for thermal energy storage. PCT measurements of Ca_2NH at 615 °C revealed that the hydriding kinetics were fast (~30 minutes to reach equilibrium) between a hydrogen absorption content of 0.1 wt% and ~1.0 wt% at an equilibrium plateau pressure of ~1 bar. Beyond a hydrogen absorption capacity of 1 wt%, the shape of the PCT curve began to slope as the absorption rate slowed down (slow kinetics), where a maximum hydrogen capacity of 2.2 wt% was achieved after 45 hours. XRD and TPA-VM analysis revealed that at a temperature of ~489 °C, the absorption of Ca_2NH was most pronounced, forming the hydrogenated products CaNH and CaH_2.

The LVA-NCHC method was performed on the hydrogenation of Ca_2NH to obtain fast thermodynamic data that satisfies the conditions to plot the van't Hoff equation. For $Ca_2NH + H_2$ (1:1) measured between a temperature of 500 °C and 650 °C, an enthalpy and entropy of absorption was calculated to be −107.8 ± 6.5 kJ $(mol\ H_2)^{-1}$ and −128.3 ± 7.3 J $(mol\ H_2)^{-1}\ K^{-1}$, respectively, and an enthalpy and entropy of desorption was calculated to be 119.3 ± 4.6 kJ $(mol\ H_2)^{-1}$ and 140.2 ± 5.0 J $(mol\ H_2)^{-1}\ K^{-1}$, respectively. The practical heat storage capacity of $Ca_2NH + H_2$ (1:1) was calculated to be 959 ± 58 kJ kg^{-1} for a practical hydrogen content of 1.79 wt%. Using the absolute enthalpy and entropy values, the equilibrium hydrogen pressure was predicted to have an average equilibrium pressure of ~31 bar (~29 and ~33 bar for absorption and desorption, respectively) at an operation temperature of 800 °C, conditions suitable for thermal energy storage.

The substitution of Ca_2FeH_6 for CaH_2 in the Ca–N–H system was investigated by *in situ* SXRD to study its effect at high temperatures as a thermal storage material. *In situ* SXRD revealed that the reaction between CaNH and Ca_2FeH_6 in a 2:1 molar ratio, showed no change at temperatures $\leq$ 500 °C. However, the starting reagents started to decompose at a temperature of ~450 °C, and an unknown phase appeared briefly between 275 °C and 350 °C, where oxygen contamination of the sample led to the appearance of oxides at temperatures $>$ 350 °C. Because of the maximum temperature safety limits of the Australian Synchrotron, *in situ* SXRD measurements at temperatures $>$ 500 °C were not permitted due to the involvement of hydrogen gas. Given the decomposition of starting reagents at ~450 °C, further investigation of the substitution of Ca_2FeH_6 for CaH_2 in the Ca–N–H system is required to investigate the possible formation of Ca_2NH at higher temperatures ($>$ 500 °C) for thermal energy storage.

CHAPTER 7: MIXED CATION Li–Mg–N–H SYSTEMS

7.1 Introduction

The Li–Mg–N–H system involves the mixture of lithium ($LiNH_2$) or magnesium ($Mg(NH_2)_2$) amide with lithium (LiH) or magnesium (MgH_2) hydride. Because of the ultra-fast reaction between LiH and ammonia (NH_3), LiH can be substituted in the $Mg(NH_2)_2$–MgH_2 reaction to supress the release of ammonia in desorption measurements, improving the release of hydrogen (Hu and Ruckenstein 2006; Nakamori, Kitahara and Orimo 2004). In this chapter, the hydrogen release of two imide-hydride reactions were investigated (Equation 7.1 and 7.2):

$$Li_2Mg(NH)_2 + 2LiH \rightarrow LiMgN + Li_3N + 2H_2 \quad (7.1)$$

$$MgNH + LiH \rightarrow LiMgN + H_2 \quad (7.2)$$

The reaction in Equation 7.1 looks at the interaction between lithium magnesium imide ($Li_2Mg(NH)_2$) and LiH to form lithium magnesium nitride (LiMgN) and lithium nitride (Li_3N). For time saving purposes, a different starting mixture is prepared using $LiNH_2$, MgH_2 and LiH to investigate the possibility of a two-step reaction involving the amide-hydride and imide-hydride reactions in Equation 7.3 and 7.1a, respectively.

$$2LiNH_2 + MgH_2 + 2LiH \rightarrow Li_2Mg(NH)_2 + 2LiH + 2H_2 \quad (7.3)$$

$$Li_2Mg(NH)_2 + 2LiH \rightarrow LiMgN + Li_3N + 2H_2 \quad (7.1a)$$

The reaction in Equation 7.2 looks at the interaction between magnesium imide (MgNH) and LiH to form LiMgN. From previous experiments (Chapter 5: Section 5.2.2), $Mg(NH_2)_2$ will readily react with MgH_2 during the ball-milling treatment. Therefore, a mixture of $Mg(NH_2)_2$, MgH_2 and LiH is also prepared to investigate the possibility of a two-step reaction involving the amide-hydride and imide-hydride reactions in Equation 7.4 and 7.2a, respectively.

$$\frac{1}{2}Mg(NH_2)_2 + \frac{1}{2}MgH_2 + LiH \rightarrow MgNH + LiH + H_2 \quad (7.4)$$

$$MgNH + LiH \rightarrow LiMgN + H_2 \quad (7.2a)$$

The reaction between lithium imides and magnesium halides were investigated by Anderson et al. (2011) who reported that mixed imide halide compounds hydrogenate more rapidly than pure lithium imide. Based on the investigation of $Li_3Mg_{0.5}(NH_2)_3Cl$ + LiH (1:3), which releases hydrogen at a temperature of ~275 °C, the hydrogenation of lithium magnesium imide halide ($Li_6Mg_{0.5}(NH_2)_3Cl$) was investigated, and is expressed in Equation 7.5.

$$Li_6Mg_{0.5}(NH)_3Cl + 3H_2 \rightarrow Li_3Mg_{0.5}(NH_2)_3Cl + 3LiH \quad (7.5)$$

In this chapter, five reactions in the amide-imide-hydride system were investigated involving the cation species lithium and magnesium, and one mixed imide halide compound. Table 7.1 summarises the list of samples, starting reagents and their molar ratios used. Given the date of the beamline visit at the Australian Synchrotron, a number of samples had to be prepared in a short period of time to maximise the productivity of the Powder Diffraction beamline. Because of this deadline, some samples with impure starting reagents were used for synchrotron X-ray diffraction (SXRD) measurements. Therefore, temperature programmed desorption (TPD) and pressure-composition-temperature (PCT) measurements were made on the same impure samples to help understand the SXRD analysis.

Table 7.1: List of potential amide-imide-hydride systems investigated in Chapter 7.

	Reagents
Sample 1	$Li_2Mg(NH)_2$* + LiH (1:2)
Sample 2	$LiNH_2$ + MgH_2 + LiH (2:1:2)
Sample 3	MgNH* + LiH (1:1)
Sample 4	$Mg(NH_2)_2$ + MgH_2 + LiH (1:1:2)
Sample 5	LiMgN + H_2 (1:1)
Sample 6	$Li_6Mg_{0.5}(NH)_3Cl$* + H_2 (1:3)

* Impure starting reagent, prepared for synchrotron X-ray diffraction.

7.2 Results

7.2.1 $Li_2Mg(NH)_2$ + LiH (1:2)

7.2.1.1 Preparation of Sample 1 and 2

$Li_2Mg(NH)_2$ was synthesised by ball-milling using the starting reagents $LiNH_2$ (Sigma-Aldrich, 95%) and MgH_2 (Alfa-Aesar, 98%). The starting reagents were thoroughly mixed in a planetary ball-mill for 4 hours in a 2:1 molar ratio ($LiNH_2$:MgH_2) and operated at 400 RPM with a BTP ratio of 30:1 using 316 stainless-steel balls sized at 10 mm and 6 mm. The ball-milled sample was heated at 300 °C under dynamic vacuum for 18 hours. XRD analysis after the preparation of Sample 1 for *in situ* SXRD revealed a mixture of $Li_2Mg(NH)_2$, $Li_xMg_yN_z$ ($0.51 \leq x \leq 1.12$, $0.88 \leq y \leq 2.49$, $0.96 \leq z \leq 1.83$) and $Li_{2-y}NH_{1+y}$ ($0 \leq y \leq 1$). These phases suggest that the synthesis temperature may have been too high and as a result, impure $Li_2Mg(NH)_2$* was identified by XRD analysis in Appendix A (Figure A.13).

Sample 1 – $Li_2Mg(NH)_2$* + LiH (1:2) was prepared for *in situ* SXRD by thoroughly mixing impure $Li_2Mg(NH)_2$* (laboratory synthesised) with LiH (Sigma-Aldrich, 95%) in a planetary ball-mill for 4 hours in a 1:2 molar ratio ($Li_2Mg(NH)_2$:LiH). The planetary ball-mill was operated at 400 RPM with a BTP ratio of 30:1 using 316 stainless-steel balls sized at 10 mm and 6 mm. The ball-milled sample was packed in 0.5 mm borosilicate capillaries with polyimide/graphite ferrules using a custom mount in preparation for SXRD.

Figure 7.1 shows the XRD analysis of $Li_2Mg(NH)_2$* + LiH (1:2) after ball-milling, revealing a mixture of $Li_2Mg(NH)_2$, $Li_xMg_yN_z$ and $Li_{2-y}NH_{1+y}$. Because of the overlapping XRD patterns from these phases and the possible solid-solutions formed, it is difficult to determine the quantity (wt%) of each phase after heat treatment of $Li_2Mg(NH)_2$ and ball-milling. However, it was estimated from Rietveld refinement of Figure A.13 that the impure $Li_2Mg(NH)_2$* (starting reagent) contained $Li_2Mg(NH)_2$ (~50 wt%), $Li_xMg_yN_z$ (~10 wt%) and Li_2NH (~32 wt%), with ~4 wt% of contaminant phases (Li_2O and MgO) and ~4 wt% of starting reagents

* Impure starting reagent, prepared for synchrotron X-ray diffraction.

(MgH_2 and $LiNH_2$). Therefore, the presence of $Li_xMg_yN_z$ and Li_2NH confirmed that the synthesis temperature for $Li_2Mg(NH)_2$ was too high. The appearance of non-stoichiometric $Li_{2-y}NH_{1+y}$ in Figure 7.1 could have also been promoted by the decomposition of residual $LiNH_2$ (originating from impure $Li_2Mg(NH)_2$*) with the addition of LiH in Sample 1.

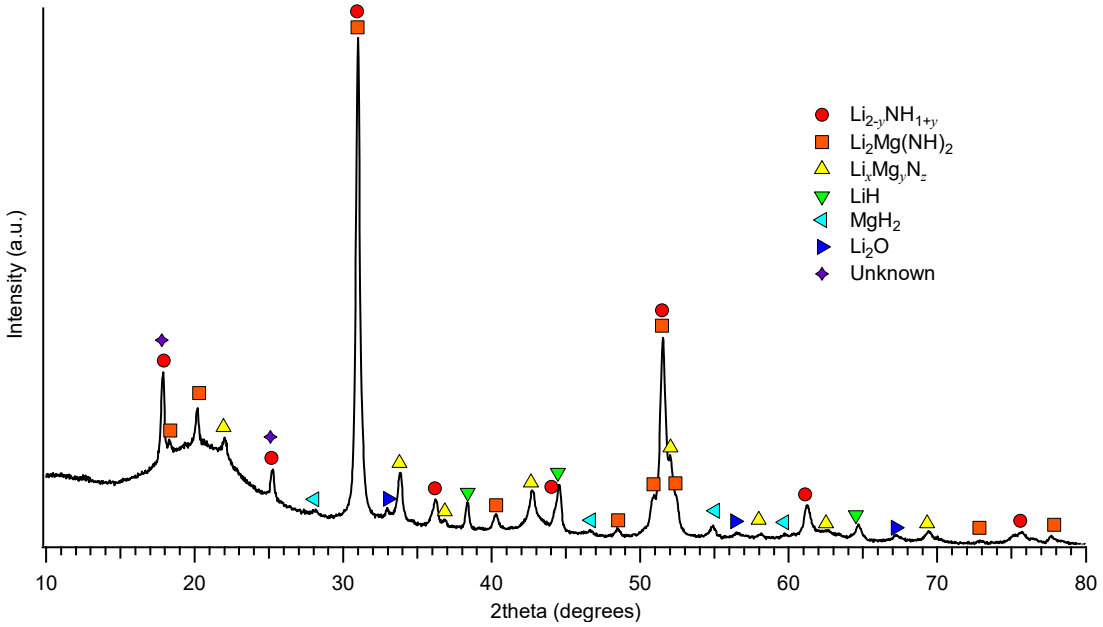

Figure 7.1: XRD analysis of Sample 1 – $Li_2Mg(NH)_2$* + LiH (1:2) after ball milling for 4 hours.

Sample 2 – $LiNH_2$ + MgH_2 + LiH (2:1:2) was prepared by ball-milling using the starting reagents $LiNH_2$ (Sigma-Aldrich, 95%), MgH_2 (Alfa-Aesar, 98%) and LiH (Sigma-Aldrich, 95%). The starting reagents were thoroughly mixed in a planetary ball-mill for 4 hours in a 2:1:2 molar ratio ($LiNH_2$:LiH:MgH_2) and operated under the same ball-milling conditions as Sample 1.

7.2.1.2 Temperature programmed desorption with the volumetric method (TPD-VM) of Sample 2

Temperature programmed desorption measurements were performed on Sample 2 to determine the reaction pathway by measuring the release of gases as a function of temperature using the volumetric approach (TPD-VM). TPD-VM analysis in Figure 7.2a revealed a large desorption event starting at ~180 °C that

* Impure starting reagent, prepared for synchrotron X-ray diffraction.

peaked at ~246 °C and another smaller event that peaked at ~386 °C. The desorption event at ~246 °C is in agreement with Lohstroh and Fichtner (2007), who reported a reaction between $LiNH_2$ and MgH_2, led to the formation $Li_2Mg(NH)_2$ at approximately 250 °C. However, this temperature is also in agreement with the reaction between $LiNH_2$ and LiH to form Li_2NH (Chen et al. 2002). Because of a temperature safety limit built into the software of the PCT-Pro E&E, which closes all valves, one of the measurements stopped recording at temperatures > 400 °C. Therefore, the TPD measurement was repeated with a final temperature of 500 °C. The second TPD-VM analysis, performed in the temperature range of 25 – 500 °C, revealed an additional desorption event that peaked at ~458 °C (Figure 7.2b).

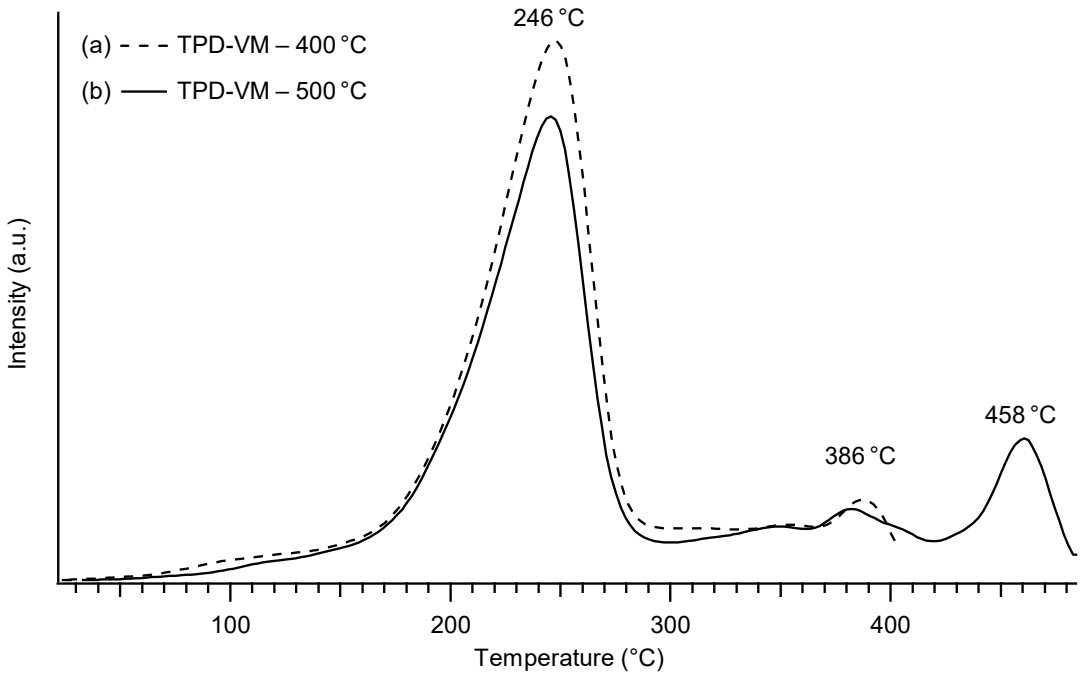

Figure 7.2: TPD-VM analysis of Sample 2 – $LiNH_2$ + MgH_2 + LiH (2:1:2) halted at (a) 400 °C and (b) 500 °C, where the heating rates were 2 °C min^{-1} starting at vacuum.

After the TPD measurement was halted at 500 °C, Sample 2 was cooled down to room temperature and a Rietveld refinement was modelled on the XRD data (Figure 7.3). The sample was revealed to contain ~68 wt% of non-stoichiometric $Li_{2-y}NH_{1+y}$ ($0 \leq y \leq 1$), where y in this case was ~0. This phase suggests that $LiNH_2$ reacted with LiH to form Li_2NH, corresponding to the desorption event at ~246 °C as seen in TPD-VM analysis (Figure 7.2). A non-stoichiometric phase of $Li_xMg_yN_z$ ($0.51 \leq x \leq 1.12$, $0.88 \leq y \leq 2.49$, $0.96 \leq z \leq 1.83$) was also identified but at a

lower quantity (~10 wt%). This phase suggests that the small desorption event at ~458 °C corresponded to the formation of $Li_xMg_yN_z$ or an unknown imide-hydride to nitride reaction. Oxide phases, Li_2O (4.2 wt%) and MgO (7 wt%), were observed as a result of contamination from the commercial reagents used.

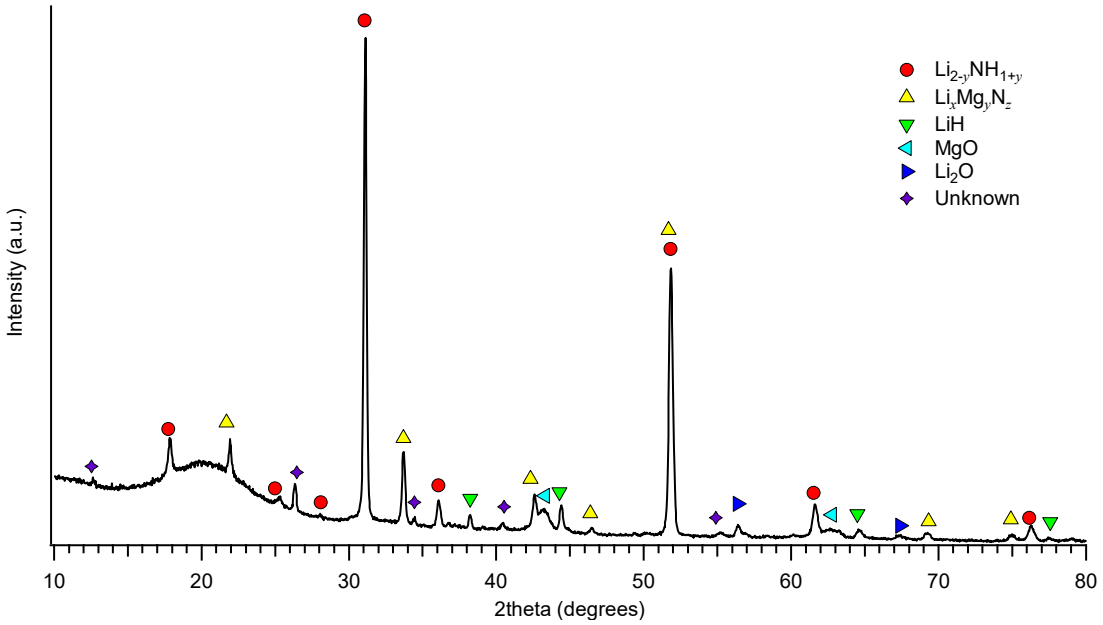

Figure 7.3: XRD analysis of Sample 2 – $LiNH_2$ + MgH_2 + LiH (2:1:2) after TPD measurement halted 500 °C.

7.2.1.3 *In situ* synchrotron X-ray diffraction (SXRD) analysis of Sample 1

In situ SXRD analysis is a powerful technique to determine phase changes *in situ* for investigating reaction pathways using the Powder Diffraction beamline at the Australian Synchrotron. The *in situ* SXRD measurement was performed with a heating rate of 30 °C min^{-1} at temperatures ≤ 150 °C (excluded in Figure 7.4), and then 5 °C min^{-1} in the temperature range of 150 – 500 °C. Figure 7.4 shows the *in situ* SXRD analysis of Sample 1, where the initial phases near ~150 °C were in agreement with the impure sample of $Li_2Mg(NH)_2$* identified by laboratory XRD (Appendix A: Figure A.13). As the intensity of MgH_2 (5) decreased at temperatures > 250 °C, the formation of non-stoichiometric phases of lithium imide ($Li_{2-y}NH_{1+y}$ 1) and lithium magnesium nitride ($Li_xMg_yN_z$ 3) appeared with increasing intensity. At temperatures > 300 °C, the α-phase of $Li_2Mg(NH)_2$ (2) disappears and transformed into a non-stoichiometric phase of $Li_xMg_yN_z$ (3). At

* Impure starting reagent, prepared for synchrotron X-ray diffraction.

temperatures > 450 °C, the γ-phase of $Li_2Mg(NH)_2$ (6) reappeared and remained as it cooled. The formation of non-stoichiometric $Li_xMg_yN_z$ (3) is in agreement with the hydrogen release event seen in TPD-VM analysis at ~458 °C (Figure 7.2), which suggests that the reaction in Equation 7.1 did not go to completion.

Figure 7.5 shows the *in situ* SXRD analysis under a hydrogen back pressure performed with a heating rate of 5 °C min^{-1} in the temperature range of 100 – 500 °C. The pressure in the gas handling system dropped from 2 bar to ~1 bar as the pressurised reference volume was open to the evacuated sample capillary. This pressure change is greater than previous SXRD measurements (1.4 bar), and given the appearance of MgO (8) at 250 °C, it was confirmed that the sample capillary seal was not air tight and leaking. Besides the increasing intensity of $Li_xMg_yN_z$ (3) between 375 °C and 500 °C in Figure 7.4, the initial phases (at 100 °C) in Figure 7.5 were the same as those observed in the *in situ* SXRD measurement under dynamic vacuum. However, a phase change occurs with $Li_2Mg(NH)_2$ from the α- to β-phase (2 to 7) and β- to γ-phase (7 to 6) at ~200 °C and 400 °C, respectively. Unusually, the β-phase was not observed under dynamic vacuum (Figure 7.4).

When the sample was allowed to cool (above the white line in Figure 7.5), the γ-phase of $Li_2Mg(NH)_2$ (6) immediately reverted to the β-phase (7). It is possible that the oxygen contamination (MgO 8) affected the formation of stoichiometric LiMgN, where an oxide layer inhibited the release of hydrogen from the α-phase of $Li_2Mg(NH)_2$ (2). The $Li_2Mg(NH)_2$ (α to β) phase changes observed in the *in situ* SXRD measurement were also in agreement with those reported by Rijssenbeek et al. (2008) within the same temperature range (≤ 500 °C).

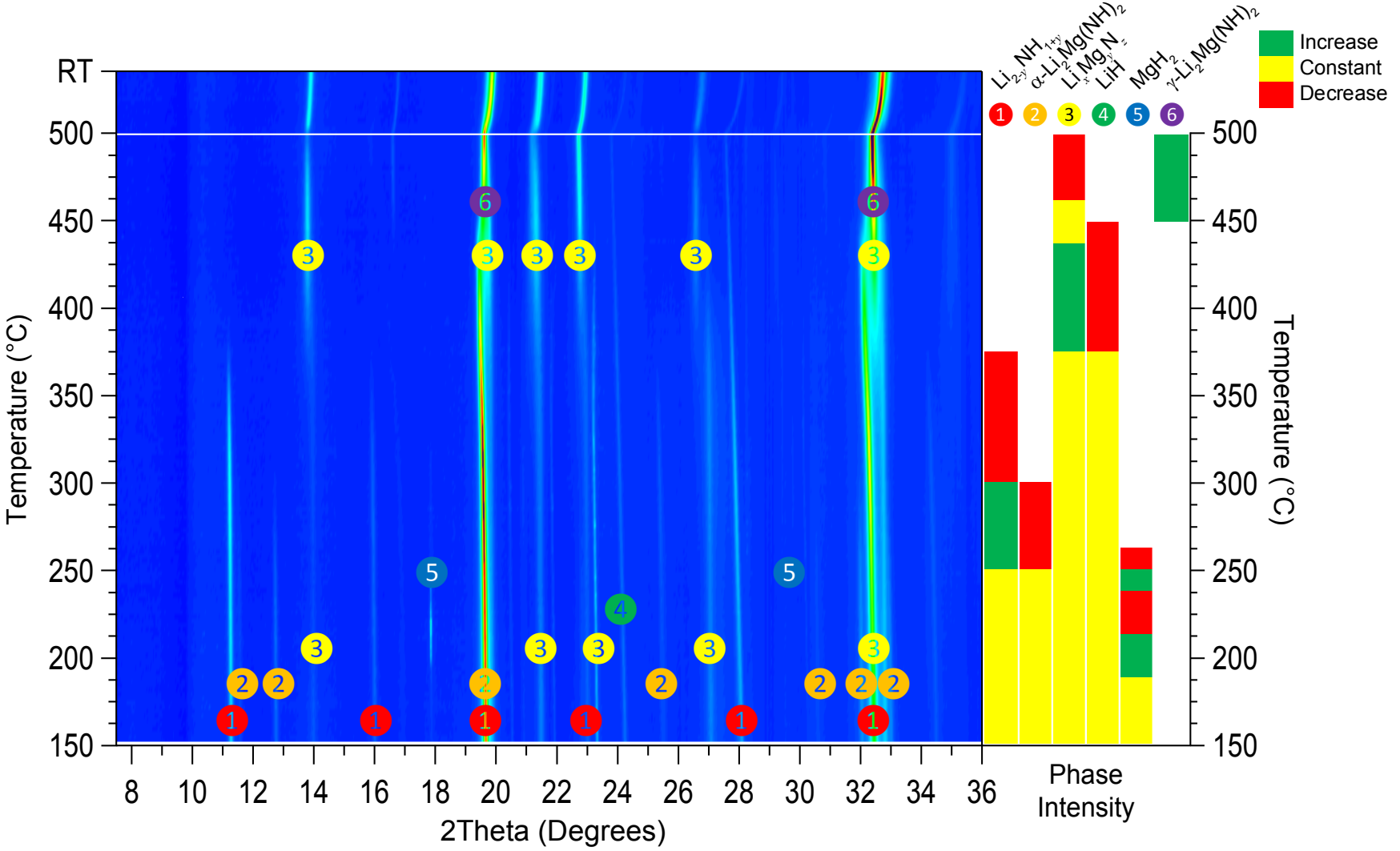

Figure 7.4: *In situ* SXRD analysis (λ = 1.00036 Å) of Sample 1 – $Li_2Mg(NH)_2$* + LiH (1:2) under dynamic vacuum with phase identification.

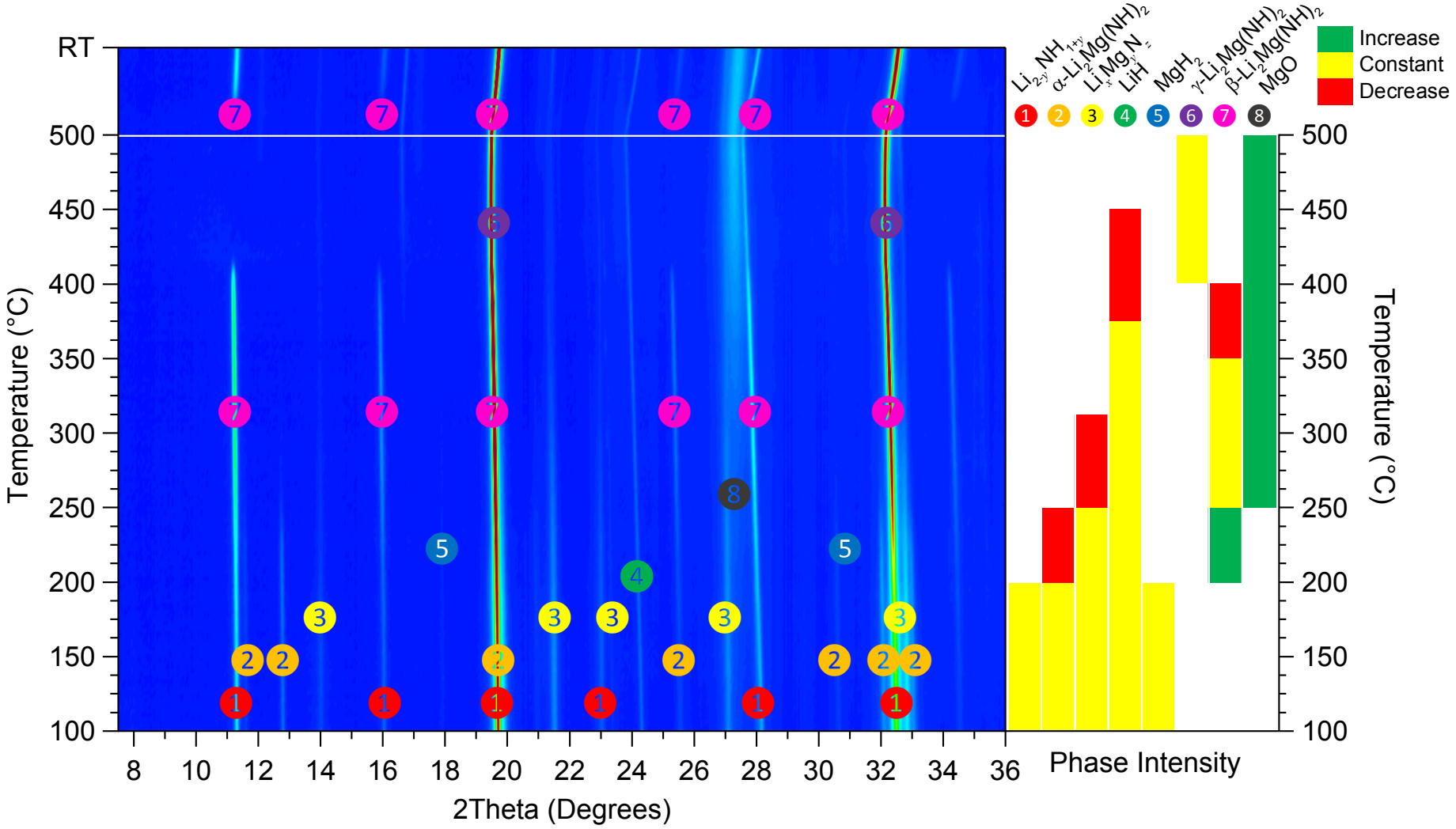

Figure 7.5: *In situ* SXRD analysis (λ = 1.00036 Å) of Sample 1 – $Li_2Mg(NH)_2$* + LiH (1:2) under a H_2 pressure of ~1 bar with phase identification.

7.2.1.4 Discussion

In situ SXRD of Sample 1 – $Li_2Mg(NH)_2$* + LiH (1:2) and TPD-VM measurements of Sample 2 – $LiNH_2$ + MgH_2 + LiH (2:1:2) revealed that the hydrogen release event at ~250 °C corresponds to the formation of Li_2NH from the interaction of $LiNH_2$ with LiH, where residual $LiNH_2$ in Sample 1 originated from impure $Li_2Mg(NH)_2$*. These measurements also confirmed that the hydrogen release event at ~458 °C of Sample 2 corresponded to the formation of non-stoichiometric $Li_xMg_yN_z$. However, from the expected imide-hydride reaction pathway in Equation 7.1, the absence of Li_3N with the formation of non-stoichiometric $Li_xMg_yN_z$, suggests that a different reaction pathway took place. Furthermore, based on the Li–N–H system investigated in Chapter 4, the formation of Li_3N was never observed under similar conditions. Therefore, further investigation of the anticipated imide-hydride reaction in Equation 7.1 is required for thermal energy storage.

7.2.2 MgNH + LiH (1:1)

7.2.2.1 Preparation of Sample 3 and 4

MgNH was synthesised by ball-milling using THF-washed $Mg(NH_2)_2$ (laboratory synthesised; Chapter 5: Section 5.2.1) and MgH_2 (Alfa-Aesar, 98%). Furthermore, as-synthesised MgNH was annealed at 200 °C for 19 hours under dynamic vacuum to decompose residual $Mg(NH_2)_2$ to MgNH. However, considering MgNH becomes X-ray amorphous after ball milling, the reaction was incomplete with the starting reagents present, which can be seen in Appendix A (Figure A.14). Therefore, MgNH* will denote the incomplete synthesis of MgNH at 200 °C that contains amorphous MgNH and an unreacted mixture of $Mg(NH_2)_2$ and MgH_2. The starting reagents for Sample 3 were MgNH* (laboratory synthesised) and LiH (Sigma-Aldrich, 95%) and the starting reagents for Sample 4 were $Mg(NH_2)_2$ (laboratory synthesised), MgH_2 and LiH. For Sample 3 and 4, the reagents were thoroughly mixed in a planetary ball-mill for 4 hours in a 1:1 molar ratio (MgNH:LiH) and 1:1:2 molar ratio ($Mg(NH_2)_2$:MgH_2:LiH). The planetary ball-mill was operated at 400 RPM with a BTP ratio of 30:1 using 316 stainless-steel balls sized at 10 mm and 6 mm. Sample 3 was also packed in

0.5 mm borosilicate capillaries with polyimide/graphite ferrules using a custom mount in preparation for SXRD. A summary of the reagents used to prepare Sample 3 and 4 can be seen in Table 7.2.

Table 7.2: Summary of reagents used to prepare Sample 3 and 4.

	Reagents
Sample 3	MgNH* + LiH (1:1)
Sample 4	$Mg(NH_2)_2$ + MgH_2 + LiH (1:1:2)

* Impure starting reagent, prepared for synchrotron X-ray diffraction.

X-ray diffraction analysis of Sample 3 in Figure 7.6 confirmed that the laboratory synthesis of MgNH* was incomplete at 200 °C with an unreacted mixture of $Mg(NH_2)_2$ and MgH_2 (Figure A.14). Rietveld refinement of this pattern revealed that the sample contained $Mg(NH_2)_2$, MgH_2 and LiH in a 1:1:4 molar ratio, with no trace of MgNH by XRD analysis. Therefore, if MgNH was X-ray amorphous and given the starting mass reagents, it was calculated that the missing percentage of amorphous MgNH was approximately ~50 wt% from the molar ratios obtained through Rietveld refinement; hence, the synthesis of MgNH had a product yield of 50%. The low amount of MgO (< 10 wt%) in Figure 7.6 suggest that oxide contamination was already present in the starting reagents.

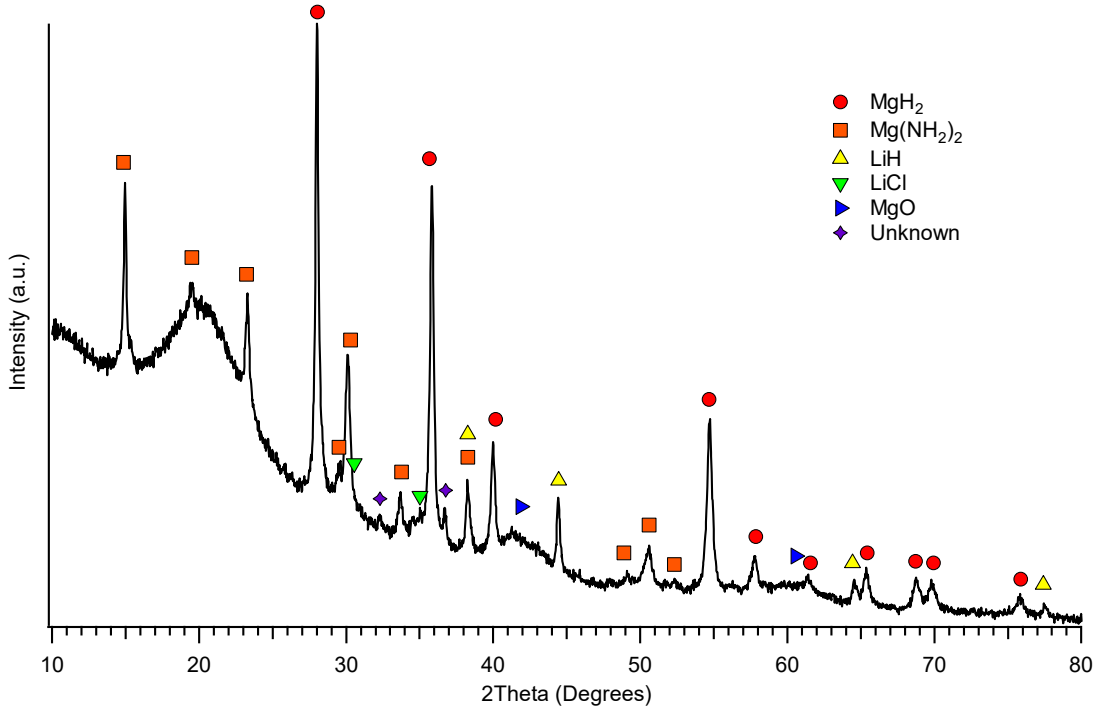

Figure 7.6: XRD analysis of the mixture MgNH* and LiH after ball milling.

7.2.2.2 Temperature programmed desorption with the volumetric method (TPD-VM) of Sample 3 and 4

The TPD-VM analysis of Sample 3 and 4 in the temperature range of 25 – 500 °C is shown in Figure 7.7 with a heating rate of 2 °C min^{-1}. In the TPD comparison, as a result of Sample 3 and 4 containing similar species because of impure MgNH* (containing an unreacted mixture of $Mg(NH_2)_2$ and MgH_2), the gaseous release events of Sample 3 and 4 occur similarly at 275, 338 and 378 °C. Hu et al. (2007) performed a TPD-MS measurement on the mixture of $Mg(NH_2)_2$ + LiH (1:1) with a heating rate of 5 °C min^{-1}. Although they used a different sample composition to Sample 3 and 4, the reported hydrogen and ammonia desorption events were similar to the ones observed in Figure 7.7. Mass spectrometry analysis performed by Hu et al. (2007) on the gases released revealed that the desorption events at 275 °C and 378 °C corresponded to the release of ammonia and the desorption event at 207 °C and 461 °C corresponded to the release of hydrogen that overlaps a small ammonia desorption event at 207 °C. The identification of temperature-dependent gas species released was taken from Hu et al. (2007) and has been labelled in Figure 7.7, but because of the differences in sample composition, this should be interpreted with caution.

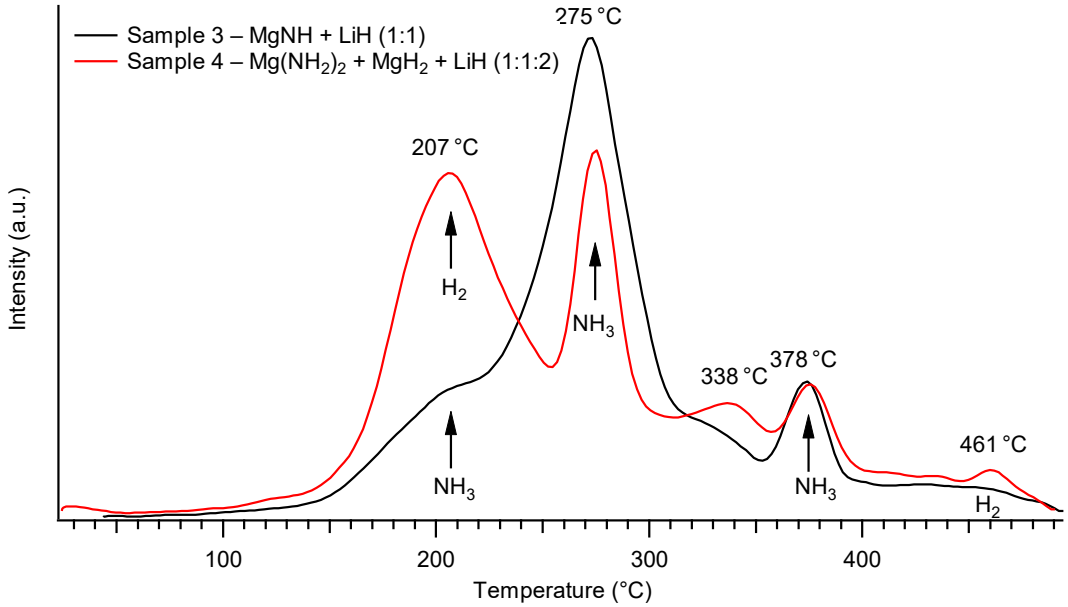

Figure 7.7: Comparitive TPD-VM analysis of $Mg(NH_2)_2$ + MgH_2 + LiH (1:1:2) and MgNH* + LiH (1:1) halted at 500 °C, where the heating rates were 2 °C min^{-1} starting at vacuum. Identification of H_2 and NH_3 signals taken from Hu et al. (2007).

The hydrogen release event that occurs at ~207 °C is greater in Sample 4 than Sample 3 (Figure 7.7). This peak could be due to the release of hydrogen from the reaction between $Mg(NH_2)_2$ and LiH according to Equation 7.6, which also occurs at ~200 °C (Xiong et al. 2005b; Zak-Fang, Lu and Sohn 2008):

$$Mg(NH_2)_2 + 2LiH \leftrightarrow Li_2Mg(NH)_2 + 2H_2 \quad (7.6)$$

Due to Sample 3 containing impure MgNH* (containing an unreacted mixture of $Mg(NH_2)_2$ and MgH_2), the hydrogen release that occurs at ~207 °C is correlated to the amount of $Mg(NH_2)_2$ available in the sample (~50% less than Sample 4).

Hu et al. (2007) proposed using XRD (at 374 °C) and TGA measurements (≤ 500 °C) that the ammonia release events at 275 °C and 378 °C corresponds to the following reaction:

$$2Mg(NH_2)_2 + 2LiH \rightarrow Li_2Mg_2(NH)_3 + NH_3 + 2H_2 \quad (7.7)$$

where TGA measurements revealed a loss of 16.3 wt% of mass that is in agreement with the theoretical loss of 16.4 wt% of mass. However, the mechanism for $Mg(NH_2)_2$ + LiH (1:1) between 275 °C and 500 °C is not clearly

understood with conflicting results reported in the literature (Hu et al. 2007; Leng, Ichikawa and Fujii 2006; Rijssenbeek et al. 2008; Zak-Fang, Lu and Sohn 2008). To clarify the conflicting results, XRD analyses of samples that were heated to 500 °C (Figure 7.8) and at 300 °C (Figure 7.9) were conducted, and compared to the TPD-VM results in Figure 7.7.

X-ray diffraction analysis of Sample 3 and 4 heated to 500 °C (Figure 7.8), showed that the final product of both samples were near identical with matching patterns containing a mixture of Mg_3N_2, LiMgN and LiH. This observation confirms that the starting reagents in the single-step (Equation 7.1) and two-step reaction (Equation 7.3 and 7.1a) resulted in a similar reaction pathway because of the same products after decomposition at temperatures $\leq$ 500 °C (Figure 7.8). XRD analysis and Rietveld refinement of Sample 3 after heating to 500 °C (Figure 7.8a) showed that the final products contained a mixture of Mg_3N_2, LiMgN and Li_2NH. However, due to the overlapping XRD patterns of these phases, Rietveld refinement could not reliably measure the experimental quantity (wt%) of phases. The identification of Li_2NH and LiCl in Figure 7.8a are a result of residual products from the synthesis of $Mg(NH_2)_2$ (Chapter 5: Section 5.2.1). To identify the reaction corresponding to the desorption event at 275 °C from TPD-VM measurements (Figure 7.7), XRD analysis and Rietveld refinement of Sample 4 after heating to 300 °C (Figure 7.9) revealed a mixture of magnesium-rich $Li_{0.51}Mg_{2.49}N_{1.83}$ (~44 wt%) and $Li_2Mg(NH)_2$ (~20 wt%) phases.

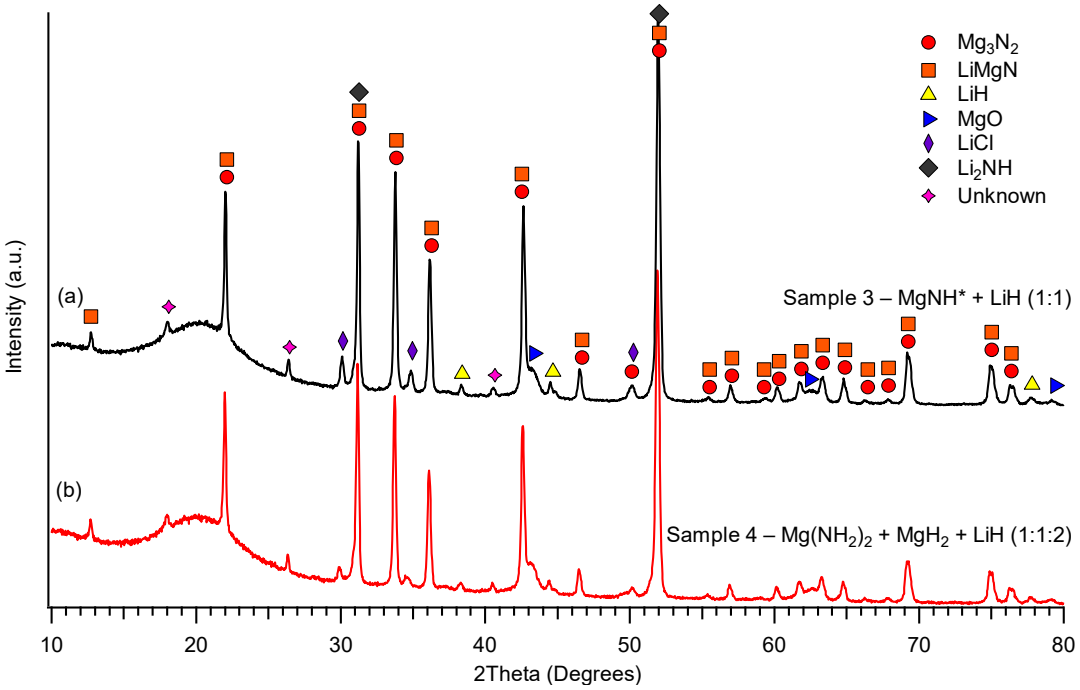

Figure 7.8: Comparitive XRD analysis of (a) MgNH* + LiH (1:1) and (b) $Mg(NH_2)_2$ + MgH_2 + LiH (1:1:2) after the TPD measurements halted at 500 °C.

Akbarzadeh, Ozoliņš, and Wolverton (2007) proposed a reaction between $LiNH_2$ + MgH_2 (1:1) to form a mixture of $Mg(NH_2)_2$, MgH_2 and LiH in a 1:1:2 molar ratio that decomposes to LiMgN at temperatures > 400 °C. Therefore, based on those reactions and the phases identified by XRD analyses at 300 °C and 500 °C, the possible reaction pathway for $Mg(NH_2)_2$ + MgH_2 + LiH (1:1:2) is as follows:

$$Mg(NH_2)_2 + MgH_2 + 2LiH$$

$$\rightarrow \frac{1}{2}Li_2Mg(NH)_2 + \frac{1}{2}Mg(NH_2)_2 + MgH_2 + LiH + H_2 \quad (7.8)$$

$$\rightarrow \frac{1}{2}Li_2Mg(NH)_2 + \frac{1}{2}Mg_3N_2 + LiH + 3H_2 \quad (7.9)$$

$$\rightarrow 2LiMgN + 4H_2 \quad (7.10)$$

where $Mg(NH_2)_2$ reacts with LiH to form $Li_2Mg(NH)_2$, corresponding to the hydrogen release event at 207 °C (Equation 7.8). $Mg(NH_2)_2$ then reacts with MgH_2 to form Mg_3N_2 (via MgNH as an intermediate phase) between 220 °C and 390 °C (Liu et al. 2008; Equation 7.9). Given the appearance of magnesium-rich $Li_{0.51}Mg_{2.49}N_{1.83}$ at temperatures > 300 °C, the formation of Mg_3N_2 likely occurred at 275 °C to allow the formation of $Li_{0.51}Mg_{2.49}N_{1.83}$ between $Li_2Mg(NH)_2$ and Mg_3N_2. Lastly, $Li_2Mg(NH)_2$ reacts with MgH_2 to form LiMgN with the release of hydrogen

in Equation 7.10, corresponding to the possible TPD desorption event at 461 °C (Figure 7.7).

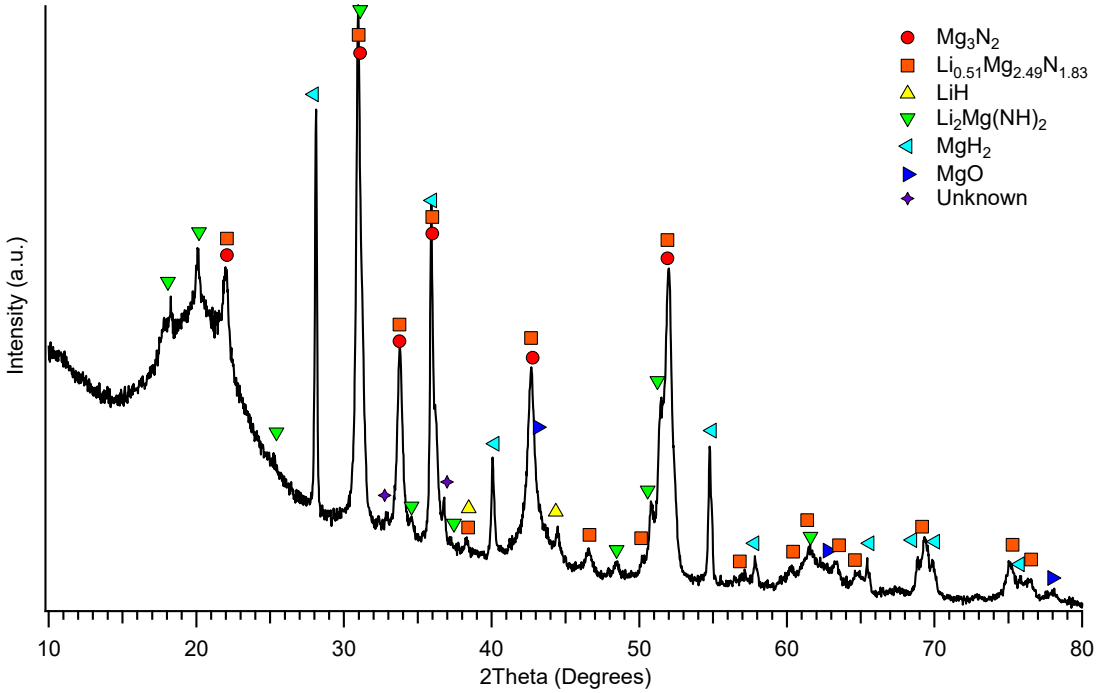

Figure 7.9: XRD analysis of Sample 4 – $Mg(NH_2)_2$ + MgH_2 + LiH (1:1:2) heated to 300 °C.

The reaction between $Mg(NH_2)_2$ and LiH (Equation 7.6) and $Mg(NH_2)_2$ and MgH_2 (Equation 7.4) have an enthalpy of desorption (ΔH_{des}) value of 44.3 kJ (mol H_2)$^{-1}$ and 3.5 kJ (mol H_2)$^{-1}$, respectively (Chen et al. 2006; Hu et al. 2006a). Therefore, it is not possible to study the imide-hydride reaction between MgNH and LiH (Sample 3) as the hydrogen release from the amide-hydride reaction, $Mg(NH_2)_2$ + MgH_2 (1:2), is mildly endothermic such that the equilibrium hydrogen pressure would be impractical at non-ambient temperature. Hence, the interaction between $Mg(NH_2)_2$ and LiH is thermodynamically favoured under the applied hydrogen pressure. This result is observed as the final products for Sample 3 and 4 were near identical after TPD measurements were halted at 500 °C (Figure 7.8).

7.2.2.3 *In situ* synchrotron X-ray diffraction (SXRD) analysis of Sample 3

In situ SXRD analysis of MgNH* + LiH (1:1) is shown in Figure 7.10 with a heating rate of 5 °C min^{-1} in the temperature range of 50 – 500 °C under dynamic

* Incomplete synthesis and contains a mixture of amorphous-MgNH, $Mg(NH_2)_2$ and MgH_2.

vacuum. High oxygen contamination was found in the sample as a result of a leak in the capillary seal that contaminated the sample during transit. Figure 7.10 revealed that the starting reagents consisted of lithium hydroxide (LiOH (3)), MgH_2 (2) and LiH (1). The absence of $Mg(NH_2)_2$ and MgNH is because impure MgNH* was ball milled again with LiH for SXRD, resulting in the transformation of X-ray amorphous phases. As the oxygen-contaminated sample was heated from 50 °C to 300 °C, MgH_2 (2) oxidised to form MgO (5) that increased in peak intensity between 300 °C and 500 °C. By ~400 °C, further oxidation is observed from a reaction between LiH (1) and LiOH (3) to form Li_2O (4) as follows (Kawakami et al. 2009; Equation 7.11):

$$LiH + LiOH \rightarrow Li_2O + H_2 \qquad (7.11)$$

Due to the severity of contamination in this sample, no further conclusions could be made from the imide-hydride reaction, MgNH* + LiH (1:1), under dynamic vacuum.

To observe the desorption properties of the sample under different conditions, Figure 7.11 shows the *in situ* SXRD analysis under a hydrogen back pressure with a heating rate of 5 °C min^{-1}. The initial hydrogen pressure of 2 bar in the gas handling system decreased to ~1 bar (atmospheric pressure) as the reference volume was opened to the sample capillary. This pressure drop suggests a leak caused by the polyimide/graphite ferrules used to seal the capillary to the mount. Furthermore, this leak was confirmed by the same observation of oxide phases compared to the contaminated sample under dynamic vacuum (Figure 7.10). Therefore, no conclusions could be made for the imide-hydride reaction between MgNH* and LiH under a hydrogen back pressure.

* Incomplete synthesis and contains a mixture of amorphous-MgNH, $Mg(NH_2)_2$ and MgH_2.

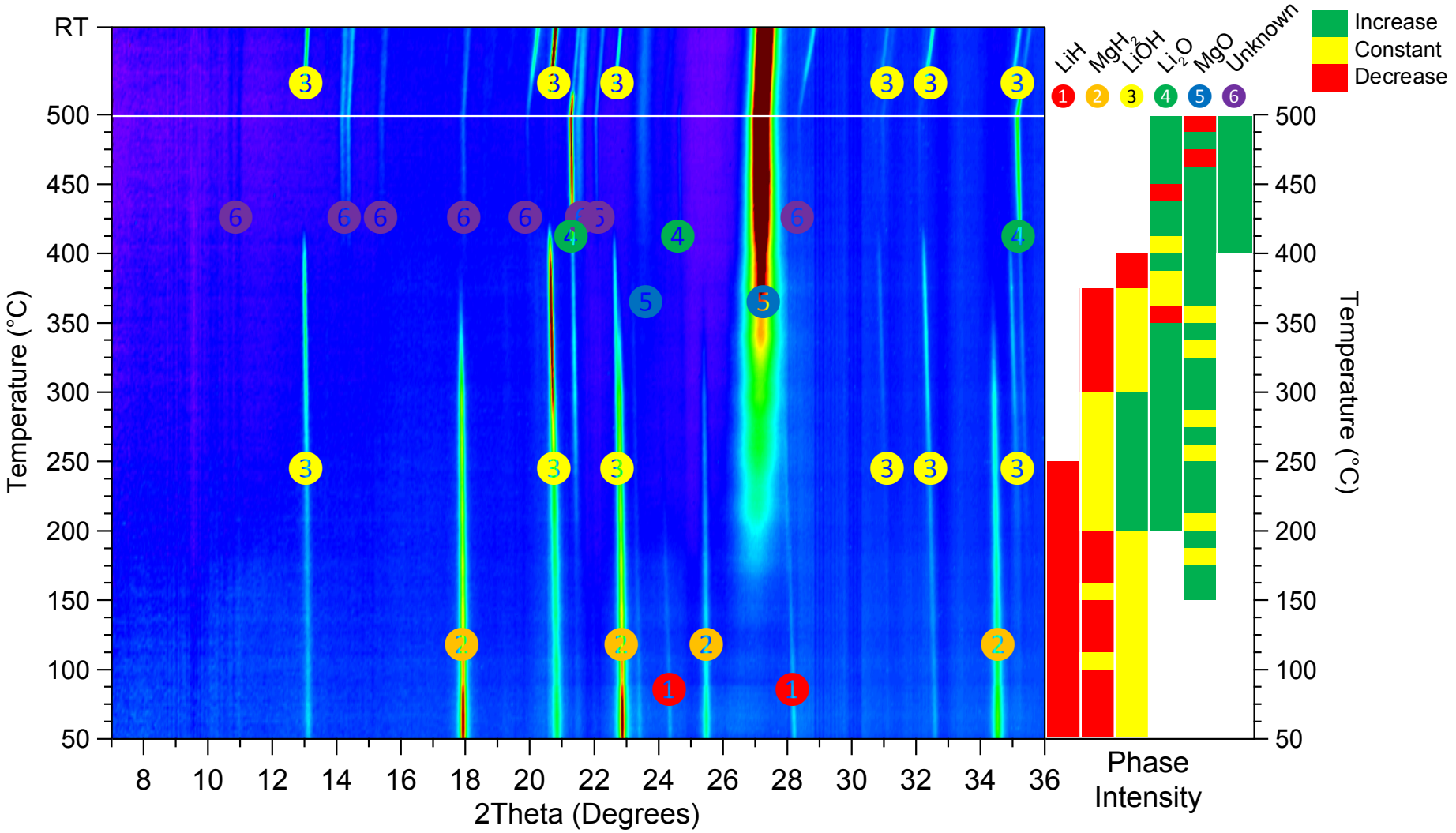

Figure 7.10: *In situ* SXRD analysis (λ = 1.00036 Å) of Sample 3 – MgNH* + LiH (1:1) under dynamic vacuum with phase identification.

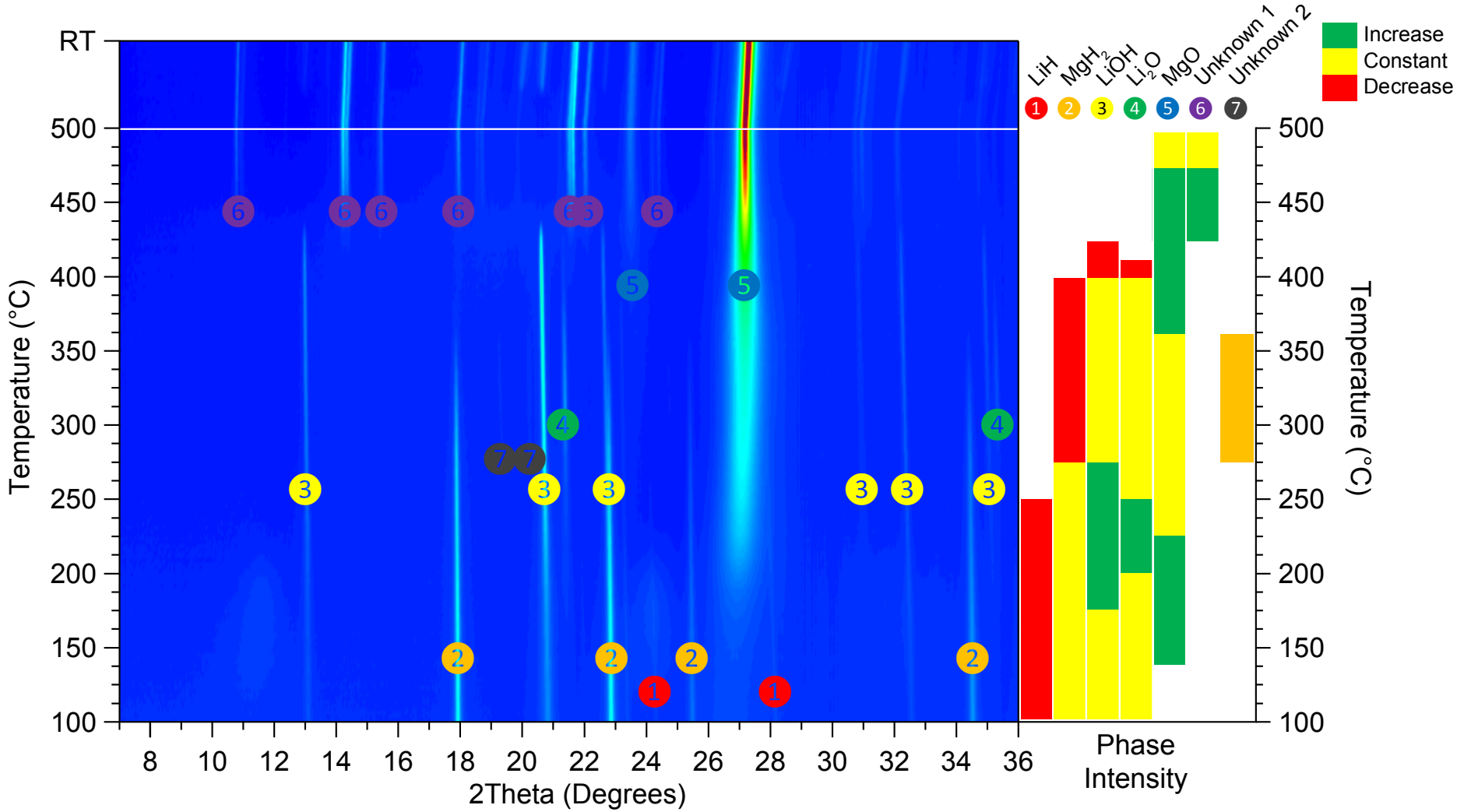

Figure 7.11: *In situ* SXRD analysis (λ = 1.00036 Å) of Sample 3 – MgNH* + LiH (1:1) under a H_2 pressure of ~1 bar with phase identification.

7.2.2.4 Discussion

The dehydrogenation reaction of Sample 4 – $Mg(NH_2)_2$ + MgH_2 + LiH (1:1:2) was investigated by means of TPD-VM and XRD measurements. The proposed mechanism for Sample 4 can be summarised in the following reactions:

$$Mg(NH_2)_2 + MgH_2 + 2LiH \rightarrow \frac{1}{2}Li_2Mg(NH)_2 + \frac{1}{2}Mg(NH_2)_2 + MgH_2 + LiH + H_2 \quad (7.8a)$$

$$\rightarrow \frac{1}{2}Li_2Mg(NH)_2 + \frac{1}{2}Mg_3N_2 + LiH + 3H_2 \quad (7.9a)$$

$$\rightarrow 2LiMgN + 4H_2 \quad (7.10a)$$

where $Mg(NH_2)_2$ and LiH react in Equation 7.8a to release hydrogen at ~200 °C (Zak-Fang, Lu and Sohn 2008). $Mg(NH_2)_2$ and MgH_2 react in Equation 7.9a to release hydrogen at 275 °C (Liu et al. 2008). Lastly, $Li_2Mg(NH)_2$, Mg_3N_2 and LiH react in Equation 7.10a to form LiMgN corresponding to the release hydrogen at ~461 °C (Akbarzadeh, Ozoliņš and Wolverton 2007). The temperatures were derived from the desorption events in the TPD-VM analysis (Figure 7.7) and the reaction pathway was derived by XRD analyses at 500 °C and 300 °C (Figure 7.8 and 7.9, respectively).

Temperature programmed desorption using the volumetric method can only measure the total gas pressure of evolved gases within the Sieverts' system. Therefore, a mass spectrometry measurement was required to identify the gas species to clarify the TPD-MS results from Hu et al. (2007), and confirm the proposed reaction pathway in Equation 7.8a, 7.9a and 7.10a. Furthermore, this measurement is required because the ammonia desorption events they described did not match with the products seen in XRD analysis due to the absence of $Li_2Mg_2(NH)_3$. Hence, further investigation is required on this system, particularly in the temperature range between 275 °C and 500 °C. However, it was concluded that the overall reaction pathway for Sample 4 – $Mg(NH_2)_2$ + MgH_2 + LiH (1:1:2), does not form MgNH (from the amide-hydride reaction) to react with LiH in the anticipated two-step amide-hydride to imide-hydride reaction in Equation 7.3 and 7.1a as the operating pressures to form MgNH were impractical at high temperatures.

7.2.3 LiMgN + H_2 (1:2)

An important characteristic of thermal storage materials is the reversibility of the system by investigating whether the expected dehydrogenated products can absorb hydrogen in the reverse reaction. To investigate the reversibility of the imide-hydride reaction, MgNH + LiH (1:1), LiMgN was hydrogenated to study the reverse reaction of Equation 7.2 with the theoretical reaction pathway as follows:

$$LiMgN + 2H_2 \rightarrow MgNH + LiH + H_2 \rightarrow \frac{1}{2}Mg(NH_2)_2 + \frac{1}{2}MgH_2 + LiH \qquad (7.12)$$

where the hydrogenation products could be MgNH and LiH from the nitride to imide-hydride reaction or a mixture of $Mg(NH_2)_2$, MgH_2 and LiH from the imide to amide-hydride reaction. Furthermore, LiMgN + H_2 (1:2) has a theoretical absorption capacity of ~8.2 wt% of H_2.

7.2.3.1 Synthesis of Sample 5

LiMgN was prepared by ball milling the starting reagents Li_3N (Sigma-Aldrich, ≥ 99.5%) and Mg_3N_2 (Alfar-Aesar, 99.6%) followed by heat treatment. The reagents were thoroughly mixed in a planetary ball-mill for 4 hours in a 1:1 molar ratio (Li_3N_2:Mg_3N_2) and operated at 400 RPM with a BTP ratio of 30:1 using 316 stainless-steel balls sized at 10 mm and 6 mm. The mixture was annealed at 500 °C under a static nitrogen pressure of 3.8 bar for 6 hours (Figure 7.12b) and a further 5 days under 3.4 bar (Figure 7.12d), based on the experimental method that has been published by Bailey et al. (2010).

There were minimal differences observed between annealing the sample for 6 hours and for 5 days by *ex situ* XRD analysis (Figure 7.12b and 7.12d). However, oxide contamination was present in the synthesis of LiMgN after annealing for 5 days, which suggests either increased crystallinity of MgO because of the long annealing time or a small leak in the sample-cell reactor. Non-stoichiometric $Li_xMg_yN_z$ ($0.24 \leq x \leq 1.04$, $0.96 \leq y \leq 2.76$, $0.96 \leq z \leq 1.83$) can be found after heating a mixture of Li_3N and Mg_3N_2 to 500 °C. However, the crystal structure of $Li_xMg_yN_z$ and Mg_3N_2 have similar peak positions that make it difficult to determine the experimental quantity (wt%) using Rietveld refinement.

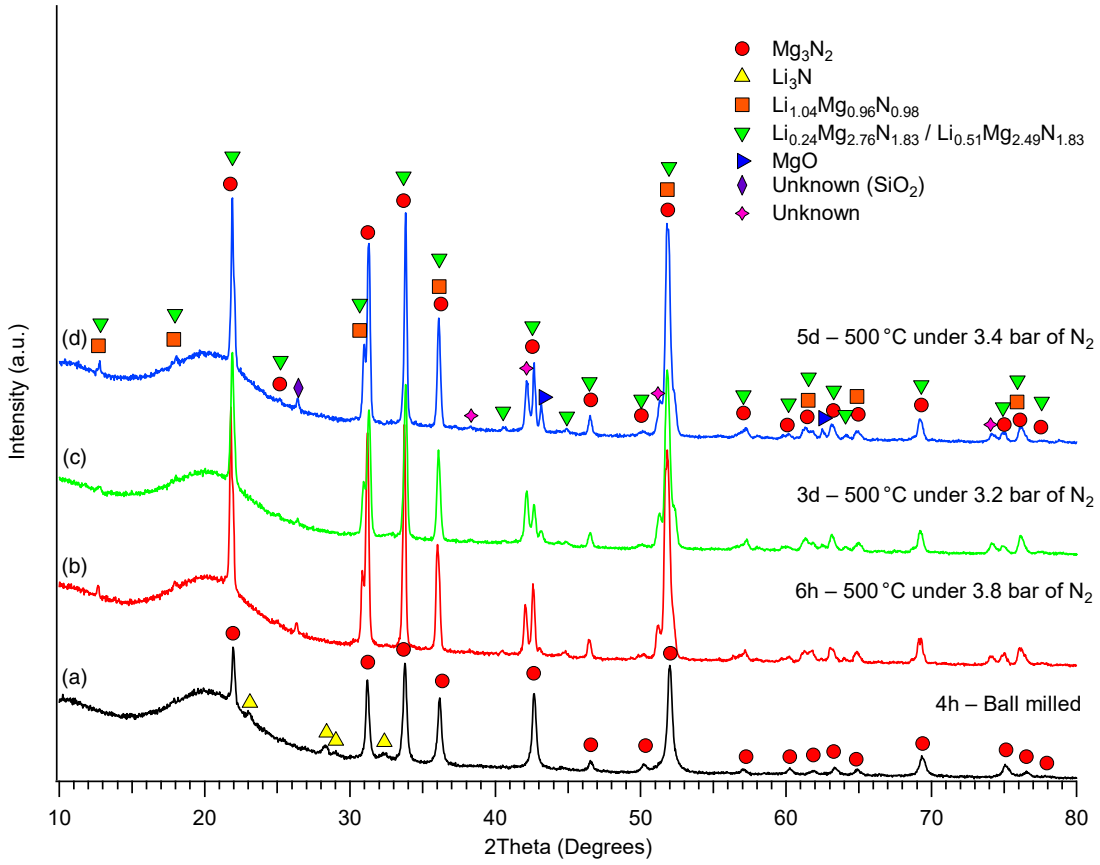

Figure 7.12: Comparitive XRD analysis of synthesised LiMgN after (a) ball-milling and annealing at 500 °C for (b) 6 hours under 3.8 bar of N_2, (c) 3 days under 3.2 bar of N_2 and (d) 5 days under 3.4 bar of N_2.

7.2.3.2 Temperature programmed absorption/desorption (TPA and TPD) with the volumetric method (VM)

Temperature programmed absorption (TPA) measurements were performed to measure the absorption of hydrogen corresponding to the change in absolute gas pressure in a closed volume. Because of the low pressure changes recorded in the system, the FilterFIR command in Igor Pro 6.31 (WaveMetrics, Oregon, USA) was used to reduce the background noise by applying a high-pass and low-pass filter on the TPA-VM data, these results can be viewed in Appendix A (Figure A.15). Using the volumetric approach, the absorption intensity (a.u.) corresponds to the rate of change in hydrogen content of the sample (i.e. the amount of hydrogen absorbed). All TPA and TPD measurements were performed using a sample mass of ~554 mg of LiMgN in the temperature range of 50 – 520 °C in a closed system with a heating and cooling rate of 1 °C min^{-1}. The first absorption measurement (TPA #1; —) began at room temperature with an initial hydrogen

pressure of 30 bar. The TPA-VM analysis in Figure 7.13a showed that for as-synthesised LiMgN, the absorption of hydrogen began at ~200 °C and peaked at a temperature of 362 °C with evidence of a shoulder peak at ~290 °C. After reaching 520 °C, the sample was cooled to room temperature and evacuated before the desorption measurement was performed commencing at vacuum (0 bar). However, a power failure during the measurement resulted in loss of TPD-VM data but, with the sample now in its dehydrogenated state, it was cooled to room temperature before the next absorption measurement was performed.

The second TPA-VM measurement (TPA #2; —) was performed with an initial hydrogen pressure of 45 bar at room temperature. The TPA-VM analysis in Figure 7.13b showed that the sample started to absorb hydrogen in two steps (previously one-step) at 232 °C and 362 °C. The sample was cooled to room temperature and evacuated before the sample was dehydrogenated by performing a TPD-VM measurement starting at vacuum (0 bar). The TPD-VM analysis (TPD #2) of the rehydrogenated state in Figure 7.14 revealed multiple desorption events at 215, 364, 440 and 493 °C. The sample was cooled to room temperature and evacuated before the third TPA-VM measurement (TPA #3; —) was performed with an initial hydrogen pressure of 15 bar. The TPA-VM analysis in Figure 7.13c showed similar absorption events to TPA #2 with two absorption events peaking at a temperature of 232 °C and 362 °C.

After the third TPA-VM measurement (TPA #3; —), to ensure the sample was in its hydrogenated state, the sample was rehydrided with a hydrogen pressure of 45 bar at ~500 °C to prepare for XRD analysis (Figure 7.15). The final rehydrogenated products of LiMgN in Figure 7.15 appeared to be a mixture of phases including: α-$Li_2Mg(NH)_2$ (~40 wt%), β-$Li_2Mg(NH)_2$ (~6 wt%) and LiH (~7 wt%). Because of the overlapping XRD patterns for non-stoichiometric $Li_{0.51}Mg_{2.49}N_{1.83}$ and Mg_3N_2 phases, they could not be effectively quantified (wt%) by Rietveld refinement but amount to ~40 wt% of the entire sample. The appearance of MgO (7.98 wt%) was due to contaminants already present in the starting materials.

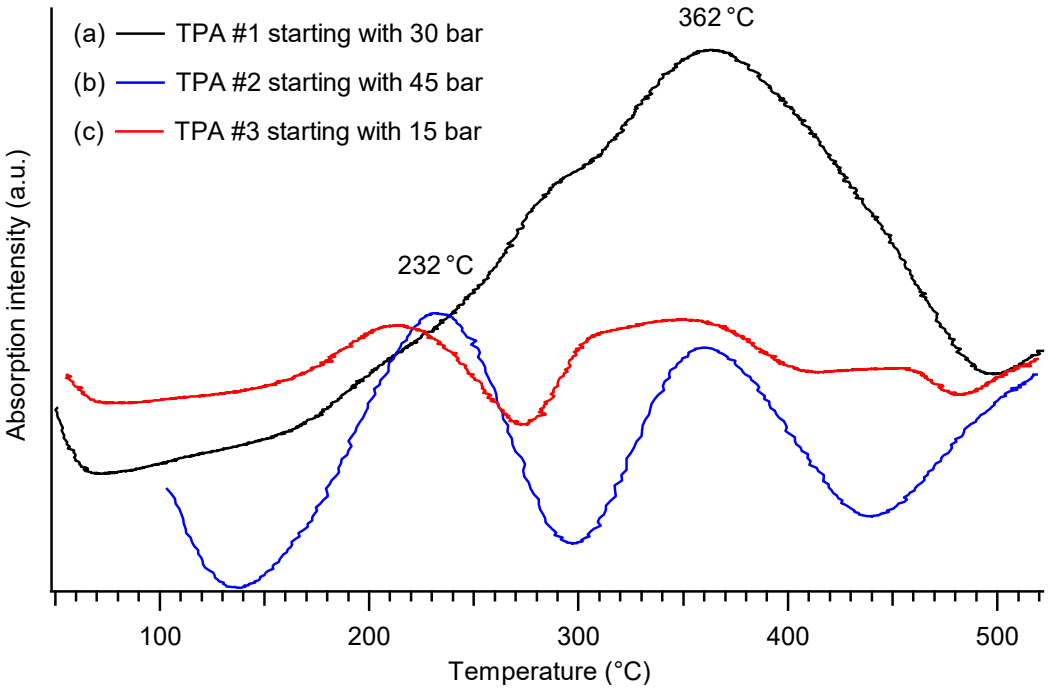

Figure 7.13: TPA-VM analysis of the hydrogenation of LiMgN in the temperature range of 50 – 520 °C. The heating rates were 1 °C min^{-1} starting at a hydrogen pressure of (a) 30 bar, (b) 45 bar and (c) 15 bar.

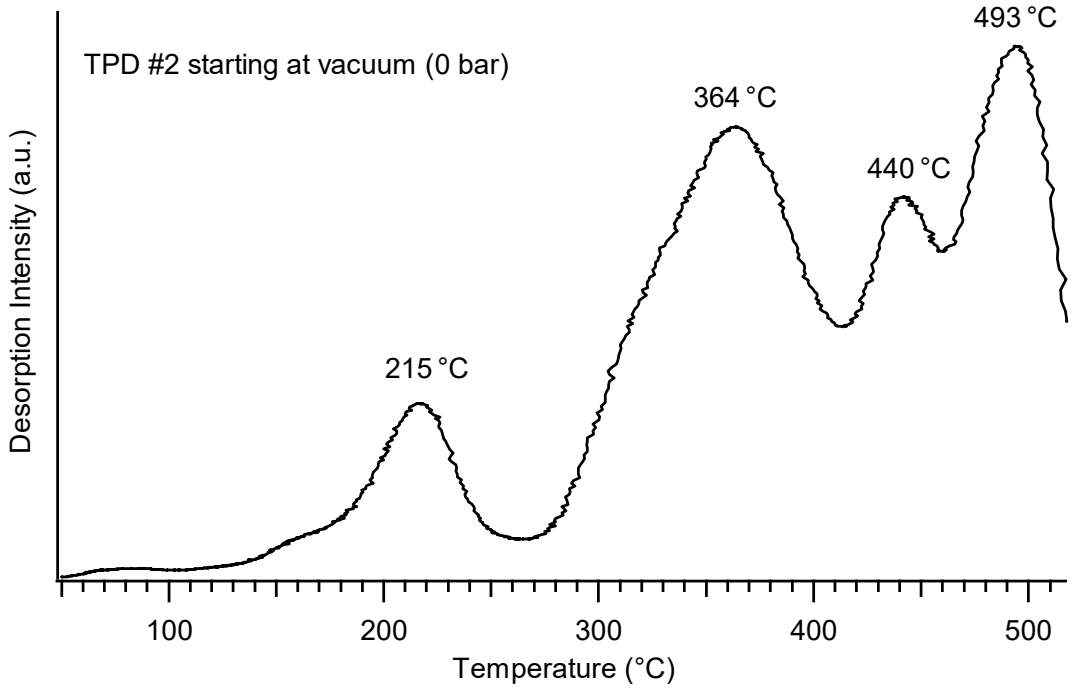

Figure 7.14: TPD-VM analysis of hydrogenated products of LiMgN in the temperature range of 50 – 520 °C after performing TPA #2. The heating rate was 1 °C min^{-1} starting at vacuum.

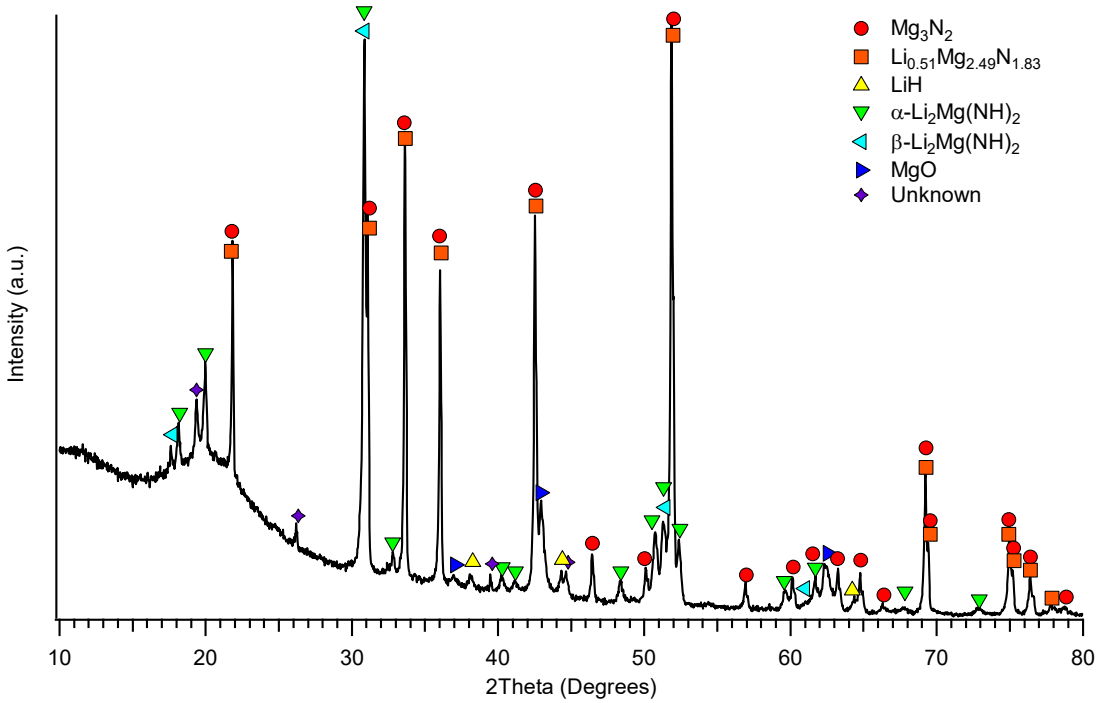

Figure 7.15: XRD analysis after the rehydrogenation of LiMgN at ~500 °C under a hydrogen pressure of 45 bar.

7.2.3.3 Pressure-composition-temperature (PCT) measurements

Pressure-composition-temperature measurements were performed on the hydrogenation of LiMgN to understand the thermodynamic properties of the imide-nitride-hydride system. Figure 7.16a shows the PCT measurement of the hydrogenation of LiMgN at 365 °C, where a plateau region occurred at a hydrogen content of 0.7 – 1.2 wt% with an equilibrium pressure of ~1.7 bar. Beyond a hydrogen content of ~1.2 wt%, the sloping shape of the curve suggests a solid-solution behaviour up to a hydrogen content of ~1.9 wt%. LiMgN + H_2 (1:2), however, has a theoretical hydrogen content of ~8.2 wt%. Therefore, PCT measurements were repeated at 450 °C to investigate the loss of hydrogen capacity of ~6.3 wt% and to re-examine the plateau region between 0.7 wt% and 1.2 wt% of H_2.

The PCT measurements of LiMgN at 450 °C; however, had a problem with the software used to automate the hydrogen sorption apparatus. The software recorded data every 5×10^{-2} seconds, resulting in PCT measurements ending abruptly because of the large data files created (~1 gigabyte per day). Therefore, repeat measurements were set aside for the LVA-NCHC method described in

Chapter 3. Figure 7.16b shows the PCT measurements of LiMgN at 450 °C, where the same plateau region (0.7 – 1.2 wt% of H_2) can be seen from the hydrogenation at 365 °C (Figure 7.16a), confirming a distinct hydrogen absorption reaction with an equilibrium pressure of 2.92 bar at 450 °C. Because of the diffusion and absorption of hydrogen through 316 stainless steel, corrections were made to compensate the loss of hydrogen between PCT measurements using the procedure detailed in Chapter 2: Section 2.5.1. The second absorption (or rehydrogenation) PCT curve in Figure 7.16b shows that beyond a hydrogen content of 1.2 wt%, the sample was able to go up to a maximum hydrogen content of ~1.9 wt%. However, the shape of this region corresponds to a solid-solution behaviour as seen previously in the PCT measurement at 365 °C (Figure 7.16a).

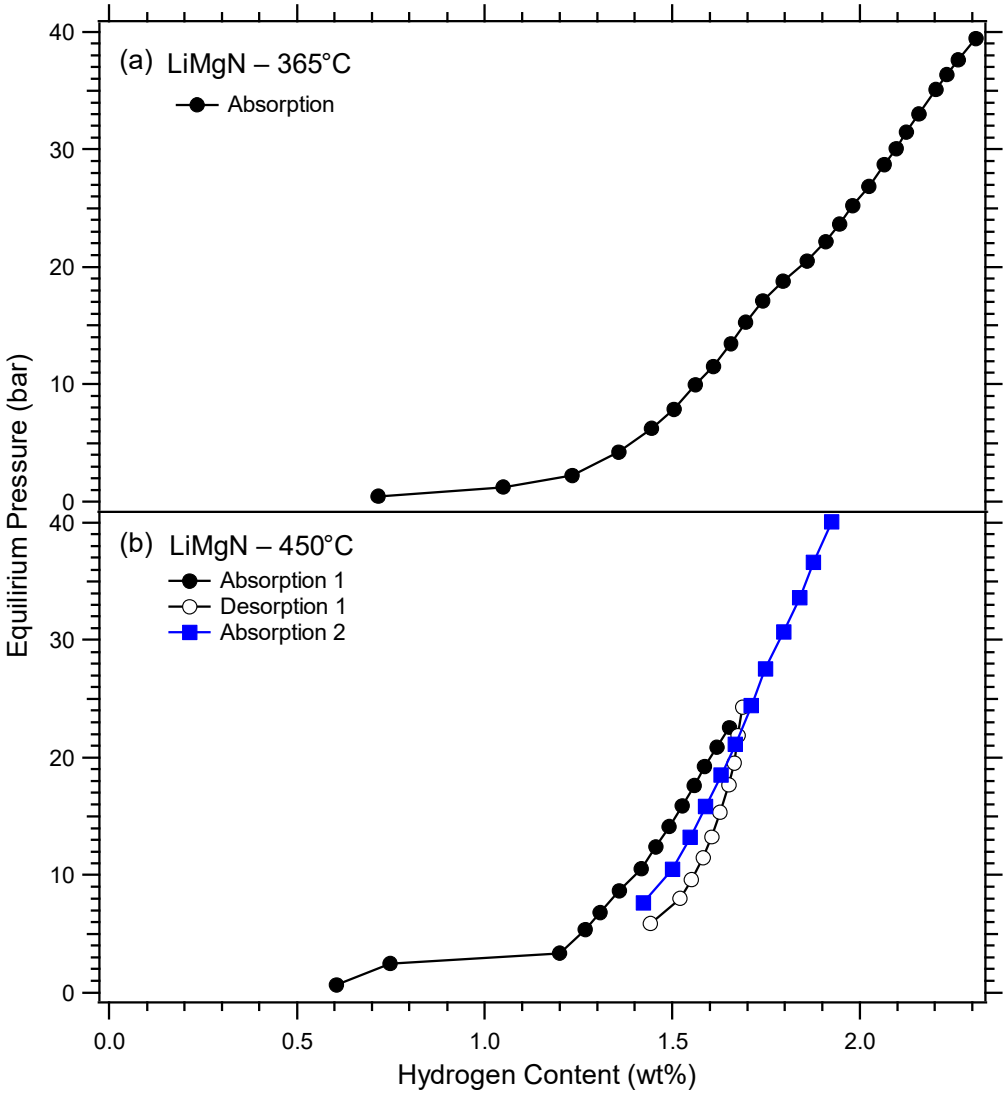

Figure 7.16: PCT measurement of LiMgN at (a) 365 °C and (b) 450 °C.

X-ray diffraction measurements (Figure 7.17a) was performed after the re-absorption PCT measurement at 450 °C. The hydrogenated products of LiMgN were identified to be similar to the products found in the rehydrogenated products after TPA-VM measurements (Figure 7.17b), having a mixture of α-$Li_2Mg(NH)_2$, β-$Li_2Mg(NH)_2$, $Li_{0.51}Mg_{2.49}N_{1.83}$, Mg_3N_2 and LiH.

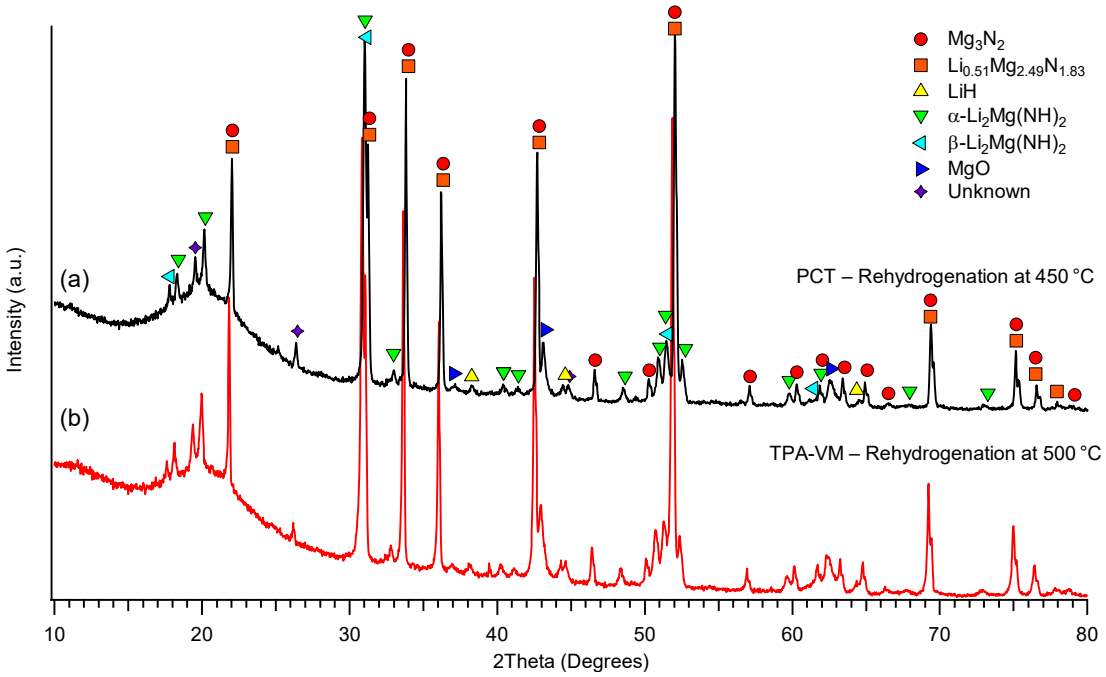

Figure 7.17: Comparison of the rehydrogenation products of LiMgN after (a) PCT measurement at 450 °C and after (b) TPA-VM measurement halted at 500 °C.

7.2.3.4 Discussion

The hydrogenation/dehydrogenation of LiMgN was characterised by TPA/TPD-VM analysis, PCT measurements and XRD analysis. In the TPA-VM analysis (Figure 7.13a), the first absorption of hydrogen of as-synthesised LiMgN revealed a large absorption event at ~362 °C, and the TPD-VM analysis (Figure 7.14) revealed four hydrogen desorption events at 215, 364, 440 and 493 °C. The second and third absorption of hydrogen (rehydrogenation) on the dehydrogenated product revealed absorption events that occurred at 232 °C and 362 °C with the same relative peak intensities, whereas the peak at 362 °C was approximately half of the intensity seen in the initial absorption (Figure 7.13b and 7.13c). XRD analysis (Figure 7.15) on the rehydrogenated products revealed a mixture of $Li_2Mg(NH)_2$ and $Li_{0.51}Mg_{2.49}N_{1.83}$/$Mg_3N_2$ (overlapping XRD pattern). The

formation of $Li_2Mg(NH)_2$ after the initial absorption measurement could explain the hydrogen absorption event observed at 232 °C in the re-absorption measurement (TPA #2 and #3) that was not previously seen in the initial absorption measurement (TPA #1). Furthermore, the absorption peak at 362 °C was lower in intensity compared to the initial absorption measurement (TPA #1). The existence of $Li_{0.51}Mg_{2.49}N_{1.83}/Mg_3N_2$ could also be from the incomplete synthesis of LiMgN, containing residual Mg_3N_2 and non-stoichiometric phases of $Li_xMg_yN_z$.

Given that as-synthesised LiMgN was impure (containing Mg_3N_2), PCT measurements revealed that LiMgN absorbed a maximum hydrogen content of ~1.9 wt% at 450 °C (Figure 7.16b). Based on the proposed formation of LiMgN from a reaction between a mixture of $Li_2Mg(NH)_2$, Mg_3N_2 and LiH (Akbarzadeh, Ozoliņš and Wolverton 2007), and the same mixture of phases identified by XRD analysis at ~500 °C, the possible rehydrogenation reaction pathway of LiMgN at 500 °C is as follows:

$$2LiMgN + H_2 \rightarrow \frac{1}{2}Li_2Mg(NH)_2 + \frac{1}{2}Mg_3N_2 + LiH \qquad (7.13)$$

where Equation 7.13 has a theoretical hydrogen content of ~2.2 wt%, which is closer to the experimental value (given that LiMgN was impure) compared to a theoretical hydrogen content of ~8.2 wt% in Equation 7.12, LiMgN + H_2 (1:2).

Lu et al. (2007) reported that LiMgN (with a small amount of $TiCl_3$) could be rehydrogenated at 160 °C under a hydrogen pressure of ~140 bar. Their TGA results showed a hydrogen content of 8.0 wt% that corresponded to the reaction in Equation 7.12 with a theoretical hydrogen content of ~8.2 wt%. The difference in observed hydrogen content suggests that the working pressure was not high enough for a complete rehydrogenation reaction (Equation 7.12). Hence, only the reaction pathway in Equation 7.13 occurred (theoretical hydrogen content of ~2.2 wt%), which is in general agreement with the experimental hydrogen content of ~1.9 wt%. Furthermore, XRD analysis after the rehydrogenation of LiMgN at 450 °C revealed a mixture of $Li_2Mg(NH)_2$, LiH and Mg_3N_2 that is consistent with the reaction in Equation 7.13 given that $Li_{0.51}Mg_{2.49}N_{1.83}$ exists as a residual product.

The equilibrium pressure (2.92 bar) obtained from PCT measurements at 450 °C can be used to estimate the uncertainty on enthalpy (ΔH_{abs}) by assuming an entropy (ΔS_{abs}) range between –100 and –140 J (mol H_2)$^{-1}$ K^{-1}. Table 7.3 shows that the estimated ΔH_{abs} value ranges between –65.9 and –94.8 kJ (mol H_2)$^{-1}$. The magnitude range of $|\Delta H_{abs}|$ values in Table 7.3 were used to calculate the uncertainty on the practical heat storage capacity of LiMgN + H_2 (2:1) (Equation 7.13; ~2.2 wt% of H_2) to be between 392 and 564 kJ kg^{-1} for a practical hydrogen content of ~1.2 wt% (end of plateau region) as seen in Figure 7.16b. The enthalpy of absorption and practical heat storage capacity is lower than the values calculated for Ca_2NH at –107.8 ± 6.5 kJ (mol H_2)$^{-1}$ and 959 ± 58 kJ kg^{-1}, respectively (Chapter 5: Section 6.2.3). The lower thermodynamic values are a result of the short plateau observed (0.7 – 1.2 wt% of H_2) for LiMgN compared to Ca_2NH (0.1 – 1.8 wt% of H_2). The operating pressure at elevated temperatures is an important factor for practical thermal energy storage to reduce engineering costs. From Table 7.3, the Li–Mg–N–H system has an estimated uncertainty on the equilibrium pressure range between ~100 bar and ~500 bar at 800 °C, which is impractical for thermal energy storage by assuming ΔH_{abs} = –94.8 kJ (mol H_2)$^{-1}$.

Table 7.3: Estimated uncertainty on the enthalpy of absorption and equilibrium pressure by assuming an entropy value between –100 and –140 J (mol H_2)$^{-1}$ K^{-1}, based on the equilibrium H_2 pressure of 2.92 bar at 450 °C.

Assumed ΔS_{abs} (J (mol H_2)$^{-1}$ K^{-1})	–100	–110	–120	–130	–140
Estimated ΔH_{abs} (kJ (mol H_2)$^{-1}$)	–65.9	–79.1	–80.3	–87.6	–94.8

Temperature (°C)	Estimated absorption P_{eq} (bar)				
450	2.92	2.92	2.92	2.92	2.92
600	19.2	23.6	29.0	35.6	43.8
650	31.3	40.7	52.8	68.5	88.9
700	48.7	66.4	90.4	123.1	167.7
750	72.5	103.2	146.8	208.9	297.2
800	104.0	154.0	228.0	337.5	499.6

7.2.4 $Li_6Mg_{0.5}(NH)_3Cl + H_2$ (1:3)

7.2.4.1 Synthesis of Sample 6

$Li_6Mg_{0.5}(NH)_3Cl$ was prepared by ball-milling using the starting reagents Li_2NH (laboratory synthesised; Chapter 4: Section 4.2.2.1) and $MgCl_2$ (Sigma-Aldrich, ≥ 98%). The reagents were thoroughly mixed in a planetary ball-mill for 4 hours in a 6:1 molar ratio (Li_2NH:$MgCl_2$) and operated at 400 RPM with a BTP ratio of 30:1 using 316 stainless-steel balls sized at 10 mm and 6 mm. The mixture was annealed at 400 °C under dynamic vacuum for 13 hours based on the experimental method by Anderson et al. (2011). The ball-milled samples were packed in 0.5 mm borosilicate capillaries with polyimide/graphite ferrules using a custom mount in preparation for SXRD.

7.2.4.2 Discussion of *in situ* synchrotron X-ray diffraction (SXRD) analysis

In situ SXRD analysis of the hydrogenation of $Li_6Mg_{0.5}(NH)_3Cl$ is shown in Figure 7.18 under a hydrogen back pressure with a heating rate of 30 °C min^{-1} at temperatures ≤ 200 °C (excluded in Figure 7.18) and then 7.5 °C min^{-1} in the temperature range 200 – 500 °C. The hydrogen pressure in the gas handling system dropped from 2 bar to 1.4 bar as the pressurised reference volume was open to the evacuated sample capillary and remained the same throughout the measurement. Figure 7.18 confirms that the sample was impure with the starting material Li_2NH (1) identified in the sample at 200 °C. However, $MgCl_2$ could not be identified as a strong peak should occur at a 2θ angle of ~9.75° (Busing 1970). Furthermore, the absence of a LiH phase also suggests that the hydrogenation reaction, according to Equation 7.5, did not take place under the applied hydrogen back pressure of 1.4 bar. The peak intensities for Li_2NH (1) decrease up until 350 °C, while at 350 °C an unknown phase (Unknown 1 5) appears. This observation suggests that Li_2NH (1) and Unknown 2 (4) may have reacted to form Unknown 1 (5).

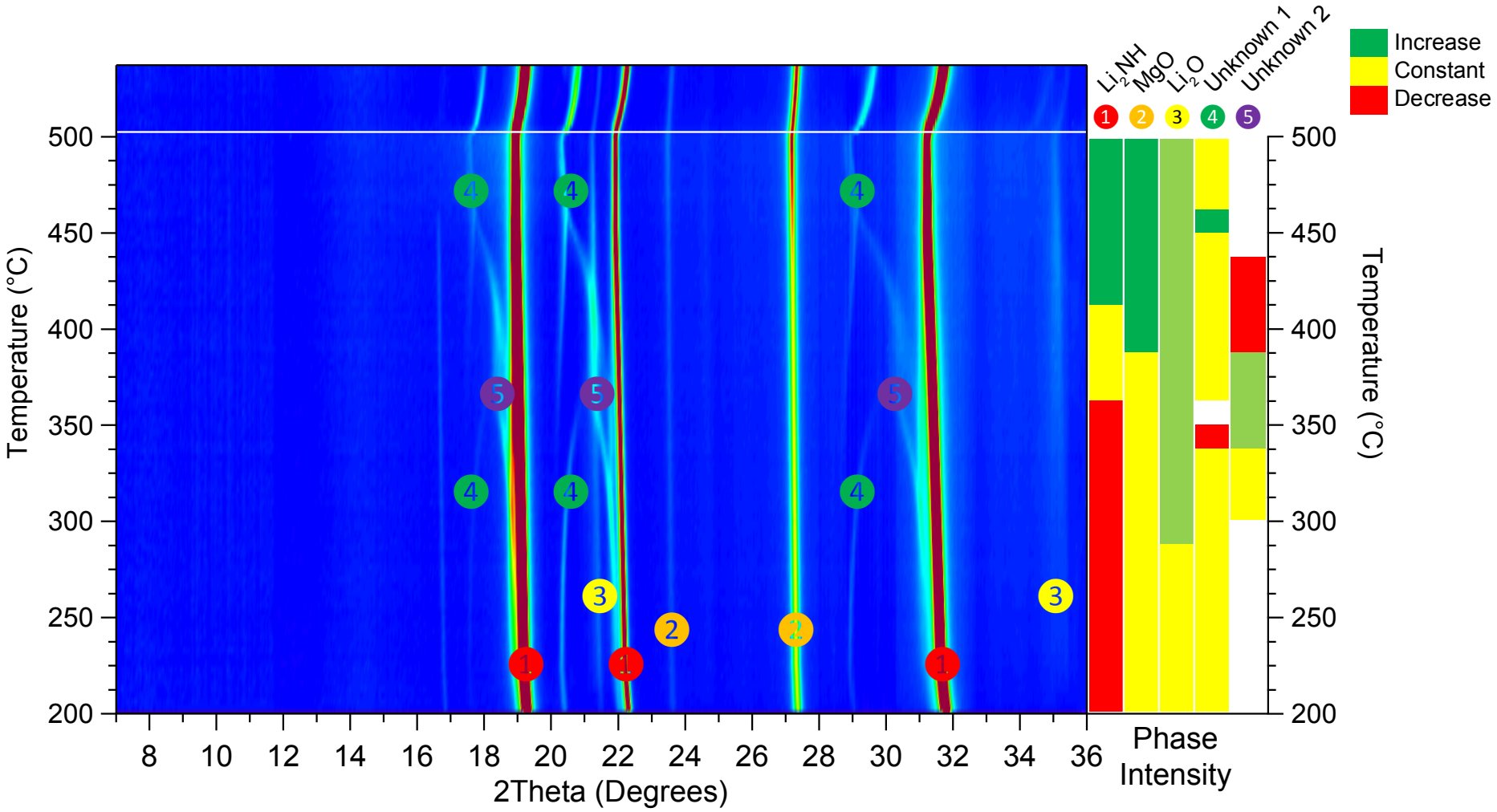

Figure 7.18: *In situ* SXRD analysis (λ = 1.00036 Å) of $Li_6Mg_{0.5}(NH)_3Cl$ under a H_2 back pressure of 1.4 bar with phase identification.

X-ray diffraction analysis performed by Anderson et al. (2011) on the same mixture after heating at 400 °C, revealed the same XRD pattern (peak position and intensities) compared to the results in Figure 7.18. However, Anderson et al. (2011) labelled the peak that occurred at 22° (2θ) in Figure 7.18 as $MgCl_2$, identified by their simulated 2D diffraction pattern that had its strongest peak at a 2θ angle of 35°, which is the equivalent of 22° for the radiation wavelength used in the present investigation (λ = 1.00036 Å). This report suggests that $MgCl_2$ could not be identified because it was overlapped by Li_2NH (1) during the *in situ* SXRD analysis (Figure 7.18).

7.3 Conclusion

The Li–Mg–N–H system was investigated using imide-hydride reactions between $Li_2Mg(NH)_2$ and LiH (Sample 1), and MgNH and LiH (Sample 3). A mixture of $LiNH_2$, MgH_2 and LiH (Sample 2) was initially investigated to study the two-step reaction pathway in which $Li_2Mg(NH)_2$ is formed ($LiNH_2$–MgH_2) and subsequently reacts with LiH to form a nitride product. TPD-VM analysis (Figure 7.2b) of this ternary mixture (Sample 2) revealed a significant hydrogen desorption event at ~246 °C and a second smaller event at ~458 °C. XRD analysis (Figure 7.3) revealed that the hydrogen desorption event at ~246 °C was associated with the reaction between $LiNH_2$ and LiH to form a non-stoichiometric imide phase ($Li_{2-y}NH_{1+y}$). However, *in situ* SXRD analysis of the impure imide-hydride reaction (Sample 1; $Li_2Mg(NH)_2$* and LiH) revealed that the hydrogen desorption event at ~250 °C was associated with the complete formation of $Li_2Mg(NH)_2$ using residual starting reagents from impure $Li_2Mg(NH)_2$*. XRD and *in situ* SXRD analysis revealed that the hydrogen desorption event at ~460 °C was associated with the formation of another non-stoichiometric phase of $Li_xMg_yN_z$. From the expected reaction pathway of the binary mixture (Sample 1) and the absence of Li_3N in the final product, the formation of stoichiometric LiMgN and Li_3N does not proceed at temperatures ≤ 500 °C for the imide-hydride reaction, Sample 1 – $Li_2Mg(NH)_2$* + LiH (1:2), and amide-imide-hydride reaction, Sample 2 – $LiNH_2$ + MgH_2 + LiH (2:1:2).

* Impure starting reagent, prepared for synchrotron X-ray diffraction.

A ternary mixture of $Mg(NH_2)_2$, MgH_2 and LiH (Sample 4) was investigated to study the two-step reaction pathway in which MgNH is formed ($Mg(NH_2)_2$–MgH_2) and subsequently reacts with LiH to form a nitride product at a higher temperature. However, the expected two-step reaction pathway was not achieved as the amide-hydride reaction between $Mg(NH_2)_2$ and LiH was thermodynamically favoured over the formation of MgNH (from the amide-hydride reaction, $Mg(NH_2)_2$–MgH_2). TPD-VM analysis (Figure 7.7) of the ternary mixture (Sample 4) revealed multiple gaseous release events, where XRD analyses (Figure 7.8 and 7.9) revealed the events were associated with the formation of $Li_2Mg(NH)_2$ and LiMgN at temperatures $\leq$ 500 °C. *In situ* SXRD analysis of the imide-hydride reaction between MgNH* and LiH (Sample 3) revealed unreliable results as the sample was severely contaminated with oxides. Hence, no conclusions for Sample 3 – MgNH* + LiH (1:1) could be made, where further investigation is required.

The reverse reaction in the Li–Mg–N–H system was investigated by the hydrogenation of LiMgN (Sample 5). TPA-VM analysis (Figure 7.13) revealed that a large absorption event occurred at ~362 °C and TPD-VM analysis (Figure 7.14) of the hydrogenated products revealed four desorption events at 215, 364, 440 and 493 °C. TPA-VM analysis of the desorption products (rehydrogenation) revealed two absorption events at 232 °C and 362 °C. Therefore, the absorption of hydrogen on as-synthesised LiMgN occurred in one step (232 °C), whereas the re-absorption of hydrogen (after desorption) occurred in two steps (232 °C and 362 °C). XRD analysis (Figure 7.15) of the rehydrogenated products revealed a mixture of α-$Li_2Mg(NH)_2$, β-$Li_2Mg(NH)_2$, $Li_{0.51}Mg_{2.49}N_{1.83}$/$Mg_3N_2$ (overlapping XRD pattern) and LiH. PCT measurements of impure LiMgN (containing Mg_3N_2) at 365 °C and 450 °C, revealed a short plateau region from 0.7 – 1.2 wt% of H_2 at an equilibrium pressure of 2.92 bar at 450 °C. Based on the experimental hydrogen capacity (~1.9 wt%) and XRD analysis, the reversible reaction involves the formation of LiMgN via a reaction between $Li_2Mg(NH)_2$, Mg_3N_2 and LiH. By assuming an entropy (ΔS_{abs}) range between –100 and –140 J $(mol\ H_2)^{-1}\ K^{-1}$), the uncertainty on the enthalpy of absorption was estimated to range between –65.9 and –94.8 kJ $(mol\ H_2)^{-1}$ corresponding to a

* Impure starting reagent, prepared for synchrotron X-ray diffraction.

practical heat storage capacity that ranges between 392 and 564 kJ kg^{-1} for a reversible practical hydrogen content of ~1.2 wt%.

The hydrogenation of $Li_6Mg_{0.5}(NH)_3Cl$ (Sample 6) was investigated based on the TPD analysis by Anderson et al. (2011) who reported that the amide halide-hydride reaction, $Li_3Mg_{0.5}(NH_2)_3Cl$ + LiH (1:3), released hydrogen at ~275 °C. In contrast to the expected reaction pathway, *in situ* SXRD analysis revealed that the hydrogenation of the imide halide ($Li_6Mg_{0.5}(NH)_3Cl$) did not proceed under the applied experimental conditions due to the absence of LiH at temperatures $\leq$ 500 °C. Therefore, further investigation is required on the lithium-magnesium-imide-halide system as the *in situ* SXRD analysis was inconclusive for thermal energy storage properties.

The lithium magnesium imide-hydride mixtures in this chapter revealed that at temperatures $\leq$ 500 °C, $Li_2Mg(NH)_2$ and non-stoichiometric phases of $Li_xMg_yN_z$ were formed as confirmed by TPD-VM, XRD and *in situ* SXRD analysis. However, given the low estimated range of heat-storage capacity values (392 – 564 kJ kg^{-1}) and their respective hydrogen pressure requirements (104 – 500 bar at 800 °C), the Li–Mg–N–H system may not be viable as a potential candidate for thermal energy storage.

CHAPTER 8: MIXED CATION Li–Ca–N–H SYSTEMS

8.1 Introduction

By analogy of the Li–Mg–N–H system, the Li–Ca–N–H system involves imide-hydride reactions between various mixtures of lithium calcium imide ($Li_2Ca(NH)_2$) with lithium hydride (LiH) and calcium imide (CaNH) with LiH. Most of the work done on the Li–Ca–N–H system have been on the amide-hydride to imide reaction that releases hydrogen at a temperature of ~210 °C (Tokoyoda et al. 2007; Equation 8.1):

$$Ca(NH_2)_2 + 2LiH \rightarrow Li_2Ca(NH)_2 + 2H_2 \quad (8.1)$$

where operating temperatures ≤ 400 °C revealed intermediates between $Ca(NH_2)_2$–LiH and $Li_2Ca(NH)_2$ (Tokoyoda et al. 2007; Wu et al. 2007). Furthermore, compared to the Li–Mg–N–H system, little information can be found on the imide-hydride reactions (Equation 8.2 and 8.3) at high temperatures as the information available on the structure of LiCaN is limited (Cordier et al. 1989; Sorbie 2011). Therefore, two potential imide-hydride to nitride reactions were investigated as expressed in Equation 8.2 and 8.3:

$$Li_2Ca(NH)_2 + 2LiH \rightarrow Li_3N + LiCaN + 2H_2 \quad (8.2)$$

$$CaNH + LiH \rightarrow LiCaN + H_2 \quad (8.3)$$

The reverse reaction in Equation 8.3 was also investigated to study the hydrogenation of LiCaN using manual PCT measurements (for the LVA-NCHC method) and XRD analysis to characterise the thermodynamics and reaction pathways at high temperatures suitable for thermal energy storage.

In this chapter, $Li_2Ca(NH)_2$ and CaNH was synthesised and mixed with LiH to investigate the hydrogen desorption properties using *in situ* synchrotron X-ray diffraction (SXRD). However, pre-mounting the samples at Curtin University before the synchrotron-beam deadline; meant that a number of starting materials used for SXRD measurements were prepared without being able to first check

the purity (using laboratory XRD analysis). In this case, XRD analysis of $Li_2Ca(NH)_2$ after *in situ* SXRD revealed that the synthesis was impure. Table 8.1 shows a summary of the list of samples investigated in this chapter, listing their starting reagents and molar ratios used.

Table 8.1: List of potential imide-hydride systems investigated in Chapter 8.

	Reagents
Sample 1	$Li_2Ca(NH)_2$* + LiH (1:2)
Sample 2	CaNH + LiH (1:1)
Sample 3	LiCaN + H_2 (1:1)

* Impure starting reagent.

8.2 Results

8.2.1 $Li_2Ca(NH)_2$ + LiH (1:2)

8.2.1.1 Preparation

Wu (2008) reportedly synthesised $Li_2Ca(NH)_2$ by annealing $LiNH_2$ and CaH_2 in a 2:1 molar ratio at 320 °C (heating rate of 1 °C min^{-1}) under a constant argon gas flow (overnight). Based on this method, $Li_2Ca(NH)_2$ was ball-milled using the starting reagents $LiNH_2$ (Sigma-Aldrich, 95%) and CaH_2 (laboratory synthesised; Chapter 6: Section 6.2.2). The starting reagents were thoroughly mixed in a planetary ball-mill for 4 hours in a 2:1 molar ratio ($LiNH_2$:CaH_2) and operated at 400 RPM with a BTP ratio of 30:1 using stainless-steel balls sized at 10 mm and 6 mm. Because the laboratory furnaces were not capable of gas flow experiments, the ball-milled sample was outgassed in a closed system and heated at 320 °C for 17 hours.

X-ray diffraction analysis in Figure 8.1 revealed that no $Li_2Ca(NH)_2$ formed under the applied experimental conditions. Furthermore, Rietveld refinement identified the sample contained a CaNH-like phase (~70 wt%), $LiNH_2$ (~16 wt%) and LiH (~12 wt%) with small amounts of contamination (~2 wt% of CaO) originating from the starting reagents. The CaNH-like phase had a cubic structure with

a = 5.0842 Å that has been reported in literature as a solid solution of $Ca(NH_2)_2$ and CaNH (Hino et al. 2005; Juza and Schumacher 1963; Xiong et al. 2003).

The absence of $Li_2Ca(NH)_2$ at 320 °C could be due to the synthesis conditions compared to the method reported by Wu (2008) (closed system against argon flow). FTIR analysis by Chu et al. (2010) reported that the rehydrogenation of $Li_2Ca(NH)_2$ at 200 °C resulted in the formation of a solid-solution phase (70.11 wt%), $LiNH_2$ (17.66 wt%) and LiH (12.23 wt%), where the composition of the solid-solution was $2CaNH–Ca(NH_2)_2$ (Xiong et al. 2007). Therefore, the synthesis of $Li_2Ca(NH)_2$ in Equation 8.4 was possible at 320 °C, but cooling the sample to room temperature under its own generated hydrogen back-pressure may have allowed the re-absorption of hydrogen in accordance with Equation 8.5 (Chu et al. 2010), consistent with the phases identified by XRD analysis in Figure 8.1 and experimental quantity (wt%) of phases by Rietveld refinement.

$$2LiNH_2 + CaH_2 \rightarrow Li_2Ca(NH)_2 + 2H_2 \tag{8.4}$$

$$Li_2Ca(NH)_2 + \frac{4}{3}H_2 \rightarrow \frac{1}{3}\left[2CaNH–Ca(NH_2)_2\right] + \frac{2}{3}LiNH_2 + \frac{4}{3}LiH \tag{8.5}$$

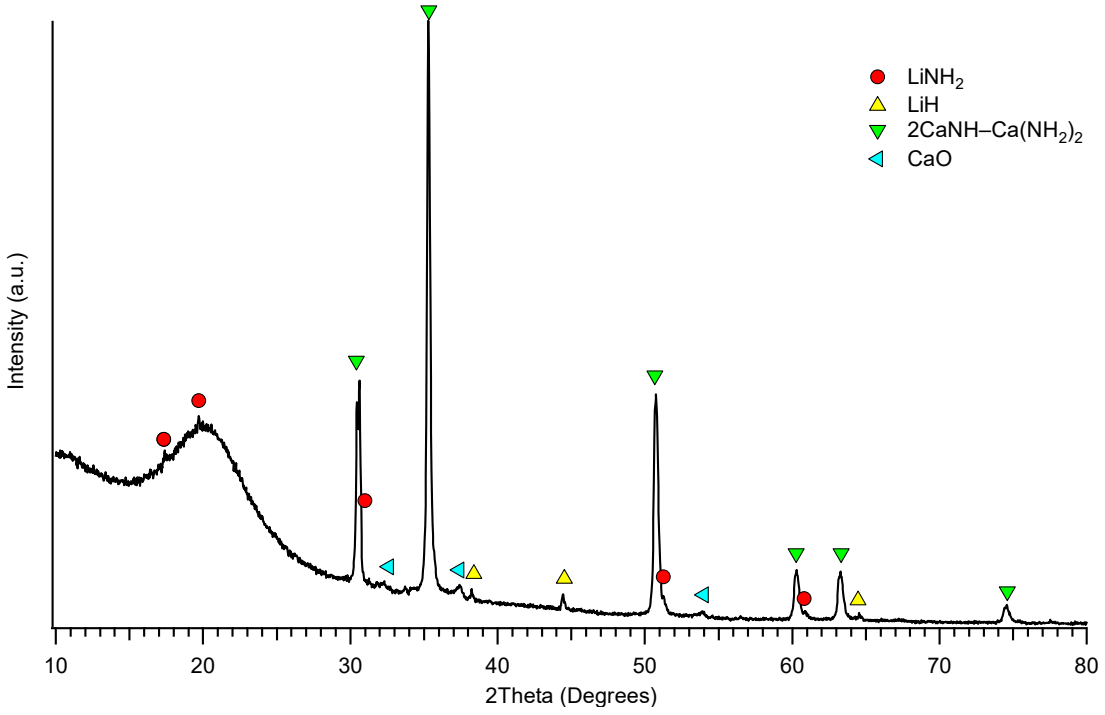

Figure 8.1: XRD analysis of $LiNH_2$ + CaH_2 (2:1) after heat treatment at 320 °C for 17 hours.

Given the challenging synchrotron-beam deadline, the sample for SXRD measurements had to be prepared before the purity of $Li_2Ca(NH)_2$ could be confirmed by laboratory XRD analysis (Figure 8.1). Impure $Li_2Ca(NH)_2$* was thoroughly mixed with LiH in a planetary ball-mill for 4 hours in a 1:2 molar ratio ($Li_2Ca(NH)_2$*:LiH) and operated at 400 RPM with a BTP ratio of 30:1 using 316 stainless-steel balls sized at 10 mm and 6 mm. The ball-milled sample of unknown purity was packed in 0.5 mm borosilicate capillaries using polyimide/graphite ferrules, and then attached to a custom mount for synchrotron X-ray diffraction measurements.

8.2.1.2 Discussion of *in situ* synchrotron X-ray diffraction (SXRD) analysis

In situ SXRD analysis is a useful technique to investigate reaction pathways using the Powder Diffraction beamline at the Australian Synchrotron. Figure 8.2 shows the *in situ* SXRD analysis of the imide-hydride reaction, $Li_2Ca(NH)_2$* + LiH (1:2), under dynamic vacuum with a heating rate of 30 °C min^{-1} at temperatures ≤ 150 °C (excluded in Figure 8.2) and then 5 °C min^{-1} in the temperature range of 150 – 500 °C. The sample at 150 °C (initial phase) was revealed to contain a CaNH-like (solid-solution) phase, LiH (2) and contaminant phases, CaO (3) and Li_2O (4). The CaNH-like phase was previously observed in the XRD analysis of impure $Li_2Ca(NH)_2$* (Figure 8.1) and was identified as a solid-solution, 2CaNH–$Ca(NH_2)_2$ (1). The absence of residual $LiNH_2$ could be due to the low intensity peaks overlapped by the solid-solution (1). The synthesis of $Li_2Ca(NH)_2$ (5) was observed to occur at ~300 °C (i.e. no re-absorption in Equation 8.5) because the sample was heated under dynamic vacuum in accordance with the synthesis method by Wu (2008).

The formation of lithium imide (Li_2NH 6) began at ~275 °C with peak intensities increasing until 375 °C, where it started to decrease in intensity but remained in the sample during cooling (above the white line in Figure 8.2). At temperatures of ~300 °C, the solid-solution (1) peak intensity decreased and began to shift to higher 2θ positions with increasing temperature. This change in angle suggests that the unit cell of the solid-solution is rapidly decreasing in size to a possible formation of cubic $Ca_{1+x}NH$ (7), where $0 \leq x \leq 1$ (Pistidda et al. 2015).

* Incomplete synthesis and contains a mixture of the following: 2CaNH–$Ca(NH_2)_2$, $LiNH_2$ and LiH.

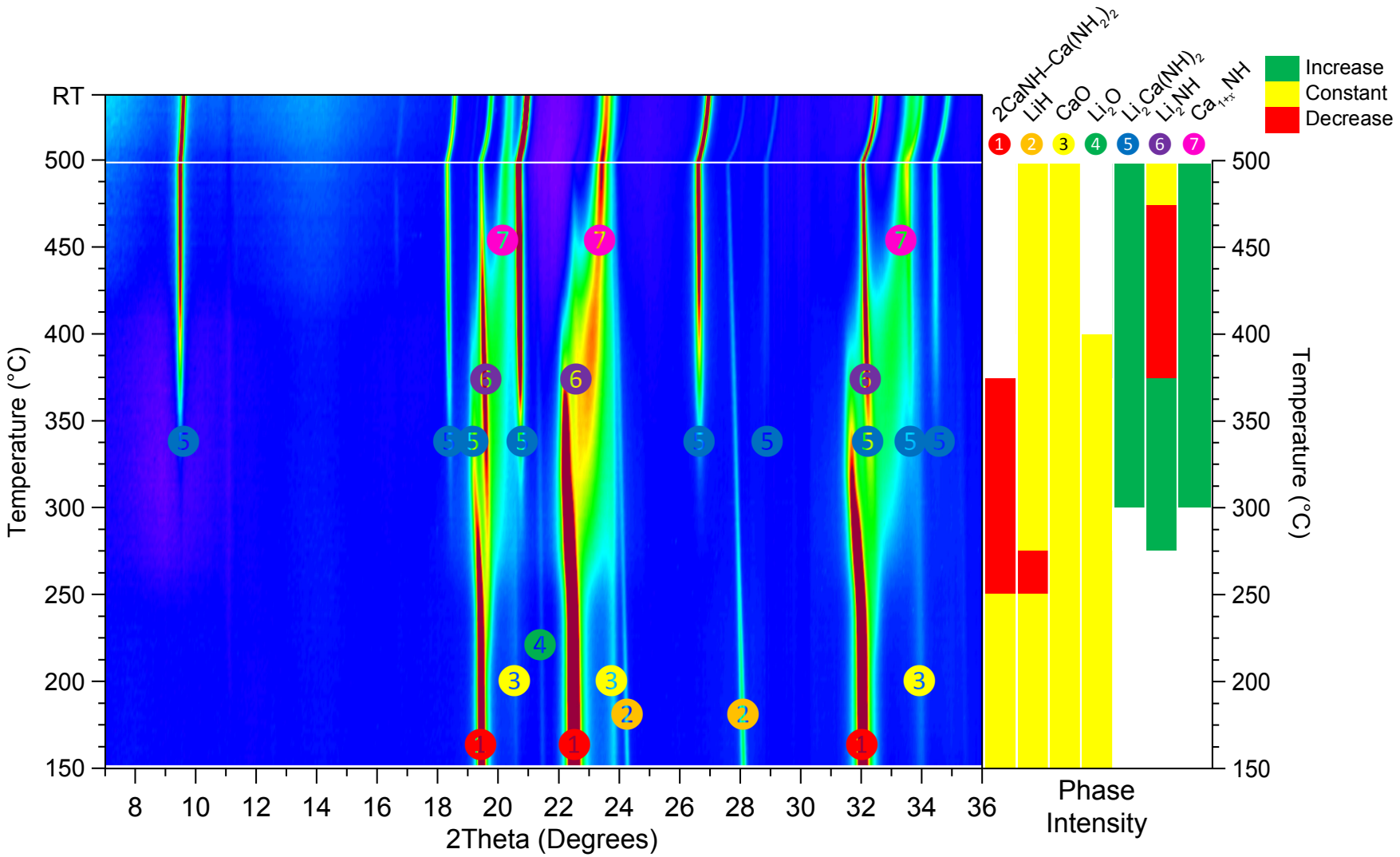

Figure 8.2: *In situ* SXRD analysis (λ = 1.00036 Å) of $Li_2Ca(NH)_2$* + LiH (1:2) under dynamic vacuum with phase identification.

The SXRD measurement under a hydrogen back pressure of 1.4 bar (Figure 8.3) was performed with a heating rate of 5 °C min^{-1} in the temperature range of 100 – 500 °C. Between a temperature of 100 °C and 300 °C, Figure 8.3 revealed some weak intensity peaks that belong to residual $LiNH_2$ (8) at a 2θ angle of ~11° and ~13°, which were not previously seen in the measurement under dynamic vacuum (Figure 8.2). The formation of $Li_2Ca(NH)_2$ (5) also occurred at a higher temperature (~350 °C) than the SXRD measurement under dynamic vacuum. This observation can be attributed to the presence of hydrogen that thermodynamically prevents $Li_2Ca(NH)_2$ formation until higher temperatures are achieved. However, the formation of Li_2NH (6) and the intermediate phase ($Ca_{1+x}NH$ 7) occur at the same temperature (~300 °C) as observed in the measurement under dynamic vacuum (Figure 8.2).

The absence of LiCaN from the anticipated imide-hydride reaction in Equation 8.2 during *in situ* SXRD measurements under dynamic vacuum or a hydrogen back pressure, suggests that the reaction did not occur at temperatures ≤ 500 °C. Because of the maximum temperature safety limits of the Australian Synchrotron, *in situ* SXRD measurements beyond 500 °C were not possible. Therefore, further investigation of this system is required to determine the exact decomposition pathway and its viability as a thermal storage material.

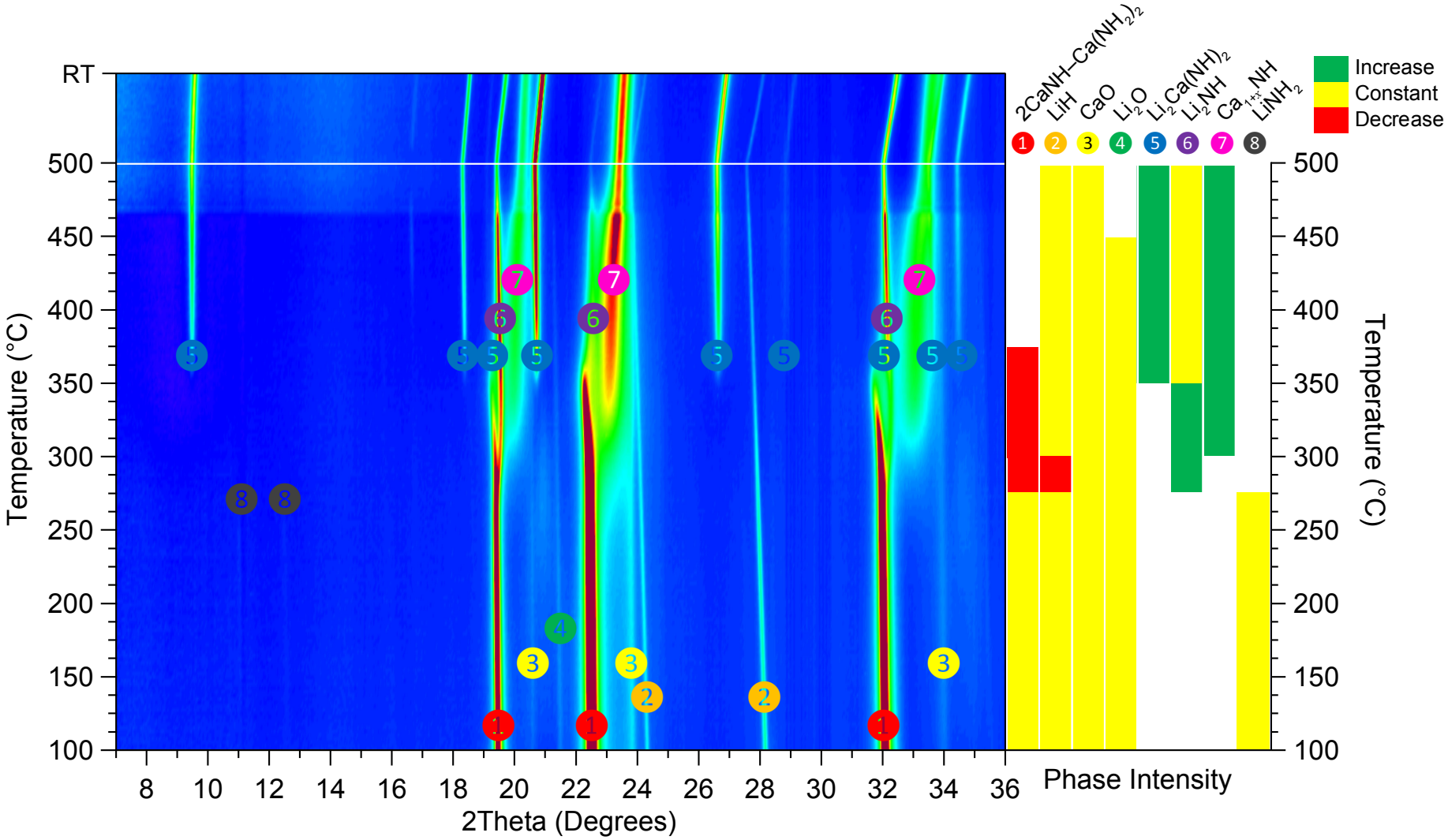

Figure 8.3: *In situ* SXRD analysis (λ = 1.00036 Å) of $Li_2Ca(NH)_2$* + LiH (1:2) under a H_2 back pressure of 1.4 bar with phase identification.

8.2.2 CaNH + LiH (1:1)

8.2.2.1 Preparation

CaNH + LiH (1:1) was prepared by ball-milling using the starting reagents CaNH (laboratory synthesised; Chapter 6: Section 6.2.1.5) and LiH (Sigma-Aldrich, 95%). XRD analysis and Rietveld refinement of as-synthesised CaNH in Chapter 6: Figure 6.3, revealed that the starting reagent consisted of CaNH (~77 wt%), LiCl (11 wt%) and CaO (~12 wt%), where an unknown (possible halide) phase could also be identified with peaks at distinct 2θ angles of ~15°, ~28° (double peak) and ~33°. The radiation of wavelength used was 1.54059 Å. The reagents were thoroughly mixed in a planetary ball-mill for 4 hours operating at 400 RPM with a BTP ratio of 30:1 using 316 stainless-steel balls sized at 10 mm and 6 mm. The ball-milled samples were packed in 0.5 mm borosilicate capillaries and pre-mounted with polyimide/graphite ferrules, in preparation for synchrotron X-ray diffraction measurements.

8.2.2.2 Discussion of *in situ* synchrotron X-ray diffraction (SXRD) analysis

In situ SXRD was performed to identify *in situ* phases as the sample was heated to high temperatures using the Powder Diffraction beamline at the Australian Synchrotron. Figure 8.4 shows the *in situ* SXRD analysis of the imide-hydride reaction, CaNH + LiH (1:1), with a heating rate of 5 °C min^{-1} in the temperature range of 100 – 500 °C under dynamic vacuum. The *in situ* SXRD analysis in Figure 8.4 revealed that the initial phase (at 100 °C) consisted of CaNH (with overlapping LiCl 1) and LiH (2) with the unknown (possible halide) phase (5) that originated from as-synthesised CaNH, identified in Chapter 6: Figure 6.3. Although the peak positions for $Li_2Ca(NH)_2$ are in agreement with the unknown phase (5) between 7° and 22° (2θ), there is an absence of a strong peak from $Li_2Ca(NH)_2$ at a 2θ angle of ~27°. Furthermore, the double peak observed at ~18° (2θ) is consistent with the XRD analysis (λ = 1.54059 Å) of an unknown (possible halide) phase that had a distinct double peak at ~28°, which is the equivalent of ~18° in Figure 8.4 (λ = 1.00036 Å). Additionally, there should not be enough lithium atoms for the formation of $Li_2Ca(NH)_2$ in this sample.

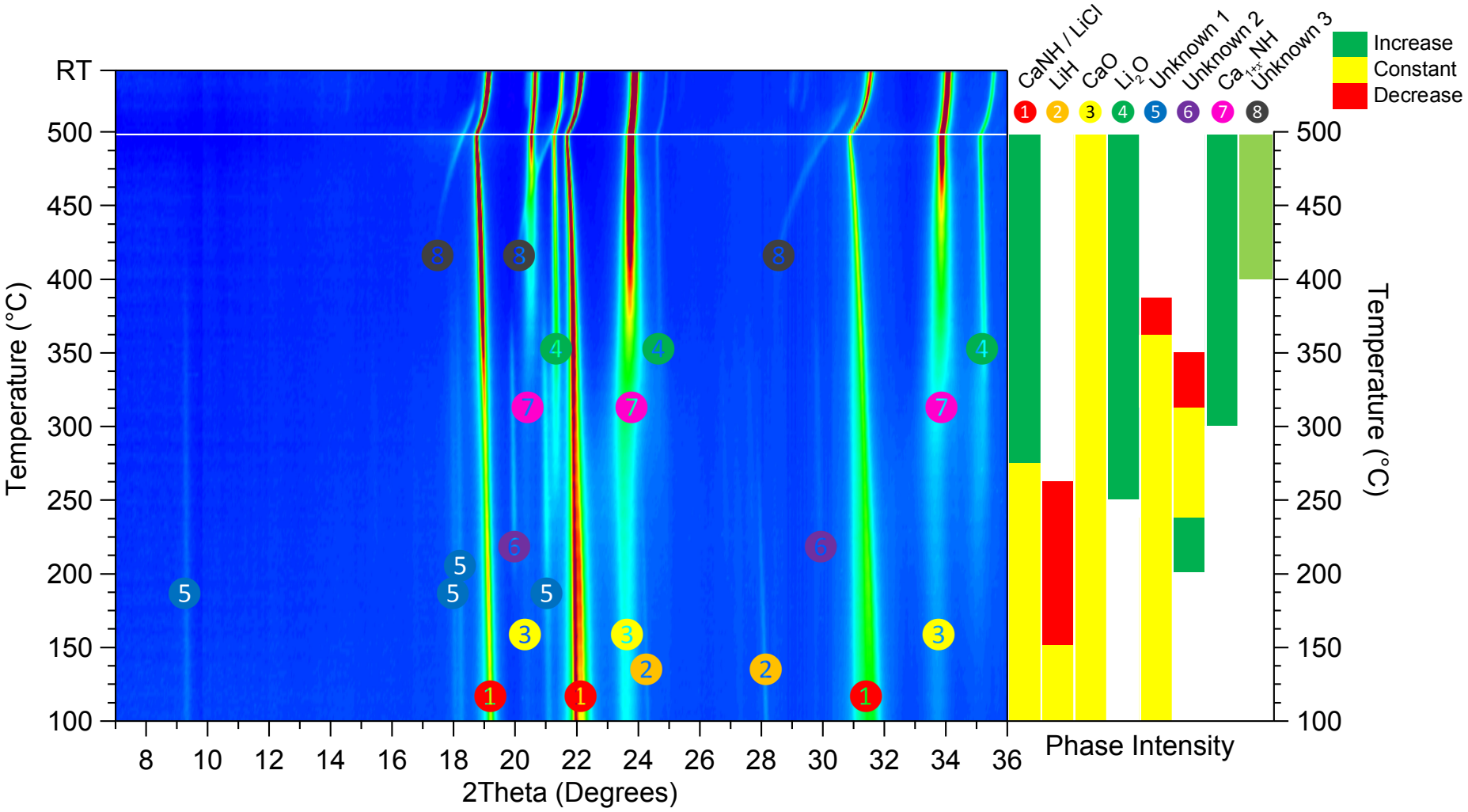

Figure 8.4: *In situ* SXRD analysis (λ = 1.00036 Å) of CaNH + LiH (1:1) under dynamic vacuum with phase identification.

LiH (2) disappears completely by ~250 °C and is associated with the brief appearance of an unknown phase (6) between 200 °C and 350 °C. By ~375 °C, the unknown (possible halide) phase (5) disappears through an unknown reaction. The overlapping CaNH and LiCl (1) peak intensities start to increase at ~375 °C, where the increasing temperature possibly resulted in the increased crystallinity of LiCl as seen from a previous measurement of LiCl at 700 °C in Chapter 5 (Figure 5.11). Furthermore, XRD analysis of as-synthesised CaNH in Chapter 6 (Figure 6.3) revealed that the LiCl peak position was at a slightly higher 2θ angle than CaNH. Therefore, to verify the peak positions, Figure 8.5 shows the magnified region where CaNH (0) and LiCl (1) overlap at a 2θ angle of ~22°. The higher 2θ position that corresponds to LiCl (1) increased in peak intensity at temperatures > 25 °C, while the peak intensity for CaNH (0) decreased (at $T > 25$ °C) and disappeared by 350 °C (Figure 8.5). Furthermore, these phases shifted to lower 2θ angles with increasing temperature and as a result, the LiCl (1) peaks appeared to overlap the low intensity CaNH (0) peaks at temperatures ≥ 350 °C. Therefore, LiCl (1) was associated with the increase in peak intensity with increasing temperature between 100 °C and 500 °C in the *in situ* SXRD analysis (Figure 8.4).

The decrease in CaNH (0) peak intensity could be explained by the possible formation of an intermediate, $Ca_{1+x}NH$ ($0 \leq x \leq 1$) phase (7) at 300 °C (Figure 8.5). This phase was also observed in the *in situ* SXRD of $Li_2Ca(NH)_2$* + LiH (1:2) in Figure 8.2 and 8.3 and by Pistidda et al. (2015), where an intermediate phase appeared with a cubic structure of CaNH but with a smaller cell parameter. By ~400 °C, an unknown phase (8) appeared, rapidly moving to higher 2θ angles with increasing temperature. This observation suggested that the unit cell of this unknown phase (8) was rapidly decreasing in size (despite the temperature increase), where this could be a result of a possible reaction involving the release of hydrogen. Oxygen contamination was also observed in the sample as a result of the polyimide/graphite ferrules used to seal the sample capillary to the mount. The leaking capillary caused Li_2O (4) to appear with increasing peak intensity at ~250 °C with increasing temperature.

* Incomplete synthesis and contains a mixture of the following: 2CaNH–$Ca(NH_2)_2$, $LiNH_2$ and LiH.

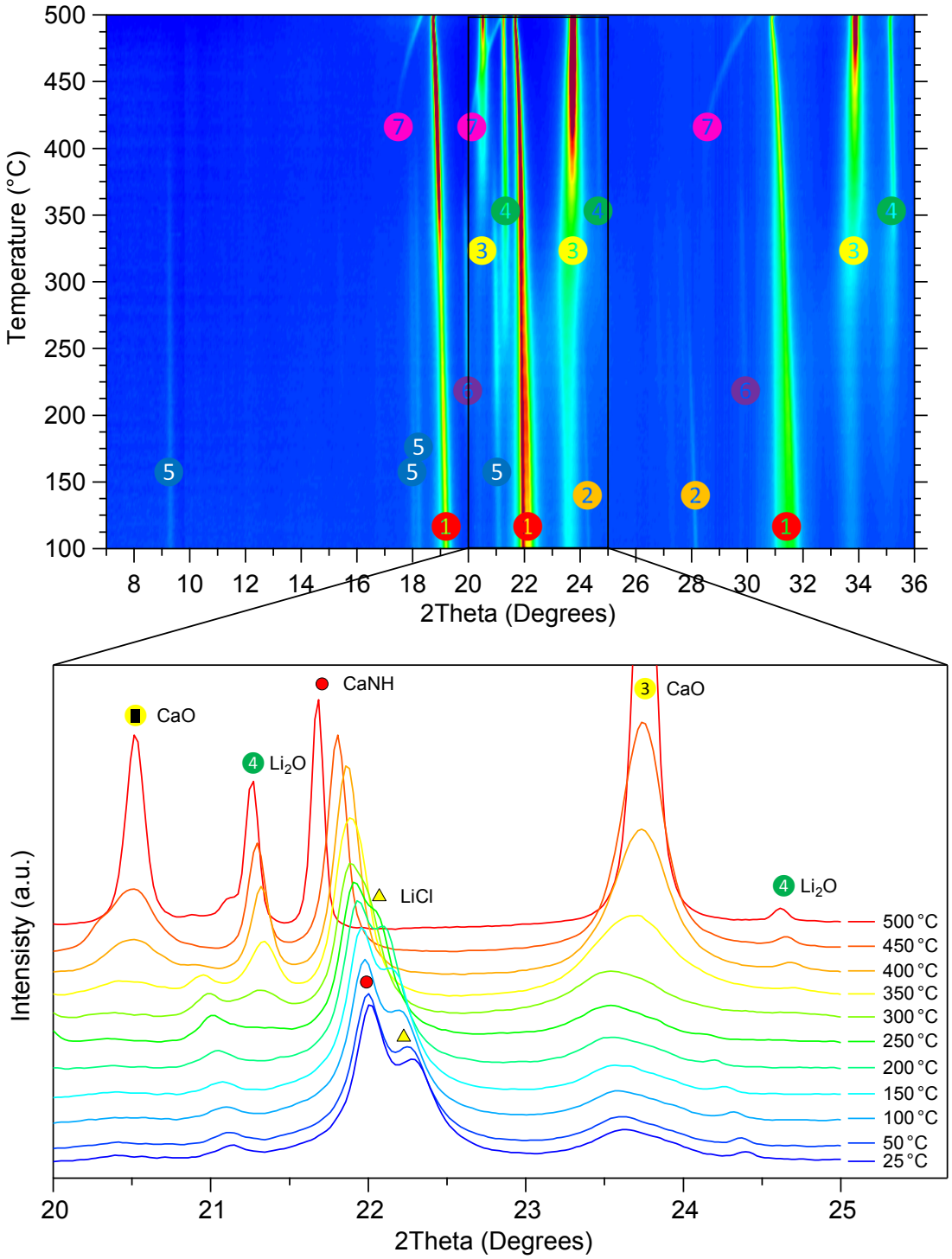

Figure 8.5: *In situ* SXRD analysis (λ = 1.00036 Å) of CaNH + LiH (1:1) under dynamic vacuum with investigation of double peak at a 2θ angle of ~22°, where LiCl is positioned at a higher 2θ value than CaNH.

To observe the desorption properties of the sample under different conditions, Figure 8.6 shows the *in situ* SXRD analysis in the temperature range of 100 – 500 °C under a hydrogen back pressure (heating rate of 5 °C min^{-1}). The initial hydrogen pressure in the gas-handling system decreased from 2 bar to ~1 bar (atmospheric pressure) as the reference volume was opened to the evacuated sample capillary, where previous SXRD measurements had the pressure drop to 1.4 bar. This pressure loss suggested a leak caused by the polyimide/graphite ferrules used, resulting in the appearance of CaO (3) while heating and Li_2O (4) as the sample cooled. Similar to the *in situ* SXRD measurement under dynamic vacuum (Figure 8.4), the same unknown phases (5 and 6) were identified in the hydrogen back-pressure SXRD measurement (Figure 8.6). Furthermore, the increased crystallinity of LiCl (1) with increasing temperature was observed at ~200 °C (Figure 8.6). However, a decrease in peak intensity of CaNH (0) was observed between 150 °C and 250 °C before it appeared again a slightly lower 2θ position with increasing peak intensity between 250 °C and 400 °C. The decreasing peak intensity of CaNH (0) corresponded to the formation of an intermediate, $Ca_{1+x}NH$ ($0 \leq x \leq 1$) phase (7) at ~300 °C (Pistidda et al. 2015). The reappearance of CaNH (0) at a lower 2θ value may have resulted from the possible rehydrogenation reaction of $Ca_{1+x}NH$ (7) under a hydrogen back pressure of ~1 bar. This reappearance is possible as Ca_2NH starts to absorb hydrogen at ~250 °C as observed by TPA-VM analysis of Ca_2NH (Chapter 6: Figure 6.6). A closer inspection of the overlapping phases can be viewed in Appendix A (Figure A.16).

During SXRD measurements performed under a hydrogen back pressure, high temperatures caused a volume change in the sample within the irradiated section of the capillary. As a result, the diffracted intensity of some peaks were reduced between 400 °C and 500 °C in Figure 8.6 (i.e. some of the sample moved out of the X-ray beam). However, as the sample cooled (above the white line in Figure 8.6), the sample moved back into the X-ray beam to allow the observation of an unknown (possible oxide) phase (9) along with the appearance of a Li_2O phase (4).

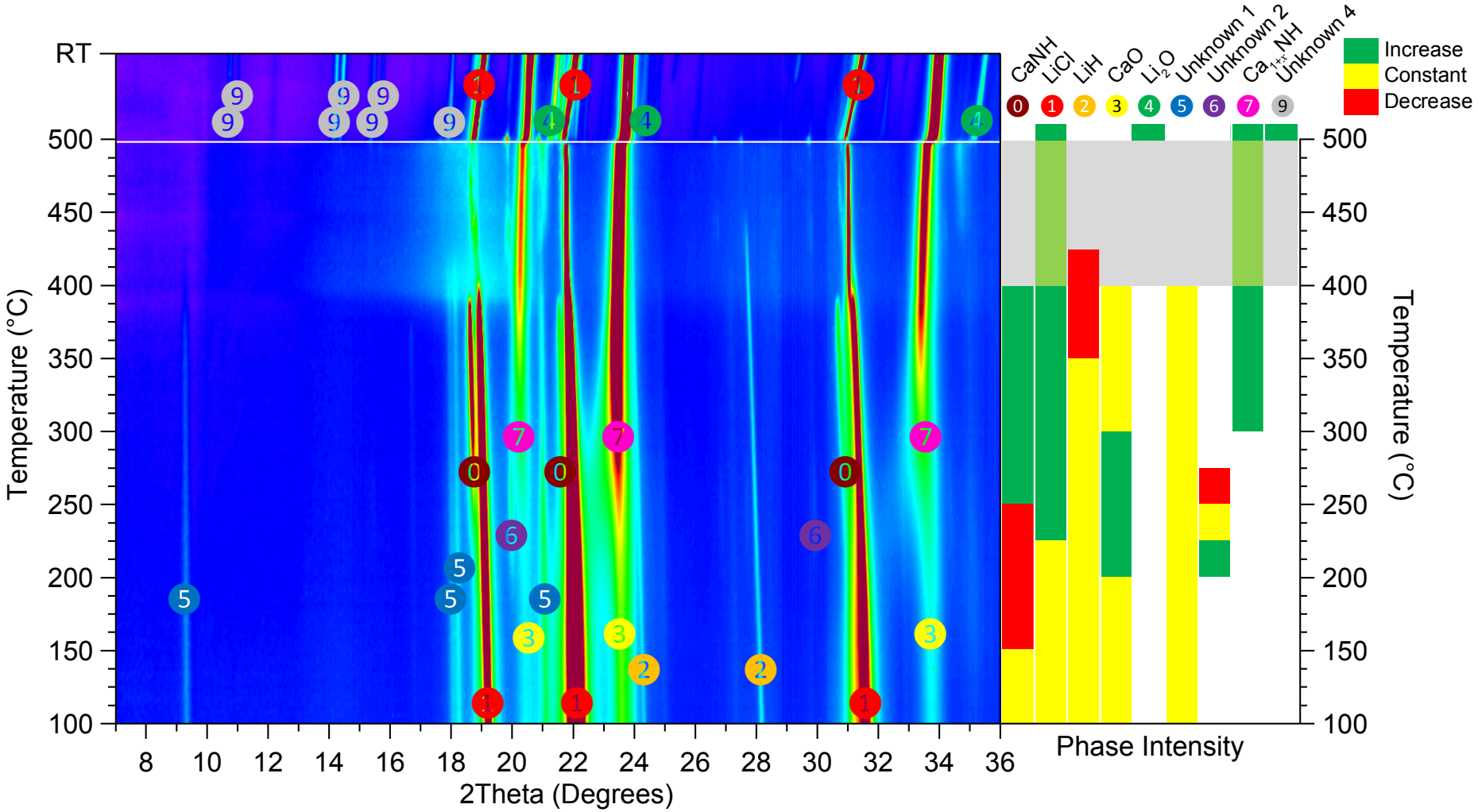

Figure 8.6: *In situ* SXRD analysis (λ = 1.00036 Å) of CaNH + LiH (1:1) under a hydrogen pressure of ~1 bar with phase identification.

8.2.3 LiCaN + H_2 (1:1)

8.2.3.1 Synthesis

Lithium calcium nitride (LiCaN) was synthesised based on the reaction predicted by Alapati, Karl Johnson, and Sholl (2007) in the Li–Mg–N–H system:

$$LiNH_2 + MgH_2 \rightarrow LiMgN + 2H_2 \quad (8.6)$$

where LiCaN was prepared by substituting MgH_2 for CaH_2 in Equation 8.6. $LiNH_2$ (Sigma-Aldrich, 95%) and CaH_2 (laboratory synthesised; Chapter 6: Section 6.2.2) are thoroughly mixed in a planetary ball-mill for 4 hours in a 1:1 molar ratio operating at 400 RPM with a BTP ratio of 30:1 using 316 stainless-steel balls sized at 10 mm and 6 mm. Figure 8.7a shows the XRD analysis after ball-milling $LiNH_2$ + CaH_2 (1:1), where Rietveld refinement confirmed a molar ratio of 1:1 ($LiNH_2$:CaH_2) with oxide phases CaO (~2.44 wt%) and Li_2O (~2.39 wt%). Oxygen contamination is possible during the XRD measurement as a result of a leak in bubble dome holder.

The ball-milled mixture of $LiNH_2$ and CaH_2 was outgassed and heat treated at 500 °C in a closed system at a pressure near vacuum to allow the following reaction to take place (Equation 8.7):

$$LiNH_2 + CaH_2 \rightarrow LiCaN + 2H_2 \quad (8.7)$$

However, room temperature XRD analysis in Figure 8.7b revealed that at temperatures ≤ 500 °C, the formation of LiCaN was absent. Furthermore, Rietveld refinement of this pattern showed that it contained a CaNH-like phase (~78 wt%), Li_2NH (~20 wt%) and $Li_2Ca(NH)_2$ (~2 wt%). Given the starting reagents for LiCaN were the same for $Li_2Ca(NH)_2$ (but with different molar ratios), the formation of $Li_2Ca(NH)_2$ is possible, which explains the trace amounts observed in Figure 8.7b. The mixture of end phases at 500 °C (Figure 8.7b) has similarities with the end product of $Li_2Ca(NH)_2$* + LiH (1:2) in Figure 8.2, where a CaNH-like phase transitioned to an intermediate phase, $Ca_{1+x}NH$ ($0 \leq x \leq 1$). Therefore, a mixture of $LiNH_2$ + CaH_2 (1:1) heated in a closed system may proceed with the following reaction pathway:

$$LiNH_2 + CaH_2 \rightarrow \frac{1}{2}Ca_2NH + \frac{1}{2}Li_2NH + \frac{3}{2}H_2 \quad (8.8)$$

However, due to the lack of LiCaN formation using this starting mixture after heating to 500 °C, this method was not pursued and an alternative method was approached.

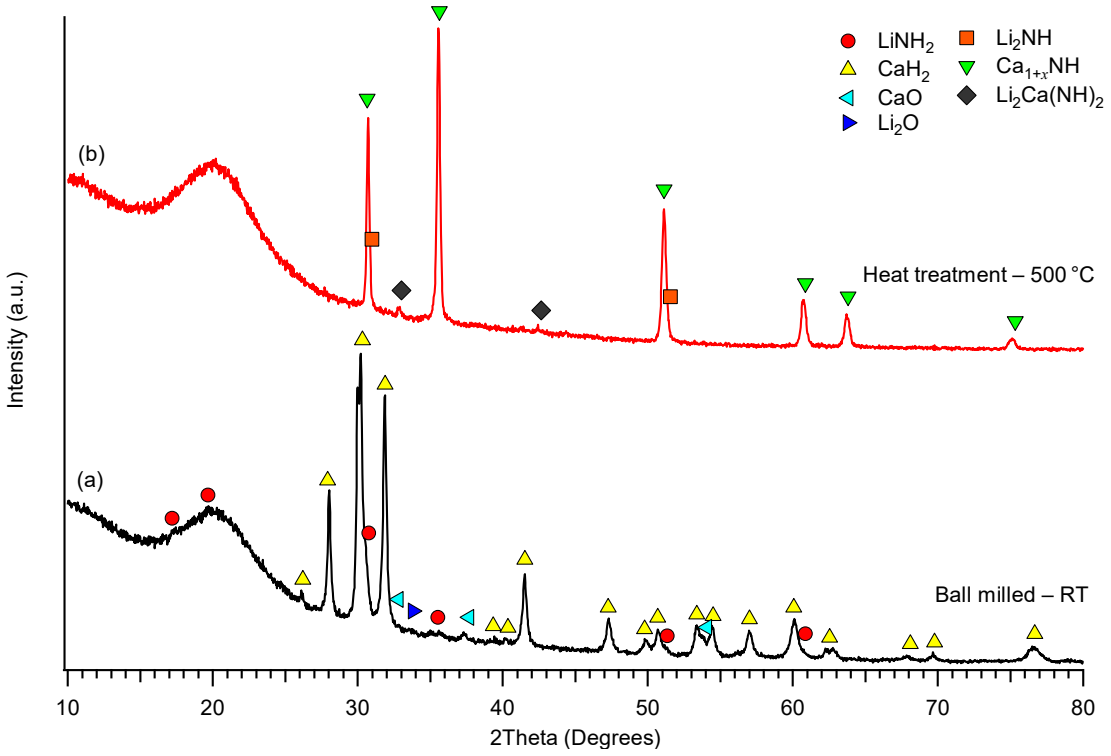

Figure 8.7: Comparitive XRD analysis of $LiNH_2$ + CaH_2 (1:1) after RT ball milling and (b) heating at 500 °C.

Yuan et al. (2006) reported that by mixing Ca_3N_2 and Li_3N in a 1:0.6 molar ratio at 500 °C under a static nitrogen pressure of 2 bar for 24 hours, the main products were identified as LiCaN along with $Ca(OH)_2$ and residual Li_3N. Therefore, in a second attempt to synthesise LiCaN, Ca_3N_2 + Li_3N (1:0.6) was prepared by ball-milling using the starting reagents Ca_3N_2 (Sigma-Aldrich, 99%) and Li_3N (Sigma-Aldrich, ≥ 99.5%). The starting reagents were thoroughly mixed in a planetary ball-mill for 4 hours operating at 400 RPM with a BTP ratio of 30:1 using 316 stainless-steel balls sized at 10 mm and 6 mm. The ball-milled sample was annealed at 580 °C under a static nitrogen pressure of ~2.3 bar for ~23 hours.

X-ray diffraction analysis of Ca_3N_2 + Li_3N (1:0.6) after heating to 580 °C under a static N_2 pressure of ~2.3 bar is shown in Figure 8.8a, where the final product

showed that it contained a mixture of LiCaN and Ca_3N_2. However, given the XRD results from the molar ratio used by Yuan et al. (2006), the presence of Ca_3N_2 and absence of Li_3N, suggests there was a deficiency of Li_3N in the initial molar ratio used. Therefore, additional Li_3N was hand mixed (with an agate mortar and pestle) to bring the sample molar ratio up to 1:1 (Ca_3N_2:Li_3N). A mixture of Ca_3N_2 + Li_3N (1:1) was then re-heated at 600 °C under a static N_2 pressure of ~2.5 bar for ~11 hours. XRD analysis in Figure 8.8b revealed that the consumption of Ca_3N_2 was successful with single phase LiCaN appearing in the sample. Rietveld refinement of this sample showed that it contained ~11 wt% of contaminant phases (CaO), consistent with contamination already present in the starting materials.

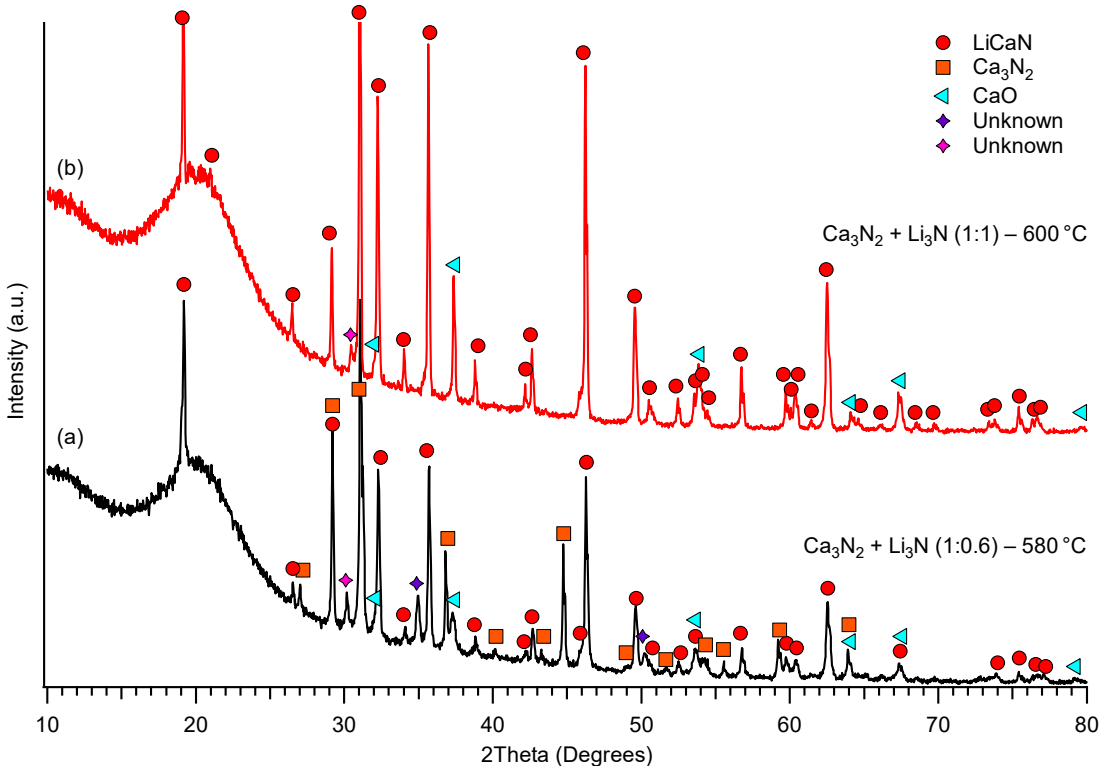

Figure 8.8: Comparitive XRD analysis of (a) Ca_3N_2 + Li_3N (1:0.6) annealed at 580 °C under ~2.3 bar of N_2 for ~23 hours and (b) Ca_3N_2 + Li_3N (1:1) annealed at 600 °C under ~2.5 bar of N_2 for ~11 hours.

8.2.3.2 Manual pressure-composition-temperature (PCT) measurement

Manual PCT measurements were performed on as-synthesised LiCaN to identify the approximate equilibrium pressure, plateau slope, hydrogen capacity and hydriding kinetics. This information is useful to understand the thermodynamic

properties using the low volume apparatus and heating at near-constant hydrogen content (LVA-NCHC method) described in Chapter 3. The theoretical hydrogen content for LiCaN is 3.2 wt% of H_2 based on the reverse reaction of Equation 8.3 (Equation 8.9).

$$LiCaN + H_2 \rightarrow CaNH + LiH \tag{8.9}$$

The manual absorption PCT measurement at 450 °C is shown in Figure 8.9, where the pressure dropped to near vacuum at a hydrogen content between 0.7 wt% and ~1.7 wt% of H_2. Beyond a hydrogen content of ~1.7 wt%, the apparent plateau region of the PCT curve begins to slope, which suggests a solid-solution behaviour up to a pressure of ~5 bar. A manual desorption measurement was performed at a pressure below 4 bar to investigate the partially hydrogenated products by XRD analysis.

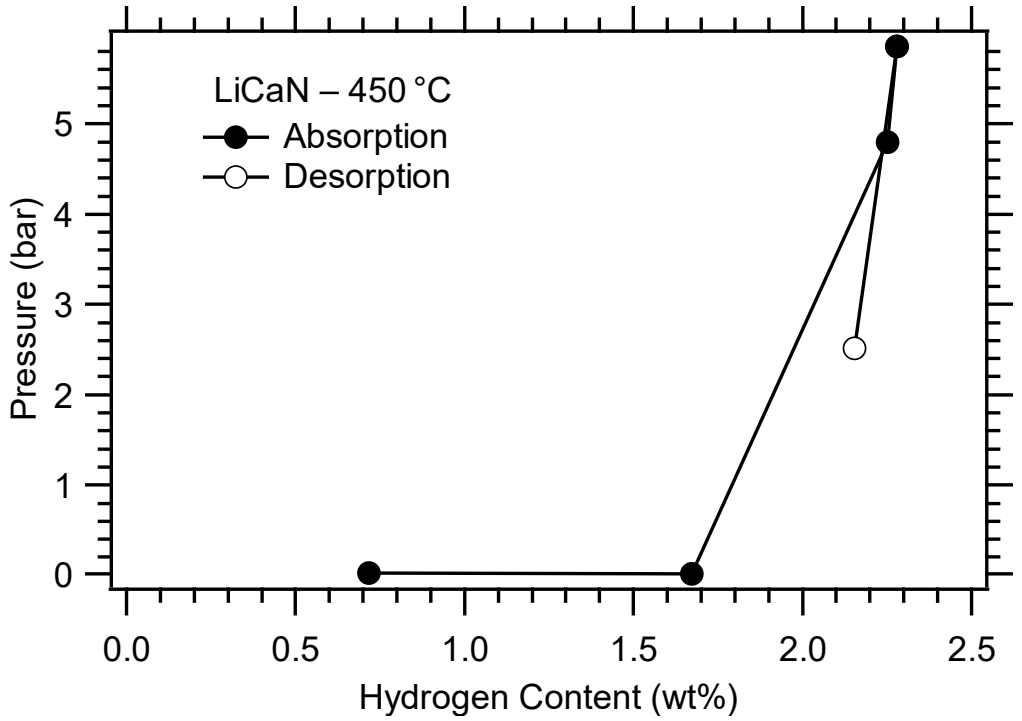

Figure 8.9: Manual PCT measurement of the hydrogenation of LiCaN at 450 °C.

Figure 8.10 shows the XRD analysis of partially hydrogenated LiCaN at 450 °C. Rietveld refinement showed the final products contained a mixture of a CaNH-like phase (~43 wt%), $Li_2Ca(NH)_2$ (~42 wt%) and LiH (~8 wt%). The CaNH-like phase had a cubic structure with a = 5.0494 Å, and had peak positions consistent with a Ca_2NH phase (higher 2θ value than CaNH). Although Ca_2NH has a larger

cell parameter than CaNH (Ca_2NH = 10.1300 Å and CaNH = 5.1430 Å), Ca_2NH is a supercell (i.e. similar structure but the lattice parameters are doubled) having an equivalent lattice parameter of ~5.0650 Å. Therefore, a slight increase in calcium atoms could have resulted in an intermediate phase ($Ca_{1+x}NH$) with a cell parameter closely related to Ca_2NH. Note that this phase was also observed during *in situ* SXRD measurements in Section 8.2.1.2 and 8.2.2.2. Furthermore, Pistidda et al. (2015) observed the appearance of the same intermediate phase with a crystalline structure of CaNH, but a smaller cell parameter at temperatures ≤ 350 °C.

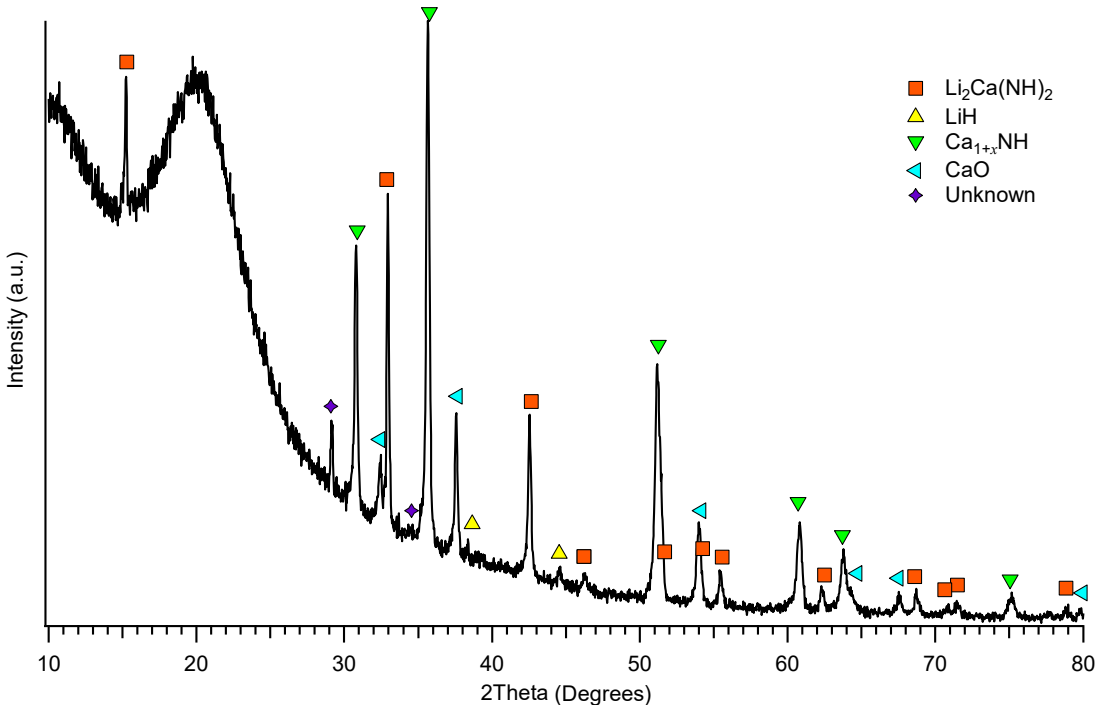

Figure 8.10: XRD analysis partially hydrogenated LiCaN at 450 °C.

Manual PCT measurements were performed on as-synthesised LiCaN at 650 °C to investigate the difference in the observed hydrogen capacity and the expected capacity for LiCaN + H_2 (1:1) (3.2 wt% of H_2) and to re-evaluate the region between 0.7 wt% and ~1.7 wt% of H_2 (Figure 8.11). However, it should be noted that because of the high temperature used with 316 stainless-steel reactors, large corrections were made on the PCT data (detailed in Chapter 2: Section 2.5.1). This correction was to account for the diffusion and absorption of hydrogen through stainless steel, resulting in high uncertainty on the hydrogen content obtained.

On the first manual absorption step, too much hydrogen was added to the reference volume such that the first measured equilibrium point at ~2.1 wt% of H_2 (~1.4 bar) did not lie on the plateau previously observed for a hydrogen content between 0.7 wt% and ~1.7 wt%, which had pressures near vacuum in the PCT measurement at 450 °C (Figure 8.9). However, it has been labelled in Figure 8.11 to give a guide to the possible shape of the PCT curve at 650 °C. The manual desorption PCT curve had a sloping plateau for a hydrogen content between 2.2 wt% and ~0 wt%, where the midpoint of the slope corresponded to an equilibrium desorption pressure of 1.13 bar of H_2. The second absorption PCT curve (Absorption 2 in Figure 8.11) revealed a sloping plateau similar to the desorption curve and corresponded to a similar pressure (1.17 bar of H_2). This similarity suggests that the system had little hysteresis at 650 °C and a reversible hydrogen content of approximately ~2.2 wt% of H_2. The different plateaux observed between Absorption 1 (from PCT-450 °C) and Absorption 2 in Figure 8.11, suggest that the reversible reaction pathway is different to the hydrogenation of as-synthesised LiCaN.

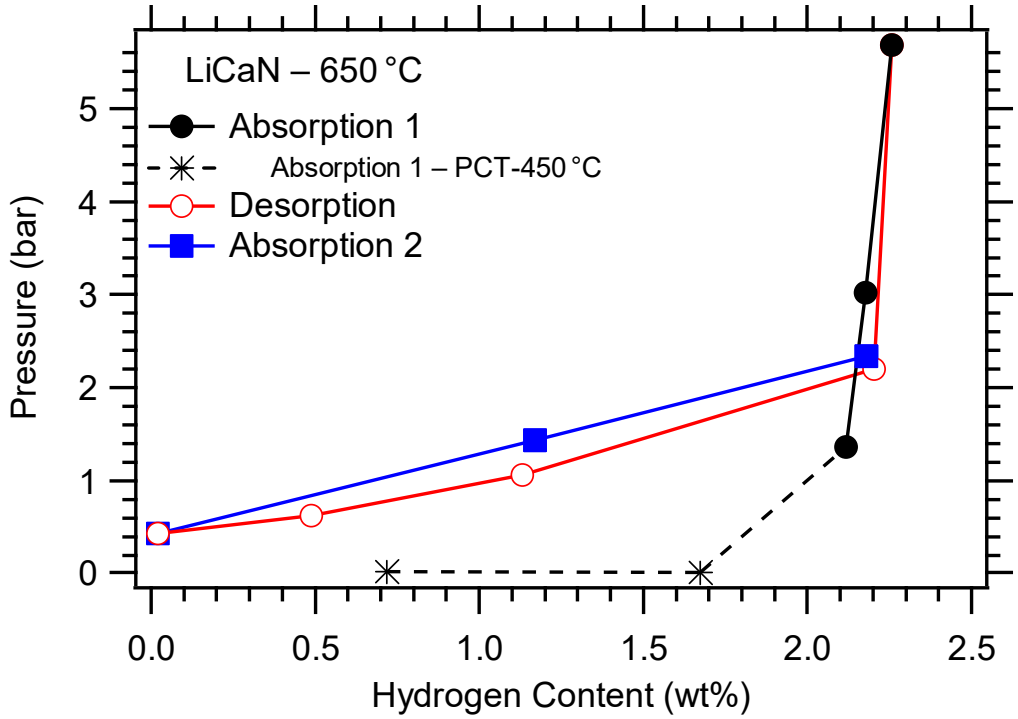

Figure 8.11: Manual PCT measurement of the hydrogenation of LiCaN at 650 °C.

8.2.3.3 Discussion

The synthesis of LiCaN was difficult using the starting reagents $LiNH_2$ and CaH_2, but was successful using the nitride reagents, Li_3N and Ca_3N_2, annealed under a nitrogen pressure at 600 °C. XRD analysis of partially hydrogenated LiCaN after PCT measurements at 450 °C (Figure 8.10) revealed that the products were a mixture of $Ca_{1+x}NH$ (~43 wt%), $Li_2Ca(NH)_2$ (~42 wt%) and LiH (~8 wt%). Based on these phases, the reaction in Equation 8.10 is the proposed reaction pathway that occurs at temperatures ≤ 450 °C.

$$3LiCaN + 2H_2 \rightarrow Ca_2NH + Li_2Ca(NH)_2 + LiH \quad (8.10)$$

where the quantity (wt%) of phases from Rietveld refinement are in close agreement with the theoretical values in Equation 8.10 (50.86 wt% of Ca_2NH, 44.89 wt% of $Li_2Ca(NH)_2$ and 4.25 wt% of LiH). At the end of the plateau region in PCT measurements at 450 °C, the practical hydrogen content (~1.7 wt% of H_2) is also in closer agreement with the theoretical hydrogen content of 2.15 wt% of H_2 for LiCaN + H_2 (3:2) (Equation 8.10) than 3.20 wt% of H_2 for LiCaN + H_2 (1:1) (Equation 8.9). PCT measurements of as-synthesised LiCaN at 450 °C and 650 °C revealed that the different plateaux observed between Absorption 1 (from PCT-450 °C) and Absorption 2 (from PCT-650 °C), suggest that the formation of LiCaN is unlikely by the analogy of efforts to obtain LiMgN in the Li–Mg–N–H system (Zhang and Wu 2017). Therefore, further investigation is required to determine the reversible reaction that occurs at 650 °C.

Unfortunately, the LVA-NCHC method was not performed because of time constraints placed by measurements on other mixed cation systems (with higher priority). However, the quick manual PCT measurements provided invaluable information on LiCaN, revealing the system had an equilibrium desorption pressure of approximately 1.13 bar at 650 °C. Using the equilibrium pressure and temperature, Table 8.2 shows the estimated uncertainty on the enthalpy (ΔH_{des}) by assuming an entropy (ΔS_{des}) range between 100 and 140 J (mol H_2)$^{-1}$ K^{-1}. The estimated ΔH_{des} value ranged between 91 and 128 kJ (mol H_2)$^{-1}$, which is in close agreement with the ΔH_{des} value obtained for the Ca–N–H system (ΔH_{des} = 119.3 ± 4.6 kJ (mol H_2)$^{-1}$). Given the low hysteresis observed between the absorption

and desorption curves in Figure 8.11, the range of ΔH_{des} values in Table 8.2 were used to calculate the uncertainty on the theoretical heat storage capacity of LiCaN + H_2 (3:2) to range between 977 and 1371 kJ kg^{-1} using the practical hydrogen content of ~2.2 wt% derived from PCT measurements in Figure 8.11. The values in this range are greater than the Ca–N–H system investigated in Chapter 6: Section 6.2.3, which had a practical heat storage capacity of 959 ± 58 kJ kg^{-1}.

Table 8.2: Estimated uncertainty on the enthalpy of desorption and equilibrium pressure by assuming an entropy value between 100 and 140 J $(mol\ H_2)^{-1}\ K^{-1}$, based on the equilibrium H_2 pressure of 1.13 bar at 650 °C.

Assumed ΔS_{des} (J $(mol\ H_2)^{-1}\ K^{-1}$)	100	110	120	130	140
Estimated ΔH_{des} (kJ $(mol\ H_2)^{-1}$)	91.4	100.6	109.8	119.1	128.3

Temperature (°C)	Estimated desorption P_{eq} (bar)				
650	1.13	1.13	1.13	1.13	1.13
700	2.1	2.2	2.4	2.5	2.7
750	3.6	4.1	4.6	5.2	5.8
800	6.0	7.1	8.4	9.9	11.7
850	9.4	11.7	14.5	17.9	22.2
900	14.3	18.5	23.9	30.9	39.9

Table 8.2 also shows the estimated equilibrium desorption pressures at a high operation temperature range (700 – 900 °C). Based on the equilibrium pressure (1.13 bar) at 650 °C, the estimated equilibrium desorption pressure at 800 °C ranges between ~6 bar and ~12 bar (Table 8.2), depending on the assumed ΔS_{des} value. This pressure is promising for thermal energy storage applications as the low hydrogen pressures at high temperature reduce the engineering costs to store hydrogen. Compared to the Ca–N–H system, although the enthalpy values for LiCaN and Ca_2NH system were similar, the LiCaN system has a higher practical heat storage capacity than the Ca_2NH system (LiCaN = 977 – 1371 kJ kg^{-1} and Ca_2NH = 959 ± 58 kJ kg^{-1}) because it has a higher practical hydrogen capacity (LiCaN = ~2.2 wt% and Ca_2NH = ~1.79 wt% of H_2). However, because this system contains lithium, the high costs are seen as a disadvantage for the Li–Ca–N–H system in thermal storage applications.

8.3 Conclusion

This chapter investigated the Li–Ca–N–H system as a potential candidate in thermal storage technology. Two imide-hydride systems were investigated, Sample 1 – $Li_2Ca(NH)_2$ + LiH (1:2) and Sample 2 – CaNH + LiH (1:1), along with the hydrogenation of LiCaN (Sample 3) to study the potential reverse reaction to that of Sample 2. The synthesis of $Li_2Ca(NH)_2$ was initially unsuccessful using a mixture of $LiNH_2$ and CaH_2 because it was heated in a closed system and as a result, a solid solution phase of CaNH and $Ca(NH_2)_2$ was formed. However, the complete synthesis of $Li_2Ca(NH)_2$ was observed during *in situ* SXRD heating measurements starting with impure $Li_2Ca(NH)_2$ mixed with LiH in a 1:2 molar ratio, where the $Li_2Ca(NH)_2$ phase appeared between 300 °C and 360 °C.

The *in situ* SXRD analysis of Sample 1 revealed the formation of Li_2NH and an intermediate phase ($Ca_{1+x}NH$), where $Ca_{1+x}NH$ first appeared at ~300 °C with increasing temperature and remained in the sample along with $Li_2Ca(NH)_2$. However, in both measurements under dynamic vacuum and a hydrogen back pressure, the formation of LiCaN was not observed at temperatures ≤ 500 °C. The absence of LiCaN suggests that the operating temperature may not be sufficient for the imide-hydride to nitride reaction to take place. *In situ* SXRD measurements of Sample 2 – CaNH + LiH (1:1) were performed under dynamic vacuum and a hydrogen back pressure (~1 bar). In both measurements, CaNH transitioned into the same intermediate phase ($Ca_{1+x}NH$) at ~300 °C that was observed during *in situ* SXRD measurements of Sample 1. However, a CaNH-like phase reappeared at a slightly lower 2θ value, suggesting the possible rehydrogenation of $Ca_{1+x}NH$ in Sample 2 at ~250 °C.

The synthesis of LiCaN (Sample 3) using a mixture of $LiNH_2$ and CaH_2 based on the synthesis method for LiMgN ($LiNH_2$ and MgH_2) was unsuccessful. However, an alternative method was accomplished using a mixture of nitrides (Ca_3N_2 and Li_3N) heated at 600 °C under a nitrogen pressure (≤ 2.5 bar). Manual PCT measurements performed on as-synthesised LiCaN at 450 °C revealed that a practical hydrogen content of ~1.7 wt% was absorbed with an equilibrium pressure near vacuum. The partially hydrogenated products were revealed by

XRD analysis to be a mixture of $Ca_{1+x}NH$, $Li_2Ca(NH)_2$ and LiH. Manual PCT measurements of Sample 3 – LiCaN at 650 °C revealed a practical hydrogen content of ~2.2 wt% with an equilibrium desorption pressure of 1.13 bar (at the midpoint of the sloping plateau). Based on the phases identified by XRD analysis in Figure 8.10 ($Ca_{1+x}NH$, $Li_2Ca(NH)_2$ and LiH), and the possible reaction pathway in Equation 8.10, the theoretical hydrogen capacity of LiCaN + H_2 (3:2) is 2.15 wt% of H_2, which is in close agreement with the experimental hydrogen content of ~2.2 wt% of H_2. The differences in hydrogen capacity are likely due to uncertainties involved with the absorption and diffusion of hydrogen through 316 stainless steel at 650 °C.

Based on the equilibrium desorption pressure of 1.13 bar observed during PCT measurements of Sample 3 – LiCaN at 650 °C (Figure 8.11), the enthalpy value of desorption was estimated to range between 91 and 128 kJ $(mol\ H_2)^{-1}$ by assuming an entropy range between 100 and 140 J $(mol\ H_2)^{-1}\ K^{-1}$). Hence, using a practical hydrogen content of ~2.2 wt%, the practical heat storage capacity was estimated to range between 977 and 1371 kJ kg^{-1} for LiCaN + H_2 (3:2). Generally, the equilibrium pressures are exponentially proportional to the operation temperature. Therefore, the low equilibrium pressures in the Li–Ca–N–H system (~1 bar) were typically desired for its practical application at high temperatures (> 650 °C), where the equilibrium pressure at 800 °C was estimated to range between ~6 bar and ~12 bar. This pressure range is ideal for reducing the engineering costs in thermal energy storage systems.

In this chapter, some inconclusive results were obtained for the Li–Ca–N–H system. Therefore, future work would include the investigation of Sample 1 and 2 at temperatures > 500 °C to verify the possible formation of LiCaN because the hydrogenation of LiCaN (Sample 3) at 450 °C revealed products containing a combination of the starting products present in Sample 1 and 2. To confirm the products after PCT absorption measurements at 450 °C, future work would also include the XRD analysis of these products to investigate the reaction pathways proposed in this chapter. Furthermore, given the low equilibrium pressure at high temperature, the Li–Ca–N–H system is promising, but requires further work to determine the reversible reactions involved and its suitability for thermal energy storage.

CHAPTER 9: MIXED CATION Na–Mg–N–H SYSTEMS

9.1 Introduction

From the investigation of the Mg–N–H system in Chapter 5, Hu et al. (2006a) found that a mixture of magnesium imide (MgNH) and magnesium hydride (MgH_2) reacted during intensive ball-milling at room temperature to form magnesium nitride (Mg_3N_2). However, for a potential thermal storage material based on this system, the operating temperature must be increased (at least 650 °C) to meet the requirements to efficiently operate the heat engine. This temperature can be achieved by substituting MgH_2 with the more stable sodium magnesium hydride ($NaMgH_3$), which has a higher decomposition temperature (~371 °C) than MgH_2 (~282 °C) (Pottmaier et al. 2011; Paskevicius, Sheppard and Buckley 2010). Therefore, the investigation of the Na–Mg–N–H system involves a reaction between MgNH and $NaMgH_3$ with an anticipated reaction pathway shown in Equation 9.1 (theoretical hydrogen content of 3.13 wt% of H_2).

$$2MgNH + NaMgH_3 \leftrightarrow Mg_3N_2 + NaH + 2H_2 \quad (9.1)$$

The imide-hydride reactions in the Na–Mg–N–H system have not been studied as the only publications on this system have started with the amide-hydride ($NaNH_2$–MgH_2 and $Mg(NH_2)_2$–NaH) interactions (Dolotko, Paulson and Pecharsky 2010; Sheppard, Paskevicius and Buckley 2011a; Xiong et al. 2005a). Dolotko, Paulson, and Pecharsky (2010) investigated the reversibility of the Li–Mg–N–H and Na–Mg–N–H system. However, under the same conditions (190 bar of H_2 at 390 °C), only partial rehydrogenation was observed in the Na–Mg–N–H system with 2.1 wt% of H_2 absorbed compared to the theoretical value of 3.13 wt% of H_2 (Equation 9.1). Furthermore, the Na–Mg–N–H system has more appeal due to the low cost of sodium compared to lithium. Therefore, $NaMgH_3$ was selected to increase the operating temperature while maintaining low costs for thermal energy storage.

MgNH (Equation 9.2) and $NaMgH_3$ (Equation 9.3) can be synthesised during reactive ball-milling at room temperature (Hu et al. 2006a; Ikeda et al. 2005).

Therefore, to increase experimental productivity, a mixture of $Mg(NH_2)_2$, MgH_2 and sodium hydride (NaH) was prepared in a 1:2:1 molar ratio to obtain the starting reagents required for the reaction in Equation 9.1, where the overall reaction is anticipated to occur in Equation 9.4.

$$Mg(NH_2)_2 + MgH_2 \rightarrow 2MgNH + 2H_2 \quad (9.2)$$

$$NaH + MgH_2 \rightarrow NaMgH_3 \quad (9.3)$$

$$\begin{aligned} &Mg(NH_2)_2 + 2MgH_2 + NaH \\ &\rightarrow 2MgNH + NaMgH_3 + 2H_2 \\ &\rightarrow Mg_3N_2 + NaH + 4H_2 \end{aligned} \quad (9.4)$$

In this chapter, two samples were investigated involving the starting reagents in Equation 9.4 (Sample 1) and Equation 9.1 (Sample 2). Table 9.1 summarises the list of samples, starting reagents and their molar ratios used. Sample 1 was investigated by means of TPD-MS and *ex situ* XRD analyses, whereas Sample 2 was investigated by *in situ* synchrotron X-ray diffraction (SXRD) analysis. Given the date of the synchrotron-beam deadline, Sample 2 was prepared for SXRD measurements without first being able to confirm the purity of the starting reagents by laboratory XRD analysis. However, the MgNH starting reagent was investigated after SXRD measurements in Chapter 7: Section 7.2.2.1 that confirmed as-synthesised MgNH* contained a mixture of amorphous-MgNH, $Mg(NH_2)_2$ and MgH_2 in a 2:1:1 molar ratio (approximately 50% yield).

Table 9.1: List of potential amide-imide-hydride systems investigated in Chapter 9.

	Reagents
Sample 1	$Mg(NH_2)_2$ + MgH_2 + NaH (1:2:1)
Sample 2	MgNH* + $NaMgH_3$ (2:1)

* Contains amorphous-MgNH, $Mg(NH_2)_2$, and MgH_2

9.2 Results

9.2.1 $Mg(NH_2)_2 + MgH_2 + NaH$ (1:2:1)

9.2.1.1 Preparation of Sample 1 and 2

Sample 1 – $Mg(NH_2)_2 + MgH_2 + NaH$ (1:2:1) was prepared by ball-milling using the starting reagents $Mg(NH_2)_2$ (laboratory synthesised; Chapter 5: Section 5.2.1), MgH_2 (Alfar-Aesar, 98%) and NaH (Sigma-Aldrich, 95%). The reagents were thoroughly mixed in a planetary ball-mill for 6 hours in a 1:2:1 molar ratio ($Mg(NH_2)_2$:MgH_2:NaH). Two batches were made in the planetary ball-mill operated at 600 RPM with a BTP ratio of 60:1 using 316 stainless-steel balls sized at 10 mm and 6 mm. Upon opening the ball-mill canisters within the argon-atmosphere glovebox, the O_2 glovebox reading spiked to 12 ppm, which could be triggered erroneously by the release of hydrogen generated during milling according to the reaction in Equation 9.2.

The expected products after ball milling the sample reagents for Sample 1 should be MgNH and $NaMgH_3$ in accordance to the reactions in Equation 9.2 and 9.3, respectively. However, XRD analysis of both batches (Figure 9.1) confirmed that only the reaction in Equation 9.2 could definitely be proven to occur with the sample containing cubic MgNH (Dolci et al. 2010). An unknown peak also appeared in both patterns at a 2θ angle of ~35° that could be matched with the second strongest peak of MgH_2, but the strongest peak (~28°) does not appear in either sample. However, the unknown peak at ~35° (2θ) could be associated with the strongest peak of $NaMgH_3$, but slightly offset from the usual 2θ value of ~33° (Ikeda et al. 2005). Therefore, further investigation of this unknown peak is required.

Sample 2 – MgNH* + $NaMgH_3$ (2:1) was prepared by ball-milling using the starting reagents MgNH* (laboratory synthesised; Chapter 7: Section 7.2.2.1) and $NaMgH_3$ (laboratory synthesised). $NaMgH_3$ was synthesised by annealing a homogenous mixture of MgH_2 and NaH in a 1:1 molar ratio at 300 °C in a closed system under its own generated hydrogen back pressure for ~25 hours, where the synthesis results could not be confirmed before SXRD measurements

because of the synchrotron-beam deadline. The reagents with unknown purities, MgNH* and $NaMgH_3$ in a 2:1 molar ratio, were thoroughly mixed in a planetary ball-mill for 4 hours operating at 400 RPM with a BTP ratio of 30:1 using 316 stainless-steel balls sized at 10 mm and 6 mm. The ball-milled samples were packed in 0.5 mm borosilicate capillaries with polyimide/graphite ferrules using a custom mount in preparation for SXRD.

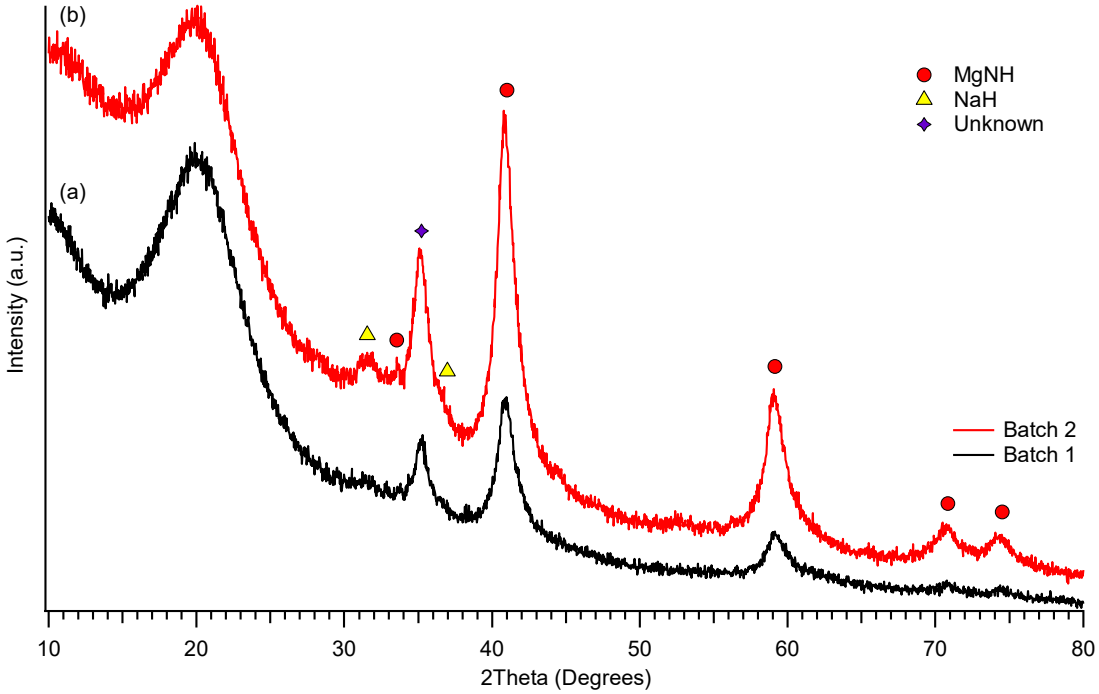

Figure 9.1: XRD analysis of Sample 1 – $Mg(NH_2)_2$ + MgH_2 + NaH (1:2:1) after ball milling for 6 hours. (a) First batch and (b) Second batch.

9.2.1.2 Temperature programmed desorption with mass spectrometry (TPD-MS) of Sample 1

Temperature programmed desorption measurements were performed to help determine the hydrogen desorption reaction pathway using mass spectrometry (MS) to identify the gases released. Figure 9.2 shows the TPD-MS analysis of Sample 1 – $Mg(NH_2)_2$ + MgH_2 + NaH (1:2:1) in the temperature range of 25 – 650 °C with a heating rate of 2 °C min^{-1} under dynamic vacuum. At least two hydrogen desorption events occurred between ~200 °C and ~300 °C before a large event occurred at 331 °C and a smaller event at ~432 °C (Figure 9.2). These events suggest that more than two reactions were capable of releasing

* Contains amorphous-MgNH, $Mg(NH_2)_2$, and MgH_2

hydrogen. The mass spectrometer was unable to detect any measureable amount of ammonia. Therefore, any ammonia released from the decomposition of $Mg(NH_2)_2$ was able to quickly react with the MgH_2 or NaH to form a possible imide phase. *Ex situ* XRD measurements were also performed on repeat TPD-MS measurements that were halted at 230 °C and 380 °C (heating rate of 2 °C min^{-1} under dynamic vacuum). These measurements showed similar desorption events to those in Figure 9.2 and can be found in Appendix A (Figure A.17).

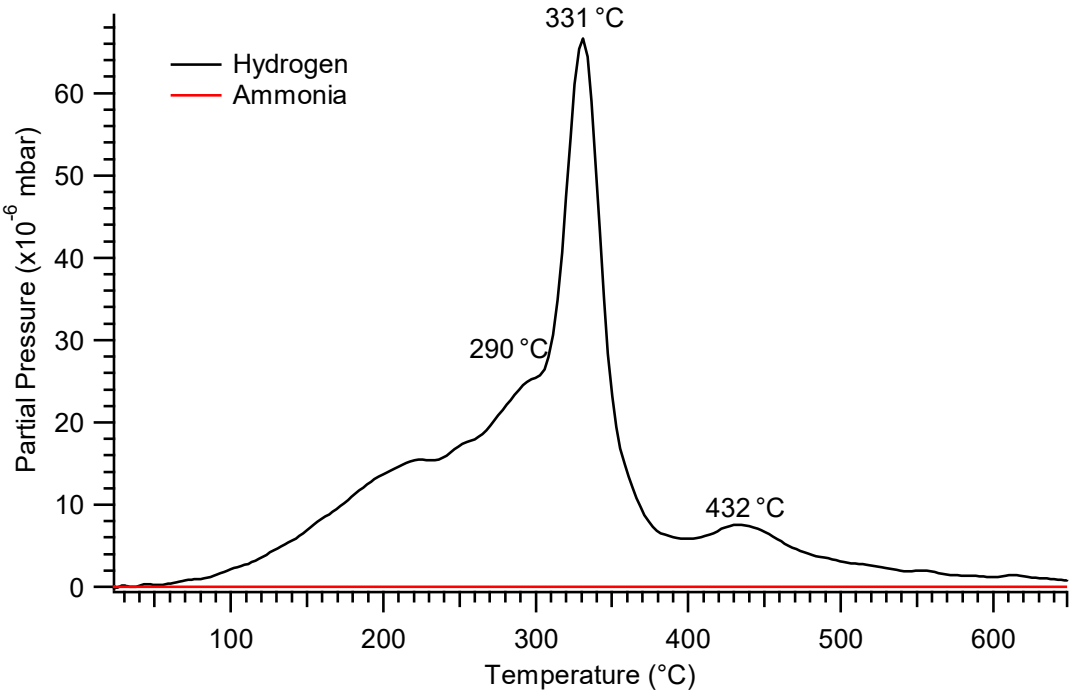

Figure 9.2: TPD-MS analysis of Sample 1 – $Mg(NH_2)_2$ + MgH_2 + NaH (1:2:1) performed under dynamic vacuum in the temperature range of 25 – 650 °C, where the heating rate was 2 °C min^{-1}.

9.2.1.3 *Ex situ* X-ray diffraction (XRD) analysis of Sample 1

Ex situ XRD analysis can identify phases to help determine the reaction pathway in this system, *ex situ* XRD (Figure 9.3) was performed on TPD-MS measurements halted at 230, 380 and 650 °C, with temperatures chosen based on the results of the first TPD-MS analysis (Figure 9.2). Because of the small amount of sample (~20 mg) used for TPD-MS, the low-background holder was required for XRD measurements that explain the low intensity peaks compared to the board hump at a 2θ angle of ~20° (produced by the PMMA dome). Between

RT and 230 °C (Figure 9.3a and 9.3b, respectively), *ex situ* XRD analysis revealed that the MgNH peaks appeared to decrease in intensity and shift slightly to higher 2θ angles. This shift could be an experimental artifact due to different sample displacements occurring from the low-background holder. The unknown (possibly $NaMgH_3$) peak intensity at ~35° (2θ) decreased by 230 °C. Given that no other phase changes were observed by XRD analysis at 230 °C, no conclusions could be made that corresponded to the hydrogen release event at ~210 °C in the TPD-MS analysis (Figure 9.2).

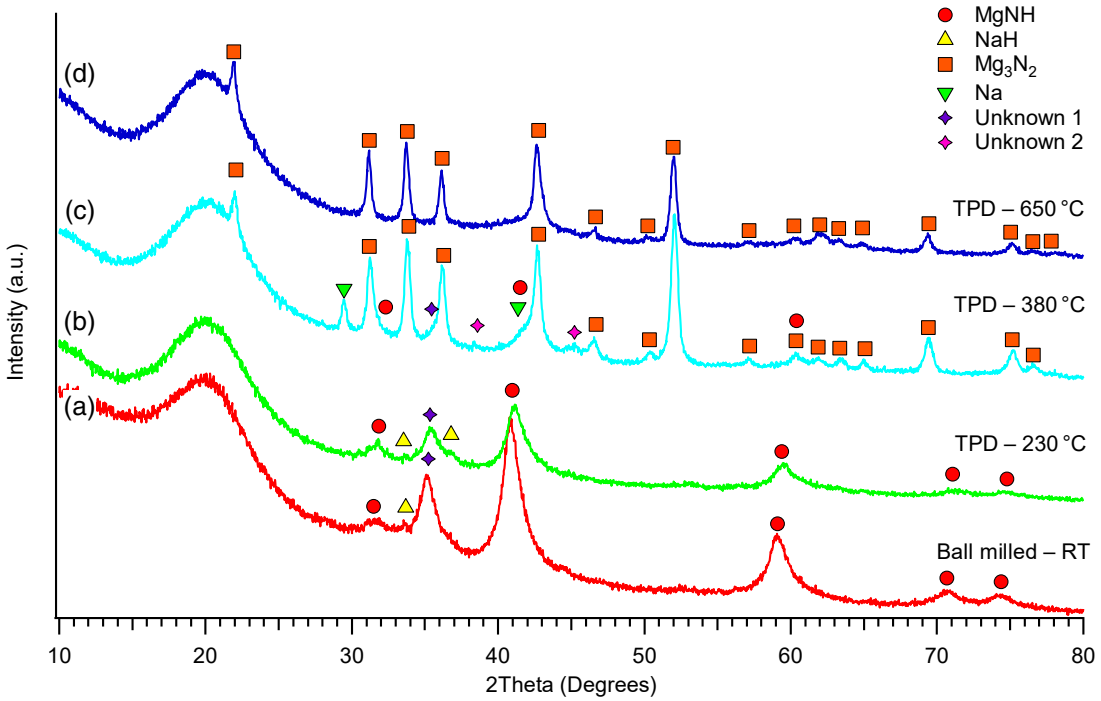

Figure 9.3: *Ex situ* XRD analysis of Sample 1 – $Mg(NH_2)_2$ + MgH_2 + NaH (1:2:1) after (a) ball milling and TPD-MS measurements that were halted at (b) 230 °C, (c) 380 °C and (d) 650 °C.

The decomposition of pure NaH in an argon atmosphere, releases hydrogen between 300 °C and 400 °C, peaking at a temperature of ~350 °C (Adelhelm, de Jong and de Jongh 2009). This decomposition explains the appearance of sodium (Na) metal in the XRD analysis at 380 °C (Figure 9.3c). The release of hydrogen from the decomposition of NaH likely contributed to the hydrogen desorption event observed at 331 °C in the TPD-MS analysis (Figure 9.2). By 380 °C, XRD analysis (Figure 9.3c) revealed that the sample reagents were completely consumed to form Mg_3N_2 with residual amounts of cubic MgNH and the unknown (possibly $NaMgH_3$) phase. However, assuming the unknown phase

is $NaMgH_3$, and given the hydrogen desorption events between 230 °C and 380 °C in the TPD-MS analysis (Figure 9.2), it is possible that the reaction in Equation 9.1 occurred at ~290 °C and by 331 °C, the NaH (formed in Equation 9.1) decomposed to Na metal. These hydrogen release events are consistent with the phases identified by XRD analysis (Figure 9.3c) and TPD-MS analysis (Figure 9.2). By 650 °C (Figure 9.3d), any remaining Na metal is possibly vaporised and evacuated by the turbo pump, leaving single phase Mg_3N_2 in the final products. However, because no new products were formed between 380 °C and 650 °C, no conclusions could be made for the hydrogen desorption event at 432 °C in the TPD-MS analysis (Figure 9.2).

9.2.1.4 *In situ* synchrotron X-ray diffraction (SXRD) analysis of Sample 2

TPD-MS and *ex situ* XRD analyses (Figure 9.2 and 9.3, respectively) were used to identify the phase changes and reaction pathway in the Na–Mg–N–H system. However, the desorption event at 432 °C (Figure 9.2) was not identified as no obvious phase change occurred between 380 °C and 650 °C (Figure 9.3). Therefore, *in situ* SXRD measurements were performed to identify the phase changes using the Powder Diffraction beamline. Given the synchrotron-beam deadline, it was not possible to confirm the purity of the starting reagents before SXRD measurements. However, as-synthesised MgNH* contained a mixture of MgNH, $Mg(NH_2)_2$ and MgH_2 in a 2:1:1 molar ratio as discussed in the synthesis of MgNH in Chapter 7: Section 7.2.2.1. Note that MgNH became X-ray amorphous after SXRD sample preparations in the Li–Mg–N–H system (Chapter 7). Therefore, the incomplete synthesis of MgNH* explains the different starting reagents observed during *in situ* SXRD analysis of Sample 2 – MgNH* + $NaMgH_3$ (2:1) compared to the starting reagents used in the *ex situ* XRD analysis of Sample 1 – $Mg(NH_2)_2$ + MgH_2 + NaH (1:2:1) (Figure 9.3).

In situ SXRD analysis of MgNH* + $NaMgH_3$ (2:1) was performed with a heating rate of 5 °C min^{-1} in the temperature range of 75 – 500 °C under a dynamic vacuum. Figure 9.4 confirmed that the synthesis of $NaMgH_3$ (③) was successful, appearing in the starting phase as anticipated. Furthermore, as-synthesised MgNH* was incomplete (as discussed previously), confirmed by the appearance

* Incomplete synthesis and contains a mixture of amorphous-MgNH, $Mg(NH_2)_2$ and MgH_2.

of starting reagents, $Mg(NH_2)_2$ (2), MgH_2 (1) and possibly amorphous MgNH (not observed in Figure 9.4). Although cubic MgNH has peak positions close to MgO (Dolci et al. 2010), the low and broad peak at a 2θ angle of ~27° does not appear to change in intensity with increasing temperature. The static peak intensity suggests that it could be MgO (8) and originated from contaminants already present in the starting reagents used. Furthermore, *ex situ* XRD analysis of cubic MgNH in Figure 9.3 revealed that the peak intensity decreases with increasing temperature as it is consumed to form Mg_3N_2, which was not observed by *in situ* SXRD analysis in Figure 9.4.

A by-product salt (LiCl 5) from the THF-washing of $Mg(NH_2)_2$ (Chapter 5: Section 5.2.1) appears in the starting phase with increasing peak intensity (increased crystallinity) at temperatures > 200 °C until its peaks are overlapped by those of other phases. Between 250 °C and 325 °C, $Mg(NH_2)_2$ (2) and MgH_2 (1) decreases in peak intensity as $Mg(NH_2)_2$ appears to transform directly into Mg_3N_2 (7) by reacting with MgH_2 (Dolotko, Paulson and Pecharsky 2010; Equation 9.5). At ~300 °C, the appearance of NaH suggests that the rest of $Mg(NH_2)_2$ (2) reacts with $NaMgH_3$ (3) forming Mg_3N_2 (7) and NaH (4) (Dolotko, Paulson and Pecharsky 2010; Equation 9.6).

$$\frac{1}{2}Mg(NH_2)_2 + MgH_2 \rightarrow \frac{1}{2}Mg_3N_2 + 2H_2 \quad (9.5)$$

$$\frac{1}{2}Mg(NH_2)_2 + NaMgH_3 \rightarrow \frac{1}{2}Mg_3N_2 + NaH + 2H_2 \quad (9.6)$$

An unknown phase (6) appears between 325 °C and 450 °C that could be related to the hydrogen desorption event at 432 °C observed in the TPD analysis of Sample 1 (Figure 9.2). At temperatures > 350 °C, NaH (4) disappears from the possible decomposition to Na metal. Because MgNH was X-ray amorphous, it is not clear from SXRD if there were any interactions between MgNH and $NaMgH_3$ (3) as anticipated in Equation 9.1 before the decomposition of NaH (< 350 °). Furthermore, it appears as though $Mg(NH_2)_2$ (2) is directly reacting with MgH_2 (1) and $NaMgH_3$ (3) to form Mg_3N_2 (7), by-passing the possible formation of MgNH. However, the result of this reaction pathway in Sample 2 are consistent with the end phases observed in the *ex situ* XRD analysis of Sample 1 (Figure 9.3).

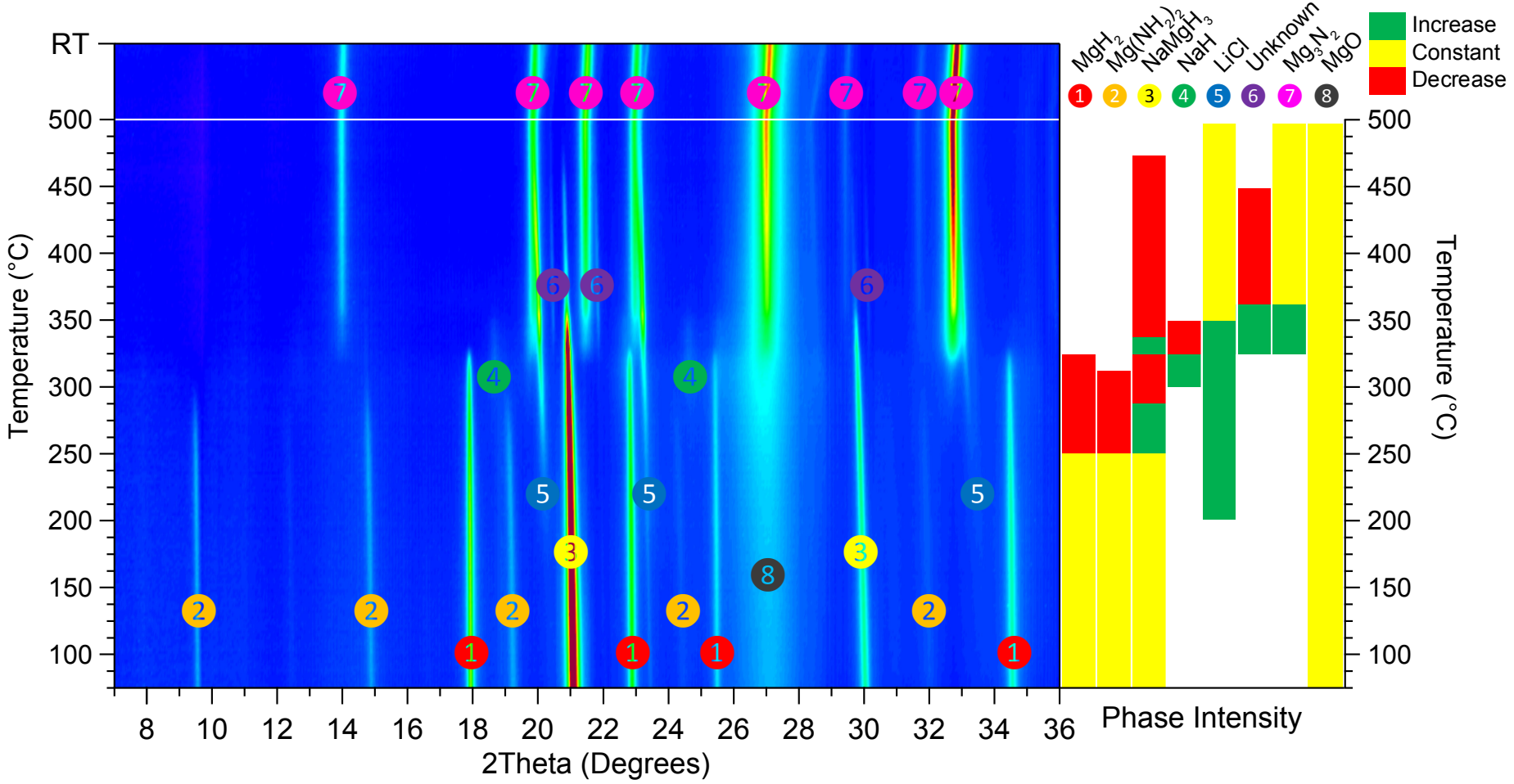

Figure 9.4: *In situ* SXRD analysis (λ = 1.00036 Å) of MgNH* + $NaMgH_3$ (2:1) under dynamic vacuum with phase identification.

To observe the desorption properties of the sample under different working conditions, Figure 9.5 shows the *in situ* SXRD analysis in the temperature range of 100 – 500 °C under a hydrogen back pressure (heating rate was 5 °C min^{-1}). As the pressurised reference volume was opened to the evacuated sample capillary, the pressure in the gas handling system dropped from 2 bar to 1.4 bar and remained the same until the end of the measurement. Similar to the measurement under dynamic vacuum (Figure 9.4), MgO (8) appeared as a low, broad peak at ~27° (2θ) and does not change with increasing temperature, originating from contaminants already present in the ball-milled sample. The main difference between this measurement and the measurement under dynamic vacuum (Figure 9.4) was the absence of the unknown phase (6) between 350 °C and 450 °C, possibly due to the presence of hydrogen. However, the starting reagents in Sample 2 – MgNH* + $NaMgH_3$ (2:1) reacted to form Mg_3N_2 (7) at ~325 °C, the same temperature observed under dynamic vacuum (Figure 9.4) and as anticipated in Equation 9.1.

* Incomplete synthesis and contains a mixture of amorphous-MgNH, $Mg(NH_2)_2$ and MgH_2.

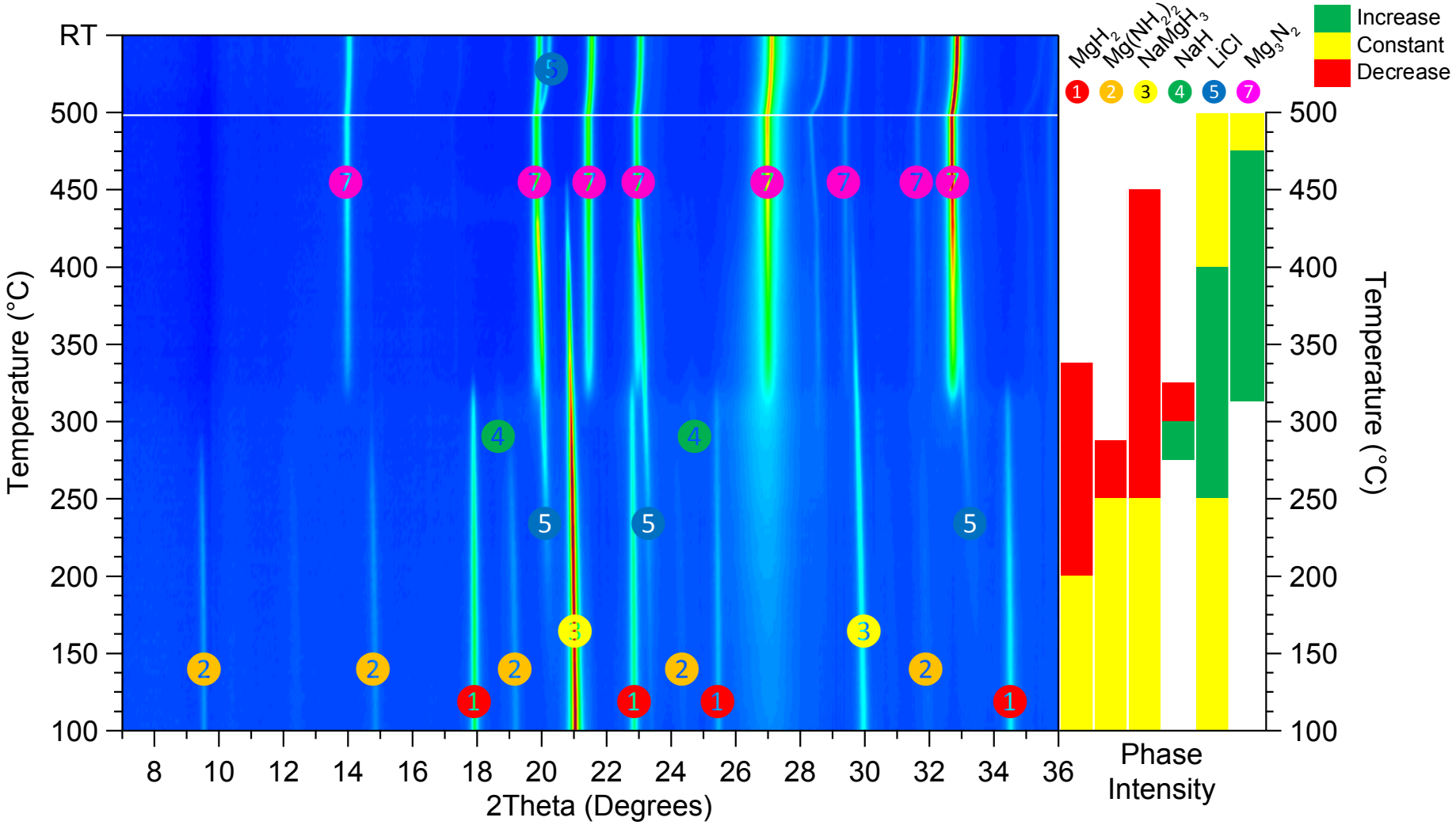

Figure 9.5: *In situ* SXRD analysis (λ = 1.00036 Å) of MgNH* + $NaMgH_3$ (2:1) under a hydrogen pressure of 1.4 bar with phase identification.

9.3 Discussion and Conclusion

Two mixtures were investigated as part of the Na–Mg–N–H system for thermal energy storage, Sample 1 – $Mg(NH_2)_2$ + MgH_2 + NaH (1:2:1) and Sample 2 – MgNH* + $NaMgH_3$ (2:1). In the preparation of Sample 1, the harsh ball-milling treatment resulted in a cubic phase of MgNH from the amide-hydride reaction between $Mg(NH_2)_2$ and MgH_2. XRD analysis revealed this cubic phase resembled periclase MgO and was modelled after MgO using Rietveld refinement, which was also done by Dolci et al. (2010). An unknown phase was identified after ball-milling and is suspected to be $NaMgH_3$. This suspicion is because *ex situ* XRD analysis revealed the formation of Mg_3N_2 and NaH after heating to 380 °C, consistent with the expected reaction pathway in Equation 9.1. However, NaH decomposed into Na metal (Equation 9.7) at temperatures > 350 °C. Therefore, the multiple hydrogen desorption events observed by the TPD-MS analysis of Sample 1 between 200 °C and 400 °C, corresponded to the possible release of hydrogen from the formation of Mg_3N_2 and NaH (Equation 9.1), and the subsequent decomposition of NaH (Equation 9.7).

$$NaH(s) \rightarrow Na(s) + \frac{1}{2}H_2(g) \tag{9.7}$$

In situ SXRD measurements were performed on Sample 2 – MgNH* + $NaMgH_3$ (2:1) under dynamic vacuum and a hydrogen back pressure (1.4 bar). Note that as-synthesised MgNH* was incompletely synthesised and contained a mixture of amorphous-MgNH, $Mg(NH_2)_2$ and MgH_2. Because MgNH was X-ray amorphous, the reaction in Equation 9.1 could not be investigated by SXRD analysis. However, the intermediate phases identified *in situ* were similar to the proposed decomposition pathway of $NaNH_2$ + MgH_2 (2:3) by Dolotko, Paulson, and Pecharsky (2010) in the following equations:

$$2NaNH_2 + MgH_2 \rightarrow Mg(NH_2)_2 + 2NaH \tag{9.8}$$

$$NaH + MgH_2 \rightarrow NaMgH_3 \tag{9.9}$$

* Incomplete synthesis and contains a mixture of amorphous-MgNH, $Mg(NH_2)_2$ and MgH_2.

$$\frac{1}{2}Mg(NH_2)_2 + MgH_2 \rightarrow \frac{1}{2}Mg_3N_2 + 2H_2 \quad (9.5a)$$

$$\frac{1}{2}Mg(NH_2)_2 + NaMgH_3 \rightarrow \frac{1}{2}Mg_3N_2 + NaH + 2H_2 \quad (9.6a)$$

Ex situ XRD analysis of Sample 1 ($Mg(NH_2)_2$–MgH_2–NaH) and *in situ* SXRD of Sample 2 (MgNH*–$NaMgH_3$) showed different reaction pathways in the Na–Mg–N–H system, but the end product at temperatures > 350 °C in either sample was the same (Mg_3N_2; Equation 9.6a). Therefore, by substituting $NaMgH_3$ for MgH_2 and reacting with $Mg(NH_2)_2$–MgH_2 (or MgNH) in the amide/imide-hydride reaction to form Mg_3N_2, the operating temperature of the amide/imide-hydride to nitride reaction was successfully increased from room temperature to approximately 350 °C. However, this temperature is not applicable for effective thermal energy storage (> 650 °C). Therefore, the Na–Mg–N–H system may not be suitable as a potential candidate for thermal energy storage technologies.

CHAPTER 10: CONCLUSIONS AND FUTURE WORK

10.1 Conclusions

The outcomes of this thesis were to provide a viable concentrated solar thermal (CST) energy storage system by identifying potential candidates for high temperature storage. The candidates were based on the study of alkali and alkaline earth metals in amide-imide-hydride systems and their metallic mixtures. A working CST energy storage system using low-cost imide-hydrides would promote the development of renewable energy systems to inevitably reduce the reliance on fossil fuels. The hydrogen release and decomposition of a wide variety of amide- and imide-hydrides covered in this thesis provided detailed experimental synthesis and characterisation of materials by investigating: desorption and absorption temperatures, plateau pressures, reaction pathways, thermodynamics, hydriding kinetics and reversibility.

A novel method of obtaining fast thermodynamic data of metal hydrides was developed and investigated in Chapter 3. Using a low volume apparatus (LVA), the hydride is maintained at near-constant hydrogen content (NCHC) during heating to satisfy the requirements of the van't Hoff equation. These conditions required a constant hydrogen to metal atomic ratio (H/M) that were met by minimising the change in hydrogen content between step-wise temperature increments and its equilibrium pressures. The objective of this chapter was to reproduce the van't Hoff plots of known metal hydride systems using the new LVA-NCHC method. The LVA-NCHC method involves step-wise temperature increments at NCHC that can be performed in three to seven days compared to as much as thirty-one days for the traditional pressure-composition-temperature (PCT) method. The magnesium-magnesium hydride system was chosen for its flat plateaux observed in PCT measurements. The van't Hoff plots obtained for the Mg–MgH_2 system revealed that the average enthalpy value of absorption and desorption was close to literature values, where $|\Delta H_{avg}|$ = 76.19 ± 0.60 kJ (mol H_2)$^{-1}$ (ΔH_{abs} = –76.03 ± 0.41 kJ (mol H_2)$^{-1}$ and ΔH_{des} = 76.35 ± 0.47 kJ (mol H_2)$^{-1}$), and confirmed the reliability of the LVA-NCHC method. However, the investigation of amide-imide-hydride systems in this thesis typically featured

sloping plateaux. Therefore, the development of this method was also advantageous for these systems known for their slow kinetics (sloping plateaux).

Lithium-, magnesium- and calcium-based amide-imide-hydride systems (Chapter 4, 5 and 6) were initially investigated as potential candidates for high-temperature thermal energy storage. They were selected as their amide-hydride to imide reactions have been widely characterised in literature for low temperature applications. However, relatively little characterisation has been done on the imide-hydride to nitride reactions that occur at high temperature; taking advantage of their endothermic/exothermic reactions with hydrogen for thermal energy storage. Therefore, the outcomes for Chapter 4, 5 and 6 will be beneficial to the academic community, even for systems that were not applicable for thermal energy storage.

The widely studied hydrogen release from the amide-hydride to imide reaction in the Li–N–H system (Chapter 4) was investigated to reproduce the results reported in the literature so as to become familiar with the characterisation methods that would be used throughout this thesis. However, conflicting results with literature led to the extensive investigation of this system, which contributed to the majority of this thesis work. Temperature-programmed desorption (TPD) revealed that the hydrogen release from the lithium amide-hydride reaction occurred at a temperature of ~230 °C, in agreement with literature, but the imide-hydride to nitride reaction did not occur as anticipated. Instead, a solid solution of the imide (Li_2NH) and nitride hydride (Li_4NH) was formed at ~530 °C, where the solid-solution became irreversible at high temperature because of its melting behaviour based on temperature-programmed photographic analysis (TPPA). Therefore, pure lithium-based imide-hydride systems may not be suitable for high-temperature thermal energy storage.

The next chapter of this thesis (Chapter 5) investigated the properties of potential imide-hydride systems based on magnesium imide (MgNH) with other magnesium-based hydrides such as magnesium hydride (MgH_2) and magnesium iron hydride (Mg_2FeH_6). The decomposition of pure magnesium amides ($Mg(NH_2)_2$) and imides were characterised to confirm the quality of the starting reagents that were used in magnesium imide-hydride to nitride reactions.

$Mg(NH_2)_2$ was synthesised using a metathesis reaction between lithium amide and magnesium chloride, where the by-product chloride salts (LiCl) were successfully removed using a tetrahydrofuran (THF) solvent. The synthesis of MgNH resulted in either a cubic structure after heating to 200 °C or an X-ray amorphous phase after intense ball milling. However, oxygen contamination of the starting reagents were often found because of the affinity of magnesium for oxygen. The substitution of MgH_2 with the more stable Mg_2FeH_6 was investigated by *in situ* synchrotron X-ray diffraction (SXRD) that revealed the formation of magnesium nitride (Mg_3N_2) started at a temperature of 300 °C. However, the hydrogenation of the nitride-iron product, $Mg_3N_2 + Fe + H_2$ (2:1:5), was irreversible at temperatures $\leq$ 400 °C because impractical hydrogen pressures were required (> 140 bar). Therefore, this substitution may not be suitable for thermal energy storage, but the decomposition process of magnesium amides and imides were useful for the investigation of mixed metal imide-hydride systems in subsequent chapters.

Hydrogen release from the imide-hydride reactions in the Ca–N–H system was investigated in Chapter 6 for high temperature applications. Calcium nitride hydride (Ca_2NH), known for sloping plateaux in PCT measurements was also used to test the LVA-NCHC method developed in Chapter 3. Using the new LVA-NCHC method on the hydrogenation of Ca_2NH, the obtained enthalpy and entropy values of absorption were used to calculate a practical heat storage capacity of 959 ± 58 kJ kg^{-1}. Furthermore, the system was estimated to operate at an equilibrium hydrogen pressure of ~31 bar and a temperature of ~800 °C. These operating conditions make the Ca_2NH system a potential candidate for high-temperature thermal energy storage while reducing the engineering costs. However, PCT measurements of Ca_2NH performed at 615 °C revealed that beyond a hydrogen content of 1 wt%, the slow kinetics may cause problems, requiring further investigation at temperatures > 615 °C. Inconclusive results were obtained from the substitution of CaH_2 with the more stable Ca_2FeH_6 in the imide-hydride reaction of the Ca–N–H system. *In situ* SXRD analysis revealed that the starting reagents started to decompose at ~450 °C and the formation of Ca_2NH was absent, suggesting a temperature requirement > 500 °C for the

imide-hydride reaction. Therefore, further investigation is required to investigate the formation of Ca_2NH at higher temperatures for thermal energy storage.

Mixed cation metal imide systems containing alkali and alkaline earth metals (Li, Mg, Ca and Na) were investigated in the subsequent chapters (Chapter 7, 8 and 9) for high temperature applications using the hydrogen release from the imide-hydride reaction. Chapter 7 investigated the Li–Mg–N–H mixed system, with lithium magnesium imide and lithium hydride, $Li_2Mg(NH)_2 + LiH$ (1:2), and magnesium imide and lithium hydride, MgNH + LiH (1:1). TPD and X-ray diffraction (XRD) revealed that at temperatures $\leq$ 500 °C, the formation of the expected nitride product (LiMgN) was absent, and instead was a mixture of α-$Li_2Mg(NH)_2$, β-$Li_2Mg(NH)_2$, LiH, Mg_3N_2 and non-stoichiometric phases of $Li_xMg_yN_z$. Furthermore, PCT measurements of LiMgN + H_2 (2:1) at 450 °C revealed a reversible hydrogen content of 1.2 wt% that resulted in the same mixture of phases. Therefore, given the anticipated imide-hydride to nitride reaction-pathway was not observed (as a result of intermediate phases and non-stoichiometric $Li_xMg_yN_z$), and the heat storage capacity estimated at a low range of 392 – 564 kJ kg^{-1} (with its high-pressure requirements), it was concluded that the Li–Mg–N–H system may not be suitable for high temperature applications.

Potential imide-hydride reactions in the Li–Ca–N–H system (Chapter 8) were investigated for high-temperature thermal energy storage. Lithium calcium imide and lithium hydride, $Li_2Ca(NH)_2 + LiH$ (1:2), and calcium imide and lithium hydride, CaNH + LiH (1:1), were investigated by *in situ* SXRD analysis, which revealed that at temperatures $\leq$ 500 °C, the anticipated imide-hydride to nitride reaction was not observed. However, manual PCT measurements of the nitride product, LiCaN + H_2 (3:2), at 650 °C revealed the reverse reaction involved a mixture of $Ca_{1+x}NH$, $Li_2Ca(NH)_2$ and LiH that had a practical hydrogen content of 2.2 wt%. Furthermore, this system was estimated to operate at low equilibrium pressures (~1 bar) with an estimated heat storage capacity that ranged between 977 and 1371 kJ kg^{-1}, which is a higher capacity than the Ca–N–H system (959 ± 58 kJ kg^{-1}). Therefore, the Li–Ca–N–H system has potential, but requires further work to investigate the reversible imide-hydride to nitride reaction for thermal energy storage.

For high temperature applications in the Na–Mg–N–H system (Chapter 9), due to its higher stability, sodium magnesium hydride ($NaMgH_3$) was chosen as a substitute for MgH_2 in the imide-hydride reaction of the Mg–N–H system. However, the incomplete synthesis of MgNH resulted in the investigation of hydrogen release from the amide-hydride reaction. The amide/imide-hydride to nitride reaction temperature was successfully improved from ~25 °C to 350 °C by substituting $NaMgH_3$ for MgH_2. However, a temperature of ~350 °C is insufficient for high temperature applications. Therefore, the Na–Mg–N–H system may not be suitable for thermal energy storage.

Table 10.1: Operation conditions and outcome of potential thermal energy storage (TES) systems in this thesis.

System	Reaction	Operation Conditions	Potential TES?
Li–N–H	Amide-Hydride	T = 415 °C, P = ~14 bar.	No
	Imide-Hydride	Not applicable at $T \leq$ 500 °C.	No
Mg–N–H	Amide-Hydride	Room temperature, atmospheric.	No
	Imide-Hydride	T = 25 – 200 °C, P = atmospheric.	No
	Imide-Iron Hydride	Not observed at $T \leq$ 500 °C and $P \leq$ 140 bar.	No
Ca–N–H	Nitride Hydride	T = 615 °C, P = ~1 bar.	Yes
	Imide-Iron Hydride	Not observed at $T \leq$ 500 °C.	Yes*
Li–Mg–N–H	Imide-Hydride	Not applicable at $T \leq$ 500 °C.	No
	Nitride	T = 450 °C, P = 2.92 bar.	No
	Imide Halide	Not observed at $T \leq$ 500 °C.	No*
Li–Ca–N–H	Imide-Hydride	Not observed at $T \leq$ 500 °C.	No*
	Nitride	T = 650 °C, P = ~1.13 bar.	Yes
Na–Mg–N–H	Amide/Imide-Hydride	T = ~350 °C, P = atmospheric.	No

* Requires further investigation at temperatures > 500 °C by utilising the LVA-NCHC method.

Summarised in Table 10.1, calcium-based systems and mixed systems containing calcium metal were the most promising candidates for high-temperature thermal energy storage. The other systems investigated in this thesis showed imide-hydride to nitride reactions that either occurred at non-applicable temperatures or formed intermediate phases and residual products (incomplete reaction). However, the characterisation of these systems was beneficial in exploring their potential in other applications such as low-cost hydrogen storage materials. Inconclusive results were obtained for $Ca_2NH + H_2$ (1:1), $CaNH + Ca_2FeH_6$ (2:1) and the reversible reaction of $LiCaN + H_2$ (3:2). Therefore, further work is required to investigate the possible imide-hydride systems for high-temperature applications.

10.2 Future Work

To further the work presented in this thesis, several problems need to be addressed before future investigations can be made. The stainless-steel samples cells used for TPD, PCT and step-wise temperature measurements for the LVA-NCHC method had problems with the absorption and diffusion of hydrogen at temperatures > 400 °C and hence, large corrections were required. These corrections were based on a combination of assumed and literature values for the hydrogen diffusion and absorption, through stainless steel. Therefore, any difference between the assumed values and actual values would introduce small but systematic errors resulting in large uncertainties. To alleviate this engineering problem, silver coated sample cells or sample cells made of silicon carbide have been proposed to minimise the direct exposure of hydrogen to the stainless-steel components.

Oxygen contamination of samples was another problem related to the sample cells leaking. This problem was often caused from the repeated use of the same sample cell, where the oxidation of steel at high temperature caused deformations on the steel ferrules, resulting in a leak. The introduction of oxygen from leaks caused the formation of oxides that would change the stoichiometry between hydrogen-active species, altering the anticipated reaction pathway. Furthermore, oxide layers inhibited the transport of hydrogen, affecting the

investigation of potential reversible reactions. Another source of contamination was caused by the hardness of the polyimide/graphite ferrules used for *in situ* SXRD measurements, resulting in contamination before the samples arrived at the Powder Diffraction beamline at the Australian Synchrotron. Therefore, future work also involves the re-investigation of the contaminated samples by using soft graphite ferrules for *in situ* SXRD measurements after solving the engineering problem with leaking sample cells used to heat treat starting reagents.

In summary, future work includes the investigation of sample cell materials to reduce the diffusion and absorption of hydrogen at high temperatures and thus, reduce the leak correction uncertainties. Once the engineering problems have been solved, further work involves the investigation of promising systems presented in this thesis at temperatures > 650 °C for thermal energy storage as summarised in Table 10.1. Inconclusive results were obtained from *in situ* SXRD analysis of CaNH + Ca_2FeH_6 (2:1) at temperatures ≤ 500 °C. Therefore, this reaction could be further characterised using the new LVA-NCHC method to obtain thermodynamic data (Chapter 3) at temperatures > 500 °C. Most of the anticipated imide-hydride to nitride reactions did not go to completion during PCT measurements at temperatures between 450 °C and 650 °C. Manual PCT measurements on the hydrogenation of LiCaN, LiCaN + H_2 (3:2), at 450 °C revealed a recognisable plateau. However, the reversible reaction at temperatures ≤ 650 °C was inconclusive. Therefore, this ternary imide can also be further characterised using the LVA-NCHC method at temperatures > 650 °C to determine its reversible reaction and viability for high-temperature thermal energy storage.

Based on the promising results from systems containing calcium metal (Ca–N–H and Li–Ca–N–H), the Mg–Ca–N–H system would be the next logical target for a low-cost imide-hydride system by performing a manual PCT measurement followed by the LVA-NCHC method. Furthermore, other alkali and alkaline earth metal imide-hydride systems can be investigated using the LVA-NCHC method to identify systems that satisfy the operating conditions for concentrated solar thermal energy storage systems.

LIST OF REFERENCES

Abedin, A. H., and M. A. Rosen. 2011. "A Critical Review of Thermochemical Energy Storage Systems." *The Open Renewable Energy Journal* 4: 42 – 46. http://dx.doi.org/10.2174/1876387101004010042.

Adelhelm, P., K. P. de Jong, and P. E. de Jongh. 2009. "How intimate contact with nanoporous carbon benefits the reversible hydrogen desorption from NaH and $NaAlH_4$." *Chemical Communications* (41): 6261 – 6263. http://dx.doi.org/10.1039/B910461E.

Akbarzadeh, A. R., V. Ozoliņš, and C. Wolverton. 2007. "First-Principles Determination of Multicomponent Hydride Phase Diagrams: Application to the Li–Mg–N–H System." *Advanced Materials* 19 (20): 3233 – 3239. http://dx.doi.org/10.1002/adma.200700843.

Alapati, S. V., J. Karl Johnson, and D. S. Sholl. 2007. "Using first principles calculations to identify new destabilized metal hydride reactions for reversible hydrogen storage." *Physical Chemistry Chemical Physics* 9 (12): 1438 – 1452. http://dx.doi.org/10.1039/B617927D.

Anderson, P. A., P. A. Chater, D. R. Hewett, and P. R. Slater. 2011. "Hydrogen storage and ionic mobility in amide-halide systems." *Faraday Discussions* 151: 271 – 284. http://dx.doi.org/10.1039/C0FD00027B.

Bailey, A. S., P. Hubberstey, R. W. Hughes, C. Ritter, and D. H. Gregory. 2010. "Tunable Defect Structure in the Li–Mg–N Ternary Phase System: A Powder Neutron Diffraction Study." *Chemistry of Materials* 22 (10): 3174 – 3182. http://dx.doi.org/10.1021/cm100243v.

Berg, P., J. Nielsen, and M. K. Sørensen. 2006. "EVA: Realized and predicted optimal genetic contributions." *Book of Abstracts: CD communication* 27–09: 246.

Bergstrom, F. W., and W. C. Fernelius. 1933. "The Chemistry of the Alkali Amides." *Chemical Reviews* 12 (1): 43 – 179. http://dx.doi.org/10.1021/CR60041A002.

Bogdanović, B., K. Bohmhammel, B. Christ, A. Reiser, K. Schlichte, R. Vehlen, and U. Wolf. 1999. "Thermodynamic investigation of the magnesium–hydrogen system." *Journal of Alloys and Compounds* 282 (1–2): 84 – 92. http://dx.doi.org/10.1016/S0925-8388(98)00829-9.

Bogdanović, B., A. Reiser, K. Schlichte, B. Spliethoff, and B. Tesche. 2002. "Thermodynamics and dynamics of the Mg–Fe–H system and its potential for thermochemical thermal energy storage." *Journal of Alloys and Compounds* 345 (1–2): 77 – 89. http://dx.doi.org/10.1016/S0925-8388(02)00308-0.

Bogdanovic, B., A. Ritter, and B. Spliethoff. 1989. Method of and device for storing and transforming heat and generating cold. United States 4829772, filed Nov 16, 1987, and issued May 16, 1989. http://www.google.la/patents/US4829772.

Bogdanović, B., A. Ritter, and B. Spliethoff. 1990. "Active MgH_2–Mg Systems for Reversible Chemical Energy Storage." *Angewandte Chemie International Edition in English* 29 (3): 223 – 234. http://dx.doi.org/10.1002/anie.199002233.

Brice, J.-F., J.-P. Motte, A. Courtois, J. Protas, and J. Aubry. 1976. "Etude structurale de Ca_2NH par diffraction des rayons X, diffraction des neutrons et résonance magnétique nucléaire du proton dans le solide." *Journal of Solid State Chemistry* 17 (1–2): 135 – 142. http://dx.doi.org/10.1016/0022-4596(76)90213-9.

Bulanov, A. D., O. Y. Troshin, and V. V. Balabanov. 2004. "Synthesis of High-Purity Calcium Hydride." *Russian Journal of Applied Chemistry* 77 (6): 875 – 877. http://dx.doi.org/10.1023/B:RJAC.0000044107.80122.61.

Bull, D. J., E. Weidner, I. L. Shabalin, M. T. F. Telling, C. M. Jewell, D. H. Gregory, and D. K. Ross. 2010. "Pressure-dependent deuterium reaction pathways in the Li-N-D system." *Physical Chemistry Chemical Physics* 12 (9): 2089 – 2097. http://dx.doi.org/10.1039/B903821N.

Busing, W. R. 1970. "An interpretation of the structures of alkaline earth chlorides in terms of interionic forces." *Transactions of the American Crystallographic Association* 6: 57 – 72.

Cao, H., G. Wu, Y. Zhang, Z. Xiong, J. Qiu, and P. Chen. 2014. "Effective thermodynamic alteration to $Mg(NH_2)_2$-LiH system: Achieving near ambient-temperature hydrogen storage." *Journal of Materials Chemistry A* 2 (38): 15816 – 15822. http://dx.doi.org/10.1039/c4ta03505d.

Chaise, A., P. de Rango, P. Marty, and D. Fruchart. 2010. "Experimental and numerical study of a magnesium hydride tank." *International Journal of Hydrogen Energy* 35 (12): 6311 – 6322. http://dx.doi.org/10.1016/j.ijhydene.2010.03.057.

Cheary, R. W., A. A. Coelho, and J. P. Cline. 2004. "Fundamental Parameters Line Profile Fitting in Laboratory Diffractometers." *J Res Natl Inst Stand Technol* 109 (1): 1 – 25. http://dx.doi.org/10.6028/jres.002.

Chen, P., Z. Xiong, J. Luo, J. Lin, and K. L. Tan. 2002. "Interaction of hydrogen with metal nitrides and imides." *Nature* 420 (6913): 302 – 304. http://dx.doi.org/10.1038/nature01210.

Chen, P., Z. Xiong, J. Luo, J. Lin, and K. L. Tan. 2003. "Interaction between Lithium Amide and Lithium Hydride." *The Journal of Physical Chemistry B* 107 (39): 10967 – 10970. http://dx.doi.org/10.1021/jp034149j.

Chen, P., Z. Xiong, L. Yang, G. Wu, and W. Luo. 2006. "Mechanistic Investigations on the Heterogeneous Solid-State Reaction of Magnesium Amides and Lithium Hydrides." *J. Phys. Chem. B* 110: 14221 – 14225. http://dx.doi.org/10.1021/jp061496v.

Chu, H., Z. Xiong, G. Wu, T. He, C. Wu, and P. Chen. 2010. "Hydrogen storage properties of Li–Ca–N–H system with different molar ratios of $LiNH_2$/CaH_2." *International Journal of Hydrogen Energy* 35 (15): 8317 – 8321. http://dx.doi.org/10.1016/j.ijhydene.2009.12.009.

Cordier, G., A. Gudat, R. Kniep, and A. Rabenau. 1989. "LiCaN and Li_4SrN_2, Derivatives of the Fluorite and Lithium Nitride Structures." *Angewandte Chemie International Edition in English* 28 (12): 1702 – 1703. http://dx.doi.org/10.1002/anie.198917021.

Dafert, F. W., and R. Miklauz. 1909. "Über einige neue Verbindungen von Stickstoff und Wasserstoff mit Metallen." *Monatshefte für Chemie und verwandte Teile anderer Wissenschaften* 30 (7): 649 – 654. http://dx.doi.org/10.1007/bf01517629.

Dinçer, İ., and M. A. Rosen. 2002. "Energy Storage Systems." In *Thermal Energy Storage: Systems and Applications*. Chichester, England: John Wiley & Sons, Ltd. http://dx.doi.org/10.1002/9780470970751.ch2.

Dolci, F., E. Napolitano, E. Weidner, S. Enzo, P. Moretto, M. Brunelli, T. Hansen, M. Fichtner, and W. Lohstroh. 2010. "Magnesium Imide: Synthesis and Structure Determination of an Unconventional Alkaline Earth Imide from

Decomposition of Magnesium Amide." *Inorganic Chemistry* 50 (3): 1116 – 1122. http://dx.doi.org/10.1021/ic1023778.

Dolotko, O., N. Paulson, and V. K. Pecharsky. 2010. "Thermochemical transformations in $2MNH_2$–$3MgH_2$ systems (M = Li or Na)." *International Journal of Hydrogen Energy* 35 (10): 4562 – 4568. http://dx.doi.org/10.1016/j.ijhydene.2010.02.104.

Dornheim, M. 2011. *Thermodynamics of Metal Hydrides: Tailoring Reaction Enthalpies of Hydrogen Storage Materials* Edited by Juan Carlos Moreno-Pirajan, *Thermodynamics - Interaction Studies - Solids, Liquids and Gases*: InTech. http://dx.doi.org/10.5772/21662.

Ermrich, M., and D. Opper. 2013. *XRD for the analyst: Getting acqured with the principles*, *X-ray Powder Diffraction*. Almelo, The Netherlands: PANalytical B. V. http://www.panalytical.com.

Felderhoff, M., and B. Bogdanović. 2009. "High Temperature Metal Hydrides as Heat Storage Materials for Solar and Related Applications." *International Journal of Molecular Sciences* 10 (1): 325 – 344. http://dx.doi.org/10.3390/ijms10010325.

Fellet, M., C. E. Buckley, M. Paskevicius, and D. A. Sheppard. 2013. "Research on metal hydrides revived for next-generation solutions to renewable energy storage." *MRS Bulletin* 38 (12): 1012 – 1013. http://dx.doi.org/10.1557/mrs.2013.288.

Geoscience Australia, and Bureau of Resources and Energy Economics. 2014. *Australian Energy Resource Assessment*. 2nd ed. Canberra. http://www.ga.gov.au/metadata-gateway/metadata/record/gcat_79675.

Gregory, D. H. 2008. "16 - Imides and amides as hydrogen storage materials A2 - Walker, Gavin." In *Solid-State Hydrogen Storage*, 450 – 477. Woodhead Publishing. http://dx.doi.org/10.1533/9781845694944.4.450.

Groll, M., A. Isselhorst, and M. Wierse. 1994. "Metal hydride devices for environmentally clean energy technology." *International Journal of Hydrogen Energy* 19 (6): 507 – 515. http://dx.doi.org/10.1016/0360-3199(94)90005-1.

Hagemann, H., V. D'Anna, L. M. Lawson Daku, S. Gomes, G. Renaudin, and K. Yvon. 2011. "Structural and vibrational properties of Ca_2FeH_6 and Sr_2RuH_6." *Journal of Physics and Chemistry of Solids* 72: 286 – 289. http://dx.doi.org/10.1016/j.jpcs.2011.01.001.

Hammersley, A. P. 1997. *FIT2D: AN Introduction and overview*. ESRF Internal. Report Number ESRF97HA02T.

Hanhong Scientific. Hanhong Group. Accessed 25/02/2017, http://www.hanhonggroup.com/.

Harries, D. N., M. Paskevicius, D. A. Sheppard, T. E. C. Price, and C. E. Buckley. 2012. "Concentrating Solar Thermal Heat Storage Using Metal Hydrides." *Proceedings of the IEEE* 100 (2): 539 – 549. http://dx.doi.org/10.1109/JPROC.2011.2158509.

Hino, S., T. Ichikawa, and Y. Kojima. 2010. "Thermodynamic properties of metal amides determined by ammonia pressure-composition isotherms." *The Journal of Chemical Thermodynamics* 42 (1): 140 – 143. http://dx.doi.org/10.1016/j.jct.2009.07.024.

Hino, S., T. Ichikawa, H. Leng, and H. Fujii. 2005. "Hydrogen desorption properties of the Ca–N–H system." *Journal of Alloys and Compounds* 398 (1–2): 62 – 66. http://dx.doi.org/10.1016/j.jallcom.2005.01.052.

Hu, J., Y. Liu, G. Wu, Z. Xiong, and P. Chen. 2007. "Structural and Compositional Changes during Hydrogenation/Dehydrogenation of the Li–Mg–N–H System." *The Journal of Physical Chemistry C* 111 (49): 18439 – 18443. http://dx.doi.org/10.1021/jp075757s.

Hu, J., G. Wu, Y. Liu, Z. Xiong, P. Chen, K. Murata, K. Sakata, and G. Wolf. 2006a. "Hydrogen Release from $Mg(NH_2)_2$–MgH_2 through Mechanochemical Reaction." *The Journal of Physical Chemistry B* 110 (30): 14688 – 14692. http://dx.doi.org/10.1021/jp061279u.

Hu, J., Z. Xiong, G. Wu, P. Chen, K. Murata, and K. Sakata. 2006b. "Hydrogen releasing reaction between $Mg(NH_2)_2$ and CaH_2." *Journal of Power Sources* 159 (1): 116 – 119. http://dx.doi.org/10.1016/j.jpowsour.2006.04.007.

Hu, Y. H., and E. Ruckenstein. 2006. "Ultrafast Reaction between Li_3N and $LiNH_2$ To Prepare the Effective Hydrogen Storage Material Li_2NH." *Industrial & Engineering Chemistry Research* 45 (14): 4993 – 4998. http://dx.doi.org/10.1021/ie060380i.

Ichikawa, T., S. Isobe, N. Hanada, and H. Fujii. 2004. "Lithium nitride for reversible hydrogen storage." *Journal of Alloys and Compounds* 365 (1–2): 271 – 276. http://dx.doi.org/10.1016/s0925-8388(03)00637-6.

Ikeda, K., Y. Kogure, Y. Nakamori, and S. Orimo. 2005. "Reversible hydriding and dehydriding reactions of perovskite-type hydride $NaMgH_3$." *Scripta Materialia* 53 (3): 319 – 322. http://dx.doi.org/10.1016/j.scriptamat.2005.04.010.

International Energy Agency. 2010. *World Energy Outlook 2010*. Paris. www.iea.org/publications/freepublications/publication/weo-2010.html.

Isobe, S., T. Ichikawa, N. Hanada, H. Y. Leng, M. Fichtner, O. Fuhr, and H. Fujii. 2005. "Effect of Ti catalyst with different chemical form on Li–N–H hydrogen storage properties." *Journal of Alloys and Compounds* 404–406: 439 – 442. http://dx.doi.org/10.1016/j.jallcom.2004.09.081.

Jain, I. P., P. Jain, and A. Jain. 2010. "Novel hydrogen storage materials: A review of lightweight complex hydrides." *Journal of Alloys and Compounds* 503 (2): 303 – 339. http://dx.doi.org/10.1016/j.jallcom.2010.04.250.

Juza, R. 1964. "Amides of the Alkali and the Alkaline Earth Metals." *Angew. Chem. internet. Edit.* 3 (7): 471 – 481. http://dx.doi.org/10.1002/anie.196404711.

Juza, R., and K. Opp. 1951. "Metallamide und Metallnitride, 24. Mitteilung. Die Kristallstruktur des Lithiumamides." *Zeitschrift für anorganische und allgemeine Chemie* 266 (6): 313 – 324. http://dx.doi.org/10.1002/zaac.19512660606.

Juza, R., and H. Schumacher. 1963. "Zur kenntnis der Erdalkalimetallamide (Solid Solution Calcium Amide)." *Z. Anorg. Allg. Chem* 324: 278 – 286. http://dx.doi.org/10.1002/zaac.19633240508.

Kawakami, M., T. Kuriiwa, A. Kamegawa, H. Takamura, M. Okada, and T. Kaburagi. 2009. "Optimum Hydrogen Desorption Properties in LiH-LiOH Composites." *MATERIALS TRANSACTIONS* 50 (7): 1855 – 1858. http://dx.doi.org/10.2320/matertrans.M2009055.

Kersting, A. L. 2011. "Light Metal Amides and Imides for Hydrogen Storage." The School of Chemistry, College of Engineering and Physical Sciences, The University of Birmingham. http://etheses.bham.ac.uk/3589/.

Kim, J. W., J.-H. Shim, S. C. Kim, A. Remhof, A. Borgschulte, O. Friedrichs, R. Gremaud, F. Pendolino, A. Züttel, and Y. W. Cho. 2009. "Catalytic effect of titanium nitride nanopowder on hydrogen desorption properties of $NaAlH_4$ and its stability in $NaAlH_4$." *Journal of Power Sources* 192 (2): 582 – 587. http://dx.doi.org/10.1016/j.jpowsour.2009.02.083.

Kojima, Y., and Y. Kawai. 2005. "IR characterizations of lithium imide and amide." *Journal of Alloys and Compounds* 395 (1–2): 236 – 239. http://dx.doi.org/10.1016/j.jallcom.2004.10.063.

Lai, Q., M. Paskevicius, D. A. Sheppard, C. E. Buckley, A. W. Thornton, M. R. Hill, Q. Gu et al. 2015. "Hydrogen Storage Materials for Mobile and Stationary Applications: Current State of the Art." *ChemSusChem* 8 (17): 2789 – 2825. http://dx.doi.org/10.1002/cssc.201500231.

Leng, H., T. Ichikawa, and H. Fujii. 2006. "Hydrogen Storage Properties of Li–Mg–N–H Systems with Different Ratios of LiH/$Mg(NH_2)_2$." *The Journal of Physical Chemistry B* 110 (26): 12964 – 12968. http://dx.doi.org/10.1021/jp061120h.

Leng, H. Y., T. Ichikawa, S. Hino, N. Hanada, S. Isobe, and H. Fujii. 2004. "New Metal–N–H System Composed of $Mg(NH_2)_2$ and LiH for Hydrogen Storage." *The Journal of Physical Chemistry B* 108 (26): 8763 – 8765. http://dx.doi.org/10.1021/jp048002j.

Leng, H. Y., T. Ichikawa, S. Isobe, S. Hino, N. Hanada, and H. Fujii. 2005. "Desorption behaviours from metal–N–H systems synthesized by ball milling." *Journal of Alloys and Compounds* 404–406: 443 – 447. http://dx.doi.org/10.1016/j.jallcom.2004.09.082.

Ley, M. B., M. Paskevicius, P. Schouwink, B. Richter, D. A. Sheppard, C. E. Buckley, and T. R. Jensen. 2014. "Novel solvates $M(BH_4)_3S(CH_3)_2$ and properties of halide-free $M(BH_4)_3$ (M = Y or Gd)." *Dalton Transactions* 43 (35): 13333 – 13342. http://dx.doi.org/10.1039/c4dt01125b.

Liang, C., Y. Liu, M. Gao, and H. Pan. 2013. "Understanding the role of K in the significantly improved hydrogen storage properties of a KOH-doped Li–Mg–N–H system." *Journal of Materials Chemistry A* 1 (16): 5031 – 5036. http://dx.doi.org/10.1039/C3TA01071F.

Liang, C., Y. Liu, K. Luo, B. Li, M. Gao, H. Pan, and Q. Wang. 2010. "Reaction Pathways Determined by Mechanical Milling Process for Dehydrogenation/Hydrogenation of the $LiNH_2/MgH_2$ System." *Chemistry – A European Journal* 16 (2): 693 – 702. http://dx.doi.org/10.1002/chem.200901967.

Libowitz, G. G. 1974. "Metal hydrides for thermal energy storage" *9th Intersociety Energy Conversion Engineering Conference, Proceedings*, *San Francisco, California*. http://adsabs.harvard.edu/abs/1974iece.conf..322L.

Linde, G., and R. Juza. 1974. "IR-Spektren von Amiden und Imden zwei- und dreiwertiger Metalle." *Z. Anorg. Allg. Chem* 409: 199 – 214. http://dx.doi.org/10.1002/zaac.19744090209.

Liu, Y., J. Hu, Z. Xiong, G. Wu, P. Chen, K. Murata, and K. Sakata. 2007. "Investigations on hydrogen desorption from the mixture of $Mg(NH_2)_2$ and CaH_2." *Journal of Alloys and Compounds* 432 (1–2): 298 – 302. http://dx.doi.org/10.1016/j.jallcom.2006.05.124.

Liu, Y., K. Zhong, M. Gao, J. Wang, H. Pan, and Q. Wang. 2008. "Hydrogen Storage in a $LiNH_2$–MgH_2 (1:1) System." *Chemistry of Materials* 20 (10): 3521 – 3527. http://dx.doi.org/10.1021/cm800271a.

Lohstroh, W., and M. Fichtner. 2007. "Reaction steps in the Li–Mg–N–H hydrogen storage system." *Journal of Alloys and Compounds* 446–447: 332 – 335. http://dx.doi.org/10.1016/j.jallcom.2006.12.060.

Luo, W. 2004. "($LiNH_2$–MgH_2): a viable hydrogen storage system." *Journal of Alloys and Compounds* 381 (1–2): 284 – 287. http://dx.doi.org/10.1016/j.jallcom.2004.03.119.

Makepeace, J. W., M. O. Jones, S. K. Callear, P. P. Edwards, and W. I. F. David. 2014. "*In situ* X-ray powder diffraction studies of hydrogen storage and release in the Li–N–H system." *Physical Chemistry Chemical Physics* 16 (9): 4061 – 4070. http://dx.doi.org/10.1039/C4CP00087K.

Marx, R. 1997. "Reindarstellung und Kristallstruktur von Lithiumnitridhydrid, Li_4NH, Li_4ND." *Zeitschrift für anorganische und allgemeine Chemie* 623 (12): 1912 – 1916. http://dx.doi.org/10.1002/zaac.19976231215.

Nakamori, Y., G. Kitahara, and S. Orimo. 2004. "Synthesis and dehydriding studies of Mg–N–H systems." *Journal of Power Sources* 138 (1–2): 309 – 312. http://dx.doi.org/10.1016/j.jpowsour.2004.06.026.

Nakamori, Y., and S. Orimo. 2004. "Complex Hydrides for Solid-state Hydrogen Storage" *Proceedings of a conference: Processing and Fabrication of Advanced Materials XIII*, *Pan-Pacific Hotel, Singapore*: Stallion Press. http://www.worldscientific.com/worldscibooks/10.1142/w001.

Okamoto, K., K. Tokoyoda, T. Ichikawa, and H. Fujii. 2007. "A process for synthesizing the Li–Mg–N–H hydrogen storage system from Mg and $LiNH_2$." *Journal of Alloys and Compounds* 432 (1–2): 289 – 292. http://dx.doi.org/10.1016/j.jallcom.2006.05.119.

Panwar, N. L., S. C. Kaushik, and S. Kothari. 2011. "Role of renewable energy sources in environmental protection: A review." *Renewable and Sustainable Energy Reviews* 15 (3): 1513 – 1524. http://dx.doi.org/10.1016/j.rser.2010.11.037.

Paskevicius, M., M. B. Ley, D. A. Sheppard, T. R. Jensen, and C. E. Buckley. 2013. "Eutectic melting in metal borohydrides." *Physical Chemistry Chemical Physics* 15 (45): 19774 – 19789. http://dx.doi.org/10.1039/C3CP53920B.

Paskevicius, M., M. P. Pitt, C. J. Webb, D. A. Sheppard, U. Filsø, E. M. Gray, and C. E. Buckley. 2012. "In-Situ X-ray Diffraction Study of γ -$Mg(BH_4)_2$ Decomposition." *The Journal of Physical Chemistry C* 116 (29): 15231 – 15240. http://dx.doi.org/10.1021/jp302898k.

Paskevicius, M., D. A. Sheppard, and C. E. Buckley. 2010. "Thermodynamic Changes in Mechanochemically Synthesized Magnesium Hydride Nanoparticles." *Journal of the American Chemical Society* 132 (14): 5077 – 5083. http://dx.doi.org/10.1021/ja908398u.

Paskevicius, M., D. A. Sheppard, K. Williamson, and C. E. Buckley. 2015. "Metal hydride thermal heat storage prototype for concentrating solar thermal power." *Energy* 88: 469 – 477. http://dx.doi.org/10.1016/j.energy.2015.05.068.

Pinkerton, F. E. 2005. "Decomposition kinetics of lithium amide for hydrogen storage materials." *Journal of Alloys and Compounds* 400 (1–2): 76 – 82. http://dx.doi.org/10.1016/j.jallcom.2005.01.059.

Pistidda, C., A. Santoru, S. Garroni, N. Bergemann, A. Rzeszutek, C. Horstmann, D. Thomas, T. Klassen, and M. Dornheim. 2015. "First Direct Study of the Ammonolysis Reaction in the Most Common Alkaline and Alkaline Earth Metal Hydrides by *in Situ* SR-PXD." *The Journal of Physical Chemistry C* 119 (2): 934 – 943. http://dx.doi.org/10.1021/jp510720x.

Pitt, M. P., M. Paskevicius, C. J. Webb, D. A. Sheppard, C. E. Buckley, and E. M. Gray. 2012. "The synthesis of nanoscopic Ti based alloys and their effects on the MgH_2 system compared with the MgH_2 + $0.01Nb_2O_5$ benchmark." *International Journal of Hydrogen Energy* 37: 4227 – 4237. http://dx.doi.org/10.1016/j.ijhydene.2011.11.114.

Polanski, M., T. K. Nielsen, Y. Cerenius, J. Bystrzycki, and T. R. Jensen. 2010. "Synthesis and decomposition mechanisms of Mg_2FeH_6 studied by *in-situ*

synchrotron X-ray diffraction and high-pressure DSC." *International Journal of Hydrogen Energy* 35 (8): 3578 – 3582. http://dx.doi.org/10.1016/j.ijhydene.2010.01.144.

Pottmaier, D., E. R. Pinatel, J. G. Vitillo, S. Garroni, M. Orlova, G. B. M. Vaughan, M. Fichtner, W. Lohstroh, and M. Baricco. 2011. "Structure and Thermodynamic Properties of the $NaMgH_3$ Perovskite : A Comprehensive Study." *Chemistry of Materials* 23 (9): 2317 – 2326. http://dx.doi.org/10.1021/cm103204p.

Rijssenbeek, J., Y. Gao, J. Hanson, Q. Huang, C. Jones, and B. Toby. 2008. "Crystal structure determination and reaction pathway of amide–hydride mixtures." *Journal of Alloys and Compounds* 454 (1–2): 233 – 244. http://dx.doi.org/10.1016/j.jallcom.2006.12.008.

Rönnebro, E., G. Whyatt, M. Powell, M. Westman, F. Zheng, and Z. Fang. 2015. "Metal Hydrides for High-Temperature Power Generation." *Energies* 8 (8): 8406. http://dx.doi.org/10.3390/en8088406.

San Marchi, C., B. Somerday, and S. Robinson. 2005. "Permeability, Solubility and Diffusivity of Hydrogen Isotopes in Stainless Steels at High Gas Pressures". *Sandia Technical Report* WSRC-STI-2007-00579. Sandia National Laboratories. Prepared under Contract no. DE-AC09-96SR18500, U. S. Department of Energy. Livermore, CA. http://dx.doi.org/10.1016/j.ijhydene.2006.05.008.

Sandrock, G., S. Suda, and L. Schlapbach. 1992. "Applications." In *Hydrogen in Intermetallic Compunds II: Surface and Dynamic Properties, Applications*, ed. Louis Schlapbach, 197 – 258. Springer Berlin Heidelberg. http://dx.doi.org/10.1007/3-540-54668-5_12.

Sandrock, G. D., and E. Snape. 1986. Reaction heat storage method for hydride tanks. United States 4566281 filed Feb 12, 1979, and issued Jan 28, 1986. https://www.google.com/patents/US4566281.

Schultze, L. E., D. J. Bauer, and R. M. Arington. 1986. Separation of lithium chloride from impurities. US Patent: 4,588,565 filed Aug 1, 1984, and issued https://www.google.com/patents/US4588565.

Sheppard, D. A., T. D. Humphries, and C. E. Buckley. 2016. "Sodium-based hydrides for thermal energy applications." *Applied Physics A* 122 (4): 1 – 13. http://dx.doi.org/10.1007/s00339-016-9830-3.

Sheppard, D. A., M. Paskevicius, and C. E. Buckley. 2011a. "Hydrogen Desorption from the $NaNH_2$–MgH_2 System." *The Journal of Physical Chemistry C* 115 (16): 8407 – 8413. http://dx.doi.org/10.1021/jp200242w.

Sheppard, D. A., M. Paskevicius, and C. E. Buckley. 2011b. "Thermodynamics of Hydrogen Desorption from $NaMgH_3$ and Its Application As a Solar Heat Storage Medium." *Chemistry of Materials* 23 (19): 4298 – 4300. http://dx.doi.org/10.1021/cm202056s.

Sheppard, D. A., M. Paskevicius, T. D. Humphries, M. Felderhoff, G. Capurso, J. Bellosta von Colbe, M. Dornheim et al. 2016. "Metal hydrides for concentrating solar thermal power energy storage." *Applied Physics A* 122 (4): 1 – 15. http://dx.doi.org/10.1007/s00339-016-9825-0.

Singh, S., S. W. H. Eijt, J. Huot, W. A. Kockelmann, M. Wagemaker, and F. M. Mulder. 2007. "The $TiCl_3$ catalyst in $NaAlH_4$ for hydrogen storage induces grain refinement and impacts on hydrogen vacancy formation." *Acta Materialia* 55 (16): 5549 – 5557. http://doi.org/10.1016/j.actamat.2007.06.028.

Soares, N., J. J. Costa, A. R. Gaspar, and P. Santos. 2013. "Review of passive PCM latent heat thermal energy storage systems towards buildings' energy efficiency." *Energy and Buildings* 59: 82 – 103. http://dx.doi.org/10.1016/j.enbuild.2012.12.042.

Solar Millennium AG. 2013. The Construction of the Andasol Power Plants. Solar Millennium AG. Accessed 31/05/2013, http://www.solarmillennium.de/english/archives/technology/references-and-projects/andasol-spain/index.html.

Sorbie, N. 2011. "Syntheis and structure of group I and II nitrides as potential hydrogen stores." School of Chemistry, College of Science and Engineering, University of Glasgow. http://theses.gla.ac.uk/id/eprint/3284.

Suda, S. 1987. "Metal hydrides." *International Journal of Hydrogen Energy* 12 (5): 323 – 331. http://dx.doi.org/10.1016/0360-3199(87)90057-7.

Suryanarayana, C. 2001. "Mechanical alloying and milling." *Progress in Materials Science* 46 (1–2): 1 – 184. http://dx.doi.org/10.1016/S0079-6425(99)00010-9.

Tamilselvi, P., A. Yelilarasi, M. Hema, and R. Anbarasan. 2013. "Synthesis of hierarchical structured MgO by sol-gel method." *Nano Bulletin* 2 (1): 130106. http://www.gosciences.com/journals/index.php/nano/article/view/nano130106.

Tapia-Ruiz, N., N. Sorbie, N. Vaché, T. Hoang, and D. Gregory. 2013. "Rapid Microwave Synthesis, Characterization and Reactivity of Lithium Nitride Hydride, Li_4NH." *Materials* 6 (11): 5410 – 5426. http://dx.doi.org/10.3390/ma6115410.

Tokoyoda, K., S. Hino, T. Ichikawa, K. Okamoto, and H. Fujii. 2007. "Hydrogen desorption/absorption properties of Li–Ca–N–H system." *Journal of Alloys and Compounds* 439 (1–2): 337 – 341. http://dx.doi.org/10.1016/j.jallcom.2006.08.234.

Ward, P. A., C. Corgnale, J. A. Teprovich, T. Motyka, B. Hardy, D. Sheppard, C. Buckley, and R. Zidan. 2016. "Technical challenges and future direction for high-efficiency metal hydride thermal energy storage systems." *Applied Physics A* 122 (4): 462. http://dx.doi.org/10.1007/s00339-016-9909-x.

Wierse, M., R. Werner, and M. Groll. 1991. "Magnesium hydride for thermal energy storage in a small-scale solar-thermal power station." *Journal of the Less Common Metals* 172–174, Part 3: 1111 – 1121. http://dx.doi.org/10.1016/S0022-5088(06)80018-4.

Wu, G., Z. Xiong, T. Liu, Y. Liu, J. Hu, P. Chen, Y. Feng, and A. T. S. Wee. 2007. "Synthesis and Characterization of a New Ternary Imide-$Li_2Ca(NH)_2$." *Inorganic Chemistry* 46 (2): 517 – 521. http://dx.doi.org/10.1021/ic060769y.

Wu, H. 2008. "Structure of Ternary Imide $Li_2Ca(NH)_2$ and Hydrogen Storage Mechanisms in Amide-Hydride System." *J. AM. CHEM. SOC.* 130: 6515 – 6522. http://dx.doi.org/10.1021/ja800300e.

Xiong, Z., P. Chen, G. Wu, J. Lin, and K. Lee Tan. 2003. "Investigations into the interaction between hydrogen and calcium nitride." *Journal of Materials Chemistry* 13 (7): 1676 – 1680. http://dx.doi.org/10.1039/B211563H.

Xiong, Z., J. Hu, G. Wu, and P. Chen. 2005a. "Hydrogen absorption and desorption in Mg–Na–N–H system." *Journal of Alloys and Compounds* 395 (1–2): 209 – 212. http://dx.doi.org/10.1016/j.jallcom.2004.10.062.

Xiong, Z., J. Hu, G. Wu, P. Chen, W. Luo, K. Gross, and J. Wang. 2005b. "Thermodynamic and kinetic investigations of the hydrogen storage in the Li–Mg–N–H system." *Journal of Alloys and Compounds* 398 (1–2): 235 – 239. http://dx.doi.org/10.1016/j.jallcom.2005.02.010.

Xiong, Z., G. Wu, J. Hu, and P. Chen. 2004. "Ternary Imides for Hydrogen Storage." *Advanced Materials* 16 (17): 1522 – 1525. http://dx.doi.org/10.1002/adma.200400571.

Xiong, Z., G. Wu, J. Hu, and P. Chen. 2007. "Ca–Na–N–H system for reversible hydrogen storage." *Journal of Alloys and Compounds* 441 (1): 152 – 156. http://dx.doi.org/10.1016/j.jallcom.2006.07.129.

Xiong, Z., G. Wu, J. Hu, P. Chen, W. Luo, and J. Wang. 2006. "Investigations on hydrogen storage over Li–Mg–N–H complex—the effect of compositional changes." *Journal of Alloys and Compounds* 417 (1–2): 190 – 194. http://dx.doi.org/10.1016/j.jallcom.2005.07.072.

Yao, J. H., C. Shang, K. F. Aguey-Zinsou, and Z. X. Guo. 2007. "Desorption characteristics of mechanically and chemically modified $LiNH_2$ and ($LiNH_2$ + LiH)." *Journal of Alloys and Compounds* 432 (1–2): 277 – 282. http://dx.doi.org/10.1016/j.jallcom.2006.05.113.

Yu, X. B., Z. X. Yang, Y. H. Guo, and S. G. Li. 2011. "Thermal decomposition performance of $Ca(BH_4)_2$/$LiNH_2$ mixtures." *Journal of Alloys and Compounds* 509, Supplement 2: S724 – S727. http://dx.doi.org/10.1016/j.jallcom.2010.11.076.

Yuan, W. X., J. Li, G. Wang, A. G. Cheng, and X. Zhao. 2006. "A study of the chemical reactions involved in Li–Ca–N system." *Journal of Crystal Growth* 290 (2): 621 – 625. http://dx.doi.org/10.1016/j.jcrysgro.2005.12.122.

Zak-Fang, Z., J. Lu, and H. Y. Sohn. 2008. Light metal based material system for hydrogen storage. US Patent: 20080226532 A1 filed October 26, 2007, and issued https://www.google.com/patents/US20080226532.

Zhang, B., and Y. Wu. 2017. "Recent advances in improving performances of the lightweight complex hydrides Li–Mg–N–H system." *Progress in Natural Science: Materials International* 27 (1): 21 – 33. http://dx.doi.org/10.1016/j.pnsc.2017.01.005.

Zhang, J., and Y. H. Hu. 2012. "Intermediate species and kinetics of lithium imide decomposition." *International Journal of Hydrogen Energy* 37 (13): 10467 – 10472. http://dx.doi.org/10.1016/j.ijhydene.2011.12.061.

Appendix A: SUPPLEMENTARY INFORMATION

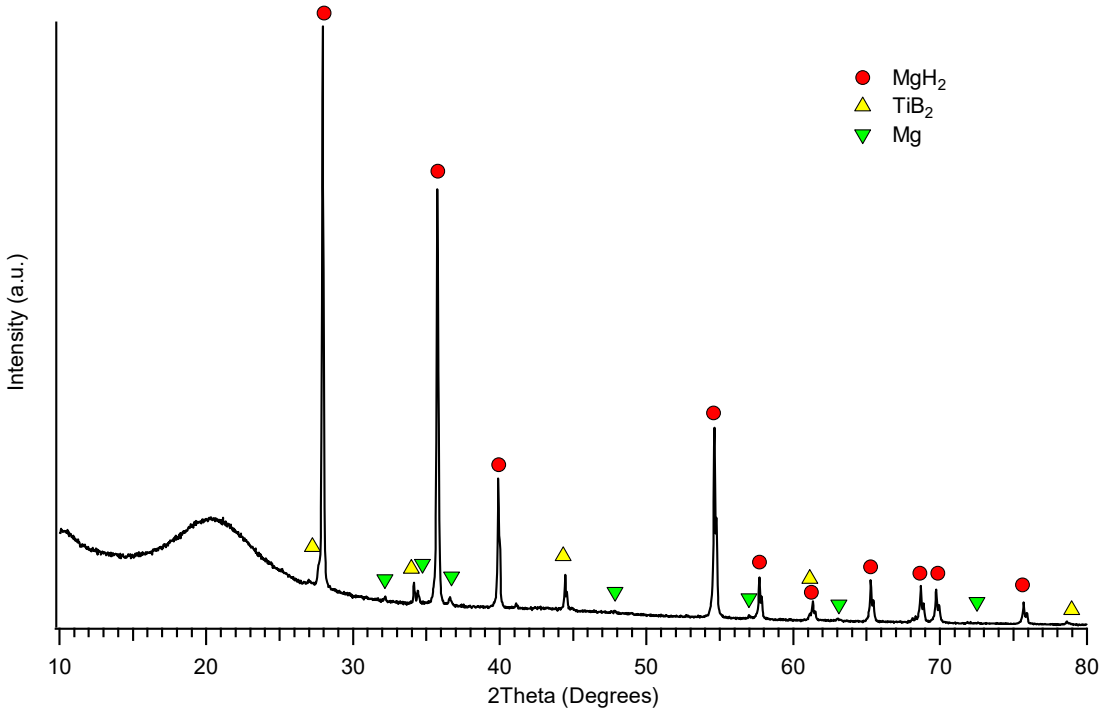

Figure A.1: XRD analysis of hydrogen cycled MgH_2 – 2 mol% TiB_2 synthesised by Terry Humphries (2015).

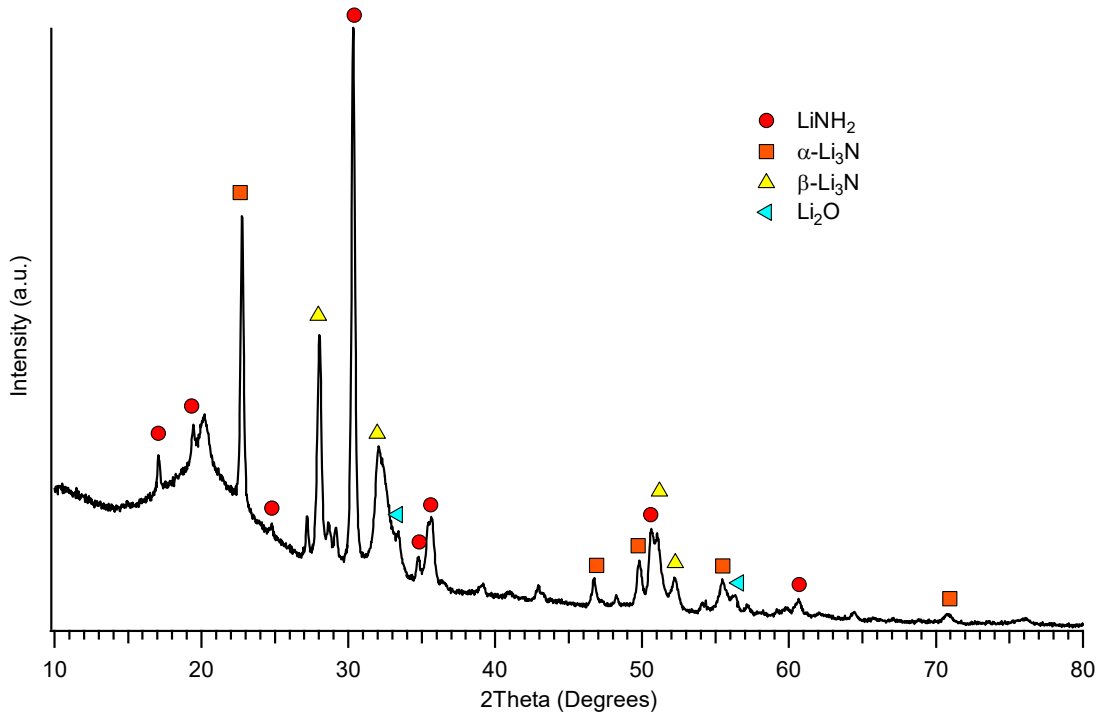

Figure A.2: XRD analysis of the mixture: Li_3N and $LiNH_2$, after heating between 170 °C and 185 °C for 30 min (furnace set point = 220 °C).

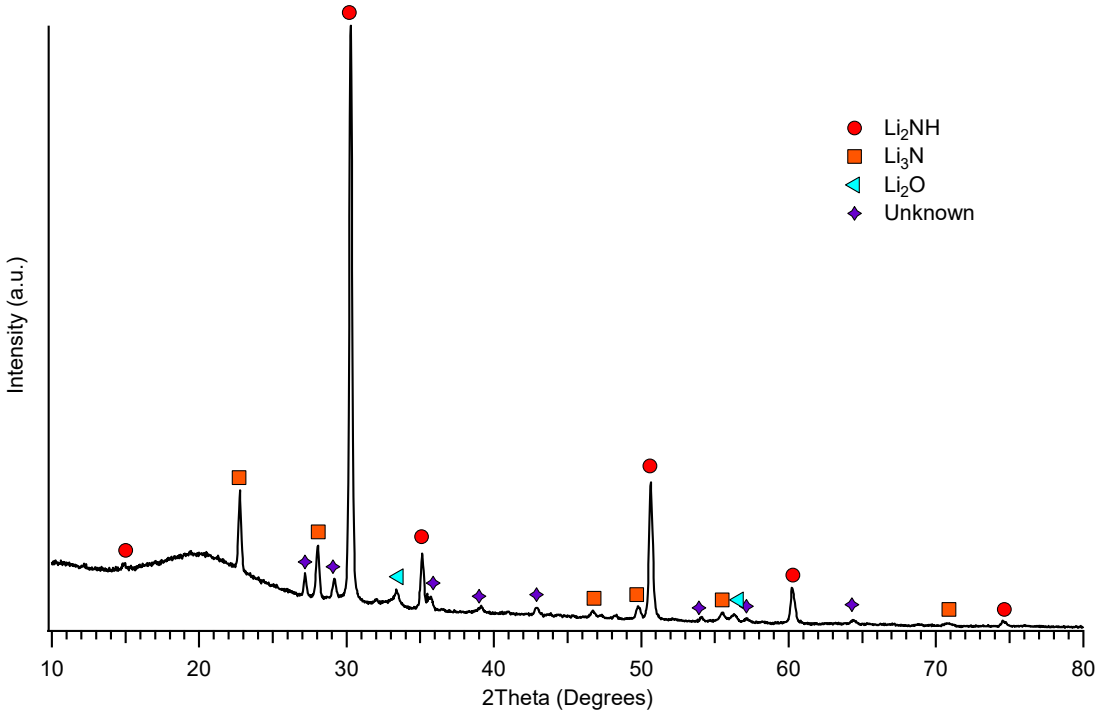

Figure A.3: XRD analysis of the mixture: Li_3N and $LiNH_2$, after further heating at 219 °C for 1 hour.

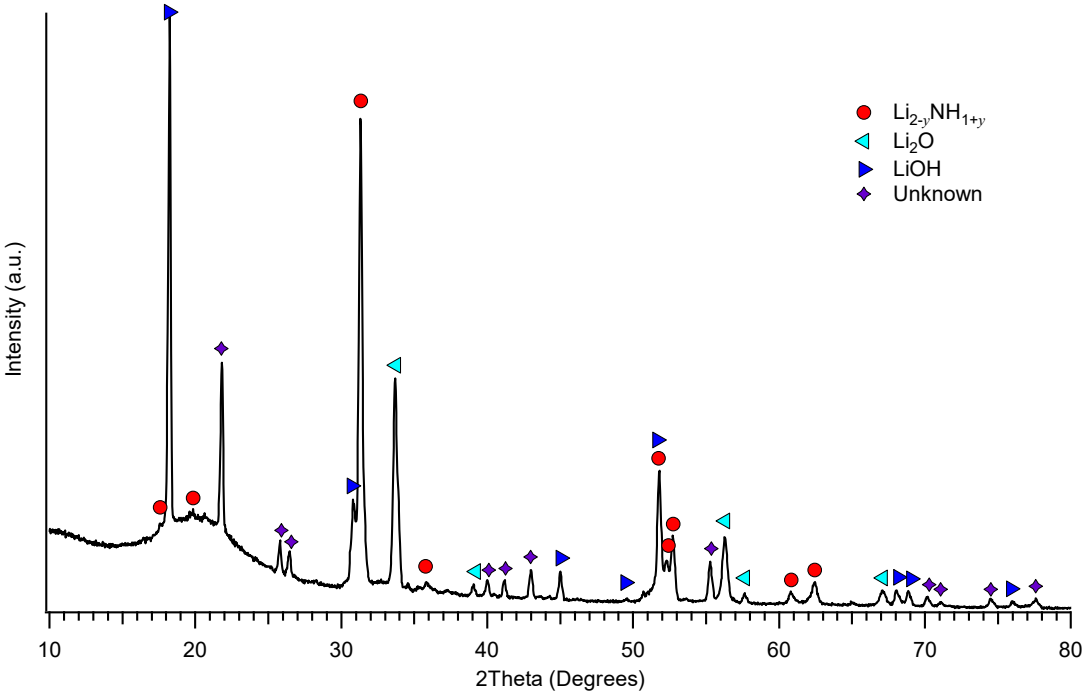

Figure A.4: XRD analysis of the white oxide layer of Li_2NH + LiH (1:2) after PCT measurement at 480 °C.

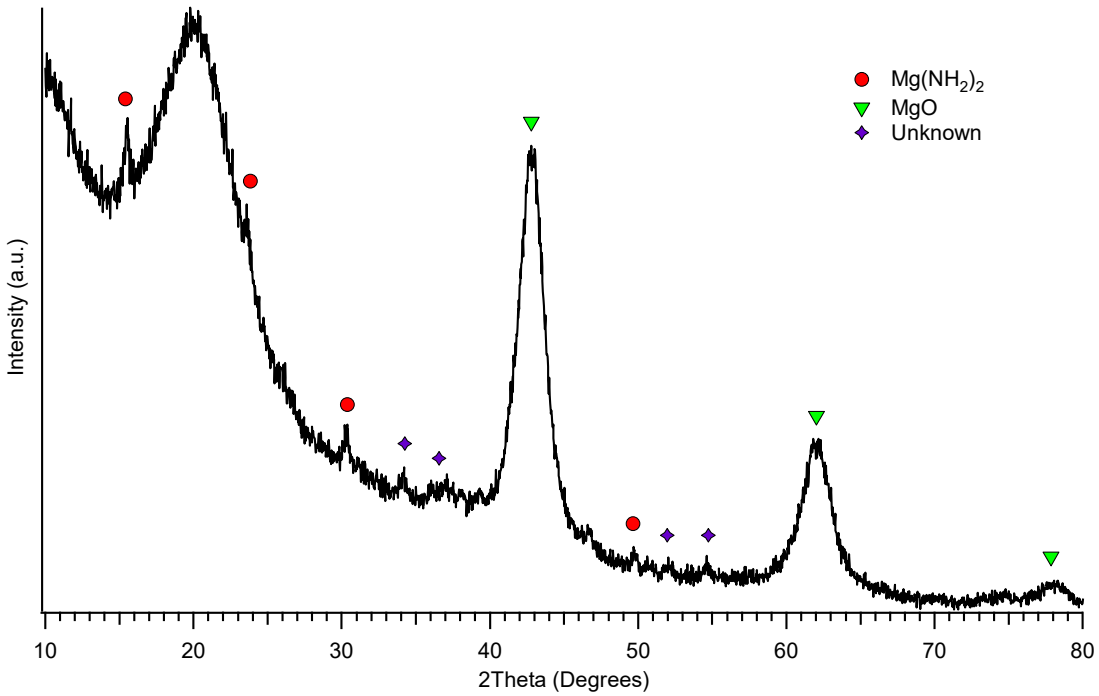

Figure A.5: XRD analysis of contaminated THF-washed $Mg(NH_2)_2$ after TPD measurement halted at 350 °C.

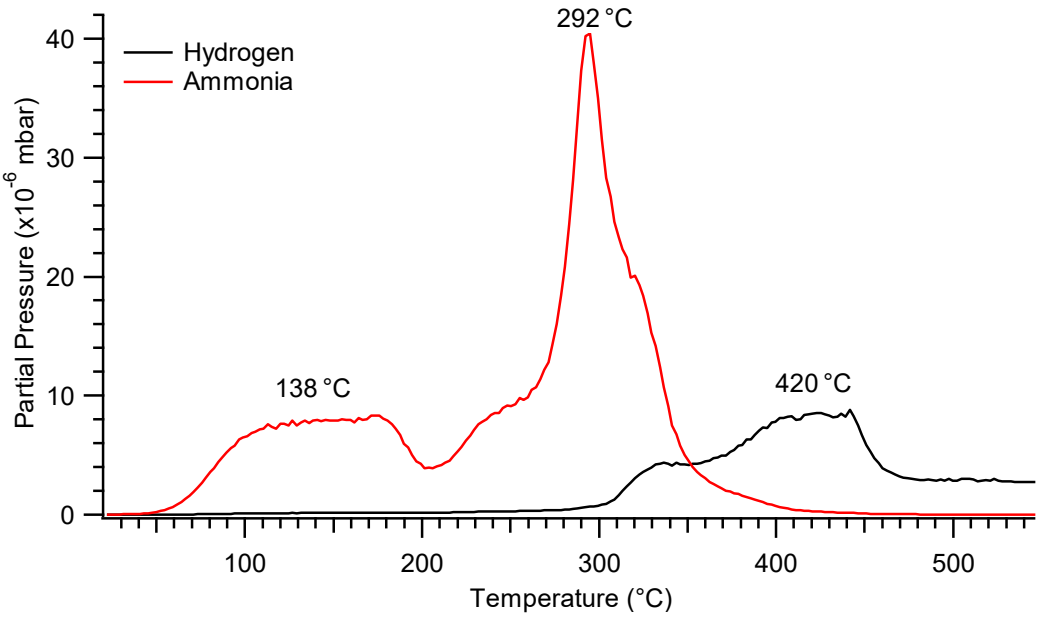

Figure A.6: TPD-MS analysis of oxygen contaminated THF-washed $Mg(NH_2)_2$ performed under dynamic vacuum in the temperature range of 25 – 550 °C, where the heating rate was 2 °C min^{-1}.

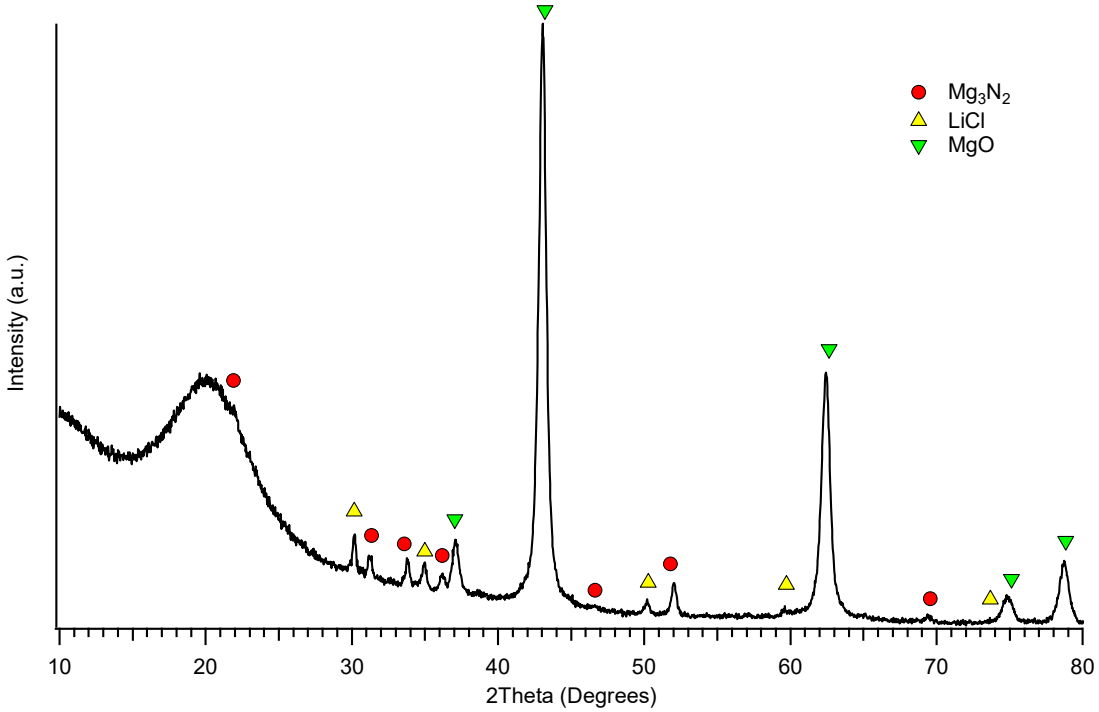

Figure A.7: XRD analysis of contaminated THF-washed $Mg(NH_2)_2$ after TPD-MS to 550 °C.

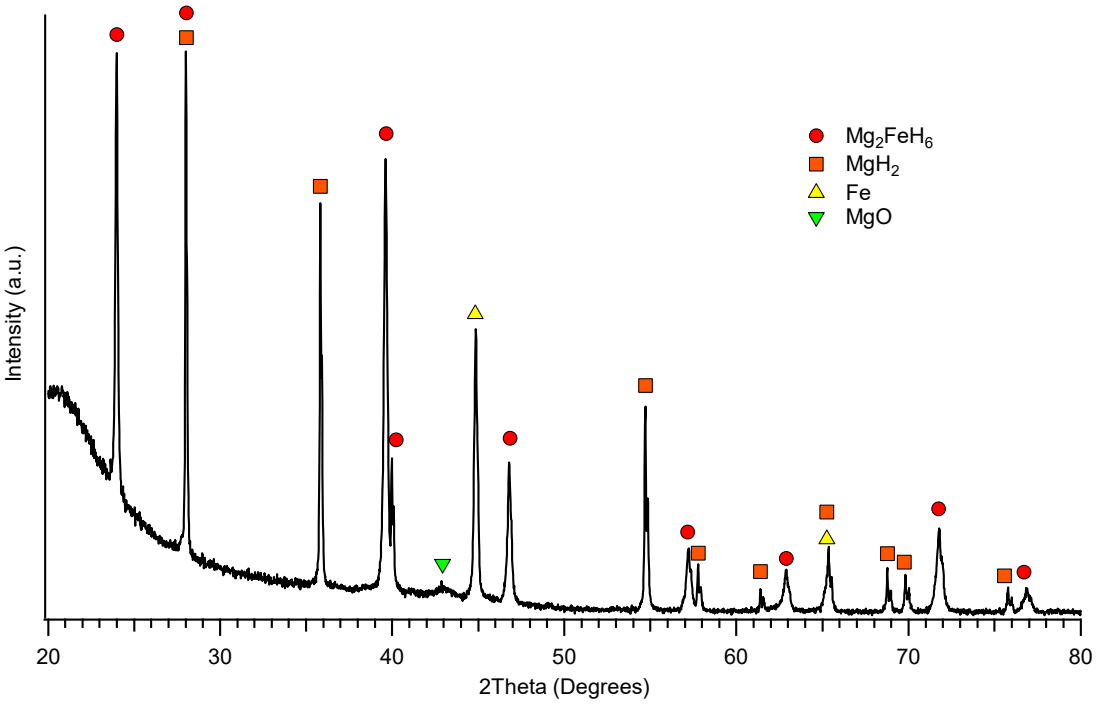

Figure A.8: XRD analysis of Mg_2FeH_6 after the 5th absorption cycle by Drew Sheppard (2013).

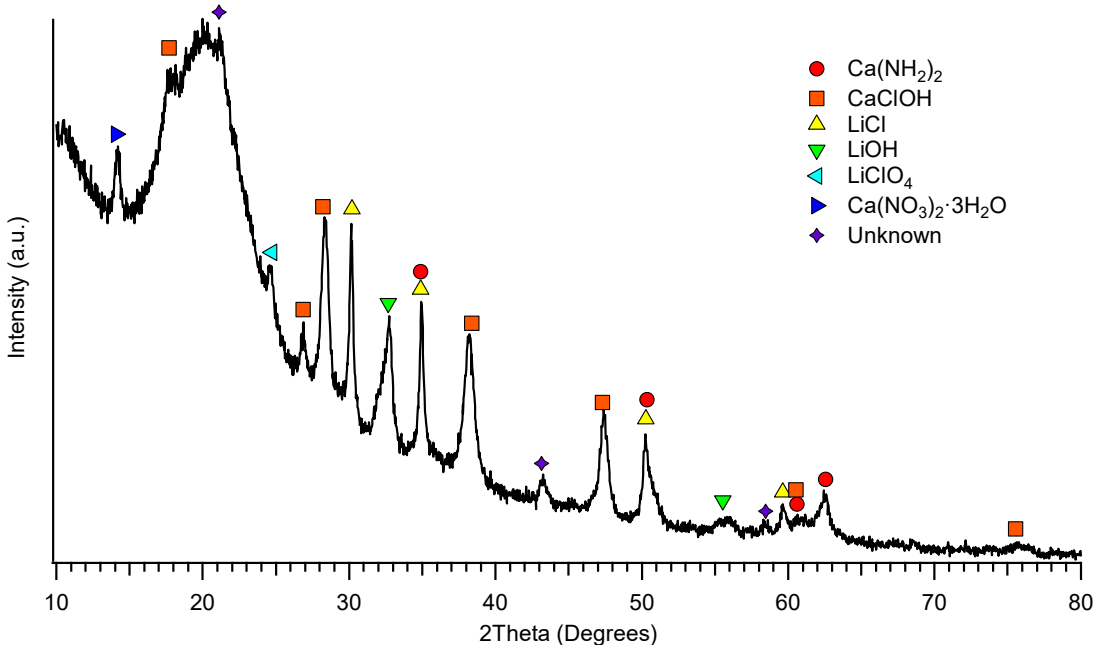

Figure A.9: XRD analysis of the metathesis reaction between $LiNH_2$ and $CaCl_2$ in a 2:1 molar ratio that was contaminated during cryogenic milling for 1 hour.

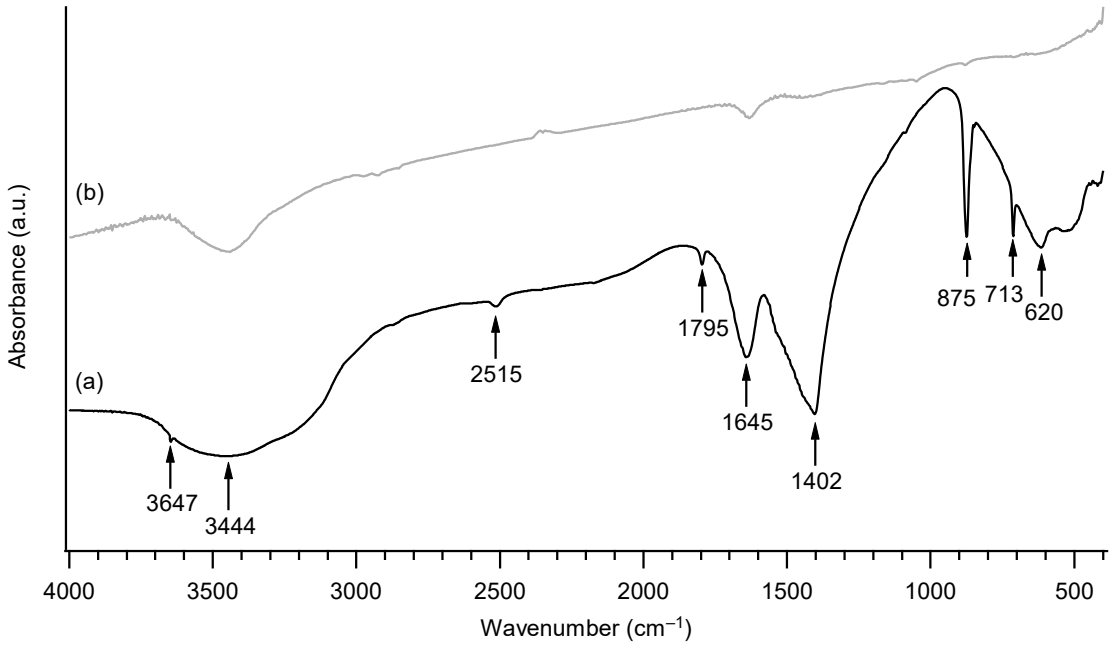

Figure A.10: FTIR spectra of (a) THF-washed CaNH and (b) blank KBr pellet.

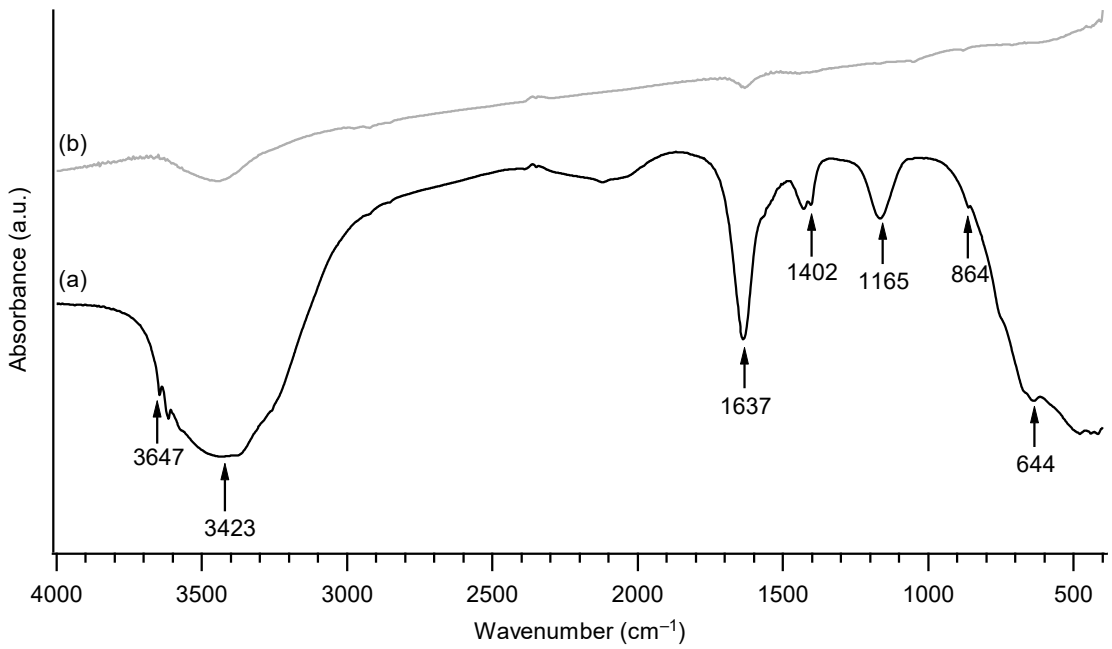

Figure A.11: FTIR spectra of (a) unwashed CaNH and (b) blank KBr pellet.

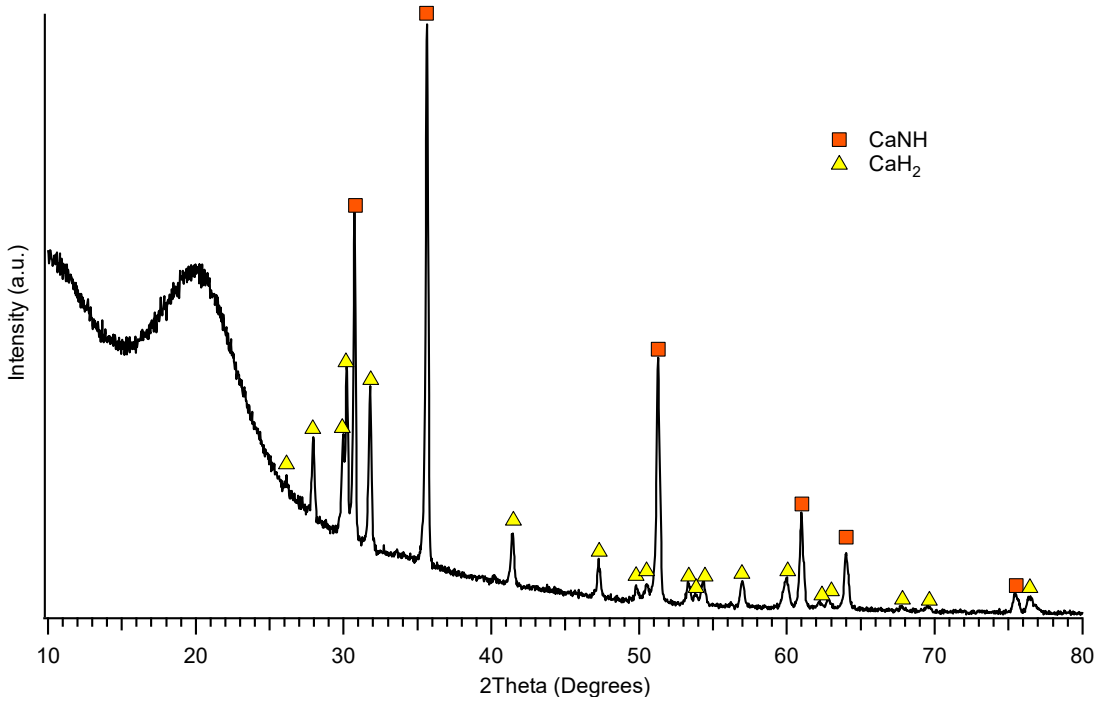

Figure A.12. XRD analysis of the hydrogenation products of Ca_2NH after step-wise temperature measurements halted at 690 °C.

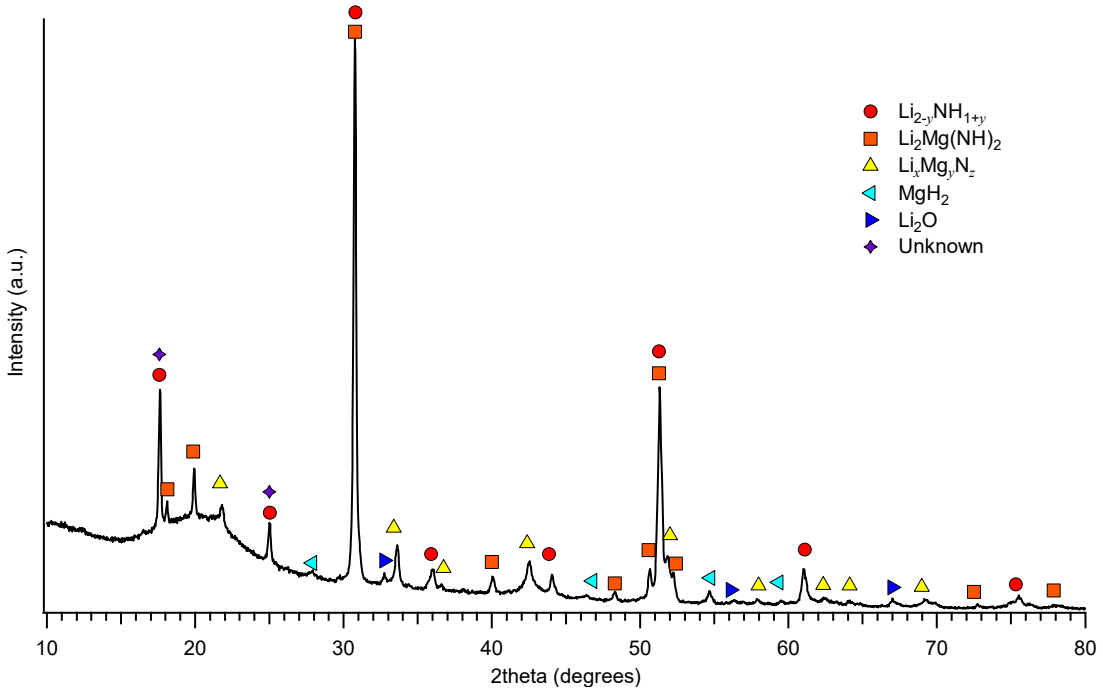

Figure A.13: XRD analysis of $LiNH_2$ + MgH_2 (2:1) after annealing at 300 °C.

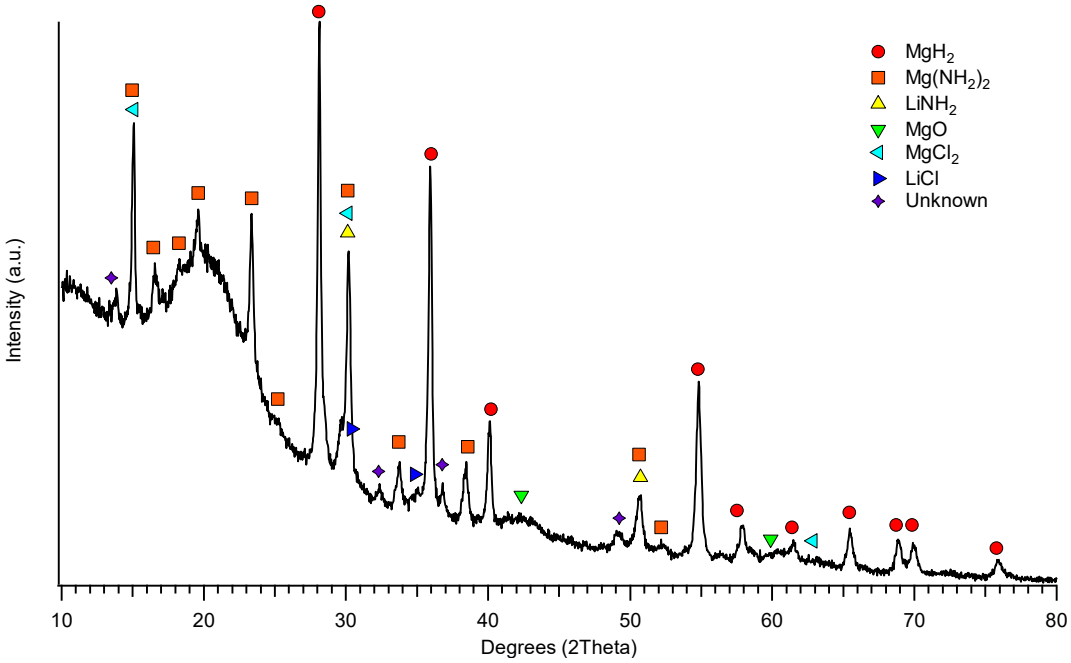

Figure A.14: XRD analysis of $Mg(NH_2)_2$ + MgH_2 (1:1) after annealing at 200 °C for 19 hours under dynamic vacuum (incomplete synthesis of MgNH).

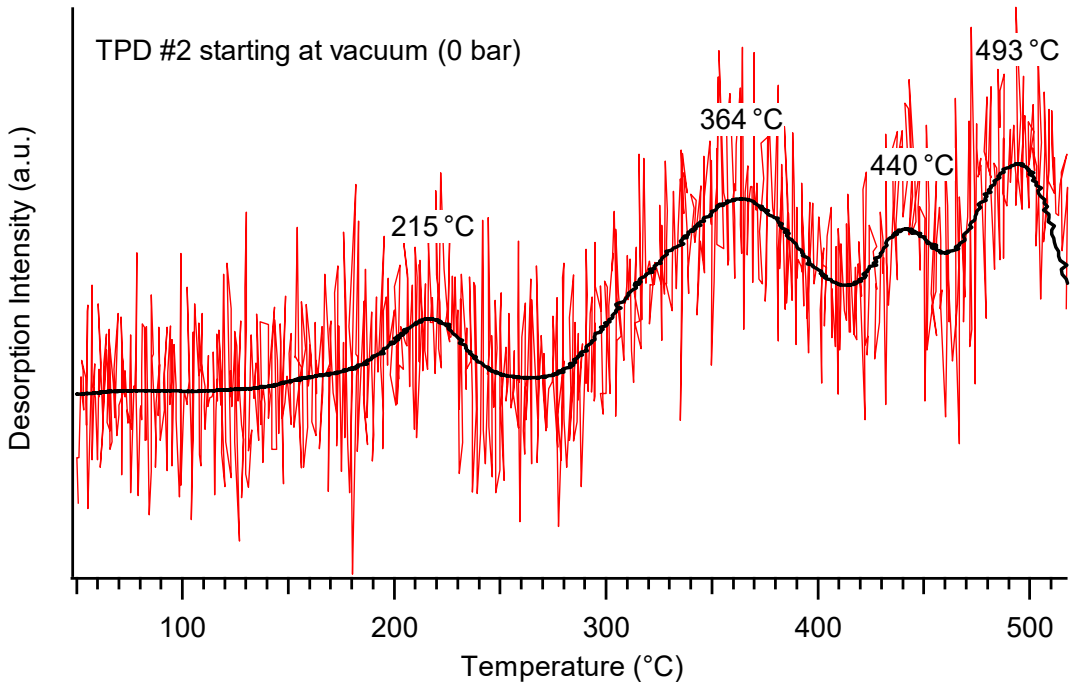

Figure A.15: Raw TPD-VM data of LiMgN (red) and refined TPD data of LiMgN using noise reduction command (black).

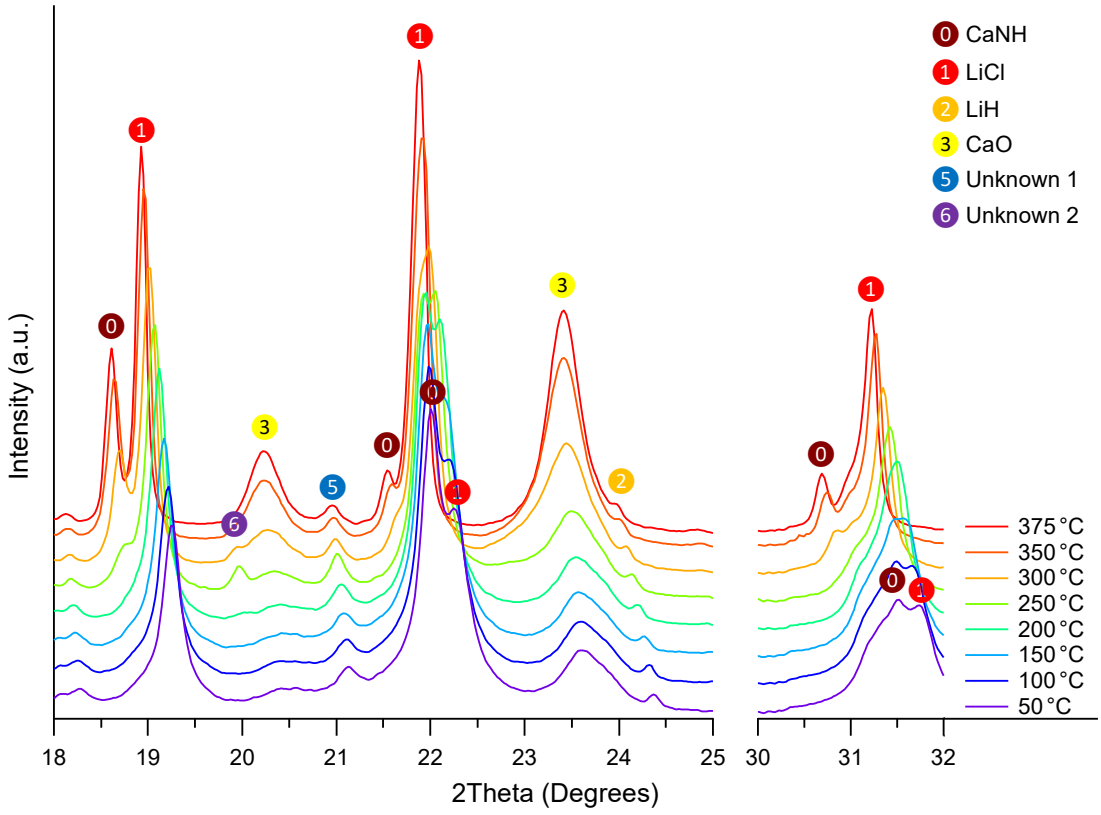

Figure A.16: *In situ* SXRD analysis (λ = 1.00036 Å) of CaNH + LiH (1:1) performed under a hydrogen back pressure of ~1 bar with investigation of overlapping phases.

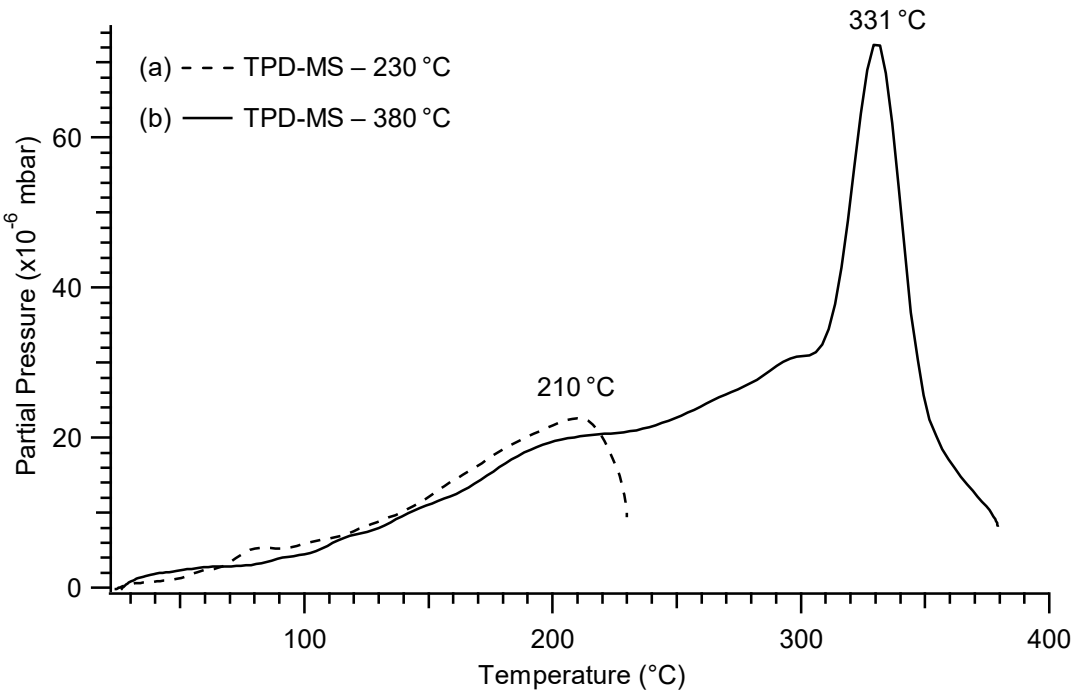

Figure A.17: TPD-MS analysis of Sample 1 – $Mg(NH_2)_2$ + MgH_2 + NaH (1:2:1) performed under dynamic vacuum and halted at (a) 230 °C and (b) 380 °C, where the heating rates were 2 °C min^{-1}.

Appendix B: HYDROGEN SORPTION CALCULATIONS

For samples at Non-Ambient Temperature

The number of hydrogen moles absorbed/adsorbed (n_{ADS}) for a given sorption measurement can be expressed as:

$$n_{ADS} = n_r + n_s - n_e - n_{leak} - n_{steel} \tag{B.1}$$

where the terms n_r, n_s and n_e are the initial number of moles in the reference volume, the initial number of moles in the sample volume and the number of moles in the entire system at equilibrium, respectively. The terms n_{leak} and n_{steel} are the number of moles leaked by the diffusion of hydrogen through 316 stainless steel and the number of moles absorbed by 316 stainless steel, respectively. The above terms can be determined by the following:

$$n_r = \frac{P_r V_r}{Z_r R T_r} \tag{B.2}$$

$$n_s = \frac{P_s\left(V_s - V_{na}\right)}{Z_s R T_s} + \frac{P_s\left(V_{na} - V_{sample}\right)}{Z_{na} R T_{na}} \tag{B.3}$$

$$n_e = \frac{P_e V_r}{Z_e R T_e} + \frac{P_e\left(V_s - V_{na}\right)}{Z_e R T_e} + \frac{P_e\left(V_{na} - V_{sample}\right)}{Z_{ena} R T_{na}} \tag{B.4}$$

$$n_{leak} = t_e\, \Phi_{na} \sqrt{P_e} \left(\frac{SA}{t_s}\right) \tag{B.5}$$

$$n_{steel} = K\, V_{steel} \sqrt{P_e} \tag{B.6}$$

where:

n_r = the initial number of moles in the reference side volume

n_s = the initial number of moles in the sample side volume

n_e = the number of moles at equilibrium

n_{leak} = the number of moles leaked by stainless steel

n_{steel} = the number of moles absorbed by stainless steel

R = the universal gas constant (8.314472 J K^{-1} mol^{-1})

P_r = the initial reference side volume pressure

P_s = the initial sample side volume pressure

P_e = the final equilibrium volume pressure

V_s = the sample side volume

V_{sample} = the solid volume based on sample mass and density

V_{na} = the sample side volume at non-ambient temperature

T_r = the initial reference side volume temperature (K)

T_s = the initial sample side volume temperature (K)

T_e = the equilibrium temperature (K)

Z_r = the compressibility value associated with P_r and T_r

Z_s = the compressibility value associated with P_s and T_s

Z_{na} = the compressibility value associated with P_s and T_{na}

Z_e = the compressibility value associated with P_e and T_e

Z_{ena} = the compressibility value associated with P_e and T_{na}

Φ_{na} = the permeability of hydrogen at T_{na} (mol m^{-1} s^{-1} $MPa^{-1/2}$)

t_e = the time elapsed (s)

SA/t_s = the surface area to thickness factor of the sample cell (m^3 s^{-1})

K = solubility of hydrogen in stainless steel (mol m^3 $MPa^{-1/2}$)

V_{steel} = the non-ambient volume of stainless steel in the sample cell (m^3)

More details about the diffusion and absorption of hydrogen through 316 stainless steel were further explained in leak corrections for non-ambient measurements in Chapter 2: Section 2.5.1.

Appendix C: PUBLICATIONS ARISING FROM THIS THESIS

Nguyen, Tam T., Drew A. Sheppard, and Craig E. Buckley. 2017. "Lithium imide systems for high temperature heat storage in concentrated solar thermal systems." *Journal of Alloys and Compounds* 716: 291 – 298. doi: 10.1016/j.jallcom.2017.04.208.

Journal of Alloys and Compounds 716 (2017) 291–298

Contents lists available at ScienceDirect

Journal of Alloys and Compounds

journal homepage: http://www.elsevier.com/locate/jalcom

Lithium imide systems for high temperature heat storage in concentrated solar thermal systems

Tam T. Nguyen*, Drew A. Sheppard, Craig E. Buckley

Department of Physics and Astronomy, Fuels and Energy Technology Institute, Curtin University, GPO Box U1987, Perth 6845, WA, Australia

ARTICLE INFO

Article history:
Received 5 October 2016
Received in revised form
11 February 2017
Accepted 19 April 2017
Available online 22 April 2017

Keywords:
Hydrogen storage
Heat storage
Lithium imide nitride

ABSTRACT

Hydrogen is touted as one of the solutions for future energy requirements. Metal hydrides typically studied for their high hydrogen capacity can be used as a thermal storage system by taking advantage of their endothermic/exothermic reactions with hydrogen. This allows the harnessing of solar energy by utilising thermal storage to alleviate its intermittent nature. Lithium amide ($LiNH_2$), imides (Li_2NH) and nitrides (Li_3N) have been widely studied for their hydrogen storage at relatively low operating temperatures, typically suited for mobile applications. However, little work has been done involving the imide to nitride reaction of lithium-based materials due to their high temperature range. The following techniques were used to characterise this system: temperature programmed desorption (TPD), temperature programmed photographic analysis (TPPA), x-ray diffraction (XRD) and pressure-composition-temperature (PCT) measurements. TPD results revealed that only a single-step reaction occurred between 100 and 600 °C. TPPA revealed that having a molten solid solution of the sample, depreciated the reversibility of hydrogen absorption and desorption. The molten sample behaved quite vigorously in TPPA measurements and consequently blocked sample filters and sintering sample cell walls; creating engineering problems at higher temperatures. The results revealed that for reactions involving Li_2NH and lithium hydride (LiH), the temperature range required for thermal storage is above the melting point of the system. The diffusion and absorption of hydrogen through stainless steel would also occur in the sample cells used, resulting in further problems. The reaction pathway of Li_2NH and LiH was also found to be far more complex than generally reported: XRD revealed that the expected final product of Li_3N could not be identified, instead a lithium imide-nitride hydride phase ($Li_{4-2x}N_{1-x}H_{1-x}(NH)_x$) was identified as the final product of this system. PCT measurements were conducted to identify the kinetic and thermodynamics of this system, but because of the molten solid-solution problem, an accurate result could not be obtained.

1. Introduction

With increasing energy demands, depletion of fossil fuels and concerns over global warming, concentrating solar-thermal power (CSP) paired with thermal energy storage is an alternative energy source that will fulfil the world's energy requirements while providing clean energy. Every year, Australia receives an average of 58 million petajoules of solar radiation, which approximates to 10,000 times more energy than its total energy consumption. However, solar energy only accounts for 0.2% of Australia's total primary energy consumption in 2011-12 [1]. Unfortunately, solar energy has an intermittent supply and an energy density inferior to fossil fuels but more importantly, the use of solar energy does not harm the environment. The International Energy Agency (IEA) has set goals to limit the global increase in temperature by limiting the concentration of greenhouse gases (carbon dioxide). It is expected that by 2035, more than 6% of global electricity will be produced from solar photovoltaics (PV) and CSP in order to limit the concentrations of greenhouse gases in the atmosphere to 450 parts per million (ppm) as reported by the IEA in 2010 [2]. Utilising solar energy and thermal storage, concentrated solar energy provides power during the day. However, during the night, power is generated from any excess energy stored earlier from the day. Solar energy is thermally stored in a coupled hydride system that takes advantage of the exothermic reaction from absorbing hydrogen. The two hydride beds will have different operating temperatures

* Corresponding author.
E-mail address: tam.nguyen@curtin.edu.au (T.T. Nguyen).

http://dx.doi.org/10.1016/j.jallcom.2017.04.208
0925-8388/

(high and low).

Most metals can combine with hydrogen to form metal hydrides. Metal hydrides have a unique property in that they can absorb and desorb hydrogen at constant pressure. The reverse process can be easily achieved by simply changing the applied hydrogen pressure or temperature. These reversible reactions are exothermic and endothermic, where the heat required for hydrogen desorption is approximately the same as that generated during absorption, which is why metal hydrides have been proposed as potential thermochemical energy stores [3].

Metal hydrides used exclusively for thermal energy storage have only been studied since the mid-1970s [4]. However, because of the limited number of known hydrides at the time, the studies were generally systems operating at temperatures below 200 °C [5–7]. With the success of CSP power plants, the next generation of thermal storage material could possibly be metal hydrides [8–11]. In comparison to existing molten salt energy storage, metal hydrides are 20 times more energy dense than molten salt mixtures [12]. The temperature range for metal hydrides for CSP must operate within 650 to 800 °C, as higher operating temperatures generate higher heat-to-electricity conversion efficiencies with the Stirling engine [13]. A thermal energy storage prototype has already been recently studied using TiH_x ($1.53 \leq x \leq 1.75$) that operated at temperatures >600 °C and H_2 pressures <5 bar with a 95% efficiency rating after 60 cycles [14].

Imides have been chosen as possible high temperature hydrides as they are notorious for operating at high temperatures ranging between 500 and 700 °C [15–16]. Lithium-based material systems are among the most promising materials owing to their high hydrogen contents. The amide-hydrides were characterised, focusing on their: decomposition mechanics, material characteristics, thermodynamic properties, sorption kinetics and their cyclic stability. X-ray diffraction (XRD) was used to characterise the decomposition structures of imides and nitrides.

The Li–N–H system has been reported by Chen et al. [17] to decompose in a two-step reaction, forming an imide (Equation (1)) and nitride (Equation (2)).

$$LiNH_2 + LiH \leftrightarrow Li_2NH + H_2, \quad 6.5\ wt\%\ H_2 \tag{1}$$

$$Li_2NH + LiH \leftrightarrow Li_3N + H_2, \quad 5.5\ wt\%\ H_2 \tag{2}$$

Lithium amide ($LiNH_2$) reacts with lithium hydride (LiH) to form lithium imide (Li_2NH), releasing hydrogen at temperatures below 200 °C. Li_2NH further reacts with LiH to form lithium nitride (Li_3N) along with another release of H_2 at temperatures above 320 °C [17]. The majority of the work done on amides and its mixtures have been on lowering the operation temperatures of the first-step reaction within a suitable thermodynamic range for mobile applications [15]. The second reaction has been little studied because the working temperature is deemed too high for mobile applications; therefore, no studies to date have taken advantage of the high-temperature reactions of imides for thermal energy storage.

Recent work on the Li–N–H system has shown that the reaction pathway may be more complex than originally indicated by Chen et al. [17]. The mechanism of both hydrogenation and dehydrogenation of the Li–N–H system involves the formation of non-stoichiometric intermediates [18]. There have been reports that a phase transition (non-stoichiometric) occurs between the tetragonal amide phase ($LiNH_2$) to a cubic imide phase (Li_4NH) [19,20]. Working above 490 °C, Li_4NH is formed from the reaction between Li_3N and LiH [21]. In this system, Li_4NH undergoes no dehydrogenation or decomposition below 400 °C, limiting the imide to nitride reaction at higher temperatures [20].

Bull et al. [19] proposed two models that show the possibility of non-stoichiometric phases between the amide to imide reaction and the imide to nitride-hydride phase transition. $Li_{2-y}NH_{1+y}$ ($0 \leq y \leq 1$) being the intermediate between $LiNH_2$ and Li_2NH and $Li_{2+y}NH$ ($0 \leq y \leq 2$) being the intermediate between Li_2NH and Li_4NH. Furthermore, Tapia-Ruiz et al. [20] proposed a possible reaction pathway between Li_4NH and Li_2NH. These phases were proposed to react and form a non-stoichiometric solid solution known as lithium imide-nitride hydride, $(Li_{4-2x}N_{1-x}H_{1-x}(NH_x)$ ($0 \leq x \leq 1$) as expressed in Equation (3):

$$(1-x)Li_4NH + xLi_2NH \rightarrow Li_{4-2x}N_{1-x}H_{1-x}(NH)_x \tag{3}$$

Given the complexity of characterising non-stoichiometric phases in the Li—N—H system. The reversibility of the cubic imide (Li_2NH) and Li_4NH phases (Equation (3)) were further investigated at high operating temperatures, suitable for thermal energy storage.

2. Experimental

2.1. Synthesis

All handling of sample materials was undertaken in an argon-atmosphere glovebox (MBraun Unilab) to minimise oxygen ($O_2 < 5$ ppm) and water ($H_2O < 5$ ppm) contamination. The starting reagents were $LiNH_2$ (Sigma-Aldrich, 95%), LiH (Sigma-Aldrich, 95%) and Li_3N (Sigma-Aldrich, 99.5%). Li_2NH was laboratory synthesised by annealing $LiNH_2$ and Li_3N at 220 °C for 1 hour using an ultrafast-reaction method reported by Hu and Ruckenstein [22].

The reagents were thoroughly mixed in a planetary ball-mill (Across International PQ-N04) for 4 hours with a 1:2 M ratio ($LiNH_2$:LiH) in a 50 mL 316 stainless steel ball-milling canister. The planetary ball-mill was operated at 400 rpm with a ball-to-powder ratio (BTP) of 30:1 using 316 stainless-steel balls sized at 10 mm and 6 mm. Li_2NH and LiH were milled with the same parameters but in a 1:1 M ratio.

3. Characterisation

3.1. Fourier transform infra-red

Fourier transform infra-red (FTIR) spectroscopy was performed using a Bruker IFS 66 FT-IR. The spectrometer was purged with dry nitrogen and samples were prepared by pressing the sample within potasium bromide (KBr) pellets. A total of 5 scans were performed on pure KBr to obtain a sufficient background scan and 3 scans were performed on the sample. The data were collected between wavenumbers 400 and 4000 cm^{-1}.

3.2. X-ray diffraction

X-ray diffraction (XRD) was performed using a Bruker D8 Advance diffractometer (Cu $K\alpha$ radiation, $\lambda = 1.540593$ Å) with a LynxEye detector. The scans were taken at a 2θ range of 10–80° with a 0.03° step size. The samples were sealed in a dome holder made of poly(methylmethacrylte) (PMMA) in argon to avoid any oxygen/moisture contamination during data collection. The dome holder produces a broad hump in the diffraction pattern centred at a 2θ value of ~21°.

3.3. Temperature programmed desorption

Temperature programmed desorption (TPD) was performed using two methods. The first, on a PCT-Pro E&E (Hy-Energy) coupled to a quadrupole mass-spectrometer residual gas analyser

(Sandford Research Systems RGA 300). Approximately 20 mg of sample was outgassed to an approximate vacuum (1×10^{-3} bar) at room temperature overnight. Under dynamic vacuum, the samples were heated up to 300 °C with a heat rate of 2 °C/min at which point the heating was halted and the sample was allowed to cool to room temperature. The second method, uses the same PCT-Pro E&E (Hy-Energy) to manually measure the partial pressure of evolved gases as the sample is heated in a calibrated Sieverts apparatus, which has a total system volume of 191.7 cm^3. Approximately 10 mg of sample was outgassed overnight. Starting with a static pressure close to vacuum, this method allowed us to heat the sample up to 600 °C with a heat rate of 2 °C/min.

3.4. Pressure-composition-temperature

Pressure-composition-temperature (PCT) data were collected on a laboratory-built hydrogen sorption apparatus using roughly ~0.4 g of sample and a total system volume of ~30–35 cm^3. The apparatus uses the volumetric (also called manometric and Sievert's) method to determine hydrogen adsorption/absorption (and desorption) of a sample. The sample was placed in a furnace at a desired temperature and isothermal measurements were taken over a 24 hour period with pressure increments between 0 and 30 bar. The permeability of hydrogen through stainless steel at high temperatures caused problems in the PCT data; therefore, blank measurements were performed in order to assess the hydrogen permeability of the sample cell.

3.5. Temperature programmed photographic analysis

Temperature programmed photographic analysis (TPPA) is a technique used to determine the macroscopic behaviour of complex hydrides during decomposition/melting at high temperatures. The identification of phases can be revealed at high temperatures by the colour and behaviour of the sample, where TPPA provides an alternative *in situ* method. Photographs were collected using a digital microscope (Plugable microscope) and heated on a specifically designed sample block holder, capable of heating samples with a heat rate of 10 °C/min from room temperature to 500 °C. The samples in a glass vial were sealed in argon and connected to a pressure relief valve set to 1 bar to maintain atmospheric pressure. A thermocouple was inserted within the glass vial to monitor the sample temperature during programmed temperature ramp. The aluminium heating block was engineered with open viewing windows for photographic analysis, provided by near-uniform heating with rod heaters, interfaced to a temperature controller.

4. Results and discussion

Fig. 1 shows the result of the FTIR measurement for the mixture of $LiNH_2$ and LiH in a 1:2 M ratio. The broad band that occurs around 3676 cm^{-1} is due to the O–H stretching vibrations that are due to atmospheric water absorbed by the KBr pellet. The N–H symmetric and asymmetric stretching vibrations of $LiNH_2$ occur at 3314 cm^{-1} and 3260 cm^{-1}, respectively. These absorption bands are in agreement with those reported by Kojima and Kawai [23]. Yu et al. [24] had reported the same $LiNH_2$ bands that occur in our measurement at 1564 cm^{-1} and 1537 cm^{-1}.

Fig. 2 shows the PCT measurements of $LiNH_2$ and LiH in a 1:2 M ratio that were performed over a period of 5 days with absorption and desorption steps varying from 1 hour (before and after the plateau) to 5+ hours (on the plateau slope). It can be seen that the equilibrium pressure is approximately 14 bar at 415 °C at the midpoint of the sloping plateau. The initial shape of the PCT curve below ~1 wt% H_2 suggests a solid-solution behaviour between

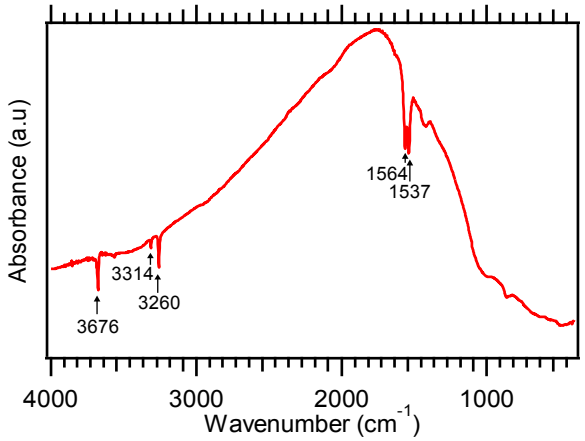

Fig. 1. FT-IR spectra for the mixtures of $LiNH_2$ and LiH (1:2 M ratio), pressed in a KBr pellet.

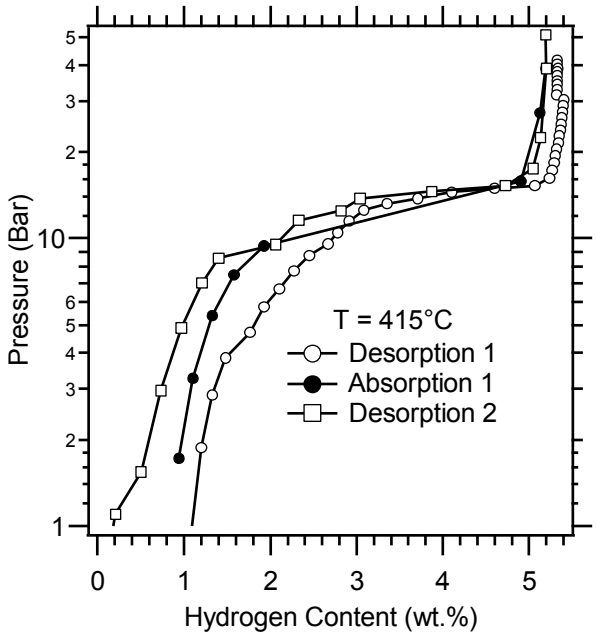

Fig. 2. PCT measurements of Batch 1, $LiNH_2$ + 2LiH at 415 °C.

$LiNH_2$ and Li_2NH. The conclusion from these observations is that only one single reaction step was observed corresponding to the sloping plateau that extends between a hydrogen capacity of 1–5 wt%. The absence of a second plateau below ~1 wt% H_2 suggests that the second reaction step (Equation (2)) reported by Chen et al. [17] did not occur under the applied experimental conditions. After performing the second desorption-step, the system was able to absorb a hydrogen capacity of ~5.5 wt%.

Fig. 3 shows the $LiNH_2$ + 2LiH system after hydrogen cycling at 475 °C. It can be seen that the yellow sample has sintered along the walls of the sample cell. Given the state of the sample cell after working at such temperatures, it is quite possible that the sample is melting into a solid solution, preventing the desirable second reaction-step as seen in Equation (2).

It can also be observed in Fig. 3, that the sintered metal filter gasket (indicated by the arrow in Fig. 3) is coated by the sample that may result in blockage with detrimental impacts on PCT data. Repeating the volume calibration for the same sample cell, a

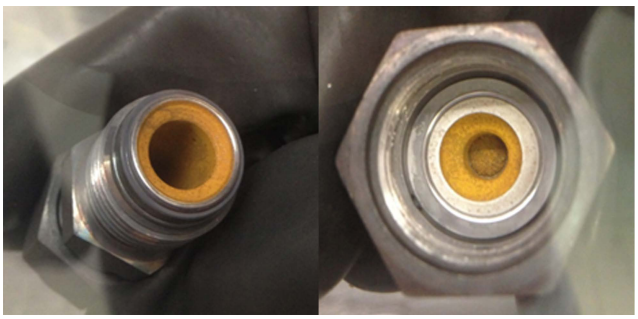

Fig. 3. Image of sample cell containing $LiNH_2$ + 2LiH after hydrogen cycling at 475 °C.

reduction in the calibrated volume confirmed that the filter was at least partially blocked. In an attempt to circumvent this problem, the mixtures of $LiNH_2$ and LiH were pressed into 3 individual 8 mm diameter pellets in a 1:2 M ratio. The remaining void in the sample cell volume was packed with stainless-steel wool to prevent any movement of the pellets as the system undergoes evacuation. At temperatures around 475 °C, the leak rate of hydrogen was large, especially when working with long step-times, where several leak corrections were performed using the permeability of hydrogen through 316 stainless steel. Fig. 4 shows the state of the sample cell after hydrogen cycling, although the problem of blocked filter gaskets was eliminated, it did not deter the sample from melting and forming a solid solution.

Given the difficulties with the PCT measurements of $LiNH_2$ + 2LiH, most likely from the sample melting. Temperature programmed photographic analysis (TPPA) was performed on a number of samples: as-recieved $LiNH_2$, $LiNH_2$ + 2LiH, synthesised Li_2NH and Li_2NH + LiH; to explore the behaviour of the starting powders at temperatures relevant to practical applications. *Ex situ* XRD only reveals information about the sample phases that exist upon cooling to room temperature. By performing TPPA measurements, additional insight is gained about the *in situ* behaviour of the samples.

Fig. 5 shows the results from the TPPA of the as-received $LiNH_2$ from Sigma-Aldrich. By observation, $LiNH_2$ starts as a white powder and the glass vial accumulates a foggy appearance between 124 and 268 °C, probably caused by impurities resulting from the commercial synthesis process. This foggy appearance was most pronounced at 203 °C (see Frame 1 of Fig. 5). Juza and Opp [23] reported that the melting point of $LiNH_2$ is 375 °C but the melting point appears to commence at approximately 357 °C in the TPPA and is associated with the deposition of yellow molten sample on the inner walls of the glass vial (see Frame 2 of Fig. 5). The difference in melting points in comparison to literature values could be due to the higher heat rate used, as a rate of 10 °C/min was used whereas Chen et al. [17] used a heat rate of 1 °C/min to achieve the same results as Juza and Opp [25]. Up until approximately 453 °C, the sample was continuously bubbling with the evolution of NH_3 according to Equation (4):

Fig. 4. Image of sample pellet ($LiNH_2$ + 2LiH) that melted over steel wool after cycling measurements above 475 °C (bottom view of open sample cell).

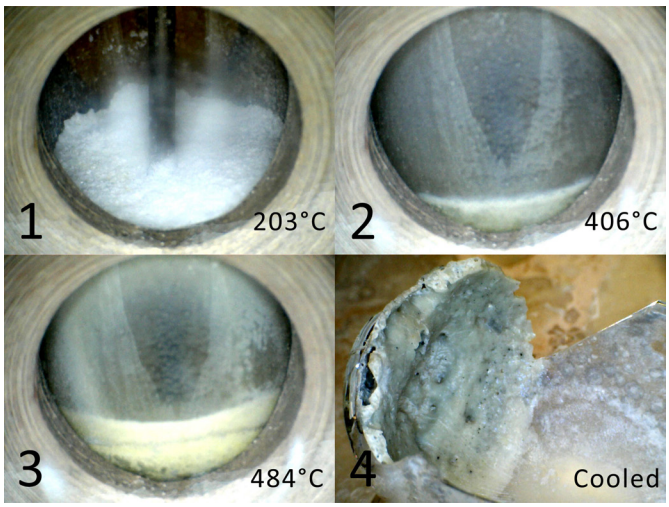

Fig. 5. TPPA of as-received $LiNH_2$ at various temperatures where physical changes were observed during heating with a heat rate of 10 °C/min.

$$LiNH_{2(s)} \rightarrow Li_2NH_{(s)} + NH_{3(g)} \quad (4)$$

At 484 °C, a second layer of molten sample begins to deposit over the first layer on the glass vial with an opaque yellow colour (see Frame 3 of Fig. 5). As the sample cooled, the sudden temperature drop caused the glass vial to crack, revealing the molten product as seen in Frame 4 of Fig. 5. The largest peak position of ammonia-release reported by Yao et al. [26] was at 480 °C, this rapid release of ammonia was due to liquid $LiNH_2$. Therefore, this result is in agreement with the TPD data reported by Yao et al. [26] of as-received $LiNH_2$ as the sample undergoes vigorous bubbling as it transitions from a solid to liquid at 484 °C (see Frame 3 of Fig. 5).

Izuhara, Takeshita and Miyake [27] reported that a mixture of $LiNH_2$ and LiH in a 1:2 M ratio has a melting temperature of 351 °C. Fig. 6 shows the results from the TPPA of $LiNH_2$ and LiH in a 1:2 M ratio. By observation, this system starts as a white powder (see Frame 1 of Fig. 6). The system beings to shrink at 200 °C which can be attributed to the release of H_2 according to Equation (5) and later confirmed by TPD measurements:

$$LiNH_2 + LiH \rightarrow Li_2NH + H_2 \quad (5)$$

Between 400 and 500 °C, the system undergoes an abrupt colour change from white to yellow. Tapia-Ruiz et al. [20] synthesised Li_4NH pellets with an appearance of a yellow/beige colour; therefore, this colour change is a good indication to the formation of Li_4NH. At approximately 531 °C, the system begins to melt with

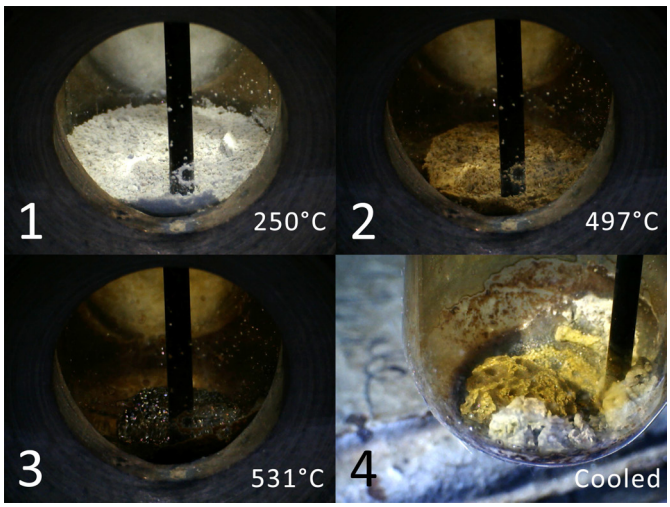

Fig. 6. TPPA of $LiNH_2$ + 2LiH at various temperatures where physical changes were observed during heating with a heat rate of 10 °C/min.

vigorous bubbling and becomes black in appearance (see Frame 3 of Fig. 6) with the evolution of gases (as confirmed by TPD measurements). The evolved gases from the TPD measurement show a release at ~535 °C, the same temperature as observed in TPPA, identified as NH_3, N_2, H_2 or a combination. This black molten state can explain the complications seen in our PCT measurement at these temperatures (sintering and filter blocking). During heating, the evolution of excess gases is vented with a pressure relief valve set to 1 bar. As the sample cools, the gases could be reabsorbed to reverse the appearance of the black colour to a yellow colour (see Frame 4 of Fig. 6), suggesting a solid solution of a mixture containing Li_2NH and Li_4NH. However, it should be noted that the colour change (from yellow to black) may also be a consequence of the temperature.

Fig. 7 shows the results from the TPPA of laboratory synthesised Li_2NH with a heat rate of 10 °C/min. By observation, Li_2NH starts as a grey powder (see Frame 1 of Fig. 7). As Li_2NH is heated to 500 °C, only a small volume change is observed in terms of size but a distinct colour change from grey to white can be seen from 275 to 475 °C. In a successful attempt to retrieve the sample without

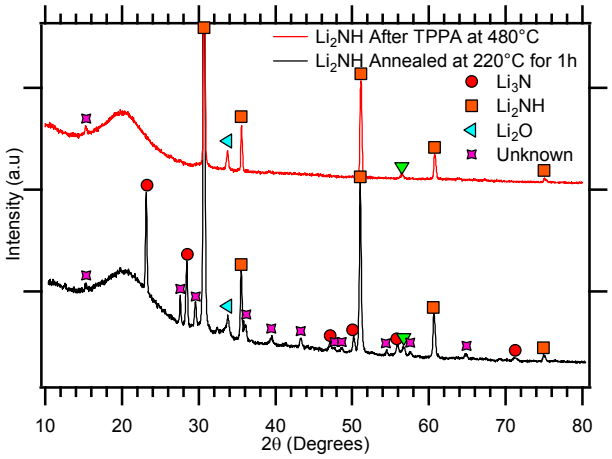

Fig. 8. XRD patterns of Li_2NH after performing a TPPA measurement at 480 °C and synthesised Li_2NH at 220 °C.

having the glass vial break (upon cooling), an XRD of the TPPA sample after it was finished at ~500 °C, showed that the initial sample reaction was incomplete and by doing the TPPA measurement, most of the unknown phase peaks that appeared previously have disappeared (see Fig. 8). After the TPPA measurement, only Li_2NH peaks can be identified along with the appearance of a Li_2O phase that may be due to oxygen contamination from a reaction with the glass vial.

Fig. 9 shows the results from the TPPA of Li_2NH and LiH in a 1:1 M ratio. By observation, this system starts as a grey powder (see Frame 1 of Fig. 9). There is a notable change in sample volume size that starts at 200 °C that can be attributed to the evolution of gases later confirmed by TPD analysis. By 400 °C, the sample appears to have changed from grey to white (see Frame 3 of Fig. 9), this colour change was previously seen in Fig. 7, and from the XRD results in Fig. 8 we can deduce this colour change to be the removal of unknown phases resulting in a high purity of Li_2NH. By 500 °C, it can be seen that the sample concludes with a yellow colour, a colour previously shown to indicate the formation of Li_4NH.

Alongside TPPA measurements, TPD measurements reveal the temperatures at which gases are released. Fig. 10 shows TPD measurements taken up to 600 °C with a heat rate of 2 °C/min.

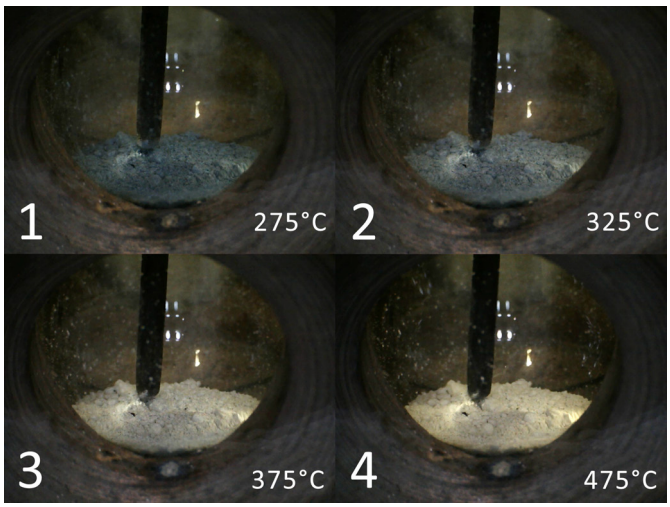

Fig. 7. TPPA of Li_2NH at various temperatures where physical changes were observed during heating with a heat rate of 10 °C/min.

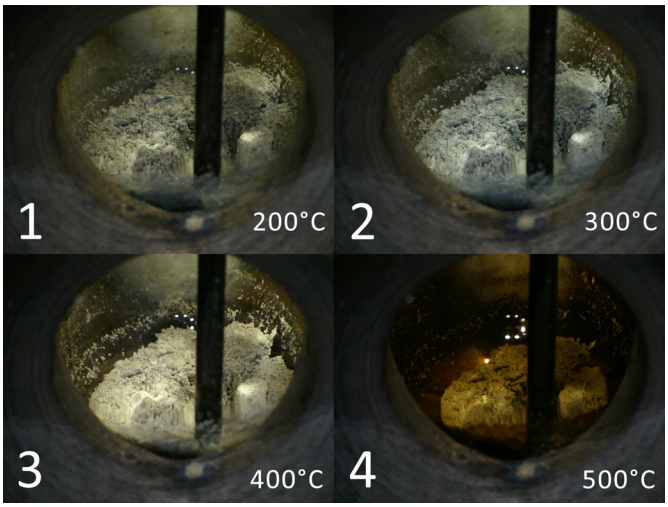

Fig. 9. TPPA of Li_2NH + LiH at various temperatures where physical changes were observed during heating with a heat rate of 10 °C/min.

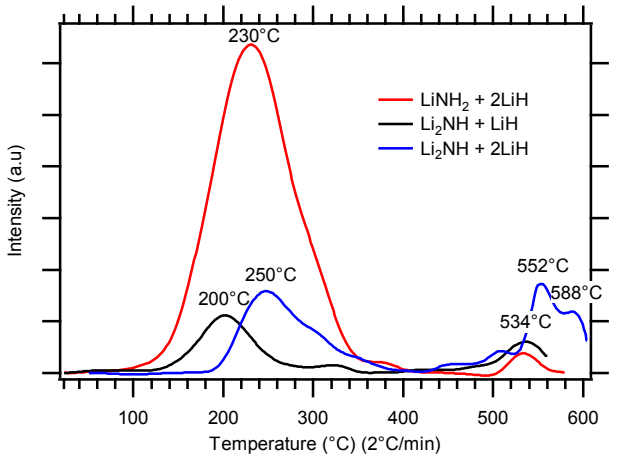

Fig. 10. TPD-600 °C of $LiNH_2$ + 2LiH, Li_2NH + LiH and Li_2NH + 2LiH with a heat rate of 2 °C/min.

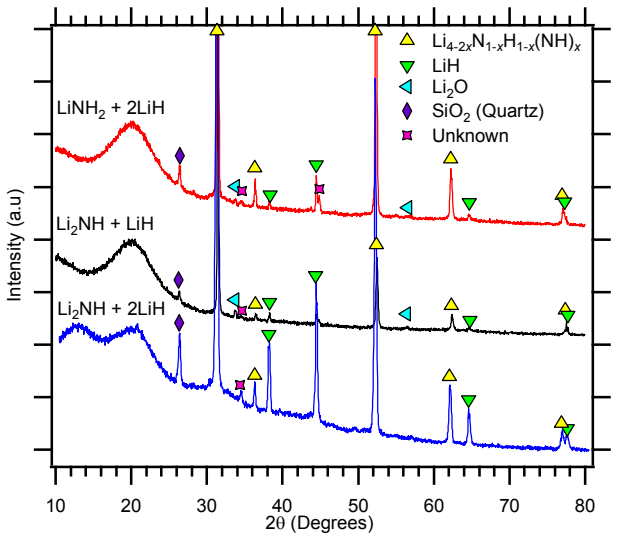

Fig. 11. XRD patterns after TPD to 600 °C for $LiNH_2$ + 2LiH, Li_2NH + LiH and Li_2NH + 2LiH, where $Li_{4-2x}N_{1-x}H_{1-x}(NH)_x$ ($0 \le x \le 1$) is a non-stoichiometric phase.

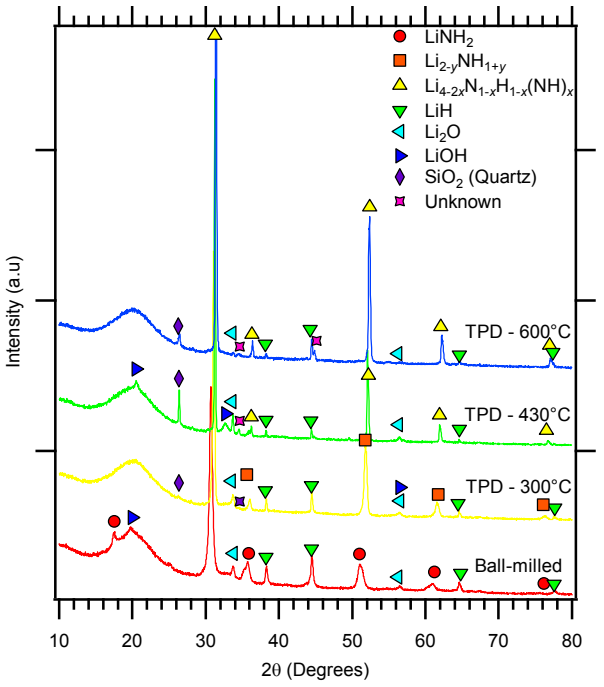

Fig. 12. *Ex situ* XRD patterns of $LiNH_2$ + 2LiH, where $Li_{2-y}NH_{1+y}$ ($0 \le y \le 1$) and $Li_{4-2x}N_{1-x}H_{1-x}(NH)_x$ ($0 \le x \le 1$) are non-stoichiometric phases.

Approximately 100 mg, 100 mg and 300 mg were used for $LiNH_2$ + 2LiH, Li_2NH + LiH and Li_2NH + 2LiH, respectively. It has been widely reported that the amide to imide reaction occurs at approximately 230 °C, which can be seen in the reaction between $LiNH_2$ + 2LiH [17,28,29]. However, the desorption peak that should represent the imide to nitride reaction seems to be absent. A peak with similar intensity to the amide to imide reaction should occur at a temperature above 230 °C, yet only a small peak can be seen at 534 °C. This peak at 534 °C, coincides with the melting behaviour and evolution of gases (bubbling) observed in the TPPA measurements of $LiNH_2$ + 2LiH (see Frame 3 Fig. 6). For the reaction between Li_2NH and LiH, a desorption peak occurs around 200 °C, this peak might correspond to residual $LiNH_2$ reacting with LiH to form Li_2NH, suggesting the synthesis of Li_2NH was incomplete in the ball-milling mixture of Li_2NH + LiH. This desorption peak may also be related to the colour change seen in TPPA measurements from grey to white, where the purity of Li_2NH increases with the removal of unknown phases that can be seen in the XRD results (Fig. 8). Similarly to $LiNH_2$ + 2LiH, a small desorption peak occurs around 534 °C.

The TPD measurement of Li_2NH + 2LiH, showed results similar to the previous two systems (Fig. 10). However, there are temperature differences associated with the first desorption event, occurring at 200 °C, 230 °C and 250 °C for Li_2NH + LiH, $LiNH_2$ + 2LiH and Li_2NH + 2LiH, respectively. Examining the XRD results after each TPD measurement (Fig. 11), we can see that some samples had oxygen contamination, probably caused by poor handling. Therefore, it is quite possible that the oxide phases in those samples had a catalytic effect on the desorption temperature for the first release of H_2. Li_2NH + LiH had higher intensity oxide peaks than $LiNH_2$ + 2LiH, which consequently had a lower temperature for the first desorption event.

X-ray diffraction measurements can identify the phases of a particular sample from TPPA and TPD measurements once they have cooled to room temperature. Fig. 12 shows *ex situ* XRD data of $LiNH_2$ and LiH in a 1:2 M ratio. All TPD measurements were conducted with a heat rate of 2 °C/min starting initially at a pressure near vacuum. By 300 °C, it is apparent that a non-stoichiometric intermediate between the amide and imide ($Li_{2-y}NH_{1+y}$), has already been formed with no Li_3N present. With increasing temperature, there is a decrease in lattice parameter of the lithium imide-nitride hydride ($Li_{4-2x}N_{1-x}H_{1-x}(NH)_x$) structure as the stoichiometry changes, resulting in a 1° peak shift to higher angles. A small amount of lithium oxide can be found due to some contaminants in the starting products and trace amounts of quartz can also be found around 27° due to XRD sample preparation with glass slides.

Having another look at Equation (3a):

$$(1-x)Li_4NH + xLi_2NH \rightarrow Li_{4-2x}N_{1-x}H_{1-x}(NH)_x \quad (3a)$$

The reversibility of this reaction was tested using PCT measurements, therefore Li_2NH and LiH were mixed in a 1:2 M ratio. With LiH in excess, this ensures the optimal formation of Li_4NH, eliminating any possible limiting reagents that would hinder the reaction pathway seen in Equation (3) to accurately test the reversibility of this reaction.

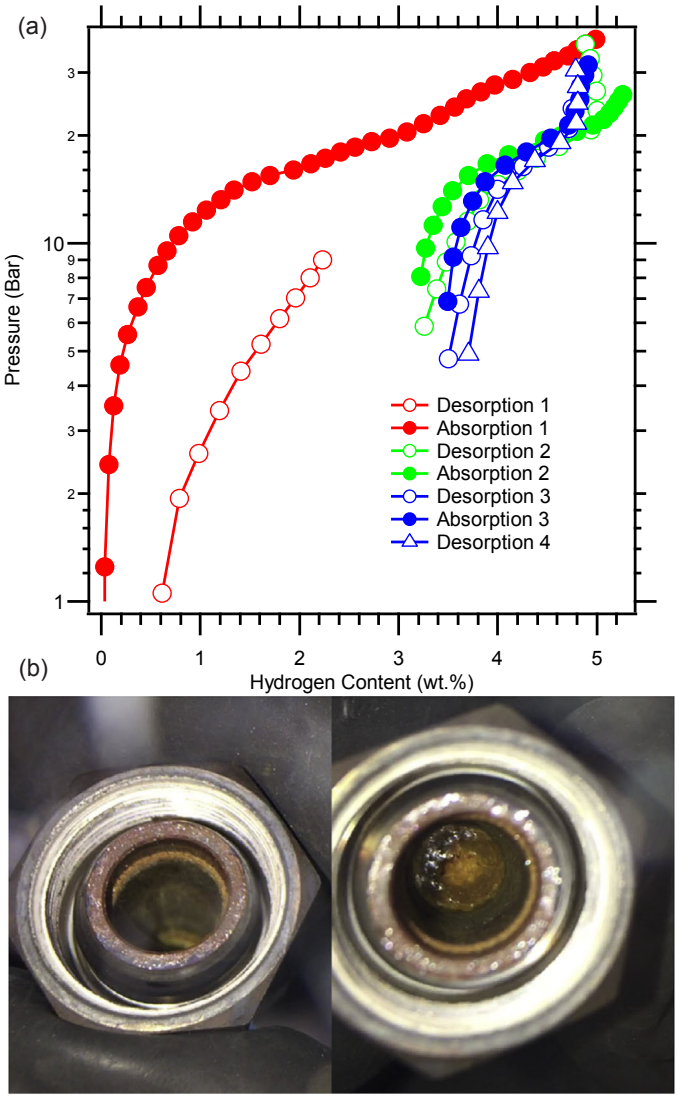

Fig. 13. (a) PCT measurements of $Li_2NH + 2LiH$ at 480 °C and (b) images of the sample state after the PCT measurements were completed.

Fig. 13a shows the PCT measurements of $Li_2NH + 2LiH$ at 480 °C. After the first absorption measurement, the reversibility of the sample is severely hindered with a decrease in hydrogen capacity due to molten sample affecting the porous filter. It is possible that any $LiNH_2$ that is formed at this temperature immediately melts to form a solid solution. Fig. 13b shows that upon cooling to room temperature, the sample was able to sinter along the walls of the sample cell from the formation of bubbles at high temperature as seen in TPPA measurements. It was also found that the molten solid would compact into a dense mass that often required a drill bit to remove (e.g. of dense mass in Fig. 14). Therefore, the reversibility of Li_4NH having excess LiH cannot be measured due to the sample melting above 480 °C.

Fig. 15 shows the *ex situ* XRD data of Li_2NH and LiH in a 1:2 M ratio. The final product is determined to be lithium imide-nitride hydride ($Li_{4-2x}N_{1-x}H_{1-x}(NH)_x$). High oxygen contamination can be seen on the hydrogen cycled sample because of an air leak found in the sample cell, which resulted in a high peak intensity for Li_2O. These results show no difference between the *ex situ* XRD results seen previously in Fig. 12.

The amide to imide reaction ($LiNH_2 + 2LiH$) was initially

Fig. 14. Image of $Li_2NH + 2LiH$ taken at RT after TPD measurement up to 600 °C.

measured to reproduce the results of Chen et al. [17]. In the initial attempts, there was difficulty in obtaining a Li_3N product as reported by Chen et al. [17], despite having similar experimental conditions. However, the main objective was to measure the reversibility of the imide to nitride reaction ($Li_2NH + LiH$) as the operation temperature range would be more suitable for thermal storage. In both reactions: $LiNH_2 + 2LiH$ and $Li_2NH + LiH$, the formation of a nitride product was absent. However, we are consistent in achieving a non-stoichiometric product proposed by Tapia-Ruiz et al. [20] as lithium imide-nitride hydride that includes a complex reaction pathway of a solid-solution formed between Li_4NH and Li_2NH (Equation (3)). This complex pathway suggests that the reversibility of this reaction can be improved if the formation of

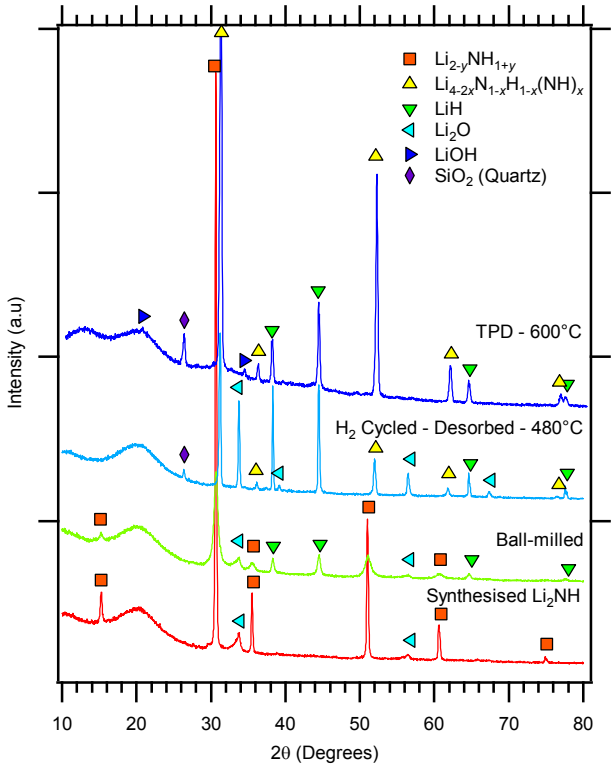

Fig. 15. *Ex situ* XRD patterns of $Li_2NH + 2LiH$, where $Li_{2-y}NH_{1+y}$ ($0 \le y \le 1$) and $Li_{4-2x}N_{1-x}H_{1-x}(NH)_x$ ($0 \le x \le 1$) are non-stoichiometric phases.

Li_4NH was more abundant, i.e. if LiH was no longer a limiting reagent. Therefore, a third reaction was measured ($Li_2NH + 2LiH$) that had LiH in excess in the hope of achieving a reversible reaction using Li_4NH, but the results showed little difference as the product phases from these systems have similar crystallographic structures resulting in overlapping peak positions in XRD patterns. The reversibility of this sample at high temperatures was found to be very poor due to the sample melting into a solid solution as seen in TPPA measurements.

As seen in the PCT measurements, the reactions: $LiNH_2 + 2LiH$, $Li_2NH + LiH$ and $Li_2NH + 2LiH$, all exhibited poor kinetics due to the molten state achieved at high temperatures that was confirmed by TPPA. This contributes to the complexity of problems that can occur in these systems. The added difficulty found in conducting these measurements were the extra factors that were needed to be taken into consideration, such as the diffusion and absorption of hydrogen when operating above the sample cell temperature range for 316 stainless steel and the engineering factors such as leaks that can be found through repeated use of the same sample cell.

5. Conclusions

Temperature programmed desorption measurements revealed similar hydrogen desorption peaks for the reactions: $LiNH_2 + 2LiH$ (Reaction 1), $Li_2NH + LiH$ (Reaction 2) and $Li_2NH + 2LiH$ (Reaction 3); with a large desorption peak occurring around 230 °C and a smaller peak around 530 °C. TPPA revealed that at high temperatures up to 500 °C, Reaction 1 melted into a solid solution and measurements with Reaction 2, also found a molten sample upon cooling. XRD revealed that for Reaction 1, 2 and 3, the final product was a mixed imide-nitride phase namely a lithium imide-nitride hydride phase ($Li_{4-2x}N_{1-x}H_{1-x}(NH)_x$). PCT measurements of Reaction 1 and 2 were performed to analyse the thermodynamics and kinetics of the sample including its reversibility, but proved difficult to measure because of the melting problems revealed by TPPA.

Looking back through all the results, it can be concluded that this system may not be suitable for high temperature thermal storage, not just due to its complexity involving non-stoichiometric phases but because the sample was not fully reversible as seen in PCT measurements at high temperatures. From a thermal storage application standpoint, a molten sample would only create a series of engineering problems for these systems if lithium imides and nitrides were to be pursued in thermal storage technologies.

Acknowledgements

The authors acknowledge the financial support of the Australian Research Council (ARC) for ARC Linkage grant LP120101848, LP150100730 and ARC LIEF grants LE0989180 and LE0775551, which enabled the XRD and gas sorption studies to be done. TN acknowledges the financial support of Curtin University for providing a Curtin University Post-Graduate Scholarship (CUPS) and the Australian Commonwealth Government for providing an Australian Post-Graduate Award (APA). The authors would also like to acknowledge Dr. Mark Paskevicius for his assistance in collecting the TPPA data.

References

[1] Geoscience Australia, BREE, Australian Energy Resource Assessment, second ed., 2014. Canberra.
[2] International Energy Agency, World Energy Outlook 2010, in, Paris, 2010.
[3] G.D. Sandrock, E. Snape, Reaction heat storage method for hydride tanks, in, Ergenics, Inc. (Wyckoff, NJ), US Patent, 1986.
[4] G.G. Libowitz, Metal hydrides for thermal energy storage, in: 9th Intersociety Energy Conversion Engineering Conference, Proceedings, San Francisco, California, 1974, pp. 322–325.
[5] B. Bogdanović, A. Ritter, B. Spliethoff, Active MgH_2–Mg systems for reversible chemical energy storage, Angew. Chemie Int. Ed. Engl. 29 (1990) 223–234.
[6] B. Bogdanović, K. Bohmhammel, B. Christ, A. Reiser, K. Schlichte, R. Vehlen, U. Wolf, Thermodynamic investigation of the magnesium–hydrogen system, J. Alloys Compd. 282 (1999) 84–92.
[7] M. Groll, A. Isselhorst, M. Wierse, Metal hydride devices for environmentally clean energy technology, Int. J. Hydrogen Energy 19 (1994) 507–515.
[8] D.N. Harries, M. Paskevicius, D.A. Sheppard, T.E.C. Price, C.E. Buckley, Concentrating solar thermal heat storage using metal hydrides, Proc. IEEE 100 (2012) 539–549.
[9] M. Fellet, C.E. Buckley, M. Paskevicius, D.A. Sheppard, Research on metal hydrides revived for next-generation solutions to renewable energy storage, MRS Bull. 38 (2013) 1012–1013.
[10] Q. Lai, M. Paskevicius, D.A. Sheppard, C.E. Buckley, A.W. Thornton, M.R. Hill, Q. Gu, J. Mao, Z. Huang, H.K. Liu, Z. Guo, A. Banerjee, S. Chakraborty, R. Ahuja, K.-F. Aguey-Zinsou, Hydrogen storage materials for mobile and stationary applications: current state of the art, ChemSusChem 8 (2015) 2789–2825.
[11] D.A. Sheppard, T.D. Humphries, C.E. Buckley, Sodium-based hydrides for thermal energy applications, Appl. Phys. A 122 (2016) 1–13.
[12] A.H. Abedin, M.A. Rosen, A critical review of thermochemical energy storage systems, Open Renew. Energy J. 4 (2011) 42–46.
[13] D. Gutkowicz-Krusin, I. Procaccia, J. Ross, On the efficiency of rate processes. Power and efficiency of heat engines, J. Chem. Phys. 69 (1978) 3898–3906.
[14] E. Rönnebro, G. Whyatt, M. Powell, M. Westman, F. Zheng, Z. Fang, Metal hydrides for high-temperature power generation, Energies 8 (2015) 8406.
[15] Z. Xiong, G. Wu, J. Hu, P. Chen, Ternary imides for hydrogen storage, Adv. Mater. 16 (2004) 1522–1525.
[16] J. Zhang, Y.H. Hu, Intermediate species and kinetics of lithium imide decomposition, Int. J. Hydrogen Energy 37 (2012) 10467–10472.
[17] P. Chen, Z. Xiong, J. Luo, J. Lin, K.L. Tan, Interaction of hydrogen with metal nitrides and imides, Nature 420 (2002) 302–304.
[18] J.W. Makepeace, M.O. Jones, S.K. Callear, P.P. Edwards, W.I.F. David, *In situ* X-ray powder diffraction studies of hydrogen storage and release in the Li–N–H system, Phys. Chem. Chem. Phys. 16 (2014) 4061–4070.
[19] D.J. Bull, E. Weidner, I.L. Shabalin, M.T.F. Telling, C.M. Jewell, D.H. Gregory, D.K. Ross, Pressure-dependent deuterium reaction pathways in the Li–N–D system, Phys. Chem. Chem. Phys. 12 (2010) 2089–2097.
[20] N. Tapia-Ruiz, N. Sorbie, N. Vaché, T. Hoang, D. Gregory, Rapid microwave synthesis, characterization and reactivity of lithium nitride hydride, Li_4NH, Materials 6 (2013) 5410–5426.
[21] R. Marx, Reindarstellung und Kristallstruktur von Lithiumnitridhydrid, Li_4NH, Li_4ND, Z. für Anorg. Allg. Chem. 623 (1997) 1912–1916.
[22] Y.H. Hu, E. Ruckenstein, Ultrafast reaction between Li_3N and $LiNH_2$ to prepare the effective hydrogen storage material Li_2NH, Ind. Eng. Chem. Res. 45 (2006) 4993–4998.
[23] Y. Kojima, Y. Kawai, IR characterizations of lithium imide and amide, J. Alloys Compd. 395 (2005) 236–239.
[24] X.B. Yu, Z.X. Yang, Y.H. Guo, S.G. Li, Thermal decomposition performance of $Ca(BH_4)_2$/$LiNH_2$ mixtures, J. Alloys Compd. 509 (Suppl. 2) (2011) S724–S727.
[25] R. Juza, K. Opp, Metallamide und Metallnitride, 24. Mitteilung. Die Kristallstruktur des Lithiumamides, Z. für Anorg. Allg. Chem. 266 (1951) 313–324.
[26] J.H. Yao, C. Shang, K.F. Aguey-Zinsou, Z.X. Guo, Desorption characteristics of mechanically and chemically modified $LiNH_2$ and ($LiNH_2$ + LiH), J. Alloys Compd. 432 (2007) 277–282.
[27] T. Izuhara, H.T. Takeshita, H. Miyake, Thermodynamic property change in Li–N–H hydrogen storage system by melting lithium amide, Nippon Kinzoku Gakkaishi/J. Jpn. Inst. Met. 75 (2011) 115–121.
[28] T. Ichikawa, S. Isobe, N. Hanada, H. Fujii, Lithium nitride for reversible hydrogen storage, J. Alloys Compd. 365 (2004) 271–276.
[29] H.Y. Leng, T. Ichikawa, S. Isobe, S. Hino, N. Hanada, H. Fujii, Desorption behaviours from metal–N–H systems synthesized by ball milling, J. Alloys Compd. 404–406 (2005) 443–447.

Appendix D: COPYRIGHT PERMISSIONS

Every reasonable effort has been made to acknowledge the owners of copyright material. I would be pleased to hear from any copyright owner who has been omitted or incorrectly acknowledged.

ELSEVIER LICENSE
TERMS AND CONDITIONS

May 16, 2017

This Agreement between Tam Nguyen ("You") and Elsevier ("Elsevier") consists of your license details and the terms and conditions provided by Elsevier and Copyright Clearance Center.

License Number	4110740613938
License date	May 16, 2017
Licensed Content Publisher	Elsevier
Licensed Content Publication	Journal of Alloys and Compounds
Licensed Content Title	Lithium imide systems for high temperature heat storage in concentrated solar thermal systems
Licensed Content Author	Tam T. Nguyen,Drew A. Sheppard,Craig E. Buckley
Licensed Content Date	5 September 2017
Licensed Content Volume	716
Licensed Content Issue	n/a
Licensed Content Pages	8
Start Page	291
End Page	298
Type of Use	reuse in a thesis/dissertation
Portion	full article
Format	both print and electronic
Are you the author of this Elsevier article?	Yes
Will you be translating?	No
Order reference number	01
Title of your thesis/dissertation	Concentrated Solar Thermal Energy Storage using Amide-Hydride systems
Expected completion date	Jul 2017
Estimated size (number of pages)	250
Elsevier VAT number	GB 494 6272 12
Requestor Location	Tam Nguyen [redacted] [redacted] Australia Attn: Tam T Nguyen
Total	0.00 AUD